UNIVERSITY OF ZULULAND

Novel Precursors for the Synthesis of Metal Selenide Nanoparticles, Thin Films and Alloys

by

Malik Dilshad Khan

201546688

MSc & MPhil (Quaid-I-Azam University, Islamabad)

Thesis

Submitted in Fulfilment of the Requirements for the Degree

DOCTOR OF PHILOSOPHY IN CHEMISTRY

Faculty of Science and Agriculture

University of Zululand

Supervisor: Prof. Neerish Revaprasadu

Department of Chemistry, Private Bag X1001, KwaDlangezwa 3886, South Africa.

DECLARATION

I hereby declare that the work described in this thesis entitled "**Novel Precursors for the Synthesis of Metal Selenide Nanoparticles, Thin Films and Alloys**" is my own work and has not been submitted in any form for another degree or qualification of the University of Zululand or any other University/Institution of tertiary education. Information derived from the published or unpublished work of others has been acknowledged in the text and a list of references is given.

Name: Malik Dilshad Khan

Signature:_____

Date:_____

CERTIFICATION BY SUPERVISOR

This is to certify that this work was carried out by Mr. Malik Dilshad Khan in the Department of Chemistry, University of Zululand and is approved for submission in fulfilment of the requirements for the degree of Doctor of Philosophy in Chemistry.

.....

Supervisor

Neerish Revaprasadu (PhD)

Professor of Inorganic Chemistry

Department of Chemistry, University of Zululand,

KwaDlangezwa, South Africa

ACKNOWLEDGEMENT

I owe my profound thanks and deepest gratitude to Almighty ALLAH, Creator of the universe, and worthy of all praises, who blessed me with the potential, ability and determination to complete this research work. This is His extreme blessing on me for which I cannot adequately thank.

I wish to express my heartfelt thanks, respect and admiration to my supervisor, Prof. Neerish Revaprasadu for his continuous guidance, encouragement, commitment and paramount support during the course of this study. He is an excellent advisor and a good friend. I also thank the love and hospitality of his wife Shaneera Revaprasadu and their kids Manav, Mahee and Aryana. I gratefully acknowledge the financial support from NRF/DST South Africa through SARChI granted to Prof. N. Revaprasadu, which enabled me to pursue this study smoothly.

I am immensely indebted to Prof. Dr. Paul O'Brien and Dr. Mohammad Azad Malik, School of Chemistry and Materials, The University of Manchester, for their assistance, useful advice and suggestions. They provided me the key knowledge for my research activities and enabled me to learn more about this field. I feel very proud to be directly guided by some of the most experts of their field. I would also like to thank to all research fellows of the O'Brien group, and especially Ghulam Murtaza, Dr. Masood Akhtar, Tahani Al-Qahtani and Dr. David Lewis for their commendable help, whenever I required. This acknowledgment will be incomplete if I do not appreciate with thanks, the moral support and wonderful company of my friends Mudabbar Sultan and Dr. Omer Rasheed.

I am equally thankful to the staff of Chemistry Department of University of Zululand and my colleagues, Sixberth Mlowe, Rekha Dunpall, Zibane Welcome, Charles Gerves, Masikane Siphamandla, Ginena Bildard, Mzimela, Sandile, Zikhona and research visitor Mohammad Aamir for their assistance, discussions and moral support. I also acknowledge warm hospitality, love and constant care from my friends Mohammad Waseem Wassi, Mohammad Usman, Nadeem Abbas, Imran bhai and Rashid for making my stay in South Africa wonderful and as memorable as possible.

Last, but not least, I would like to thank my family for their unconditional support and prayers, which played a key role in my research efforts. I wish to thank my parents and siblings for teaching me to be patient, honest, obliging, generous, and hardworking.

Abstract

Metal selenides are important semiconducting materials and are highly useful in various electronic and/or thermoelectric devices. Different synthetic protocols are available for preparation of metal selenide nanoparticles and/or thin films. Nonetheless, the use of single source precursors is usually advantageous, as they can be used for the synthesis of metal chalcogenide nanocrystals, and are equally suitable for the deposition of thin films. Furthermore, a better control over stoichiometry and phase can be achieved, due to preformed bonds between metal and chalcogen atom. Numerous sulfur based single source precursors have been used successfully for synthesis of variety of metal sulfide nanoparticles and/or deposition of thin films. However, the use of single source precursors with higher chalcogeno congeners, are not well explored. The prime reason is the difficulty in the synthesis of Se/Te based precursors. Only a limited starting materials are available and that too are usually highly toxic, such as, phosphines and/or carbon disulfide. Hence, a facile synthetic route, using comparatively less toxic materials, is highly desired for the synthesis of selenium containing molecular precursors. In this thesis, we have introduced a new one-pot synthesis of metal (Bi, Sn and Sb) selenobenzoate complexes and established their suitability for the synthesis of respective metal selenide nanoparticles, thin films and alloys.

The thesis is divided into seven chapters, in which the first chapter gives a comprehensive literature review of all the selenium based single source precursors used until the present for the synthesis of metal selenide nanocrystals and/or thin films. The second chapter describes the synthesis of selenobenzoate ligand and its antimony complex *i.e. tris*(selenobenzoato)Sb(III) complex. The crystal structure of the complex was elucidated and the complex was used as a suitable single source precursor for the synthesis of Sb_2Se_3 nanorods by hot injection method and thin films were deposited by the aerosol assisted chemical vapor deposition (AACVD) method. The nanorods synthesized by colloidal method were used for water splitting application.

In third chapter, the similar synthetic strategy was used to prepare *tris*(selenobenzoato)Bi(III) complex and the decomposition of the molecular precursor by hot injection method yields Bi_2Se_3 nanosheets. Thin films were also deposited at different temperatures on glass substrates and the water splitting efficiency of the

oleylamine capped nanosheets was investigated. Both Sb_2Se_3 and Bi_2Se_3 shows p-type behavior as cathodic currents were observed for both materials. Similarly, the fourth chapter entails the detail about the use of *bis*(selenobenzoato)Sn(IV) for the deposition of SnSe thin films and nanosheets. The electrochemical studies indicate bifunctional behavior and the material can behave either as cathodic material and/or anodic material by changing the voltage.

In chapter 5 and 6, thio- analogues of *bis*(selenobenzoato)Sn(IV) and *tris*(selenobenzoato)Sb(III) *i.e. bis*(thiobenzoato)Sn(IV) and *tris*(thiobenzoato)Sb(III) complexes were synthesized and mixture of both chalcogeno- complexes were used to prepare solid solutions ($Sb_2(S_xSe_{1-x})_3$ and SnS_xSe_{1-x}) in entire range with excellent stoichiometric control. $Sb_2(S_xSe_{1-x})_3$ was prepared by colloidal route using oleylamine as solvent and capping agent, band gap tuning was observed. For SnS_xSe_{1-x} solid solution, in addition to colloidal synthesis, solvent-less route was also used and the effect of both routes on structural behavior was investigated.

Chapter 7 gives a brief summary of all the chapters and the potential future research plan.

Table of Contents

Chapter 2. Synthesis of Sb_2Se_3 nanorods and deposition of thin films by AACVD: Potential catalyst for photoelectrochemical water reduction

Chapter 3. Facile Synthesis of Bi_2Se_3 Nanosheets and Thin Films by AACVD: Potential Catalyst for Water Reduction

Chapter 7. Summary, Conclusion and Future work

List of Figures

List of Tables

List of Schemes

Abbreviations

AACVD	Aerosol assisted chemical vapour deposition
^{t}Bu-	Tertiary butyl
CHN	Carbon, hydrogen and nitrogen
2D	Two dimensional
DDT	Dodecanethiol
DTG	Differential thermogravimetric
Et-	Ethyl
EDX	Energy Dispersive X-ray
FTO	Fluorine doped tin oxide
GaAs	Gallium Arsenide
HDA	Hexadecyl amine
HR-TEM	High resolution-Transmission electron microscopy
ICDD	International centre for diffraction data
ITO	Indium doped tin oxide
LPCVD	Low pressure chemical vapour deposition
LSV	Linear sweep voltametry
Me-	Methyl
MOCVD	Metal organic chemical vapour deposition
NMs	Nanomaterials
ODE	Octadecene
OLAc	Oleic acid
OLA	Oleylamine
Ph	Phenyl
^{i}Pr	*iso*-propyl
PL	Photoluminescence
PVP	Polyvinyl pyrrolidone
QDs	Quantum dots
SAED	Selective area electron diffraction
SEM	Scanning electron microscopy

Si	Silicon
SiO_2	Silica
SSP	Single source precursor
TBP	Tributyl phosphate
TGA	Thermo gravimetric analyser
TM	Transition metal
TOP	Trioctylphosphine
TOPO	Trioctylphosphineoxide
UV/Vis/NIR	Ultra violet/Visible/Near Infrared
p-XRD	Powder X-ray powder diffraction

List of Publications

Publications from thesis work:

1. Synthesis of Sb_2Se_3 nanorods and thin films from novel molecular precursor and photoelectrochemical water reduction catalysis (Solar Energy)
2. Facile Synthesis of Bi_2Se_3 Nanosheets and Thin Films from Novel Single Source Precursor: Potential Catalyst for Water Reduction (Submitted)
3. Organotin Selenobenzoate: Novel precursor for the synthesis of SnSe nanosheets and thin films by AACVD (*In press*, Dalton Transactions)
4. Facile synthesis of $SnS_{1-x}Se_x$ solid solution from single source precursors by colloidal and solventless routes (Submitted)
5. Synthesis, characterization and band gap tuning of the $Sb_2(S_{1-x}Se_x)_3$ solid solution using single source precursors (Submitted)
6. Progress in selenium based single source precursors for metal selenide thin films and nanomaterials (Submitted)

Other Publications:

1. Synthesis and characterization of PbS nanoparticles in an ionic liquid using single and dual source precursors (Materials Science and Engineering: B 227, 116-121)
2. Phase pure deposition of flower-like thin films by aerosol assisted chemical vapor deposition and solvent mediated structural transformation in copper sulfide nanostructures (Thin Solid Films 638, 338-344)
3. Cesium Lead Halide Perovskite Nanostructures: Tunable Morphology and Halide Composition (The Chemical Record)
4. A Facile Route to Cesium Lead Bromoiodide Perovskite Microcrystals and Their Potential Application as Sensors for Nitrophenol Explosives (European Journal of Inorganic Chemistry 2017 (31), 3755-3760)
5. Synthesis of Hybrid to Inorganic Quasi 2D-Layered Perovskite Nanoparticles (ChemistrySelect 2 (20), 5595-5599)
6. Controlled synthesis of all inorganic $CsPbBr_2I$ perovskite by non-template and aerosol assisted chemical vapour deposition (Materials Letters 190, 244-247)

7. Tuning the Phase and Shape of Copper Sulfide Nanostructures Using Mixed Solvent Systems (ChemistrySelect 1 (18), 5982-5989)
8. Deposition of morphology-tailored PbS thin films by surfactant-enhanced aerosol assisted chemical vapor deposition (Materials Science in Semiconductor Processing 46, 39-45)
9. Comparative temperature and surfactants effect on the morphologies of FeSe thin films fabricated by AACVD from a single source precursor with mechanism and photocatalytic activity (Materials Chemistry and Physics 159, 152-158)
10. A simple route to alkylamine capped antimony nanoparticles (Materials Letters 145, 239-242)
11. Effect of surfactants on the morphology of FeSe films fabricated from a single source precursor by aerosol assisted chemical vapour deposition (Journal of Chemical Sciences 127 (3), 499-507)
12. Aerosol-assisted chemical vapour deposition for iron selenide thin films from single source ferrocene-incorporated selenourea precursor in the presence of surfactants (Australian Journal of Chemistry 68 (2), 298-306)
13. Deposition of cadmium sulfide and zinc sulfide thin films by aerosol-assisted chemical vapors from molecular precursors (Turkish Journal of Chemistry 39, 169-178)
14. Investigation of PbS nanocrystals sensitized extremely thin absorber (ETA) solar cell (Materials Science in Semiconductor Processing 36, 20-26)
15. Phase-pure fabrication and shape evolution studies of SnS nanosheets (New Journal of Chemistry 39 (12), 9569-9574)
16. Iron selenide films by aerosol assisted chemical vapor deposition from single source organometallic precursor in the presence of surfactants (Thin Solid Films 567, 58-63)
17. Efficient nanostructured supercapacitor $AgBiS_2$ (Schapbachite) synthesized by using xanthates (Submitted)
18. New examples of phase control in the preparation of copper sulfide nanoparticles and deposition of thin films by AACVD from *bis*(piperidinedithiocarbamato)copper(II) complex (Submitted)

19. Preparation of cobalt sulfide thin films and nanoparticles by different routes (Submitted)
20. Xanthate Complexes for the Synthesis of ABX_2/AB_2X_4 Minerals and/or Some Important Materials by Low Temperature Melt Methods (Submitted)

Chapter # 1

Introduction and Literature Review

1.1 Introduction

The physical and chemical properties of nanomaterials are changed significantly when moving from bulk to the nanoscale range. Although, nanomaterials in the form of colorants or decorative materials have been in use for centuries, interest in them grew exponentially in the mid to late 19th century, when their true potential was realized. The synthesis of the gold nanoparticles by the colloidal synthesis was pioneered by Turkevich as early as in the 1950s.[1] Similarly, in the 1960s, the Stober method was established for the colloidal synthesis of monodispersed, size controlled silica.[2] NASA introduced a ferrofluid *i.e.* aqueous and/or organic suspension of iron oxide nanoparticles as a liquid rocket fuel.[3] Soon one of the earliest commercial product, in the form of sunscreen containing nanoparticles of TiO_2 and ZnO, appeared in the market during the 1970s. Current developments in nanotechnology is communicated effectively on different forums (e.g. http://www.nanotechproject.org)) along with their impact on health and the environment (http://cben.rice.edu/showhome.aspx). In the 1980s, quantum dots of CdS and CdSe were investigated for their semiconducting properties. A new interesting aspect of size dependent band gap tuning was discovered, also defined as the quantum confinement effect.[4]

Recently, progress in the synthesis and applications of nanomaterials has reached such a diversified level where numerous inorganic elemental and compound materials have found an application niche. Elemental nanoparticles such as Pt and Pd are used as an efficient catalysts in colloidal organic synthesis, whereas silver nanoparticles are used as suitable antimicrobial agents with enhanced activity.[5, 6] Likewise, nanostructured elemental metals and/or alloys show superparamagnetic properties. They show a high potential for use in magnetic storage devices, as magnetization of each atom can serve to store information.[7, 8] In energy conversion materials, not only size miniaturization but also effective motion of the electrons contributes towards enhancing efficiency. A typical example of such system is titania, which in the bulk state is a non-

conductor but due to the efficient electron transport in nanodimensions, it achieves a high efficiency in dye sensitized solar cells.[9] A high efficiency of 15 % was also achieved by using Si, $CuInGa(S/Se)_2$ (CIGS/Se) or CdSe nanoparticles as a light absorbing layer.[10-14]

Similarly, the high surface area of nanomaterials is of importance in lithium ion batteries, supercapacitors and fuel cells. For instance, an increase in charging and discharging rate was observed for nano based Li ion batteries, therefore cathodic materials such as $LiMnO_2$, $LiCoO_2$, $LiNiO_2$ or $LiFePO_4$ are investigated intensively.[15-17] On the other hand, anode materials consisting of Li alloys ($Li_{4.4}Sn$, Li_xB and $Li_{4.4}Si$ etc.) greatly surpassed the capacity of conventional graphite electrodes.[18-20] In fuel cells, the introduction of cathodic nanomaterials such as $LaFe_{0.8}Co_{0.2}O_3$ (LSCF), $LaMnO_3$ (LSM), or $LaFeO_3$ (LSF) results in decreased process temperature with high turnover.[21]

Thermoelectric materials are used to convert thermal energy into electric energy. The figure of merit of thermoelectric devices can be determined by a dimensionless factor *ZT*, and the expression (equation 1.1) includes Seebeck coefficient (*S*), thermal (κ) and electrical conductivity (σ) and temperature.[22]

$$Z = S^2 \kappa T \kappa^{-1} \qquad \text{(equation 1.1)}$$

The equation indicates that the quality of thermoelectric devices may depend on, seebeck coefficient, electrical conductivity and thermal conductivity. In 1993, Dresselhaus *et al*. proposed by theoretical calculations that the thermoelectric efficiency of Bi_2Te_3 can be enhanced significantly when the bulk structure is thinned down to 2D nanosheets.[23, 24] Later on, it was confirmed experimentally by Venkatasubramanian *et al*. that ZT values of almost 2.4 were achieved by epitaxial growth of Sb_2Te_3-Bi_2Te_3 layers at room temperature.[25]

The mechanical properties of nanomaterials such as hardness, modulus of elasticity and ductility are also very different than their bulk counterparts.[26] It was observed that the polyurethane paints, blended with SiO_2 nanoparticles, provide better wear and scratch resistant properties.

The applications of nanomaterials have been explored in numerous fields, and their superior nature as compared to the bulk materials is well established. However, their properties are strongly dependant on their microstructural aspects such as stoichiometry (composition), arrangement of atoms and size of particles. A slight variation of any element in the composition of the binary or ternary compound nanoparticles can significantly alter the properties of the materials.[27, 28] Hence, considerable care and attention is required in designing suitable synthetic routes which can provide reproducible results with tailored size, morphology and required composition.

Considerable progress has been made in developing synthetic routes for the preparation of nanoparticles and thin films. However, the use of the dual/multi source method for the thin films or nanoparticles has an inherent disadvantage of maintaining exact composition. The composition may vary from batch to batch and also the different reactivity of the precursors can result in slight alteration in chemical composition of the synthesized nanoparticles. Nevertheless, the use of single source precursors (SSPs) has certain advantages over other routes. In SSPs, there is a pre-existing bond between metal and chalcogen atom, which yields a product with consistent and better composition and also fewer defects.

1.2. Essential features of single source precursors

Single source precursors are equally suitable for nanoparticles synthesis as well as deposition of thin films. While designing new single source precursors, there are certain requirements which a precursor must fulfil, in order to be regarded as a suitable candidate for nanoparticles synthesis and thin film deposition.

The prime requirement is the purity of the SSP, as impurities can lead to stoichiometric variation along with the formation of some undesirable by-products. The synthetic protocol and the purification/recrystallization of the product must ensure high purity and high yield. The synthesis must be simple and the steps involved must be as few as possible. The reagents used must be non-toxic and/or alternative reagents with low toxicity must be used where

unavoidable. The complexes must be stable enough for easy characterization and storage for long duration in later use. If the protocol is successful at the laboratory level, the scale-up to bulk level must not be tedious and, the reagents and/or process must be cost effective.

In the case of thin films deposition by low pressure-chemical vapor deposition (LP-CVD), the precursor must be volatile below its decomposition temperature. Presently, CVD methods have been modified, for example in aerosol assisted-chemical vapor deposition (AA-CVD), volatility is no longer required, although good solubility in suitable solvent is important for better deposition. The precursor must decompose completely and cleanly at the surface of the substrate at elevated temperature and the by-products must be removed. A low decomposition temperature of the precursor is preferable, making the process environmentally friendly. A precursor may not have all the required properties, but properties of different precursors can be compared and the one which fulfils most of the requirements is a suitable precursor.

1.3. Selenium based single source precursors

Numerous molecular precursors have been used for the synthesis of metal chalcogenide nanomaterials and thin films by different techniques. In general sulfur based precursors have been extensively explored, but work on selenium and tellurium precursors is not well reported. The main focus of this study is to explore selenium based single source precursors, as such only selenium containing ligands, used to prepare metal selenide nanoparticles and thin films will be reviewed.

1.3.1 Diselenoimidophosphinate complexes

The bidentate organophosphorus ligand and its complexes are known for quite some time, but later resurgence of interest was observed for their use as single source precursors. The chalcogenide atoms act as donor atoms which underwent ring closure by chelating to the same metal centre, and are linked by P-N-P as a bridging unit. The generalized synthesis of the ligand and complex is shown in

Scheme 1.1, and involves reaction between dialkyl/arylchlorophosphine with hexamethyldisilazine and selenium in toluene under inert conditions.

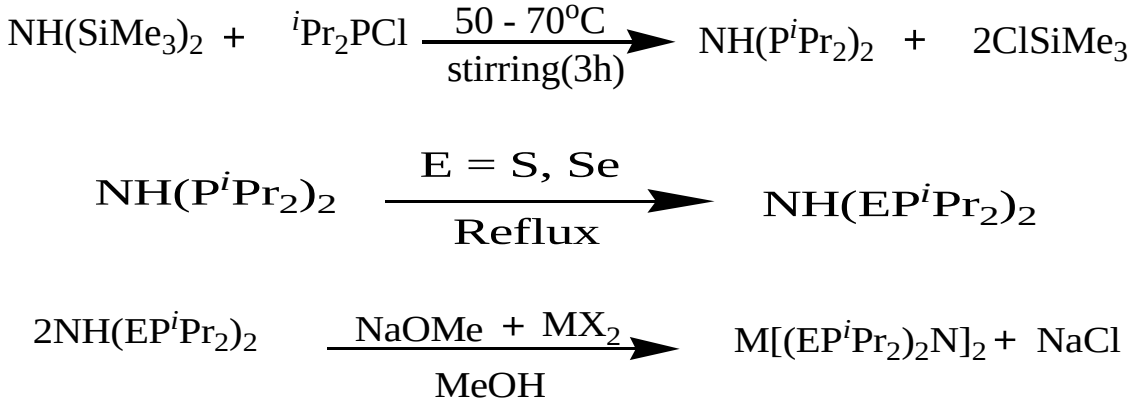

Scheme 1.1 Generalized synthesis of dialkyldiselenoimidophosphinate complex.

These complexes are versatile and have been used successfully for the synthesis of different metal selenide nanoparticles and deposition of thin films. O'Brien *et al.* have extensively investigated these complexes for metal selenide nanoparticles and thin films by various techniques. The cadmium complex $Cd[N(SeP^iPr_2)_2]_2$ was used for the synthesis of CdSe quantum dots, in a TOPO/TOP mixture by the hot injection method. The size was observed to change with duration of time. The EDX analysis indicates the presence of cadmium, selenium and phosphorus, however the use of TOPO/TOP mixture makes it difficult to conclude if the ligand is responsible for any phosphorus contamination.[29] The same complex was used for the deposition of either cadmium selenide or cadmium phosphide thin films by varying the deposition conditions in the AA-CVD method.[30] GC-MS and DFT calculations were carried out to understand the mechanism under which formation of phosphide is favourable. Argon was used as a carrier gas and films were deposited at a temperature range of 475-525 °C. It was observed that, hexagonal CdSe can be deposited dominantly at higher argon rate of 260 sccm (with phosphorus contamination of upto 10 %), whereas a lower flow rate of 160 sccm favours the

formation of Cd_3P_2, along with CdSe. GC-MS analysis shows a strong peak at *m/z* 207 and based on energy profile calculations by DFT studies, it was concluded that the peak is due to the formation of an aromatic $^{i}Pr_2N_2P_3^+$ ion, with *iso*-propyl groups residing on the nitrogen atom. The breakdown of the ionic aromatic species in to smaller fragments can yield either P_2 or Se_2, depending on conditions, and leads to the formation of CdSe or Cd_3P_2.

Interestingly, low pressure chemical vapor deposition (LP-CVD) of the $Cd[(SePPh_2)_2N]_2$, $Cd[(SeP^{i}Pr_2)_2N]_2$ and $[MeCd(SeP^{i}Pr_2)_2N]_2$ complexes yield CdSe thin films under all deposition conditions.[31-33] The $[MeCd(SeP^{i}Pr_2)_2N]_2$ complex was synthesized by comproportionation reaction between dimethyl cadmium and $Cd[(SeP^{i}Pr_2)_2N]_2$ precursor in toluene. Thin films were deposited from $Cd[N(SePPh_2)_2]_2$ and $Cd[(SeP^{i}Pr_2)_2N]_2$ complexes, in the temperature range of 475-525 °C, whereas the precursor temperature was maintained at 325 °C for $Cd[(SeP^{i}Pr_2)_2N]_2$ and 375 °C for the $Cd[N(SePPh_2)_2]_2$ complex. Hexagonal CdSe thin films were deposited from both complexes, however the preferred orientation of the crystallites was different for both complexes. The preferred orientation for films deposited from $Cd[(SeP^{i}Pr_2)_2N]_2$ complex was along the (100) plane and EDX analysis shows cadmium and selenium in 1:1 ratio with 1 % phosphorus contamination. The films from $Cd[(SePPh_2)_2N]_2$ complex preferably grow along the (101) and (002) directions and films were slightly selenium deficient with cadmium to selenium ratio of 54:46, no phosphorus was observed. The thin films from the mixed alkyl diselenoimidodiphosphinate complex yields films with (002) orientation. The films were phosphorus free and slightly cadmium rich (52:48).

Zinc selenide thin films were also deposited from the zinc complexes of similar ligands *i.e.* $Zn[(SePR_2)_2N]_2$ (where R = Ph or ^{i}Pr).[32, 33] The precursor temperature of $Zn[(SeP^{i}Pr_2)_2N]_2$ complex was comparatively lower (275 °C) than the $Zn[(SePPh_2)_2N]_2$ complex (375 °C), which shows higher volatility of the *iso*-propyl derivative. In both cases, hexagonal ZnSe thin films were deposited and better crystallinity was observed at elevated temperatures. The EDX analysis indicates that Zn and Se are almost in the 1:1 ratio, however the films deposited from both precursors contain phosphorus as an impurity.

Thin films of indium and gallium selenide were deposited by AA- and LP-CVD using mixed alkyl diselenoimidodiphosphinate complexes of indium and gallium.[34] The complexes were synthesized by reacting equimolar quantities of the ligand and the metal alkyl (Me_3Ga, Me_3In, Et_3In) compounds in dry toluene. The presence of acidic proton on ligand results in the easy removal of alkane from metal alkyls. The crystal structures of $[Me_2Ga(SeP^iPr_2)_2N]$ and $[Me_2In(SeP^iPr_2)_2N]$ were determined and in both complexes the metal atoms are in the tetrahedrally distorted coordination environment. Deposition of thin films by the AA-CVD method was performed in the temperature range of 400-475 °C, using a toluene solution. The Ga complex yields pure Ga_2Se_3 thin films, and p-XRD pattern shows preferred orientation along the (111) plane. High crystallinity was observed at an elevated temperature and EDX analysis indicates uniform distribution of Ga and Se in the required (2:3) ratio. For the LP-CVD method, a precursor temperature of 185 °C was used and deposition was observed in temperature range of 450-500 °C. The phase and the preferred orientation was similar to the thin films deposited by the AA-CVD method, however a notable increase in crystallinity was observed by p-XRD.

In_2Se_3 thin films were deposited from the $[Et_2In(SeP^iPr_2)_2N]_2$ complex by AA-CVD on glass substrates at temperatures between 400-475 °C, however, in order to avoid the use of pyrophoric trialkylindium, another complex $In[(SeP^iPr_2)_2N]_2Cl$[35] was also prepared and used for thin film deposition. The diffraction pattern indicates the presence of only the hexagonal In_2Se_3 phase at all temperatures, despite it being a high temperature phase. The films grow preferably along the (006) plane between temperatures of 400-450 °C. Nevertheless, a further increase in the temperature to 475 °C, changes the preferred orientation from (006) to the (110) plane. The thin films have both elements in the expected ratio and are phosphorus free. Thin films by LP-CVD were deposited on different substrates *i.e.* Si (100), GaAs and glass. The p-XRD pattern shows similar behaviour but poor coverage was observed on glass substrates.

Symmetrical diselenoimidodiphosphinate complex of mercury and organomercury derivatives are among the few molecular precursors available for the synthesis of HgSe nanomaterials and thin films.[36] The ligand was deprotonated by NaOMe and the complexes were isolated in high yield. The X-ray crystal structure of only the symmetrical compound $Hg[(^{i}Pr_2PSe)_2N]_2$, was determined and attempts to grow suitable crystals of organomercury derivatives were not successful, as they underwent rearrangement. Due to extreme toxicity associated with dimethyl and diethyl mercury, 2-selenyl and phenyl derivatives have been used for synthesis of mercuric chalcogenides. The chalcogenide compounds were prepared by *in vacuo* solid state decomposition of the complexes at 300 and 350 °C. The organomercury derivatives decomposed cleanly at 350 °C, yielding pure cubic HgSe (tiemannite). At lower temperature of 300 °C, some unidentified impurities were also observed. The symmetrical $Hg[(^{i}Pr_2PSe)_2N]_2$ complex decomposes at higher temperature of 400 °C to yield the same HgSe product. It shows that, the choice of suitable precursor can lead to significant decrease in the decomposition temperature.

The diselenoimidophosphinate complexes of bismuth $Bi[(SePPh/^{i}Pr_2)_2N]_3$ were synthesized in good yields and are air stable. The crystal structure of the $Bi[(^{i}Pr_2PSe)_2N]_3$ complex has been elucidated,[37] and crystalline thin films were deposited by the LP- and AA-CVD methods.[38] The precursor with alkyl groups have lower sublimation temperature than the phenyl derivative. Despite the low volatility of the phenyl derivative complex, it was used successfully for the deposition of thin films. A substrate temperature of 375-450 °C was used, while precursor temperature was maintained between 225-275 °C for deposition of films. The *iso*-propyl derivative yields rhombohedral Bi_2Se_3 thin films which are highly textured along the (006) plane. The variation in peak intensity was not consistent and the exact reason of the irregular behaviour was not clear. It was observed that the change in the precursor from alkyl to the phenyl derivative results in the deposition of hexagonal BiSe films which are oriented along the (104) plane. The difference in the phase, by changing the precursor, is probably

due to presence of electron donating *iso*-propyl groups on P atom, which may affect the bond strength and leads to a different decomposition path way.

The deposition of films by AA-CVD was observed only at 475 °C on glass substrates. The p-XRD shows deposition of pure Bi_2Se_3 phase with the most intense reflection along the (006) plane. The films were slightly selenium deficient (57 %) but much more crystalline as compared to the films deposited by LP-CVD.

PbSe thin films were deposited on glass substrates, by LP-CVD and AA-CVD method.[39, 40] Due to higher volatility of the alkyl derivative complex, $Pb[(SeP^iPr_2)_2N]_2$ was used in LP-CVD and $Pb[(SePPh)_2N]_2$ complex via the AA-CVD method. A precursor temperature of 250 °C, and substrate temperature between 400-450 °C was used for deposition by LP-CVD. Amorphous films were deposited at 400 °C, but the crystallinity improved with increasing temperature. Phase pure and densely packed PbSe films were obtained, preferably oriented along the (200) plane. EDX analysis shows Pb and Se in 1:1 ratio with no traces of phosphorus observed. The films by AA-CVD were deposited by using a THF solution of the $Pb[(SePPh)_2N]_2$ complex, and argon as the carrier gas, at a deposition temperature of 450 °C. TGA indicates a single step decomposition, but the residue was lower (20 %) than the predicted (28 %) value. The p-XRD and EDX (≈ 1:1) indicates formation of PbSe but coverage was poor, and some extra peaks were present which were attributed to the glass substrate.

Kuno *et al.* used the $Pb[(SeP^iPr_2)_2N]_2$ precursor for the synthesis of PbSe nanowires by a solution-liquid-solid method, using a $BiCl_3$ and TOPO/TOP mixture.[41] Nanowires of different diameters were prepared, the diameter increases, when higher concentration of $BiCl_3$ is introduced. They also synthesized $PbS_{1-x}Se_x$ nanowires by using a mixture of $Pb[(SeP^iPr_2)_2N]_2$ and $Pb(S_2CNEt_2)_2$ precursors by a similar method, but the composition of sulfur/selenium in alloy nanowires was slightly different than the expected value. The deviation was probably due to the difference in decomposition pathways of the two different precursors.

Silver complexes of selenium and mixed sulfur/selenium based ligands *i.e.* $[Ag((SeP^iPr_2)_2N)]_3$ and $[Ag(^iPr_2P(S)NP(Se)^iPr_2)]_3$ have been synthesized and their X-

ray single crystal structures determined.[42, 43] The molecular structure consists of trimeric units and a molecule of toluene was present as a solvate. The TGA showed single step decomposition and the final residues were in agreement with the calculated value for Ag_2Se. Thin films by AA-CVD were deposited on glass substrates in the temperature range of 325-475 °C. The p-XRD pattern of films obtained from both complexes, indicates deposition of the orthorhombic Ag_2Se phase. At deposition temperatures of 325 °C to 425 °C, the presence of an unidentified peak and cubic Ag_2Se phase was also observed. However, at 475 °C phase pure films were deposited.

Thin films by LP-CVD were also deposited on glass substrates where the deposition was performed at 425-475 °C, with precursor temperature of 300 °C. It was observed that a mixture of orthorhombic and cubic phase of Ag_2Se was deposited. Furthermore, some extra peaks matched well with elemental phosphorus and selenium or phosphorus selenide. Although, sulfur was not found in films deposited from the mixed chalcogeno complex, both films were found to be heavily deposited with phosphorus. Thus, the precursors were not appropriate for the LP-CVD method but suitable for AA-CVD.

Two new complexes of iron with selenoimidophosphinate, $Fe[(SeP^iPr_2)_2N]_2$ and $Fe[(SePPh_2)_2N]_2$ were synthesized and used for the synthesis of iron selenide nanoparticles by the colloidal method, and thin films by the AA-CVD method.[44] It was observed that, the attempt to prepare the complex with +3 oxidation state of Fe was not successful, as the Fe(III) undergoes an *in situ* reduction to Fe(II) and yields the same complex with +2 oxidation state. The crystal structure of $Fe[(SePPh_2)_2N]_2$ indicates a monomeric structure and geometry around Fe was slightly distorted tetrahedral. Both complexes were used to prepare nanoparticles by colloidal synthesis in primary amines at temperatures of 190 °C, 240 °C and 290 °C. p-XRD indicates formation of a mixture of two orthorhombic ferroselite ($FeSe_2$) phases, at all temperatures from both complexes. A change in primary amine does not affect the phase but significantly changes the morphology.

Thin films were deposited onto silicon substrates in the temperature range of 500-600 °C. A mixture of Fe_7Se_8 and $FeSe_2$ was deposited from the $Fe[(SeP^iPr_2)_2N]_2$ complex with mixed morphology whereas the thin films from $Fe[(SePPh_2)_2N]_2$ were not well defined by p-XRD and a spherical morphology was observed.

Kyritsis *et al*. also used $Fe[(SeP^iPr_2)_2N]_2$ to deposit thin films by vapour transport in CVD.[45] The precursor was placed in the temperature zone of 150 °C, while the vapours were transported by nitrogen to the hot zone, at a temperature of 600-800 °C. The substrates were palladium coated, and p-XRD indicates a mixture of FeSe and Fe_3Se_4 phases. The morphology shows irregular particles with wide size distribution. It was concluded that the absence of solvent and palladium coating did favour the formation of the FeSe phase.

Cobalt selenide thin films were deposited on glass substrates from $Co[(SeP^iPr_2)_2N]_2$ by AA-CVD.[46] A deposition temperature of 375-525 °C was used, but there was no deposition observed at 375 °C and at 400 °C, the deposition was too low to be properly characterized by p-XRD. Cobalt selenide (predominantly $CoSe_2$, with Co_3Se_4 and Co_9Se_8 as minor phase) thin films were deposited at 425-450 °C, whereas surprisingly a further increase in temperature shows that cobalt selenide and cobalt phosphide films are deposited on separate glass substrates depending on the region of the furnace. The substrates placed at the front shows cobalt selenide whereas cobalt phosphide thin films were deposited on substrates placed in the middle region. It shows that a higher temperature favours the formation of a phosphide film. p-XRD indicates a mixture of phases for cobalt selenide. Orthorhombic CoP was formed at 475 °C, while a monoclinic CoP_2 phase developed at 525 °C. The films were cobalt deficient with traces of selenium as well. Hence, in terms of purity of the deposited phase, the complex was not suitable for the AA-CVD technique.

The alkyl and phenyl based selenoimidophosphinate complexes of palladium were prepared using substituted and unsubstituted allyl palladium chloride and K_2PdCl_4 salt.[47, 48] The molecular structure of the allyl palladium complex $[Pd(\eta^3\text{-}C_3H_5)(PhP(Se)NP(Se)Ph\text{-}Se,Se')]$ and methyl substituted allyl

palladium complex [Pd(η^3-$CH_2C(CH_3)CH_2$)(PhP(Se)NP(Se)Ph-Se,Se')] were determined, both being monomeric structures. The allyl palladium complexes were used to prepare palladium selenide by solid state thermolysis. The complex [Pd(η^3-$CH_2C(CH_3)CH_2$)(PhP(Se)NP(Se)Ph-Se,Se')] was heated in the furnace at 500 °C, and the *iso*-propyldiselenoimidophosphinate analogue at 300 °C, under an argon atmosphere. The decomposition of both precursors result in the formation of cubic $Pd_{17}Se_{15}$ phase. The SEM analysis shows aggregates of spherical particles, ranging between 120-200 nm.

Thin films were deposited by the LP-CVD method from $Pd[N(^iPr_2PSe)_2]_2$ complex on glass substrates.[48] A precursor temperature of 345 °C was used and deposition was carried out at different temperatures between 400-475 °C. The phase of the deposited films was strongly dependent on the deposition temperature. At 425 °C, orthorhombic $PdSe_2$ with ribbon-like morphology was deposited, whereas at 450 °C, cubic $Pd_{17}Se_{15}$ and tetragonal Pd_4Se phases were observed.

Platinum selenide thin films were also deposited from $Pt[N(^iPr_2PSe)_2]_2$ complex by LP-CVD.[48] The deposition was performed at a temperature of 400 °C and 450 °C, while a precursor temperature of 225 °C was used. No deposition was observed at temperature below 400 °C or above 450 °C. The diffraction pattern indicates the deposition of hexagonal $PtSe_2$ at all temperatures, however the crystallinity of the films enhanced significantly with increase in temperature. The morphology was not affected by temperature and a worm-like morphology was observed, however, better coverage was indicated at comparatively lower temperature.

A series of nickel diselenoimido and mixed chalcogenidoimidophosphinate complexes were synthesized and investigated for their potential in thin film deposition.[46, 49-51] The crystallographic study of the $Ni[(SeP^iPr_2)_2N]_2$ complex shows two different types of crystals.[46] The crystallization of the complex from different organic solvents yield green and red crystals. It was observed that green crystals can be obtained solely by crystallization at -18 °C from THF. Crystallographic analysis reveals that the green crystals show square planar

geometry whereas red crystals exist in a tetrahedral geometry. The crystals with a tetrahedral form were used to deposit thin films by AA-CVD with a temperature variation of 400-500 °C. Thin films obtained at all temperatures only yield hexagonal $Ni_{0.85}Se$, and maximum crystallinity was observed at 450 °C. A change in morphology was observed from thin fibrous wires to thick wires with increase in temperature, no phosphorus contamination was observed. For LP-CVD, deposition was performed at 400-475 °C with a precursor temperature of 275-300 °C.[51] The diffraction pattern indicates deposition of a similar phase ($Ni_{0.85}Se$), whereas the morphology changed to a granular material or corrugated platelets. The optimized deposition temperature was found to be 425 °C, but the films were slightly contaminated with phosphorus. Hence, for this precursor, AA-CVD produces better films as compared to LP-CVD.

The mixed thio-seleno and seleno-telluro complexes $Ni[^{i}Pr_2P(S)NP(Se)^{i}Pr_2]_2$ and $Ni[^{i}Pr_2P(Se)NP(Te)^{i}Pr_2]_2$ were also prepared in order to deposit alloy thin films. The crystal structure of nickel complex with mixed thio-seleno ligand shows existence of monomeric unit and the nickel atom is tetrahedrally bonded to sulfur and selenium atoms. The precursor was used to selectively deposit nickel selenide or phosphide thin films by the LP-CVD method. The deposition temperature was varied between 375 °C to 475 °C, while the precursor temperature was held at 300 °C. Nickel selenide thin films were deposited at temperatures of 375 °C and 400 °C on glass substrates. The p-XRD analysis indicates the hexagonal $Ni_{0.85}Se$ phase to be dominant while traces of $NiSe_2$ and Ni_2P were also present. EDX analysis shows nickel rich films linked to the presence of the Ni_2P phase. The higher deposition temperature of 425 °C gave thin films with a mixture of Ni_2P and Ni_5P_4 phases, whereas at deposition temperature of 450 °C and 475 °C, thin films with only the hexagonal Ni_2P phase were obtained. The morphology of nickel selenide thin films shows irregular clusters of wires and for nickel phosphide, wires impregnated with granular particles were also observed. The hetero structured $Ni_{0.85}Se/Ni_2P$ films were also deposited on ITO coated glass and simple glass substrates. A plausible

mechanism of selective deposition of phases was determined by GC-MS and computational studies.[51]

Similarly, the single X-ray crystal structure of a mixed seleno-telluro complex was elucidated, indicating a square planar geometry, and the presence of only a *trans*-isomer.[50] Thin films were deposited by the AA-CVD method at temperatures of 450 °C and 500 °C on glass substrates. The p-XRD analysis indicates formation of $NiTe_2$ exclusively at both temperatures. SEM images indicate poor coverage of the thin films with irregular platelets-like morphology. It can be seen that the mixed complexes favours the formation of heavier nickel chalcogenide thin films.

Nath *et al*. have reported the use of $Ni[(SeP^iPr_2)_2N]_2$ complex, where Ni is tetrahedrally coordinated. The films were used for electrocatalysis showing high efficiency for hydrogen evolution and oxygen evolution reactions.[52]

A copper selenoimidophosphinate complex was synthesized by reacting $NH(SeP^iPr_2)_2$ with $CuCl_2$ in methanol in the presence of NaOMe.[43] Unexpectedly, a tri-nuclear Cu(I) complex was isolated, and it was presumed that the protic solvent acted as a reducing agent. The TGA showed that the complex decomposes in the temperature range of 285-385 °C, leading to the formation of copper selenide. The complex $In[(SeP^iPr_2)_2N]_2Cl$, used to prepare indium selenide, decomposes in almost similar temperature range *i.e.* 225-375 °C, hence, a 1:1 mixture of both complexes was used to prepare $CuInSe_2$ thin films by AA-CVD. The deposition was carried out at 375-450 °C on glass substrates. The p-XRD indicates formation of tetragonal $CuInSe_2$ phase, with preferred orientation along the (112) plane irrespective of deposition temperature. The morphology analysis by SEM shows randomly oriented plate-like structures, aligned perpendicularly on the substrate.

Another copper complex adduct, (triphenylphosphine) (tetraphenyldiselenoimidodiphosphinato)copper(I) was used with tin (IV) acetate, acetylacetonate complexes of iron and zinc for deposition of copper zinc tin selenide (CZTSe) or copper iron tin selenide (CFTSe) thin films.[53] Film deposition was observed at 400 °C and 450 °C on glass substrates, a tetragonal phase was

deposited for CZTSe and stannite type for CFTSe films. SEM analysis for CZTSe indicates plate like particles randomly oriented on a glass substrate, and irregular crystallites for CFTSe. Films were selenium rich at 400 °C, whereas improved stoichiometry was observed at 450 °C.

1.3.2. Diselenophosphinate complexes

Diselenophosphinates are well known ligands whose early synthesis dated back to 1960s.[54] The previous reported protocols for preparation of diselenophosphinates salts were tedious involving difficult reaction conditions. However, synthetic methods have developed over time and synthesis and applications of diselenophosphinates have been reviewed in detail.[55] Amongst different strategies, a facile and robust method is to prepare alkali metal salts of diselenophosphinates.[56] The one-pot synthesis is highly efficient and excellent yields can be obtained within a short time. The general synthesis of the alkali metal salt of diselenophosphinate is as follows.

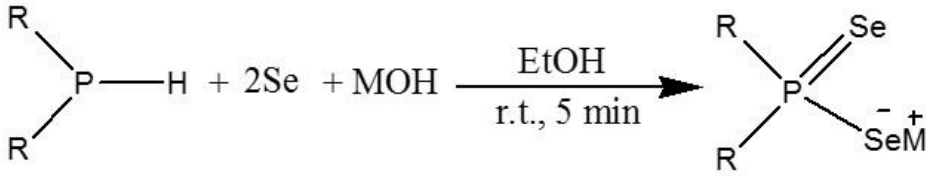

Scheme 1.2. Generalized synthesis of diselenophosphinate salts.

The synthesized ligand is versatile and a series of diselenophosphinate complexes have been synthesized.[57] The potential of these complexes for nanoparticles by colloidal synthesis and deposition of thin films was explored.

Silver complexes of diselenophosphinate and mixed thioselenophosphinate has been synthesized with the crystal structure of $[Ag(SSeP^{i}Pr_2)]_4$ also determined.[42] The structure analysis indicates that four Ag(1) atoms are arranged in a tetrahedral array and four ligand molecules ($SSeP^{i}Pr_2$) capped the silver atoms by coordinating through

sulfur and selenium atoms. The thermogravimetric analysis indicates single step decomposition of both complexes, in the temperature range of 250-360 °C. The final residue obtained from the diseleno analogue [$Ag(Se_2P^iPr_2)$] was higher than required for Ag_2Se, while the residue for thio-seleno analogue is in agreement with calculated value for Ag_2Se. Thin films were deposited on glass substrates at temperature in between 275-475 °C by the AA-CVD method. The films obtained from [$Ag(Se_2P^iPr_2)$] precursor were grey colored, well adherent films and the diffraction pattern matched well with the orthorhombic Ag_2Se phase. An unidentified peak and a peak corresponding to cubic phase of Ag_2Se was also observed. The morphology shows particles with irregular shapes and the size of all films were slightly silver rich. The films deposited from the mixed chalcogeno precursor indicates the deposition of a similar phase but without any impurity. No difference in morphology was observed, the films were slightly silver deficient. Traces of phosphorus were observed in the films from both precursors.

Cadmium selenide quantum dots (QDs) were prepared by the flow reactor synthesis from the [$Cd(Se_2P^iPr_2)_2$] precursor.[58] The effect of different reaction parameters such as concentration, temperature (180-220 °C) and residence time (4.2 s to 16.8 s) were studied in detail. Oleylamine was used to avoid clogging of the microcapillary tubes. Blue emitting CdSe QDs with different sizes were synthesized depending on the conditions. Quantum dots of size *ca*. 1.8-1.9 nm were obtained at low temperature and less residence time whereas with increase in temperature and residence time, the size increases to 2.1 nm. A large blue shift was observed in the energy band gap due to the quantum confinement effect.

Core/shell CdSe/CdS and CdSSe alloy nanomaterials were also synthesized by using the unsymmetrical dithiocarbamate complex of cadmium as the CdS source. The distinction between hexagonal and cubic phase of CdSe and CdSe/CdS nanocrystals was difficult due to excessive broadening of the peaks. The optical properties of core/shell nanoparticles were enhanced and the quantum yield increased from 7 % for CdSe to 14 % for CdSe/CdS nanoparticles. The size of the core/shell was observed to be 4.0±0.6 nm and CdSSe alloy with size of 5.0±0.8 were obtained. The emission peak for the alloy was blue shifted due to sulfur incorporation.

Donkor *et al*. performed a theoretical investigation on the dissociation path and preferred decomposition product of the mixed chalcogeno $Cd[(C_6H_5)_2PSSe]_2$ complex by the density functional theory approach.[59] Their calculations concluded that based on product stability and activation energy in the singlet potential energy surface, the CdS decomposition pathway is favorable on the doublet potential energy surface. The CdSe decomposition pathway is favored on the basis of product stability and CdS by the activation barrier.

The diselenophosphinate complexes are interesting precursors as they can provide selectively cobalt selenide or phosphide from colloidal synthesis as well as by the AA-CVD method.[46, 60] The cobalt complexes with different alkyl derivatives *i.e.* $Co(Se_2P^iPr_2)_2$, $Co(Se_2PPh_2)_2$ and $Co(Se_2P^tBu_2)_2$ were used to investigate the formation of selenide or phosphide nanoparticles[60] whereas $Co(Se_2P^iPr_2)_2$ was used for thin film deposition by AA-CVD.[46] For colloidal synthesis, the precursors were introduced into hot capping solvents such as HDA, TOPO, HDA/TOP and TOPO/TOP mixtures. Cobalt selenide was obtained when HDA or TOPO was used alone as a capping agent at 300 °C. In HDA, orthorhombic $CoSe_2$ phase was obtained whereas TOPO gave a mixture of orthorhombic and cubic $CoSe_2$ nanoparticles. The cobalt phosphide was obtained only when TOP was present and no phosphide product was obtained in the absence of TOP, at temperature less than 300 °C and time less than 60 min. Orthorhombic Co_2P was obtained after 60 min in TOPO/TOP or HDA/TOP mixture at 300 °C. However, a longer time duration of 150 min results in formation of the orthorhombic CoP phase. It was suggested that either TOP acts as the phosphorus source or catalyzes the decomposition of precursor in a way to release phosphorus.

The deposition of thin films from $Co(Se_2P^iPr_2)_2$ precursor by AA-CVD was performed on glass substrates at 450 °C. No deposition was observed below 450 °C and a mixture of cubic Co_9Se_8 and orthorhombic CoP was deposited. The morphology of the thin films consists of irregular grains of different sizes.

The X-ray crystal structure of copper diselenophosphinate was determined showing a tetrameric structure $[Cu_4(^iPr_2PSe_2)_4]$. The ligands act as bridging units with no chelation observed for any ligand.[57] Copper selenide nanoparticles were prepared by hot injection in a HDA/TOP mixture at 250 and 300 °C.[61, 62] Different concentrations of

the precursor were used but only the $Cu_{2-x}Se$ phase was deposited under all conditions. Crystalline spherical nanoparticles with a mean diameter of 14.5 nm were observed at 250 °C, the size increases at higher temperature. Thin films were deposited by AA-CVD at temperatures between 350-500 °C.[63] The TGA indicates complete decomposition around 340 °C and the residue is in accordance with the CuSe phase. However, the deposition at all temperatures indicates the formation of the $Cu_{2-x}Se$ phase, similar to the phase obtained by the colloidal method. SEM analysis indicates randomly distributed globular grains, the films become copper deficient with increasing temperature.

The X-ray crystal structure of two diselenophosphinate complexes of indium, $[In(^{i}Pr_2PSe_2)_3]$[57] and $[In(Se_2PPh_2)_3]$[64] were determined separately. The coordination of ligands to indium was in the isobidentate fashion giving rise to four-membered chelating rings (Se-P-Se-In). The $In(^{i}Pr_2PSe_2)_3$ was used to prepare indium selenide nanoparticles in a HDA/TOP mixture.[61] A temperature lower than 270 °C and/or time less than one hour resulted in an amorphous product, which cannot be characterized by p-XRD. The nanoparticles synthesized at 270 °C, for two hours, gave broad diffraction peaks with the intensity profile indicating formation of the In_2Se_3 phase. The complex was also used for thin film deposition by AA-CVD in the temperature range of 350-500 °C.[63] Thin films deposited at all temperatures gave the In_2Se_3 phase and high temperature results in better crystallinity and well adherence. Flake-like morphology was observed at 350-400 °C, whereas cylindrical grains and platelet-like morphology was observed at 450-500 °C. EDX indicates all films to be slightly indium deficient.

Nickel selenide or phosphide nanoparticles and thin films by AA-CVD were deposited from different diselenophosphinate derivatives of nickel, $Ni(Se_2P^{i}Pr_2)_2$, $Ni(Se_2P^{t}Bu_2)_2$ and $Ni(Se_2PPh_2)_2$.[65] The crystal structures of the complexes were determined which indicates a square planar geometry around the nickel atom and tetrahedral around the phosphorus atom. For the synthesis of nanoparticles, precursors dispersed in TOP, were injected into hot HDA and/or TOPO at 280 °C and 330 °C. The $Ni(Se_2P^{i}Pr_2)_2$ complex yields a mixture of Ni_2P and $Ni_{12}P_5$ in TOPO and $Ni_{12}P_5$ in HDA. Phase pure Ni_2P was obtained from the $Ni(Se_2P^{t}Bu_2)_2$ complex at 330 °C and NiSe phase at 280 °C in TOPO, whereas $Ni_{12}P_5$ was obtained in HDA at 330 °C and a

mixture of hexagonal and rhombohedral NiSe at 280 °C. The phenyl derivative gave Ni_2P in TOP and a mixture of NiSe and Ni_2Se_3 in HDA at both temperatures. Unlike the selenoimidophosphinate complex of nickel, where TOP was responsible for the entire phosphide formation, the alkyl groups and capping agents show significant effect on phase in selenophosphinate complexes. However, the thin films deposited by AA-CVD method, results only in the formation of $Ni_{0.85}Se$ using the $Ni(Se_2P^iPr_2)_2$ complex.[46] The films were deposited at temperatures between 350-450 °C. The SEM shows a mixture of spherical and wire-like morphology.

There are few examples of single source precursors of F-block elements. Diselenophosphinate complexes of divalent and trivalent europium were synthesized, the crystal structure of the divalent europium complex was determined and used for the synthesis of EuSe nanoparticles.[66] A coordinate number of 8 was observed for the europium atom, as two ligands and two molecules of dimethoxyethane were attached in a bidentate fashion with the geometry being distorted dodecahedron. EuSe was synthesized in HDA at temperature of 310 °C.

A mixed thioselenophosphinate complex of lead was synthesized in anticipation of preparing the $PbS_{1-x}Se_x$ alloy semiconductor.[67, 68] The X-ray crystal structure shows distorted square pyramidal geometry, where the lone pair is at the axial position and the chalcogenide atoms form the base. The nanoparticles were prepared at room temperature in a OLA/DT mixture. It was interesting to note that only PbSe was formed without the presence of sulfur. Mixed cubic and rectangular morphology was observed. Thin films were deposited at temperature of 450 °C and 500 °C. The deposited films also indicates only the PbSe phase. The coverage was not uniform and disordered cubic particles were deposited. EDX did not show the presence of sulfur, however, phosphorus was present as an impurity. Computational studies were performed to determine the plausible decomposition mechanism of the precursor, leading towards the PbSe formation. The study indicates that the Se-P bond breaks easily in comparison to S-P and PbSe is thermodynamically favored rather than kinetically controlled. However, Donkor *et al*. performed only theoretical calculations by DFT and indicates that on singlet and doublet potential surface, formation of PbSe is favorable by kinetic factors.[68]

Krauss *et al*. while investigating the role of phosphine chalcogenides in the synthesis of metal chalcogenide nanoparticles, found that the reaction between excess secondary diphenyl phosphine selenide and lead oleate leads to the formation of *bis*(diphenyldiselenophosphinato)Pb(II) complex.[69] The study of the X-ray crystal structure shows that the monomeric units in packing geometry arrange themselves in a octahedral rock salt crystal structure. The complex upon decomposition produces PbSe quantum dots in high yields. The quantum dots were arranged in a closed packing superlattice like structure due to high size uniformity.

SnSe thin films were deposited by the AA-CVD method from the $[Sn(Ph_2PSe_2)_2]$ complex.[70] Thermogravimetric analysis indicates decomposition between the temperature range of 350-400 °C. However, the films were deposited only at 450 °C, on glass substrates. The morphology by SEM indicates uniform sheet-like structures, while the EDX indicates that the films were slightly selenium rich.

Different diselenophosphinate complexes of Zn were synthesized and the structure of some derivatives were also reported.[71-73] The nanoparticles were prepared from the $Zn(Se_2P^iPr_2)_2$ complex in HDA at 300 °C.[73] Different concentrations of the precursors were used but only the wurtzite phase of ZnSe was confirmed by p-XRD and peaks were broad due to nanosized particles. TEM analysis indicates the formation of nanorods with average diameter of 6.6 nm and length of 24 nm. A computational study on mixed thioselenophosphinate complex of zinc indicates that the formation of $ZnS_{1-x}Se_x$ is both favored kinetically and thermodynamically, over the formation of ZnS or ZnSe [74]

The potential of the diselenophosphinate complexes was also investigated for the ternary and/or quaternary metal chalcogenide nanoparticles and thin films. Colloidal synthesis of $CuInSe_2$, $CuGaSe_2$ and $CuIn_{1-x}Ga_xSe_2$ nanoparticles were carried out by using stoichiometric combinations of $In(^iPr_2PSe_2)_3$, $Ga(^iPr_2PSe_2)_3$ and $[Cu_4(^iPr_2PSe_2)_4]$ complexes.[75] The crystal structures of the copper and indium complexes have been discussed earlier in this chapter, whereas the studies on $Ga(^iPr_2PSe_2)_3$ complex indicates that gallium shows a coordination number of four unlike the $In(^iPr_2PSe_2)_3$ complex, where a coordination number of six was observed.[57] A mixture of copper, indium and/or gallium complex was dispersed in TOP and injected into HDA for the

synthesis of respective ternary/quaternary material. A tetragonal phase was observed for $CuInSe_2$, $CuGaSe_2$ or $CuIn_{1-x}Ga_xSe_2$ nanoparticles. It was shown that the materials with any desirable composition can be attained by using a mixture of complexes in required stoichiometries.

The same precursors were also used to deposit thin films by AA-CVD on glass substrates, at deposition temperature of 350-500 °C.[63] Thin films of $CuInSe_2$ shows better coverage and crystallinity whereas the thin films of $CuGaSe_2$ were of poor crystallinity. Phosphorus contamination was observed at lower deposition temperatures which decreases with increase in temperature. Spherical to plate-like morphology was observed for $CuInSe_2$, and $CuGaSe_2$ shows wire-like to spherical morphology depending on deposition temperature. Crystalline thin films of desired stoichiometry, with uniform plates like morphology were deposited for $CuIn_{1-x}Ga_xSe_2$. It shows that these precursors are equally useful for NPs or thin film deposition.

Cu_2SnSe_3 thin films were deposited by AA-CVD on the glass substrates using a mixture of $Sn(Ph_2PSe_2)_2$ and $Cu(acac)_2$ complexes.[70] Uniform film deposition was observed at 400 °C and 450 °C, and the p-XRD indicates the formation of the cubic Cu_2SnSe_3 phase. The morphology changes from flakes (400 °C) to semicircle like crystallites (450 °C), with films deposited at 400 °C, showing better stoichiometry.

1.3.3. Diselenophosphate complexes

The coordination chemistry of diselenophosphates was started in 1968,[76] and they behave similarly to that of diselenophosphinate ligands. The ligand was prepared by reacting phosphorus pentaselenide with alcohols, and alkali salts can be prepared by treating $(RO)_2PSe_2H$ with ethanolic KOH solution.

Scheme 1.3. Generalized synthesis of diselenophosphoric acid.

The coordination chemistry of diselenophosphates is well reported,[77, 78] and is used for the preparation of different metal complexes.[79, 80] Various metal complexes of diselenophosphates with interesting chemistry, have been synthesized and discussed.[81-89] However, only those complexes will be discussed, which have been used either for the synthesis of nanoparticles or deposition of thin films. Although, various complexes have been synthesized, they are not well explored for nanomaterials.

Hydride-centered heptanuclear silver clusters were prepared by treating the diselenophosphate complex of silver with stoichiometric amounts of $NaBH_4$ in dichloromethane.[90] Silver nanoparticles were prepared by using an excess of reducing agent ($NaBH_4$) in methanol. The metallic nanoparticles were highly monodispersed with an average size of 30 nm.

The presence of oxygen in diselenophosphate complexes can result in the formation of phosphate or selenide selectively, unlike other diselenoimido and selenophosphinate complexes, where the phosphide was observed along with the selenide product. Liu *et al*. determined the crystal structure of $Bi[Se_2P(O^iPr)_2]_3$ and used the precursor to deposit $BiPO_4$ and Bi_2Se_3 thin films by MOCVD.[91] $BiPO_4$ and Bi_2Se_3 were deposited on gold platted silicon substrates at temperatures of 450 °C and 350 °C respectively. Bi_2Se_3 shows a plate like structure, whereas due to low melting point of phosphate product, $BiPO_4$ shows a nanowire-like structure by the vapor-liquid-solid (VLS) mechanism. They also reported the synthesis of the $Sb[Se_2P(O^iPr)_2]_3$ complex with its crystal structure similar to its bismuth analogue.[92] Sb_2Se_3 nanowires were prepared by the solvothermal method in the 100-150 °C temperature range. The length of nanowires was in the range of microns and diameter of the wires was observed to increase with temperature. A detailed spectroscopic analysis on a single Sb_2Se_3 nanorod was also performed.[93]

A tetrameric copper complex $[Cu_4(Se_2P(O^iPr)_2)_4]$, where the Cu_4 unit is present in the slightly distorted tetrahedral form, was used to prepare $Cu_{2-x}Se$ thin films, by the MO-CVD method.[94] The precursor complex was heated at 100 °C and deposition was performed at 360 °C on fused silica substrates. Phase determination of copper chalcogenides is difficult, however, careful inspection of the results indicates formation

of $Cu_{2-x}Se$ phase and wire like morphology was observed with diameters of 30-50 nm. Further investigation reveals that initially the CuSe phase was formed which then changes to the $Cu_{2-x}Se$ phase. A plausible decomposition mechanism of the precursor to both phases was also given.

The reaction of the diselenophosphate ligand with $Pb(OAc)_2$ can lead to two different isomeric structures depending on the synthesis temperature.[95] At 0 °C, a polymeric chain of monoclinic form, where one ligand was in chelating mode and other acts as bridging unit was obtained, while reaction performed at room temperature results in triclinic form and all four selenium atoms surrounding Pb atom are bridging units. The SEM analysis of PbSe nanoparticles synthesized by the solvothermal method at 150 °C, indicates that the presence of PVP changes the morphology from irregular to regular cubic shape particles. The use of ethylenediamine results in truncated octahedral shape and higher concentration changes morphology to eight horned rod dendrites.

PbSe thin films were also deposited by the diselenophosphonate complex $Pb[Ph(RO)PSe_2]_2$ (R = Me, Et) by AA-CVD.[96] Effect of temperature (300-500 °C) and substrate (glass and Si) was observed. Irregular morphology was observed for glass substrates whereas octahedron like morphology was obtained on silicon substrates. A higher temperature results in high crystallinity, better coverage and defined morphology.

The phosphorus based can sometimes lead to phosphorus incorporation as impurity in thin films or nanoparticles, and toxicity of phosphines is also an issue. Hence, some non-phosphorus based ligands were also prepared for metal selenide nanomaterials and thin films.

1.3.4. Diselenocarbamate complexes

Carbon diselenide (CSe_2) is a malodorous and toxic reagent, which was synthesized by the reaction between elemental selenium and dichloromethane at high temperature.[97] Diselenocarbamate ligand can be prepared by reaction between CSe_2 and secondary amine in presence of a base. Various metal diselenocarbamate complexes have been synthesized and used for the synthesis of nanomaterials and thin films.

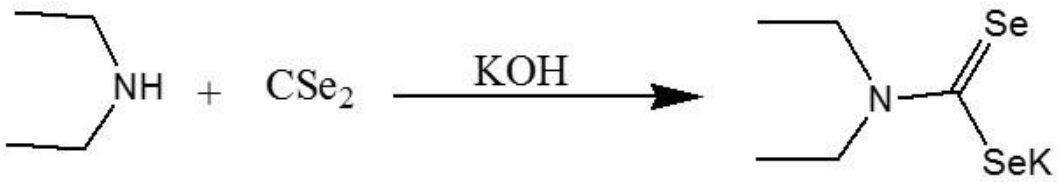

Scheme 1.4. Generalized synthesis of diselenocarbamte ligand.

Bi_2Se_3 thin films were deposited by AA-CVD using symmetrical and unsymmetrical complexes.[98] The X-ray crystal structure of $Bi[Se_2CN(C_4H_9)_2]_3$ shows asymmetric chelation of ligands with the metal center. Thin films of rhombohedral Bi_2Se_3 phase were deposited by all precursors and the morphology was found to be temperature dependent.

A dimeric cadmium complex $[Cd_2(Se_2CNEt_2)_4]$ was used for the synthesis of CdSe by pyrolysis.[99] The decomposition of the complex yields hexagonal CdSe powder and attempts to deposit CdSe thin films by LP-CVD were not successful as only selenium was observed. However, the same complex was used by AA-CVD method and thin films of CdSe with hexagonal phase were deposited and rhombohedral to florat- like morphology was observed.[100] Mixed CdSSe thin films were also deposited using diethyldithiocarbamate complex of cadmium as the sulfur analogue. Shim *et al.* used cadmium complexes of different cyclic and aliphatic asymmetric ligands for the deposition of thin films by MO-CVD in the temperature range of 300-400 °C.[101] Thick uniform deposition with regular hexagonal morphology was observed at 400 °C. O'Brien *et al.* also deposited CdSe thin films by MO-CVD using diselenocarbamate of unsymmetrical amine $(Cd(Se_2CNMeHex)_2)$.[102] They proposed a mechanism to indicate the suitability and effectiveness of the unsymmetrical precursor over simple precursors. The $Cd(Se_2CNMeHex)_2$ was also used for preparation of TOPO capped CdSe quantum

dots by the hot injection method at 250 °C.[103, 104] A time based study indicates that the size of the particles increase with time whereas the particle size distribution narrows.

The diselenocarbamate complex of Cu(II) is stable and the crystal structure shows geometry closely related to tetragonal pyramidal,[105] whereas the Cu(I) complex is unstable and highly air and moisture sensitive. Liu *et al.* managed to isolate and determine the crystal structure of the $[Cu_4(Se_2CN^nPr_2)_4$ complex.[106] The geometry was similar to the $[Cu_4(Se_2P(O^iPr)_2)_4]$ analogue, where a tetrahedral framework was formed by copper atoms and are capped by diselenocarbamate ligands. A neutral hydrido-centered $[Cu_7(H)[Se_2CNR_2]_6]$ complex and monocationic $[Cu_8(H)(Se_2CN^nPr_2)6]PF_6$ complex was also prepared and characterized. The monocationic analogue was used for synthesis of CuSe by heating in an autoclave at 200 °C in the presence of 1-dodecanethiol. Particles with irregular morphology were formed, a mixture of CuSe and $Cu_{2-x}Se$ phase was observed. A small amount of $Cu_{2-x}Se$ phase was presumably formed by disproportionation of CuSe phase at higher temperature.

Cobalt selenide thin films were synthesized by AA-CVD from the $Co(Se_2CNEt_2)_3$ complex.[46] Films were deposited on glass substrates at a high temperature of 450 °C, selenium rich phase $CoSe_2$ was deposited as confirmed by p-XRD and EDX. A bundle of fibre like morphology was observed by SEM.

An assymetric complex of indium $In(Se_2CNMe^nhexyl)_3$, was used by LP-CVD, at a substrate temperature of 475 °C and precursor temperature of 250 °C.[107] A single prominent peak was observed that matches well with the In_2Se_3 phase. Shim *et al*. also reported use of unsymmetrical complexes *tris*(*N,N*-2-ethylpiperidine diselenocarbamato) indium(III) and *tris*(*N,N*-ethylbutyldiselenocarbamato)indium(III) as MO-CVD precursors.[108] The films from the piperidine derivative were of poor quality and the ethylbutyl amine shows formation of the In_2Se_3 phase on glass and ITO-glass substrates. The simplest diselenocarbamate complex of indium $In(Se_2CNEt_2)_3$ was used to synthesize InSe nanoparticles in TOPO/TOP mixture and 4-ethyl-pyridine.[109] Irregular shaped amorphous nanoparticles were obtained from TOPO/TOP mixture at 250 °C, whereas 4-ethylpyridine yields uniform spherical nanoparticles. Similarly, cubic phase $NiSe_2$ films were deposited from $Ni(Se_2CNEt_2)_2$ by AA-CVD at a temperature of 400 °C

and 450 °C.[46] A significant change in morphology from interwined wires to plate-like morphology was shown by varying the temperature.

Diselenocarbamate complexes of ethyl zinc and Zn(II) salts have been used to prepare ZnSe QDs[110] and ZnS_xSe_{1-x} thin films by AA-CVD.[111] Quantum dots were synthesized by thermolysis of the $EtZnSe_2CNEt_2$ complex in TOPO/TOP solution at 250 °C, which shows strong quantum confinement. p-XRD and SAED indexing shows the formation of the hexagonal phase. The capping of QDs by TOPO was confirmed by the presence of phosphorus in the EDX spectrum. Thin films of ZnSe were deposited from the $Zn(Se_2CNEt_2)_2$ complex on glass substrates at 350 °C. Densely packed thin films with small crystallites were obtained, the cubic phase of ZnSe was formed. The $Zn(Se_2CNEt_2)_2$ complex was also used in combination with $Zn(S_2CNEt_2)_2$ complex for the deposition of ZnS_xSe_{1-x} films. Both complexes were used in the equimolar quantities but films were slightly selenium rich as indicated by EDX. Irregular shaped cubic ZnSe phase particles were obtained.

The diselenocarbamate complexes were also used successfully for thin film deposition of ternary metal chalcogenide systems.[112] The films were deposited by LP- and AA-CVD techniques and the effect of temperature and substrate (glass, Si (100), ITO-glass) was studied on the deposited films. A growth temperature of 400-450 °C was used for LP-CVD, where the films on glass substrates gave mixed acicular and hexagonal morphology, whereas better uniformity of shape and size was observed on ITO-glass and Si (100) substrates. p-XRD indicated $CuInSe_2$ with chalcopyrite structure on all substrates. For AA-CVD, a deposition temperature of 425-475 °C was used and the tetragonal $CuInSe_2$ phase was obtained. Mixed morphology was observed and films with poor coverage were obtained as compared to LP-CVD.

1.3.5. Selenourea complexes

Selenourea ligands can be categorized into N,N-tetraalkyl selenourea and acyl selenourea ligands. Simple tetraalkyl selenourea ligands are commercially available or they can be synthesized easily by the reaction of isocyanides with selenium to form isoselenocyanate, which on reaction with amine yields selenourea.[113, 114]

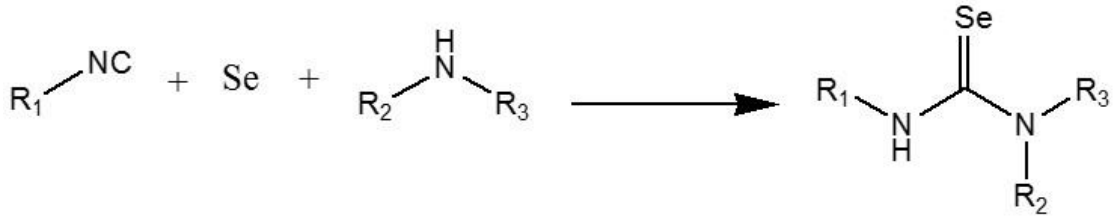

Scheme 1.5. Generalized synthesis of alkylselenourea.

The substituents can be alkyl or aryl and either a primary or secondary amine can be used. Acyl selenoureas were reported by Douglas in 1937 and can be synthesized by treating acid chlorides with potassium selenocyanate to form acyl isoselenocyanate, which on reaction with an amine yields the acyl selenourea ligand.[115]

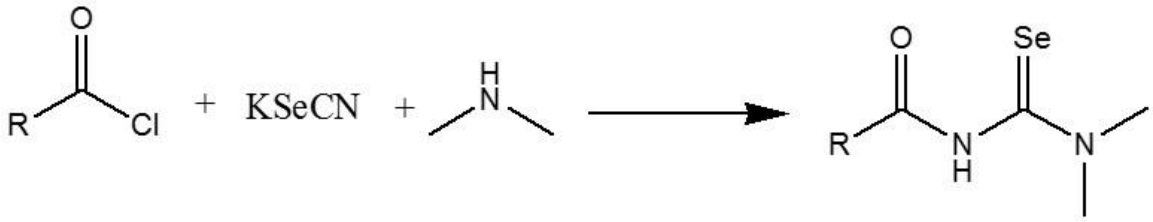

Scheme 1.6. Generalized synthesis of acyl selenourea.

Both kinds of selenourea ligands can form metal complexes easily and the resulting complexes have been used as single source precursors. Bi_2Se_3 thin films were deposited by chemical bath deposition using N,N-dimethylselenourea as the selenium source.[116] The films were amorphous showing the hexagonal Bi_2Se_3 phase. The films became slightly selenium deficient on annealing and showed n-type behavior. CdSe QDs were prepared by a biphasic liquid/liquid system.[117] Cadmium myristate (Cd-MA) was dissolved in TOPO/dimethylbenzene mixture and selenourea in ethylene glycol was added at 140 °C. Decomposition of selenourea results in the formation of zinc-blend CdSe, the size was in the range of 2.5-3 nm displaying the quantum confinement effect. Wang *et al.* used Cd-MA in oleic acid/heptane mixture and aqueous selenouea in

biphasic method to prepare CdSe nanocrystals. They treated the as prepared CdSe nanocrystals with aqueous thiourea to prepare core shell nanoparticles.[118] The cubic phase was obtained for both CdSe and CdSe/CdS core shell nanoparticles with their detailed photoluminescence studies also carried out.

Koch *et al*. reported the crystal structure of N,N-diethyl-N'-benzoylselenourea, which was used to prepare the cadmium complex.[119] The precursor was used to prepare CdSe QDs by hot injection in a HDA/TOP mixture at different temperatures (100-250 °C). It was difficult to assign the cubic or hexagonal phase due to the broadness of the peaks, however, the intensity pattern predominantly shows the formation of the cubic CdSe phase.

O'Brien *et al*. also reported the use of acyl selenourea complexes for metal selenide nanoparticles and thin films. The iron complex *tris*(*N*,*N*-diethyl-*N*′-naphthoylselenoureato) iron(III) was synthesized and its crystal structure determined.[120] OLA capped nanocrystals were synthesized at temperatures of 190-290 °C, the $FeSe_2$ phase was formed at all temperatures. The morphology changes from sheet-like to rod-like structures with increase in temperature. Thin films were deposited only at a higher temperature of 625 °C by AA-CVD on Si substrates. p-XRD pattern and EDX analysis were conflicting, the film was too thin to be characterized by ICP or XPS for phase identification. Likewise, a similar ligand was used to prepare Pb and Pd complexes as well. The crystal structure of the Pb complex was reported and used for the preparation of the PbSe nanowires by the solution-liquid-solid method.[121] Au@Bi solution was used with *bis*[*N*,*N*-diethyl-*N*′-naphthoylselenourea]lead(II) complex and injected in TOPO at 190 °C and 290 °C. The amount of Au@Bi determines the diameter of the nanowire. Higher temperature and concentration of Au@Bi resulted in the formation of a network like structure. In another study, a similar complex was used in combination with the *bis*(dodecylxanthato)lead(II) complex for deposition of PbSe and $PbS_{1-x}Se_x$ thin films by the spin coating method.[122] The films were annealed at 250 °C and all films were Pb enriched. The formation of a solid solution was observed by p-XRD and a shift in lattice parameters. The Pd complex [*bis*(*N,N*-diethyl-*N*'-naphthoylselenoureato)palladium(II)] was used by AA-CVD to deposit the cubic phase of palladium selenide (palladesite $Pd_{17}Se_{15}$) thin films, in the temperature range of 400-500 °C.[123] Globular morphology was observed at 400 °C whereas rods were formed at

deposition temperature of 500 °C. The colloidal synthesis of nanoparticles in OLA yields a mixture of the $PdSe_2$ and $Pd_{17}Se_{15}$ phase, however in the presence of DDT only the $Pd_{17}Se_{15}$ phase was formed.

A different selenourea analogue complex of Pb, [*bis*(*N,N*-di-iso-butyl-*N*-4-nitrobenzoylselenoureato)lead(II)] was characterized by X-ray crystallography and thin films were deposited by AA-CVD in temperature range of 250-500 °C.[124] Globular crystallites were obtained at lower temperature and a wire like morphology was observed at 500 °C. The precursor decomposes cleanly in a mixture of TOP/OLAc/octadecene at 200 °C, to yield cubic shaped nano crystallites.

Owen *et al*. synthesized a library of *N,N,N*'-trisubstituted selenourea precursors and used them as a selenium source to produce OLAc capped PbSe nanocrystals.[125] The reactivity of the precursors can be tuned by changing the alkyl substituents and high monodispersity was achieved. Seok *et al*. used $(SbL_2Cl_2)Cl$ (where L = *N,N*-dimethyl selenourea) in ethylene glycol and prepare Sb_2Se_3 crystalline nanorods.[126] The nanorods were used as a light sensitizer and an organic-inorganic hybrid solar cell was fabricated by deposition on TiO_2 using spin coating followed by annealing.[127] A power conversion efficiency of 3.2 % was achieved. Koposov *et al*. reported tuning of morphology by varying the amount of selenourea to antimony salt in OLA and OLAc mixture.[128] Under judicious conditions Sb_2Se_3 nanorods, nanospheres and nanorings can be generated. Badshah *et al*. synthesized a series of novel ferrocene incorporated selenourea and deposited thin films by AA-CVD.[129-132] They thoroughly investigated the effect of temperature and the effect of surfactant on the deposited thin films. There are only a few examples of use of surfactants in AA-CVD method,[133, 134] and it was shown that the morphology is significantly affected by the presence of surfactants even in the vapor phase.

1.3.6. Selenoether complexes

Selenium complexes of some of the metals (such as Ta, Nb and V) are difficult to prepare, in such cases, selenoether complexes have been proven to be the suitable complexes for fabrication of metal selenide thin films and nanoparticles. Reid *et al*. prepared $[NbCl_5(Se^nBu_2)]$ and $[TaCl_5(Se^nBu_2)]$ complexes and used them to prepare

$NbSe_2$ and $TaSe_2$ thin films by LP-CVD.[135] The $NbSe_2$ films were deposited on silica substrates at 650 °C. Traces of Nb_2O_5 were also observed which is presumably due to slight hydrolysis of the precursor. Hexagonal plate like structures were formed and complete coverage of the substrate was observed. The EDX analysis indicates selenium deficient films and the presence of Cl was not observed. Deposition of $TaSe_2$ films was attempted using the $[TaCl_5(Se^nBu_2)]$ precursor, but no deposition was observed, probably due to the high molecular weight and low volatility associated with the complex.

$[(GaCl_3)_2(^nBuSeCH_2CH_2Se^nBu)]$, $[GaCl_3(Se^nBu_2)]$ and $[GaBr_3(Se^nBu_2)]$ complexes were used for the deposition of Ga_2Se_3 thin films by LP-CVD on SiO_2 and TiN substrates.[136] The films were deposited in the temperature range of 500-600 °C,the monoclinic Ga_2Se_3 phase was deposited from all precursors. Halogen incorporation was observed at 500 °C, whereas no traces of halogen were found at the higher deposition temperature of 600 °C. Hall measurements indicate the p-type nature of the films.

Palladium selenide nanoparticles were synthesized by Singh *et al*. and their role in C-C and C-O coupling was investigated.[137-139] They reported the first synthesis of Pd_4Se and Pd_7Se_4 phases from single molecular precursors.[139] The thermolysis of $[PdCl_2(PhSe\text{-}CH_2CH_2CH_2\text{-}NH_2)]$ complex selectively yielded Pd_4Se nanocrystals in TOP at 280-300 °C, whereas the $PdCl[C_6H_4CH(C_6H_4\text{-}2OH)\text{-}NHCH_2CH_2CH_2\text{-}SePh]$ complex with secondary amine substituent, yielded only the Pd_7Se_4 phase. They also prepared pyrazolated selenoether complexes and used them as catalysts for Suzuki-Miyaura coupling.[138] It was found that the complexes are converted *insitu* to Pd_4Se and PdSe nanoparticles which are responsible for catalytic activity. The complexes were thermolyzed in TOP at 200-250 °C. The p-XRD confirms the formation of Pd_4Se and PdSe nanoparticles, which shows that the phase depends on the precursor being used. Similarly, the $((Ph_2NCOCH_2)_2Se)_2PdCl_2$ was characterized by X-ray crystal analysis and used for C-C and C-O coupling.[137] The decomposition of precursor in TOP at 280 °C yields $Pd_{17}Se_{15}$ nanoparticles. The nanoparticles had a prismatic morphology with particle sizes in the range of 35-45 nm. All these results indicate that the structure of the precursor is critical in determining the phase of the nanoparticles.

Sampath *et al*. synthesized thin films of palladium selenide with different phases by varying the concentration of didodecylselenide and palladium acetate.[140] Thin films were deposited by spin coating and the precursor decomposition was carried out at 250 °C. A high concentration of palladium acetate results in Pd_4Se whereas an increasein concentration of didodecylselenide results in the formation of thin films with the Pd_7Se_4 and $Pd_{17}Se_{15}$ phase. The films were used for hydrogen evolution reactions, the Pd_4Se shows comparatively better performance.

Parkin *et al*. deposited SnSe and $SnSe_2$ thin films by AP-CVD on silica coated glass substrates.[141] The concentration of $SnCl_4$ and Et_2Se were varied in the temperature range of 350-650 °C. $SnSe_2$ films were deposited between 350-550 °C, whereas SnSe films were deposited at above 550 °C with excess of $SnCl_4$. The presence of Cl was not observed and a sheet like morphology was obtained in all the depositions. Reid *et al*. reported that the crystal structure of the $[SnCl_4(Et_2Se)_2]$ complex shows a distorted octahedral geometry, with the Et_2Se groups arranged in a *trans*-fashion.[142] The $[SnCl_4(Et_2Se)_2]$ and $[SnCl_4(o\text{-}C_6H_4(CH_2SeMe)_2)]$ complexes were used for the deposition of thin films by LP-CVD at 500 °C. Substrates placed near the precursor source showed deposition of the $SnSe_2$ phase whereas the substrate placed in the middle (hot zone of furnace) shows the formation of the SnSe phase, when $[SnCl_4(Et_2Se)_2]$ was used. Films from the $[SnCl_4(o\text{-}C_6H_4(CH_2SeMe)_2)]$ complex were of poor quality and deposition took place at higher temperature of 600 °C, perhaps due to the low volatility as compared to the $[SnCl_4(Et_2Se)_2]$ complex. The crystal structure of $[SnCl_4(^nBuSe(CH_2)_nSe^nBu)]$ (n = 2 and 3), complexes were also reported by Reid *et al*.,thin films of $SnSe_2$ were deposited by LP-CVD.[143] The films were deposited at a temperature range of 400-600 °C on Si, SiO_2 and TiN substrates. The use of diselenoether only resulted in $SnSe_2$ films under all conditions. Highly selective deposition of films on surface of patterned Si/SiO_2 and Si/TiN substrates, etched with HF fumes, were also observed.

Ag_2Se nanoparticles were prepared from the $[Ag_5(TFA)_5(Me_2Se)_4]$ complex in 1-octadecene at 315 °C.[144] A small amount of Ag nanoparticles were also formed along with β-Ag_2Se. The use of selenoether with bulky alkyl groups *i.e. t*-Bu- results in the formation of Ag_2Se at room temperature via formation of the $[Ag(TFA)(t\text{-}Bu_2Se)_2]$ in

intermediate step. Ag_2Se-TiO_2 nanocomposites were synthesized using TiO_2 along with *t*-Bu_2Se for enhanced photocatalytic activity.

Different vanadium complexes were synthesized using the bidentate selenoether ligand $MeSe(CH_2)_nSeMe$ (n = 2 or 3), and dialkyl selenoether complexes, $[VCl_3(SeMe_2)_2]$ and $[(Cp)_2V(Se^tBu)_2]$.[145] The $[(Cp)_2V(Se^tBu)_2]$ complex is extremely moisture sensitive and cannot be purified completely as crystallization leads to the decomposition. The suitability of complexes for thin film deposition was studied by LP-CVD between 500 °C to 600 °C. No deposition was observed from the bidentate selenoether complexes. Thin films of poor quality and high Se deficiency, were obtained from $[VCl_3(SeMe_2)_2]$ complex, whereas the stoichiometry of films deposited from $[(Cp)_2V(Se^tBu)_2]$ complex was close to VSe_2, although, still Se deficient.

Similarly, $TiCl_4(Se(CH_3)_2)_2$ and $TiCl_4(Se(CH_2CH_3)_2)_2$ complexes were used for the deposition of $TiSe_2$ thin films by LP-CVD at 500-600 °C.[146] The $TiCl_4(Se(CH_3)_2)_2$ precursor yielded $TiSe_2$ thin films with poor morphology and no reproducibility was observed. Good quality thin films were deposited from $TiCl_4(Se(CH_2CH_3)_2)_2$ complex, however the films were not stable on exposure to atmosphere and within few days the films degraded to amorphous Ti-O-Se or TiO_2. The o-xylyl selenoether complex of titanium $TiCl_4[o\text{-}C_6H_4(CH_2SeMe)_2]$, was also used for the deposition of $TiSe_2$ thin films by LP-CVD at 500 °C.[142] However, a notable presence of titania was also detected by p-XRD.

1.3.7. Selenolate complexes

Selenolate complexes are versatile single molecular precursors and have been used extensively for materials synthesis. The amine based cadmium selenolate complex *bis*(2-*N,N*-dimethylamnioethyl-selenolato)cadmium was prepared and treated with $Cd(OAc)_2$. $2H_2O$ to afford the $[Cd_3(OAc)_2(SeCH_2CH_2NMe_2)_4]$ complex.[147] CdSe nanoparticles were synthesized by hot injection in HDA/TOPO mixture at 185 °C and also by thermally decomposing the complex in a furnace at 180-200 °C. The cubic phase of CdSe was observed by colloidal synthesis, whereas the solventless synthesis, under vacuum, provides CdSe with the hexagonal phase. The complex of zinc with similar a selenolate was also prepared, which upon decomposition yields ZnSe.[148]

Polymeric alkyl/arylselenolate copper(I) complexes [Cu(RSe)$_\infty$] (R = Ph, Me. *t*-Bu) were thermally decomposed under different conditions to synthesize copper selenide nanoparticles by thermal decomposition of solid precursors.[149] The decomposition at 180 °C under vacuum indicates the formation of orthorhombic Cu_2Se, whereas cubic Cu_2Se was formed when nitrogen or an argon environment was used. Particles with irregular shape and sizes were formed and dialkyl/arylselenide was observed as the by-product. Similarly, solid state pyrolysis of the distorted tetrahedral structured complex [Cu(SeC$_5$H$_3$(Me-3)N)]$_4$ was carried out at 400 °C under an argon atmosphere giving cubic $Cu_{1.8}Se$ nanoparticles.[150] The high temperature is probably the cause of selenium deficiency. Colloidal synthesis from same precursor, was performed in TOPO at 170 °C and in TOP/HDA mixture at 150 °C. TOPO capped polygon shaped nanoparticles show a cubic $Cu_{1.8}Se$ phase whereas Cu_7Se_4 phase was developed in a mixture of capping agents with spherical morphology. The precursor was also used for the deposition of thin films by AA-CVD at 360-400 °C giving only the Cu_5Se_4 phase. The films were composed of vertically stacked platelet- like morphology. Pyridylselenolate complexes of copper [Cu(SePy)]$_4$ and [Cu(3-Me$_3$Si-2-SeNC$_5$H$_3$)]$_4$, and indium complex In(SePy)$_3$, were thermolyzed in evacuated tubes at 220-250 °C.[151] A mixture of CuSe and $Cu_{2-x}Se$ was obtained at all reaction conditions, except thermolysis of [Cu(3-Me$_3$Si-2-SeNC$_5$H$_3$)]$_4$ at 220 °C, which yields pure $Cu_{2-x}Se$ phase. In_2Se_3 was the only phase obtained from decomposition of indium pyridylselenolate. Brennan *et al*. synthesized fluorinated selenolate complexes of Cu, In, Sn and Pb, by treating amalgamated metals with (SeC$_6$F$_5$)$_2$ in pyridine.[152]. The decomposition of the complexes yielded respective metal selenides by elimination of pyridine and Se(C$_6$F$_5$)$_2$.

2-Pyridyl selenolate complexes of antimony and bismuth were prepared for respective metal selenide nanostructures.[153] The geometry of the molecular structure of the antimony complex [Sb(SeC$_5$H$_3$(Me-3)N)$_3$], is trigonal pyramidal, the ligands show monodentate attachment to the metal center. In contrast, the bismuth complex [Bi(SeC$_5$H$_3$(Me-3)N)$_3$], shows a distorted square pyramidal geometry, where two ligands are chelating and one ligand shows monodentate attachment. The colloidal (HDA, 200 °C) and solventless decomposition of the antimony complex yields orthorhombic rod shaped Sb_2Se_3 nanoparticles. In the case of the Bi complex, the solvent less

decomposition yields the hexagonal BiSe phase and the HDA capped nanoparticles indicates rhombohedral Bi_2Se_3 phase. Sb_2Se_3 films deposited in the temperature range of 375-500 °C, by AA-CVD showed nanowire like morphology with best results attained at 425 °C. The deposition from bismuth complex indicates the formation of BiSe in the temperature range of 375-425 °C, whereas Bi_3Se_4 and Bi_3Se_2 phases were deposited at 450 °C and 500 °C respectively. Sb_2Se_3 thin films were also deposited from the $MeSb(Se^nBu)_2$ precursor on silica substrates. The diffraction pattern and EDX analysis indicates the Sb_2Se_3 phase, however, the films were non-uniform and poorly adherent to the substrate.

The molecular precursors $Me_2InSePh$ and $In(SePh)_3$ have been used, in an attempt to synthesize phase selective InSe and In_2Se_3 thin films.[154] Nonetheless, the expected phases were dominantly deposited by the spray MO-CVD process, but In_xSe_y phase was also present as an impurity. Similarly, a volatile precursor $[(^tBu)_2In(Se^tBu)]_2$ was also used to favor the formation of InSe phase by LP-CVD, but despite the fact that the In:Se ratio in precursor is 1:1, selenium deficient films were obtained.[155] The selenium deficiency is probably due to high volatility of Se at high temperatures. Shim *et al*. reported that, the use of a relatively simple complex $[Me_2In(SeMe)]_2$, which leads to the formation of phase pure InSe thin films by MO-CVD.[156] The 1:1 stoichiometry of In to Se was confirmed by p-XRD and XPS analysis. The precursor was also used to deposit InSe thin films on GaAs substrates by MO-CVD.[157]

The $[In(SeC_5H_3(Me\text{-}3)N)_3]$ complex was decomposed in different capping agents (OLA, HDA, TOPO) at 330 °C.[158] Hexagonal In_2Se_3 was formed in HDA and TOPO, whereas OLA facilitated the rhombohedral In_2Se_3 phase. Mixed or agglomerated morphology was obtained in all the surfactants, probably due to the high temperature. The complex was used in conjunction with the copper analogue $[Cu(SeC_5H_3(Me\text{-}3)N)]_4$ under similar reaction conditions to synthesize $CuInSe_2$. Tetragonal $CuInSe_2$ nanoparticles were formed and the attempt to synthesize In_2Se_3 and/or $CuInSe_2$ nanoparticles at temperatures lower than 300 °C, results in a mixture of phases.

A bimetallic selenolate complex $(PPh_3)_2CuIn(SePh)_4$ was synthesized for low temperature synthesis of $CuInSe_2$ nanoparticles.[159] The complex was dissolved in dioctyl phthalate and heated at different temperatures (200-300 °C). The p-XRD of

powder obtained at 200 °C indicates presence of an unidentifiable peak along with diffraction pattern of $CuInSe_2$, whereas at 250 °C and 300 °C, phase pure crystalline $CuInSe_2$ was obtained.

Besides pyridyl based complexes, substituted pyrimidyl selenolate complexes of Cu and Ag with formula $[M(SeC_4H(Me\text{-}4,6)_2N_2)]_6$ (M = Cu and Ag) were reported and both show a hexanuclear structure.[160] The hot injection method was used to synthesize respective metal selenides in DDT at 150 °C, and the copper complex was also used by CVD for deposition of thin films. Orthorhombic Ag_2Se and cubic Cu_7Se_4 nanocrystals were obtained by thermolysis of the complexes. Similar phase Cu_7Se_4 was obtained for thin films deposited by AA-CVD at 400 °C with a wool like morphology. Silver selenide was also obtained by decomposition of a trinuclear $[Ag_3(\mu\text{-}Se\text{-}4\text{-}py)_3(PPh_3)_4]$ complex and a mononuclear $[Ag(Se\text{-}4\text{-}py)(PPh_3)_3]$ complex.[161] The solid state pyrolysis of the complex in furnace or thermolysis in HDA or TOPO at 270 °C results in the formation of Ag_2Se nanoparticles.

There are only a few examples of lanthanide molecular precursors available in the literature. Brennen *et al*. synthesized lanthanide (Ho, Er, Eu, Yb, Tm) chalcogenolate complexes and observed that the decomposition of complexes leads to their respective metal chalcogenides.[162] The divalent complexes leads to the formation of LnE and trivalent complexes and results in the formation of Ln_2E_3 phase, except La and Ho, where a mixture of phases was obtained.

Selenolates of lead with amine or carboxylic acid substituents were synthesized by Jain *et al*. and their crystal structures determined.[163] Both solution based (HDA, 120 °C) and solventless synthesis (250 °C) have been used to prepare PbSe nanoparticles. They also used similar kinds of ligands and procedure for the synthesis of palladium selenide nanoparticles.[164] The $[Pd_2Cl_2(\mu\text{-}SeCH_2CH_2COOMe)_2(PPr_3)_2]$ complex, on solvothermal and solid state decomposition, only provides the $Pd_{17}Se_{15}$ phase, whereas a mixture of $Pd_{16}Se_7$ and $Pd_{17}Se_{15}$ was obtained from the $[Pd(OAc)(SeCH_2CH_2CH_2NMe_2)]_2$ complex. The allyl based complexes $[Pd(\mu\text{-}SeC_5H_4N\text{-}2)(\eta^3\text{-}C_4H_7)]_2$ and $[Pd(\mu\text{-}SeC_5H_4N\text{-}4)(\eta^3\text{-}C_4H_7)]_2$ shows that the phase is dependent on temperature and decomposition method.[165] The thermolytic decomposition in furnace provides Pd_7Se_4 nanoparticles, whereas in OLA or TOPO $Pd_{17}Se_{15}$ phase was obtained

exclusively. The deposition of thin films by AA-CVD also shows Pd_7Se_4 phase with spherical crystallites. Sampath *et al*. synthesized palladium didodecylselenolate and the palladium selenide films were prepared by drop casting method followed by annealing.[166] Different phases ($Pd_{17}Se_{15}$, Pd_7Se_4) were deposited by variations in Pd:Se precursor ratio, and a solar conversion efficiency of 7.45 % and 6.88 % was observed for $Pd_{17}Se_{15}$ and Pd_7Se_4 respectively. However, the decomposition of the phenyl analogue in toluene/HDA mixture at 220 °C results in the formation of PdSe nanoparticles.[167]

Jain *et al*. reported a series of organotin complexes of pyridyl[168] and pyrimidyl[169] ligands for tin selenide nanoparticles and thin films. The decomposition of $[Me_2Sn(2\text{-}SeC_5H_4N)_2]$ and $[^tBu_2Sn(2\text{-}SeC_5H_4N)_2]$ complexes yields SnSe in OLA at 220 °C, whereas the $[Et_2Sn(2\text{-}SeC_5H_4N)_2]$ and $[Et_2Sn(2\text{-}SeC_5H_3(Me\text{-}3)N)_2]$ complexes gave the $SnSe_2$ phase. The morphology was also found to be dependent on OLA concentration. Thin films were also deposited from the $[^tBu_2Sn(2\text{-}SeC_5H_4N)_2]$ complex by AA-CVD in the temperature range of 490-530 °C. SnSe films were deposited and selenium deficiency was observed at high deposition temperature. Interestingly, the use of pyrimidyl complexes $[R_2Sn(SeC_4H(Me\text{-}4,6)_2N_2)_2]$ (R = Et, ^nBu, ^tBu), results in the formation of the $SnSe_2$ phase in OLA. Similarly, the $SnSe_2$ phase was also obtained for thin films deposited by AA-CVD. The complexes provide a good example of phase and shape tuning of nanoparticles and thin films by using suitable molecular precursors.

1.3.8. Selenocarboxylate complexes

Although the chemistry of thiocarboxylate complexes have been explored extensively, the higher congener (Se and Te) analogues are scarcely reported. The prime difficulty is synthesis and stability of the seleno/telluro carboxylates and their metal complexes. This maybe the major reason the scarcity literature on seleno/telluro carboxylate complexes. Vittal *et al*. has reported use of the selenocarboxylate complexes as molecular precursors for metal selenides. A series of copper complexes $[(Ph_3P)_2Cu(SeOCR)_2Cu(PPh_3)]$ (R = C_6H_5, CH_3-*p*-C_6H_4, CH_3O-*p*-C_6H_4, Cl-*p*-C_6H_4, F-*p*-C_6H_4, -CH_3) were synthesized and the crystal structures of toluic acid and acetyl derivative were determined.[170] Attempts to prepare the complex in 1:1 ratio also results

in a dimeric complex. The pyrolysis of the complexes in furnace under nitrogen results in a mixture of CuSe and $Cu_{2-x}Se$ phases. The para substitution doesn't have any effect on the nature of the product formed. Nonetheless, the nanoparticles synthesized in TOPO/TOP mixture yields only the $Cu_{2-x}Se$ phase. Similarly, the selenobenzoate complex of silver $[(Ph_3P)_3Ag_2(SeOCPh)_2]$ was reported. [171] It was observed that the complex decomposes in primary amines, even at room temperature. Different reaction parameters were investigated (time duration, temperature and concentration) which shows that the morphology was strongly dependent on temperature and precursor to capping agent ratio. They also synthesized a series of hetero-bimetallic $[(Ph_3P)_2M'In(SeOCPh)_4]$ (M′ = Ag, Cu) and anionic complexes $[A(MeCN)_xM(SeOCPh)_4]$ (A= Na, K; M = In, Ga; x = 0, 2). Crystal structures of bimetallic complexes and anionic complexes of indium were elucidated.[172] The molecular precursors were thermally pyrolyzed under inert conditions, to obtain In_2Se_3, $KInSe_2$, $KGaSe_2$, $CuInSe_2$, and $AgInSe_2$. The diffraction pattern for $NaGaS_2$ and $NaInS_2$ was unidentified.

The synthesis of $AgInSe_2$ nanoparticles was investigated thoroughly in OLA/DT mixture by using $[(PPh_3)_2AgIn(SeOCPh)_4]$ precursor at different temperatures and precursor to surfactant ratios.[173] The results indicate that the complex decomposes first to Ag_2Se and indium containing intermediate species, which on extended heating, reacts and yields $AgInSe_2$ nanoparticles. An attempt to synthesize $AgIn(SSe)_2$ nanoparticles by using a mixture of thio/seleno molecular precursors, was unsuccessful as a mixture of products was obtained. The non-linear optical response of $AgInSe_2$ nanoparticles was also investigated, the analysis indicates that $AgInSe_2$ is highly suitable candidate for saturable absorption devices.[174]

Jain *et al*. reported selenobenzoate complexes of platinum and palladium.[175] The decomposition of palladium complex $[Pd(SeOCPh)_2(P^nPr_3)_2]$ in furnace was carried out at 350 °C, under argon flow and residue was characterized as $Pd_{17}Se_{15}$. A similar phase was also obtained in tri-butylphosphate solution but at a lower temperature of 200 °C.

A summary of all the complexes used in preparation of nanoparticles and for thin films by different methods is given in Table 1.1 and Table 1.2.

Table 1.1. Molecular precursors used for the deposition of metal selenide thin films.

Precursor	Crystal structure elucidated	Material	Method	Substrate/ Temperature	Ref
$Cd[N(SeP^iPr_2)_2]_2$	-	$CdSe/Cd_3P_2$	AACVD	Glass/475-525 °C	30
$[MeCd(SeP^iPr_2)_2N]_2$	Yes	CdSe	LPCVD	Glass/450 °C	31
$Cd[(SeP^iPr_2)_2N]_2$	-	CdSe	LPCVD	Glass/425-500 °C	32
$Cd[(SePPh_2)_2N]_2$	-	CdSe	LPCVD	Glass/475-525 °C	33
$Zn[(SeP^iPr_2)_2N]_2$ (R= Ph, ^{i}Pr)	Yes	ZnSe	LPCVD	Glass/400-525 °C	32-33
$[Me_2M(SeP^iPr_2)_2N]$ (M= In, Ga)	Yes	M_2Se_3	LPCVD/ AACVD	Glass/400-500 °C	34
$In[(SeP^iPr_2)_2N]_2Cl$	-	In_2Se_3	LPCVD/ AACVD	Glass/Si/GaAs/ 400-525 °C	35
$Bi[(SePR_2)_2N]_3$ (R= Ph, ^{i}Pr)	Yes	Bi_2Se_3	LPCVD/ AACVD	Glass/375-475 °C	37-38
$Pb[(SePR_2)_2N]_2$ (R= Ph, ^{i}Pr)	-	PbSe	LPCVD/ AACVD	Glass/400-450 °C	39-40
$[Ag(^iPr_2P(X)NP(Se)^iPr_2)]_3$ (X=S, Se)	Yes	Ag_2Se	LPCVD/ AACVD	Glass/325-475 °C	42-43
$Fe[(SePR_2)_2N]_2$ (R= Ph, ^{i}Pr)	Yes	$Fe_7Se_8/FeSe_2$	AACVD	Glass/500-600 °C	44
$Fe[(SeP^iPr_2)_2N]_2$	-	$FeSe/Fe_3Se_4$	Vapor transport	Glass/600-800 °C	45
$Co[(SeP^iPr_2)_2N]_2$	-	$CoSe_2/CoP/\ CoP_2$	AACVD	Glass/375-525 °C	46
$Pd[N(^iPr_2PSe)_2]_2$	-	$PdSe_2/Pd_{17}Se_{15}/Pd_4Se$	LPCVD	Glass/400-475 °C	48
$Pt[N(^iPr_2PSe)_2]_2$	-	$PtSe_2$	LPCVD	Glass/400-475 °C	48
$Ni(^iPr_2P(S)NP(Se)^iPr_2)_3$	Yes	$Ni_{0.85}Se/Ni_2P$	AACVD/ LPCVD	Glass/ITO-Glass/375-475 °C	49-51
$Ni[(SeP^iPr_2)(TeP^iPr_2)N]_2$	Yes	$NiTe_2$	AACVD	Glass/450-500 °C	50
$Ni[(SeP^iPr_2)_2N]_2$	Yes	$Ni_{0.85}Se$	AACVD	Glass/450-500 °C	46
$[Cu((SeP^iPr_2)_2N)]_3$	Yes	$CuInSe_2$	AACVD	Glass/375-450 °C	43
$[Ag(XSeP^iPr_2)]_4$ (X= S, Se)	Yes	Ag_2Se	AACVD	Glass/275-475 °C	42

$Co(Se_2P^iPr_2)_2$	-	Co_9Se_8/CoP	AACVD	Glass/450 °C	46
$[Cu_4(^iPr_2PSe_2)_4]$	Yes	$Cu_{2-x}Se$	AACVD	Glass/350-500 °C	63
$In(^iPr_2PSe_2)_3$	Yes	In_2Se_3	AACVD	Glass/350-500 °C	63
$Ni(Se_2P^iPr_2)_2$	Yes	$Ni_{0.85}Se$	AACVD	Glass/350-500 °C	46
$Pb(SeSPPh_2)_2$	Yes	PbSe	AACVD	Glass/450-500 °C	67
$[Sn(Ph_2PSe_2)_2]$	-	$SnSe/Cu_3SnS_2$	AACVD	Glass/400-450 °C	70
$M(^iPr_2PSe_2)_3$ (M= In, Ga) and $Cu(^iPr_2PSe_2)$	Yes	$CuMSe_2$	AACVD	Glass/350-500 °C	63
$Bi[Se_2P(O^iPr)_2]_3$	Yes	$Bi_2Se_3/BiPO_4$	AACVD	Si(Au)/350-450 °C	91
$[Cu_4(Se_2P(O^iPr)_2)_4]$	Yes	$Cu_{2-x}Se$	MOCVD	Si/360 °C	94
$Pb[Ph(RO)PSe_2]_2$ (R = Me, Et)	-	PbSe	AACVD	Glass/Si/300-500 °C	96
$Bi[Se_2CN(C_4H_9)_2]_3$	Yes	Bi_2Se_3	AACVD	Glass/450-500 °C	98
$[Cd_2(Se_2CNEt_2)_4]$	Yes	CdSe/CdSSe	AACVD	Glass/300 °C	100
$Cd(Se_2CNEtBu)_2$	-	CdSe	MOCVD	Glass/300-400 °C	101
$(Cd(Se_2CNMeHex)_2)$	-	CdSe	MOCVD	Glass/400-450 °C	102
$Co(Se_2CNEt_2)_3$	-	$CoSe_2$	AACVD	Glass/450 °C	46
$In(Se_2CNMe^nhexyl)_3$	-	In_2Se_3	AACVD	Glass/InP/450-500 °C	107
$In(Se_2CNEtBu)_3$	-	In_2Se_3	MOCVD	Glass/ITO-glass/330 °C	108
$Ni(Se_2CNEt_2)_2$	-	$NiSe_2$	AACVD	Glass/400-450 °C	46
$Zn(Se_2CNEt_2)_2$	-	ZnSe/ZnSSe	AACVD	Glass/350 °C	111
$[Fe(C_{10}H_7CONCSeN(C_2H)_2)_3]$	Yes	FeSe	AACVD	Si/650 °C	120
$[Pb(C_{10}H_7CONCSeN(C_2H)_2)_2]$	-	PbSe/PbSSe	Spin coating	Glass/250 °C	122
$[Pd(C_{10}H_7CONCSeN(C_2H)_2)_2]$	-	$Pd_{17}Se_{15}$	AACVD	Glass/400-500 °C	123
$[(4\text{-}NO_2\text{-}C_6H_4CONHCSeN^iBu_2)Pb(II)]$	Yes	PbSe	AACVD	Glass/250-500 °C	124
$[MCl_5(Se^nBu_2)]$ (M= Nb, Ta)	-	MSe_2	LPCVD	SiO_2/600-750 °C	135
$[GaCl_3(Se^nBu_2)]$	-	Ga_2Se_3	LPCVD	SiO_2/TiN/500-600 °C	136
$Pd[(SeR_2)_2(OAc)_2]$ (R=	-	Pd_7Se_4/Pd_4Se	Spin	Glass/250 °C	140

dodecyl)		/$Pd_{17}Se_{15}$	coating		
$[SnCl_4(Et_2Se)_2]$	Yes	SnSe/$SnSe_2$	LPCVD	SiO_2/500 °C	142
$[SnCl_4(^nBuSe(CH_2)_n Se^nBu)]$	Yes	$SnSe_2$	LPCVD	Si/SiO_2/TiN/400-600 °C	143
$[(Cp)_2V(Se^tBu)_2]$	-	VSe_2	LPCVD	SiO_2/500-600 °C	145
$TiCl_4(Se(CH_2CH_3)_2)_2$	Yes	$TiSe_2$	LPCVD	Glass/500-600 °C	146
$TiCl_4$[*o*-$C_6H_4(CH_2SeMe)_2$]	-	$TiSe_2$	LPCVD	SiO_2/500 °C	142
$[Cu(SeC_5H_3(Me\text{-}3)N)]_4$	Yes	Cu_5Se_4	AACVD	Glass/360-400 °C	150
$[M(SeC_5H_3(Me\text{-}3)N)_3]$ (M= Sb, Bi)	Yes	M_2Se_3	AACVD	Glass/375-500 °C	153
$Me_2InSePh$ and $In(SePh)_3$	-	InSe/In_2Se_3	Spray MOCVD	GaAs/Si/350-550 °C	154
$[(^tBu)_2In(Se^tBu)]_2$	-	InSe	MOCVD	GaAs/Si/SiO_2/ 350 °C	155
$[Me_2In(SeMe)]_2$	-	InSe	MOCVD	GaAs/250-370 °C	156
$[Cu(SeC_4H(Me\text{-}4,6)_2 N_2)]_6$	Yes	Cu_7Se_4	AACVD	Glass/ 400 °C	160
$[Pd(\mu\text{-}SeC_5H_4N\text{-}2)(\eta^3\text{-}C_4H_7)]_2$	Yes	Pd_7Se_4	AACVD	Glass/Si/265 °C	165
$Pd(SeR)_2$ (R= dodecyl)	-	Pd_7Se_4/$Pd_{17}Se_{15}$	Drop cast	Glass/FTO/250 °C	166
$[^tBu_2Sn(2\text{-}SeC_5H_4N)_2]$	Yes	SnSe	AACVD	Glass/490-530 °C	168
$[R_2Sn(SeC_4H(Me\text{-}4,6)_2 N_2)_2]$ (R = Et, ^{n}Bu, ^{t}Bu)	Yes	$SnSe_2$	AACVD	Si/375 °C	169

Table 1.2. Molecular precursors used for the synthesis of metal selenide nanoparticles.

Precursor	Crystal structure elucidated	Material	Method	Capping agent/ Temperature	Ref
$Cd[N(SeP^iPr_2)_2]_2$	-	CdSe	Hot injection	TOPO/TOP/250 °C	29
$Hg[(^iPr_2PSe)_2N]_2$	yes	HgSe	Solid state decomposition	300-400 °C	36
$Pb[(SeP^iPr_2)_2N]_2$	-	PbSe/PbSSe	Hot injection	TOPO/TOP/210 °C	41

$Fe[(SePR_2)_2N]_2$ (R= Ph, ^iPr)	yes	$FeSe_2$	Colloidal synthesis	OLA/HDA/ 190-270 °C	44
[Pd(allyl)$(PhPSe)_2$N-Se,Se')]	yes	$Pd_{17}Se_{15}$	Solid state decomposition	300-500 °C	47
$[Cd(Se_2P^iPr_2)_2]$	-	CdSe	Flow reactor	OLA/180-220 °C	58
$Co(Se_2PR_2)_2$ (R= Ph, ^iPr, ^tBu)	-	$CoSe_2$/CoP	Hot injection	HDA/TOPO/TOP/ 300 °C	60
$[Cu_4(^iPr_2PSe_2)_4]$	yes	$Cu_{2-x}Se$	Hot injection	HDA/TOP/250-300 °C	61-62
$In(^iPr_2PSe_2)_3$	yes	In_2Se_3	Hot injection	HDA/TOP/270 °C	61
$Ni(Se_2PR_2)_2$ (R= Ph, ^iPr, ^tBu)	yes	Ni_2P/$Ni_{12}P_5$/ NiSe	Hot injection	HDA/TOPO/TOP/ 280-330 °C	65
$Eu(Se_2PPh_2)_2$	yes	EuSe	Solvothermal	HDA/310-330 °C	66
$Pb(SeSPPh_2)_2$	yes	PbSe	Solvothermal	OLA/DT/25 °C	67
$Pb(Se_2PPh_2)_2$	Yes	PbSe	Solvothermal	OLAc/80 °C	69
$Zn(Se_2P^iPr_2)_2$	-	ZnSe	Solvothermal	HDA/300 °C	73
$M(^iPr_2PSe_2)_3$ (M= In, Ga) and $Cu(^iPr_2PSe_2)$	Yes	$CuMSe_2$	Hot injection	HDA/300 °C	75
$Sb[Se_2P(O^iPr)_2]_3$	yes	Sb_2Se_3	Solvothermal	100-150 °C	92
$Pb[Se_2P(O^iPr)2]_2$	Yes	PbSe	Solvothermal	PVP/150 °C	95
$[Cd_2(Se_2CNEt_2)_4]$	Yes	CdSe	Pyrolysis	320 °C	99
$Cd(Se_2CNMeHex)_2$	-	CdSe	Solvothermal	TOPO/250 °C	103-104
$[Cu_8(H)(Se_2CN^nPr_2)6]PF_6$	Yes	CuSe	Autoclave	1-DDT/200 °C	106
$In(Se_2CNEt_2)_3$	-	InSe	Solvothermal	TOPO/TOP/250 °C	109
$EtZnSe_2CNEt_2$	-	ZnSe	Solvothermal	TOPO/TOP/250 °C	110
$Cd[(C_6H_5CONCSe\ N(C_2H_5)_2]_2$	-	CdSe	Hot injection	HDA/TOP/100-250 °C	119
$[Fe(C_{10}H_7CONCSeN\ (C_2H)_2)_3]$	Yes	$FeSe_2$	Solvothermal	OLA/190-290 °C	120
$[Pb(C_{10}H_7CONCSeN\ (C_2H)_2)_2]$	Yes	PbSe	Hot injection	TOPO/190-290 °C	121
$[Pd(C_{10}H_7CONCSeN\ (C_2H)_2)_2]$	-	$PdSe_2$/ $Pd_{17}Se_{15}$	Solvothermal	OLA/DT/240 °C	123
$[(4\text{-}NO_2\text{-}C_6H_4CONH\ CSeN^iBu_2)Pb(II)]$	Yes	PbSe	Hot injection	TOP/OLAc/1-ODE /200 °C	124
$(SbL_2Cl_2)Cl$ (L= *N*,*N*-dimethyl selenourea)	Yes	Sb_2Se_3	Solvothermal	Ethylene glycol/120 °C	126
$((Ph_2NCOCH_2)_2Se)_2PdCl_2$	Yes	$Pd_{17}Se_{15}$	Solvothermal	TOP/280 °C	137
[PdLCl]X (X= BF_4, L= pyrazolated selenoether)	Yes	Pd_4Se/PdSe	Solvothermal	TOP/200-250 °C	138
$[PdCl_2(PhSe\text{-}C_3H_6\text{-}NHR)]$(R= H, $C_6H_4CH(C_6H_4\text{-}2OH)$)	-	Pd_4Se/ Pd_7Se_4	Solvothermal	TOP/280-300 °C	139
$[Ag_5(TFA)_5(Me_2Se)_4]$	Yes	Ag_2Se	Solvothermal	1-ODE/315 °C	144
$[Cd_3(OAc)_2(SeCH_2\ CH_2NMe_2)_4]$	Yes	CdSe	Solvothermal/ Solventless	HDA/TOPO/180-200 °C	147

$Zn(SeCH_2CH_2NMe_2)$	Yes	ZnSe	Solventless	320-450 °C	148
$[Cu(RSe)_\infty]$ (R = Ph, Me, *t*-Bu)	Yes	Cu_2Se	Solventless	180 °C	149
$[Cu(SeC_5H_3(Me3)N)]_4$	Yes	$Cu_{1.8}Se$	Solventless	400 °C	150
$[Cu(SePy)]_4$	Yes	CuSe/ $Cu_{2-x}Se$	Solventless	220-250 °C	151
$In(SePy)_3$	Yes	In_2Se_3	Solventless	220-250 °C	151
$M(SeC_6F_5)_n$ (M= Cu, In, Sn, Pb)	Yes	M_xSe_y	Solventless	650 °C	152
$[M(SeC_5H_3(Me-3)N)_3]$ (M= Sb, Bi)	Yes	M_2Se_3	Solvothermal	HDA/200 °C	153
$[In(SeC_5H_3(Me-3)N)_3]$	Yes	In_2Se_3	Solvothermal	HDA/TOPO/OLA/ 330 °C	158
$(PPh_3)_2CuIn(SePh)_4$	Yes	$CuInSe_2$	Solvothermal	Dioctyl phthalate/ 200-300 °C	159
$[M(SeC_4H(Me-4,6)_2N_2)]_6$ (M = Cu and Ag)	Yes	Ag_2Se/ Cu_7Se_4	Hot injection	DDT/150 °C	160
$[Ag(Se-4-py)(PPh_3)_3]$	Yes	Ag_2Se	Solvothermal/ Solventless	HDA/TOPO/270 °C	161
$Ln(ER)_2$ or $Ln(ER)_3$	Yes	LnE/Ln_2E_3	Solventless	-	162
$[Pb(SeC_2H_4R)_2]$ (R= NMe_2, COOMe)	Yes	PbSe	Hot injection/ Solventless	HDA/180-250 °C	163
$[Pd_2Cl_2(\mu\text{-}Se\ C_2H_4\ COOMe)_2(PPr_3)_2]$	-	$Pd_{17}Se_{15}$	Solvothermal	TBP/195 °C	164
$[Pd(\mu\text{-}SeC_5H_4N\text{-}2)(\eta^3\text{-}C_4H_7)]_2$	yes	Pd_7Se_4/ $Pd_{17}Se_{15}$	Solvothermal/ Solventless	OLA/TOPO/220 °C	165
$Pd(SeR)_2$ (R= C_6H_5)	-	PdSe	Solvothermal	Toluene/HDA/220 °C	167
$[R_2Sn(2\text{-}SeC_5H_4N)_2]$ (R= Me, Et, ^{t}Bu)	Yes	$SnSe/SnSe_2$	Solvothermal	OLA/220 °C	168
$[R_2Sn(SeC_4H(Me-4,6)_2N_2)_2]$ (R = Et, ^{n}Bu, ^{t}Bu)	Yes	$SnSe_2$	Solvothermal	OLA/210 °C	169
$[(Ph_3P)_2Cu(SeOCR)_2Cu(PPh_3)]$ (R= acetyl, tolyl)	Yes	$Cu_{2-x}Se$/ CuSe	Hot injection/ Solventless	TOPO/TOP/200-300 °C	170
$[(Ph_3P)_3Ag_2(SeOCPh)_2]$	Yes	Ag_2Se	Hot injection	OLA/90-180 °C	171
$[A(M)(SeOCPh)_4]$ (A= Na, K; M = In, Ga)	Yes	$AMSe_2$	Solventless	300-500 °C	172
$[(PPh_3)_2AgIn(SeOCPh)_4]$	-	$AgInSe_2$	Solvothermal	OLA/DT/119-132 °C	173-174
$[M(SeOCPh)_2(P^nPr_3)_2]$ (M= Pd, Pt)	Yes	$Pd_{17}Se_{15}$	Solvothermal/ Solventless	TBP/200-350 °C	175

1.4. Statement of Research Problem

It is well established fact that the electronic properties are dependent on the morphology and phase of the metal chalcogenides and that can be tuned by changing the nature of the ligands. Similarly the ease with which a single source precursor decomposes depends on the type of the ligand used. Some of the ligands after decomposition incorporate inseparable impurities, for example phosphorus containing ligand after decomposition gives either phosphorus as impurity or sometimes purely results in formation of metal phosphides. Similarly some of the metal chalcogenides like copper, cobalt, iron, manganese and tin *etc.* exist in various phases. For such materials phase pure material is necessarily required for the applications, without presence of any other phase as an impurity. Controlling the phase for such materials is interesting as well as a challenging study. Some of the metal complexes are not soluble so it is difficult to use them for thin films deposition by aerosol assisted chemical vapor deposition. There are a few selenium based ligands which are phosphine free for synthesis of metal selenides, herein lies considerable potential in this regard which needs to be explored.

As observed by the literature survey, selenobenzoate complexes are not very well explored. It prompted this study to use selenobenzoate complexes of unexplored metals, which have not been used for the nanomaterials synthesis, and establish their suitability for the preparation of respective metal selenide nanoparticles, thin films and alloys. The potential of the as synthesized nanomaterials for water splitting will also be investigated.

The results will be compared for improved discernment of judicious reaction conditions which can be used to tune the desirable properties of the nanomaterials and their suitability when scaling up to industrial nanomaterial synthesis.

1.5. Aims and Objectives

The present research is aimed to develop a simple and an efficient route for the synthesis of new selenobenzoate metal complexes. It is well known fact that the efficiency of nanomaterials can be enhanced multifold by introducing anisotropy. Hence, in this study, such metals will be used whose selenides, intrinsically have anisotropic

structures for *e.g.* Sn, Bi and Sb. The selenides of all these metals have layered structures and their complexes will be used to prepare anisotropic nanomaterials and thin films. The complexes will also be used to prepare alloys with tunable electronic and optical properties.

Main objectives are as follow:

- To develop a facile route for a selenobenzoate ligand.
- To use selenobenzoate ligand for the synthesis of metal (Sn, Bi and Sb) complexes and their characterization.
- To prepare metal selenide thin films and nanoparticles of the respective metal complexes.
- To study the effect of various deposition parameters such as deposition temperature, solvent, and molar ratio of precursors on optical properties and stoichiometric composition of as deposited thin films and nanoparticles.
- To investigate the effectiveness of anisotropic nanomaterials in photocatalytic water splitting.
- To synthesize solid solution of alloys with tunable composition and properties.

1.6 References

1. J. Turkevich, P. C. Stevenson and J. Hillier, *Discussions of the Faraday Society*, 1951, **11**, 55-75.
2. W. Stöber, A. Fink and E. Bohn, *Journal of Colloid and Interface Science*, 1968, **26**, 62-69.
3. P. S. Stephen, *Journal*, 1965.
4. P. V. Kamat, *The Journal of Physical Chemistry C*, 2008, **112**, 18737-18753.
5. H. Goesmann and C. Feldmann, *Angewandte Chemie International Edition*, 2010, **49**, 1362-1395.
6. S. Shrivastava, T. Bera, A. Roy, G. Singh, P. Ramachandrarao and D. Dash, *Nanotechnology*, 2007, **18**, 225103.
7. S. Sun, C. B. Murray, D. Weller, L. Folks and A. Moser, *Science*, 2000, **287**, 1989-1992.
8. A. Ethirajan, U. Wiedwald, H. G. Boyen, B. Kern, L. Han, A. Klimmer, F. Weigl, G. Kaestle, P. Ziemann and K. Fauth, *Advanced Materials*, 2007, **19**, 406-410.
9. S. Colodrero, A. Mihi, L. Häggman, M. Ocaña, G. Boschloo, A. Hagfeldt and H. Míguez, *Advanced Materials*, 2009, **21**, 764-770.
10. D. Timmerman, I. Izeddin, P. Stallinga, I. Yassievich and T. Gregorkiewicz, *Nature Photonics*, 2008, **2**, 105-109.
11. C.-Y. Liu, Z. C. Holman and U. R. Kortshagen, *Nano Letters*, 2008, **9**, 449-452.
12. T. K. Todorov, K. B. Reuter and D. B. Mitzi, *Advanced Materials*, 2010, **22**.
13. P. Jackson, D. Hariskos, E. Lotter, S. Paetel, R. Wuerz, R. Menner, W. Wischmann and M. Powalla, *Progress in Photovoltaics: Research and Applications*, 2011, **19**, 894-897.
14. L. J. Diguna, Q. Shen, J. Kobayashi and T. Toyoda, *Applied Physics Letters*, 2007, **91**, 023116.
15. P. Gibot, M. Casas-Cabanas, L. Laffont, S. Levasseur, P. Carlach, S. Hamelet, J.-M. Tarascon and C. Masquelier, *Nature Materials*, 2008, **7**, 741-747.
16. X. Xiao, L. Wang, D. Wang, X. He, Q. Peng and Y. Li, *Nano Research*, 2009, **2**, 923-930.
17. X. Xiao, X. Liu, L. Wang, H. Zhao, Z. Hu, X. He and Y. Li, *Nano Research*, 2012, 1-7.
18. H. S. Kim, K. Y. Chung and B. W. Cho, *Journal of Power Sources*, 2009, **189**, 108-113.

19. N. Liu, H. Wu, M. T. McDowell, Y. Yao, C. Wang and Y. Cui, *Nano Letters*, 2012, **12**, 3315-3321.
20. C.-M. Park, J.-H. Kim, H. Kim and H.-J. Sohn, *Chemical Society Reviews*, 2010, **39**, 3115-3141.
21. J. M. Vohs and R. J. Gorte, *Advanced Materials*, 2009, **21**, 943-956.
22. G. A. Slack and D. Rowe, *CRC, Boca Raton, FL*, 1995, **407**.
23. L. Hicks and M. S. Dresselhaus, *Physical Review B*, 1993, **47**, 12727.
24. L. Hicks and M. S. Dresselhaus, *Physical review B*, 1993, **47**, 16631.
25. R. Venkatasubramanian, E. Siivola, T. Colpitts and B. O'quinn, *Nature*, 2001, **413**, 597-602.
26. J. Karch, R. Birringer and H. Gleiter, *Nature*, 1987, **330**, 556-558.
27. E. Breckenfeld, R. Wilson, J. Karthik, A. Damodaran, D. Cahill and L. Martin, *Chemistry of Materials*, 2012, **24**, 331-337.
28. J. Yu and A. Kudo, *Advanced Functional Materials*, 2006, **16**, 2163-2169.
29. D. Crouch, P. O'Brien, M. Malik, P. Skabara and S. Wright, *Chemical Communications*, 2003, 1454-1455.
30. T. Oyetunde, M. Afzaal, M. A. Vincent and P. O'Brien, *Dalton Transactions*, 2016, **45**, 18603-18609.
31. M. Afzaal, D. Crouch, M. A. Malik, M. Motevalli, P. O'Brien and J.-H. Park, *Journal of Materials Chemistry*, 2003, **13**, 639-640.
32. M. Afzaal, D. Crouch, M. A. Malik, M. Motevalli, P. O'Brien, J. H. Park and J. D. Woollins, *European Journal of Inorganic Chemistry*, 2004, **2004**, 171-177.
33. M. Afzaal, S. M. Aucott, D. Crouch, P. O'Brien, J. D. Woollins and J. H. Park, *Chemical Vapor Deposition*, 2002, **8**, 187-189.
34. J.-H. Park, M. Afzaal, M. Helliwell, M. A. Malik, P. O'Brien and J. Raftery, *Chemistry of Materials*, 2003, **15**, 4205-4210.
35. M. Afzaal, D. Crouch and P. O'Brien, *Materials Science and Engineering: B*, 2005, **116**, 391-394.
36. D. J. Crouch, P. M. Hatton, M. Helliwell, P. O'Brien and J. Raftery, *Dalton Transactions*, 2003, 2761-2766.

37. D. J. Crouch, M. Helliwell, P. O'Brien, J.-H. Park, J. Waters and D. J. Williams, *Dalton Transactions*, 2003, 1500-1504.
38. J. Waters, D. Crouch, J. Raftery and P. O'Brien, *Chemistry of Materials*, 2004, **16**, 3289-3298.
39. N. O. Boadi, P. D. McNaughter, M. Helliwell, M. A. Malik, J. A. Awudza and P. O'Brien, *Inorganica Chimica Acta*, 2016, **453**, 439-442.
40. M. Afzaal, K. Ellwood, N. L. Pickett, P. O'Brien, J. Raftery and J. Waters, *Journal of Materials Chemistry*, 2004, **14**, 1310-1315.
41. A. C. Onicha, N. Petchsang, T. H. Kosel and M. Kuno, 2012.
42. A. Panneerselvam, C. Q. Nguyen, M. A. Malik, P. O'Brien and J. Raftery, *Journal of Materials Chemistry*, 2009, **19**, 419-427.
43. M. Afzaal, D. J. Crouch, P. O'Brien, J. Raftery, P. J. Skabara, A. J. White and D. J. Williams, *Journal of Materials Chemistry*, 2004, **14**, 233-237.
44. M. Akhtar, M. A. Malik, J. Raftery and P. O'Brien, *Journal of Materials Chemistry A*, 2014, **2**, 20612-20620.
45. N. Levesanos, W. P. Liyanage, E. Ferentinos, G. Raptopoulos, P. Paraskevopoulou, Y. Sanakis, A. Choudhury, P. Stavropoulos, M. Nath and P. Kyritsis, *European Journal of Inorganic Chemistry*, 2016, **2016**, 5332-5339.
46. A. Panneerselvam, C. Q. Nguyen, J. Waters, M. A. Malik, P. O'Brien, J. Raftery and M. Helliwell, *Dalton Transactions*, 2008, 4499-4506.
47. A. Singhal, D. Dutta, S. Kulshreshtha, S. Mobin and P. Mathur, *Journal of Organometallic Chemistry*, 2006, **691**, 4320-4328.
48. P. Musetha, N. Revaprasadu, G. Kolawole, R. V. Pullabhotla, K. Ramasamy and P. O'Brien, *Thin Solid Films*, 2010, **519**, 197-202.
49. A. Panneerselvam, M. A. Malik, M. Afzaal, P. O'Brien and M. Helliwell, *Journal of the American Chemical Society*, 2008, **130**, 2420-2421.
50. S. D. Robertson, T. Chivers, J. Akhtar, M. Afzaal and P. O'Brien, *Dalton Transactions*, 2008, 7004-7011.
51. A. Panneerselvam, G. Periyasamy, K. Ramasamy, M. Afzaal, M. A. Malik, P. O'Brien, N. A. Burton, J. Waters and B. E. van Dongen, *Dalton Transactions*, 2010, **39**, 6080-6091.

52. J. Masud, P. C. Ioannou, N. Levesanos, P. Kyritsis and M. Nath, *ChemSusChem*, 2016, **9**, 3128-3132.
53. P. Kevin, S. N. Malik and M. A. Malik, *Materials Letters*, 2015, **152**, 60-64.
54. W. Kuchen and B. Knop, *Angewandte Chemie International Edition*, 1965, **4**, 244-245.
55. A. V. Artem'ev, N. K. Gusarova, S. F. Malysheva and B. A. Trofimov, *Organic Preparations and Procedures International*, 2011, **43**, 381-449.
56. A. V. Artem'ev, S. F. Malysheva, N. K. Gusarova and B. A. Trofimov, *Synthesis*, 2010, **2010**, 2463-2467.
57. C. Q. Nguyen, A. Adeogun, M. Afzaal, M. A. Malik and P. O'Brien, *Chemical Communications*, 2006, 2182-2184.
58. A. L. Abdelhady, M. Afzaal, M. A. Malik and P. O'Brien, *Journal of Materials Chemistry*, 2011, **21**, 18768-18775.
59. F. Opoku, N. K. Asare-Donkor and A. A. Adimado, *Chemistry Central Journal*, 2016, **10**, 4.
60. W. Maneeprakorn, M. A. Malik and P. O'Brien, *Journal of Materials Chemistry*, 2010, **20**, 2329-2335.
61. S. N. Malik, M. Akhtar, N. Revaprasadu, A. Q. Malik and M. A. Malik, 2014.
62. S. N. Malik, H. Ahmed, M. Shahid, N. Haider, M. Malik and P. O'Brien, 2013.
63. S. Mahboob, S. N. Malik, N. Haider, C. Nguyen, M. A. Malik and P. O'Brien, *Journal of Crystal Growth*, 2014, **394**, 39-48.
64. R. P. Davies, C. V. Francis, A. P. Jurd, M. G. Martinelli, A. J. White and D. J. Williams, *Inorganic Chemistry*, 2004, **43**, 4802-4804.
65. W. Maneeprakorn, C. Q. Nguyen, M. A. Malik, P. O'Brien and J. Raftery, *Dalton Transactions*, 2009, 2103-2108.
66. M. Burin, A. Pushkarev, G. Fukin, R. Rumyantsev, A. Konev and M. Bochkarev, *Nanotechnologies in Russia*, 2017, **12**, 66-72.
67. J. Akhtar, M. Afzaal, M. A. Vincent, N. A. Burton, J. Raftery, I. H. Hillier and P. O'Brien, *The Journal of Physical Chemistry C*, 2011, **115**, 16904-16909.
68. F. Opoku, N. K. Asare-Donkor and A. A. Adimado, *Canadian Journal of Chemistry*, 2014, **93**, 317-325.

69. C. M. Evans, M. E. Evans and T. D. Krauss, *Journal of the American Chemical Society*, 2010, **132**, 10973-10975.
70. P. Kevin, S. N. Malik, M. A. Malik and P. O'Brien, *Chemical Communications*, 2014, **50**, 14328-14330.
71. R.-Y. Jhang, J.-H. Liao, C. Liu, A. V. Artem'ev and V. A. Kuimov, *Journal of Organometallic Chemistry*, 2015, **781**, 72-76.
72. R.-Y. Jhang, J.-H. Liao, C. Liu, V. A. Kuimov, N. K. Gusarova and A. V. Artem'ev, *Journal of Organometallic Chemistry*, 2014, **758**, 60-64.
73. C. Q. Nguyen, M. Afzaal, M. A. Malik, M. Helliwell, J. Raftery and P. O'Brien, *Journal of Organometallic Chemistry*, 2007, **692**, 2669-2677.
74. F. Opoku, N. K. Asare-Donkor and A. A. Adimado, *SpringerPlus*, 2015, **4**, 266.
75. S. N. Malik, S. Mahboob, N. Haider, M. A. Malik and P. O'Brien, *Nanoscale*, 2011, **3**, 5132-5139.
76. M. V. Kudchadker, R. A. Zingaro and K. J. Irgolic, *Canadian Journal of Chemistry*, 1968, **46**, 1415-1424.
77. T. S. Lobana, J.-C. Wang and C. Liu, *Coordination Chemistry Reviews*, 2007, **251**, 91-110.
78. J. R. Wasson, G. M. Woltermann and H. J. Stoklosa, in *Inorganic Chemistry*, Springer, 1973, pp. 65-129.
79. V. Krishnan and R. A. Zingaro, *Inorganic Chemistry*, 1969, **8**, 2337-2340.
80. V. Krishnan and R. A. Zingaro, *Journal of Coordination Chemistry*, 1971, **1**, 1-6.
81. R. S. Dhayal, J. H. Liao, X. Wang, Y. C. Liu, M. H. Chiang, S. Kahlal, J. Y. Saillard and C. Liu, *Angewandte Chemie International Edition*, 2015, **54**, 13604-13608.
82. R. S. Dhayal, J. H. Liao, S. Kahlal, X. Wang, Y. C. Liu, M. H. Chiang, W. E. van Zyl, J. Y. Saillard and C. Liu, *Chemistry-A European Journal*, 2015, **21**, 8369-8374.
83. C. Liu, I.-J. Shang, C.-M. Hung, J.-C. Wang and T.-C. Keng, *Journal of the Chemical Society, Dalton Transactions*, 2002, 1974-1979.
84. R. S. Dhayal, Y. R. Lin, J. H. Liao, Y. J. Chen, Y. C. Liu, M. H. Chiang, S. Kahlal, J. Y. Saillard and C. Liu, *Chemistry-A European Journal*, 2016, **22**, 9943-9947.
85. B. K. Santra, B.-J. Liaw, C.-M. Hung, C. Liu and J.-C. Wang, *Inorganic Chemistry*, 2003, **42**, 8866-8871.

86. B. K. Santra, C.-M. Hung, B.-J. Liaw, J.-C. Wang and C. Liu, *Inorganic Chemistry*, 2004, **43**, 7570-7572.
87. C.-S. Fang, Y.-J. Huang, B. Sarkar and C. Liu, *Journal of Organometallic Chemistry*, 2009, **694**, 404-410.
88. J.-M. Chen, B. K. Santra and C. Liu, *Inorganic Chemistry Communications*, 2004, **7**, 1103-1105.
89. B.-J. Liaw, L. Yu, J.-C. Wang and C. Liu, *Polyhedron*, 2008, **27**, 1818-1824.
90. C. Liu, Y.-R. Lin, C.-S. Fang, C. Latouche, S. Kahlal and J.-Y. Saillard, *Inorganic Chemistry*, 2013, **52**, 2070-2077.
91. Y.-F. Lin, H.-W. Chang, S.-Y. Lu and C. Liu, *The Journal of Physical Chemistry C*, 2007, **111**, 18538-18544.
92. H.-W. Chang, B. Sarkar and C. Liu, *Crystal Growth and Design*, 2007, **7**, 2691-2695.
93. K. W. Sun, C.-H. Yang, T.-Y. Ko, H.-W. Chang and C.-W. Liu, *Pure and Applied Chemistry*, 2009, **81**, 1511-1522.
94. Y.-J. Hsu, C.-M. Hung, Y.-F. Lin, B.-J. Liaw, T. S. Lobana, S.-Y. Lu and C. Liu, *Chemistry of Materials*, 2006, **18**, 3323-3329.
95. W.-S. Chang, Y.-F. Lin, B. Sarkar, Y.-M. Chang, L.-K. Liu and C. Liu, *Dalton Transactions*, 2010, **39**, 2821-2830.
96. K. Ahmad, M. Afzaal, P. O'Brien, G. Hua and J. Derek Woollins, *Chemistry of Materials*, 2010, **22**, 4619-4624.
97. W. H. Pan, J. P. Fackler, D. Anderson, S. Henderson and T. Stephenson, *Inorganic Syntheses, Volume 21*, 1982, 6-11.
98. O. C. Monteiro, T. Trindade, F. A. A. Paz, J. Klinowski, J. Waters and P. O'Brien, *Journal of Materials Chemistry*, 2003, **13**, 3006-3010.
99. M. B. Hursthouse, M. A. Malik, M. Motevalli and P. O'Brien, *Polyhedron*, 1992, **11**, 45-48.
100. P. Kevin, Y. G. Alghamdi, D. J. Lewis and M. A. Malik, *Materials Science in Semiconductor Processing*, 2015, **40**, 848-854.
101. D.-Y. Chae, K.-W. Seo, S.-S. Lee, S.-H. Yoon and I.-W. Shim, *Bulletin of the Korean Chemical Society*, 2006, **27**, 762-764.
102. M. Chunggaze and J. McAleese, *Chemical Communications*, 1998, 833-834.

103. M. Lazell, S. J. Nørager, P. O'Brien and N. Revaprasadu, *Materials Science and Engineering: C*, 2001, **16**, 129-133.
104. B. Ludolph and M. Malik, *Chemical Communications*, 1998, 1849-1850.
105. M. Bonamico and G. Dessy, *Journal of the Chemical Society A: Inorganic, Physical, Theoretical*, 1971, 264-269.
106. R. S. Dhayal, J.-H. Liao, H.-N. Hou, R. Ervilita, P.-K. Liao and C. Liu, *Dalton Transactions*, 2015, **44**, 5898-5908.
107. P. O'Brien, D. J. Otway and J. R. Walsh, *Chemical Vapor Deposition*, 1997, **3**, 227-229.
108. S.-S. Lee, K.-W. Seo and I.-W. Shim, *Bulletin of the Korean Chemical Society*, 2006, **27**, 147-149.
109. M. Azad Malik and P. O'Brien, *Journal of Materials Chemistry*, 1999, **9**, 2885-2888.
110. M. Azad Malik and M. Zulu, *Journal of Materials Chemistry*, 1998, **8**, 1885-1888.
111. Y. Alghamdi, *Materials Sciences and Applications*, 2017, **8**, 726.
112. J.-H. Park, M. Afzaal, M. Kemmler, P. O'Brien, D. J. Otway, J. Raftery and J. Waters, *Journal of Materials Chemistry*, 2003, **13**, 1942-1949.
113. M. Lipp, F. Dallacker and I. M. zu Köcker, *Monatshefte für Chemie und verwandte Teile anderer Wissenschaften*, 1959, **90**, 41-48.
114. N. Sonoda, G. Yamamoto and S. Tsutsumi, *Bulletin of the Chemical Society of Japan*, 1972, **45**, 2937-2938.
115. I. B. Douglass, *Journal of the American Chemical Society*, 1937, **59**, 740-742.
116. V. Garcia, M. Nair, P. Nair and R. Zingaro, *Semiconductor Science and Technology*, 1997, **12**, 645.
117. Y. Zhang and X. Nie, *Colloids and Surfaces A: Physicochemical and Engineering Aspects*, 2016, **506**, 378-382.
118. X. Ma, W. Nie, D. Pan, X. Ji, C. Wang and W. Zhang, *CrystEngComm*, 2011, **13**, 5243-5249.
119. J. C. Bruce, N. Revaprasadu and K. R. Koch, *New Journal of Chemistry*, 2007, **31**, 1647-1653.
120. M. Akhtar, J. Akhtar, M. A. Malik, F. Tuna, M. Helliwell and P. O'Brien, *Journal of Materials Chemistry*, 2012, **22**, 14970-14975.

121. J. Akhtar, M. Akhtar, M. A. Malik, P. O'Brien and J. Raftery, *Journal of the American Chemical Society*, 2012, **134**, 2485-2487.
122. S. A. Saah, P. D. McNaughter, M. A. Malik, J. A. Awudza, N. Revaprasadu and P. O'Brien, *Journal of Materials Science*, 1-11.
123. J. Akhtar, R. F. Mehmood, M. A. Malik, N. Iqbal, P. O'Brien and J. Raftery, *Chemical Communications*, 2011, **47**, 1899-1901.
124. J. Akhtar, M. A. Malik, S. K. Stubbs, P. O'Brien, M. Helliwell and D. J. Binks, *European Journal of Inorganic Chemistry*, 2011, **2011**, 2984-2990.
125. M. P. Campos, M. P. Hendricks, A. N. Beecher, W. Walravens, R. A. Swain, G. T. Cleveland, Z. Hens, M. Y. Sfeir and J. S. Owen, *Journal of the American Chemical Society*, 2017, **139**, 2296-2305.
126. N. Maiti, S. H. Im, Y. H. Lee, C.-H. Kim and S. I. Seok, *CrystEngComm*, 2011, **13**, 3767-3772.
127. Y. C. Choi, T. N. Mandal, W. S. Yang, Y. H. Lee, S. H. Im, J. H. Noh and S. I. Seok, *Angewandte Chemie International Edition*, 2014, **53**, 1329-1333.
128. A. Y. Koposov, *CrystEngComm*, 2017, **19**, 3098-3102.
129. R. A. Hussain, A. Badshah, A. Younis, M. D. Khan and J. Akhtar, *Thin Solid Films*, 2014, **567**, 58-63.
130. R. A. Hussain, A. Badshah, F. Yasmin, M. D. Khan and M. N. Tahir, *Australian Journal of Chemistry*, 2015, **68**, 298-306.
131. R. A. Hussain, A. Badshah, N. Haider, M. D. Khan and B. Lal, *Journal of Chemical Sciences*, 2015, **127**, 499-507.
132. R. A. Hussain, A. Badshah, M. D. Khan, N. Haider, S. I. Khan and A. Shah, *Materials Chemistry and Physics*, 2015, **159**, 152-158.
133. M. D. Khan, S. Hameed, N. Haider, A. Afzal, M. C. Sportelli, N. Cioffi, M. A. Malik and J. Akhtar, *Materials Science in Semiconductor Processing*, 2016, **46**, 39-45.
134. M. Aamir, M. Sher, M. D. Khan, M. A. Malik, J. Akhtar and N. Revaprasadu, *Materials Letters*, 2017, **190**, 244-247.
135. S. L. Benjamin, Y.-P. Chang, C. Gurnani, A. L. Hector, M. Huggon, W. Levason and G. Reid, *Dalton Transactions*, 2014, **43**, 16640-16648.

136. K. George, C. H. de Groot, C. Gurnani, A. L. Hector, R. Huang, M. Jura, W. Levason and G. Reid, *Chemistry of Materials*, 2013, **25**, 1829-1836.
137. P. Singh and A. K. Singh, *Dalton Transactions*, 2017, **46**, 10037-10049.
138. K. N. Sharma, H. Joshi, V. V. Singh, P. Singh and A. K. Singh, *Dalton Transactions*, 2013, **42**, 3908-3918.
139. V. V. Singh, G. K. Rao, A. Kumar and A. K. Singh, *Dalton Transactions*, 2012, **41**, 1142-1145.
140. S. Kukunuri, P. M. Austeria and S. Sampath, *Chemical Communications*, 2016, **52**, 206-209.
141. N. D. Boscher, C. J. Carmalt, R. G. Palgrave and I. P. Parkin, *Thin Solid Films*, 2008, **516**, 4750-4757.
142. S. D. Reid, A. L. Hector, W. Levason, G. Reid, B. J. Waller and M. Webster, *Dalton Transactions*, 2007, 4769-4777.
143. C. De Groot, C. Gurnani, A. L. Hector, R. Huang, M. Jura, W. Levason and G. Reid, *Chemistry of Materials*, 2012, **24**, 4442-4449.
144. S. Mishra, D. Du, E. Jeanneau, F. Dappozze, C. Guillard, J. Zhang and S. Daniele, *Chemistry–An Asian Journal*, 2016, **11**, 1658-1663.
145. A. L. Hector, M. Jura, W. Levason, S. D. Reid and G. Reid, *New Journal of Chemistry*, 2009, **33**, 641-645.
146. P. J. McKarns, T. S. Lewkebandara, G. P. Yap, L. M. Liable-Sands, A. L. Rheingold and C. H. Winter, *Inorganic Chemistry*, 1998, **37**, 418-424.
147. G. Kedarnath, S. Dey, V. K. Jain, G. K. Dey and B. Varghese, *Polyhedron*, 2006, **25**, 2383-2391.
148. S. Dey, V. K. Jain, S. Chaudhury, A. Knoedler and W. Kaim, *Polyhedron*, 2003, **22**, 489-491.
149. K.-H. Low, C.-H. Li, V. A. Roy, S. S.-Y. Chui, S. L.-F. Chan and C.-M. Che, *Chemical Science*, 2010, **1**, 515-518.
150. R. K. Sharma, G. Kedarnath, V. K. Jain, A. Wadawale, C. Pillai, M. Nalliath and B. Vishwanadh, *Dalton Transactions*, 2011, **40**, 9194-9201.
151. Y. Cheng, T. Emge and J. Brennan, *Inorganic Chemistry*, 1996, **35**, 7339-7344.

152. K. Holligan, P. Rogler, D. Rehe, M. Pamula, A. Y. Kornienko, T. J. Emge, K. Krogh-Jespersen and J. G. Brennan, *Inorganic Chemistry*, 2015, **54**, 8896-8904.
153. R. K. Sharma, G. Kedarnath, V. K. Jain, A. Wadawale, M. Nalliath, C. Pillai and B. Vishwanadh, *Dalton Transactions*, 2010, **39**, 8779-8787.
154. H. J. Gysling, A. A. Wernberg and T. N. Blanton, *Chemistry of Materials*, 1992, **4**, 900-905.
155. S. L. Stoll and A. R. Barron, *Chemistry of Materials*, 1998, **10**, 650-657.
156. J.-Y. Cho, H.-C. Jeong, K.-S. Kim, D.-H. Kang, H.-K. Kim and I.-W. Shim, *Bulletin of the Korean Chemical Society*, 2003, **24**, 645-646.
157. I.-H. Choi and P. Y. Yu, *Journal of Applied Physics*, 2003, **93**, 4673-4677.
158. R. K. Sharma, G. Kedarnath, N. Kushwah, M. K. Pal, A. Wadawale, B. Vishwanadh, B. Paul and V. K. Jain, *Journal of Organometallic Chemistry*, 2013, **747**, 113-118.
159. S. L. Castro, S. G. Bailey, R. P. Raffaelle, K. K. Banger and A. F. Hepp, *Chemistry of Materials*, 2003, **15**, 3142-3147.
160. R. K. Sharma, A. Wadawale, G. Kedarnath, D. Manna, T. K. Ghanty, B. Vishwanadh and V. K. Jain, *Dalton Transactions*, 2014, **43**, 6525-6535.
161. G. K. Kole, K. Vivekananda, M. Kumar, R. Ganguly, S. Dey and V. K. Jain, *CrystEngComm*, 2015, **17**, 4367-4376.
162. A. Kornienko, D. Freedman, T. J. Emge and J. G. Brennan, *Inorganic Chemistry*, 2001, **40**, 140-145.
163. G. Kedarnath, L. B. Kumbhare, S. Dey, A. P. Wadawale, V. K. Jain and G. K. Dey, *Polyhedron*, 2009, **28**, 2749-2753.
164. V. K. Jain, L. B. Kumbhare, S. Dey and N. D. Ghavale, *Phosphorus, Sulfur, and Silicon*, 2008, **183**, 1003-1008.
165. K. R. Chaudhari, D. K. Paluru, A. P. Wadawale and S. Dey, *Inorganica Chimica Acta*, 2017, **467**, 221-226.
166. S. Kukunuri, S. Karthick and S. Sampath, *Journal of Materials Chemistry A*, 2015, **3**, 17144-17153.
167. S. S. Y. Chui, K. H. Low, J. Lu, V. Roy, S. L. F. Chan and C. M. Che, *Chemistry–An Asian Journal*, 2010, **5**, 2062-2074.

168. R. K. Sharma, G. Kedarnath, A. Wadawale, C. Betty, B. Vishwanadh and V. K. Jain, *Dalton Transactions*, 2012, **41**, 12129-12138.
169. A. Tyagi, G. Kedarnath, A. Wadawale, A. Y. Shah, V. K. Jain and B. Vishwanadh, *RSC Advances*, 2016, **6**, 8367-8376.
170. Z. Lu, W. Huang and J. J. Vittal, *New Journal of Chemistry*, 2002, **26**, 1122-1129.
171. M. T. Ng, C. Boothroyd and J. J. Vittal, *Chemical Communications*, 2005, 3820-3822.
172. M. T. Ng and J. J. Vittal, *Inorganic Chemistry*, 2006, **45**, 10147-10154.
173. L. Tian, M. T. Ng, N. Venkatram, W. Ji and J. J. Vittal, *Crystal Growth & Design*, 2010, **10**, 1237-1242.
174. H. I. Elim, W. Ji, M.-T. Ng and J. J. Vittal, *Applied Physics Letters*, 2007, **90**, 033106.
175. L. B. Kumbhare, V. K. Jain and B. Varghese, *Inorganica Chimica Acta*, 2006, **359**, 409-416.

Chapter # 2

Synthesis of Sb_2Se_3 nanorods and deposition of thin films by AACVD: Potential catalyst for photo-electrochemical water reduction

2.1. Introduction

Absorber materials such as, copper indium gallium sulfide, cadmium telluride and organic-inorganic hybrid perovskites (for example, $CH_3NH_4PbI_3$) have achieved remarkable device efficiencies.[1] However, the high cost of gallium/indium, the toxicity of lead and cadmium and instability of perovskite materials are important factors which limit their use at the industrial scale. Similarly, copper zinc tin sulfide (CZTS) has been introduced as a cost effective and environment friendly material but the complexity created by defects and rigorous control over the phase and stoichiometry of these materials, are serious obstacles for their large scale fabrication.[2, 3]

Antimony selenide belongs to V_2VI_3 binary metal chalcogenide materials (V = Sb, Bi or As; VI = S, Se or Te), which are an important class of semiconducting materials with anisotropic structures which find applications in photovoltaics and thermoelectric materials.[4-6] Sb_2Se_3 is a direct band gap (approximately 1.1-1.3eV) semiconductor that crystallizes in the orthorhombic system (pbnm space group) and is isomorphic with Bi_2S_3 and Sb_2S_3. It is considered a relatively non-toxic and earth abundant material with an excellent light absorption coefficient (>105 cm^{-1} at short wavelength).[7, 8] It is also cost effective and can be easily scaled up as a light absorber in thin film solar cells. In addition, Sb_2Se_3 based solid state cells[9] and photo electrochemical cells[10] exhibit high performance which attracts attention to its photo- response activity.

The structure of Sb_2Se_3 is composed of infinite $(Sb_4Se_6)_n$ chains stacked together along the [001] direction and connected by strong Sb-Se covalent bonds, whereas the chains are held together by weak Van der Waals forces. Structural anisotropy is an interesting aspect of Sb_2Se_3 which introduces features that are difficult to achieve by simple particle size manipulation. A small variation in shape may have a significant effect on the desired properties.[11, 12] For instance, a dramatic increase in the efficiency of dye sensitized solar cells was observed by using vertically aligned nanorods.[12-14] Recently, anisotropic materials such as nanorods,[15, 16] nanowires,[17, 18] nanotubes,[19] nanosheets[20, 21] and

nanoplates[22, 23] have found increased interest due to their applications in photovoltaic and thermoelectric devices.

In order to enhance the efficiency of nanomaterials and facile deposition of thin films, various single molecular precursors have been designed, for efficient control over size and morphology. However, there are only a few reports on the use of single source precursors for the synthesis of Sb_2Se_3 nanostructures or thin films. Some of the common selenium based complexes used for the deposition of metal selenide nanoparticles or thin films are dialkyldiseleno phosphates,[24, 25] 2-pyridyl selenolates,[26] and selenophosphinate precursors.[27] Sb_2Se_3 was also synthesized by alkylselenostibines and selenourea complexes.[28, 29] However selenostilbines require toxic metal alkyl compounds for their synthesis, phosphorus based complexes may lead either to phosphorus contamination or formation of an entirely different phosphate product.[24] Similarly, diselenocarbamate precursors has been used for metal selenide thin films but the synthesis requires the use of highly toxic carbon diselenide (CSe_2).

The development of reliable and efficient strategies for artificial photosynthesis has been an intensive research focus over the last decade. Water splitting using nanostructures avoiding precious metals such as platinum, gold and ruthenium is highly desirable to meet the competitive market demands. The development of materials with surface chemistry that can have better charge carrier life times and electrical capabilities is very significant for H_2 production from water.[30, 31] Sb_2Se_3 is abundant in the geosphere and have attractive thermoelectric and electrical conductivity properties.[32, 33] However, their solar water splitting properties have not been sufficiently explored.

In this chapter, an efficient synthesis of a new complex *tris*(selenobenzoato)antimony(III), its single X-ray structure, and use as single source precursor for the synthesis of the Sb_2Se_3 nanoparticles by the hot injection method and deposition of highly crystalline thin films by AACVD is reported. The as synthesized Sb_2Se_3 nanorods were also used as low cost nanomaterials for the photoelectrochemical (PEC) production of H_2 from water under sunlight illumination.

2.2. Experimental

2.2.1. Materials

The reagents and solvents *i.e.* $SbCl_3$, $NaBH_4$, benzoyl chloride, elemental selenium, ethanol, THF, I-octadecene and oleylamine were purchased from Sigma Aldrich and used without further purification.

2.2.2. Synthesis of *tris*(selenobenzoato)antimony(III) complex

NaHSe was prepared by adding ethanolic solution of $NaBH_4$ (0.5 g, 12.0 mmol in 15.0 mL ethanol) into ethanolic solution of metallic Se powder (0.5 g, 6.0 mmol, in 15.0 mL) under inert conditions using a Schlenk line at room temperature. The reddish solution becomes colourless within 5 min. of stirring indicating the formation of NaHSe. Benzoyl chloride (0.89 g, 6.0 mmol) was then added dropwise into the freshly prepared NaHSe solution. The colour of the solution changed from colourless to yellow, indicating the formation of the seleno benzoate ligand. The stirring was continued for a further 15 min, after which $SbCl_3$ (0.48 g, 2.0 mmol of in 15.0 mL ethanol) was added dropwise while stirring. A dark yellow precipitate was formed which was filtered. The dried complex was then recrystallized from the THF solution to give yellowish crystalline needles. Elemental analysis Calc: (%) for $C_{21}H_{15}O_3SbSe_3$: C 37.42, H 2.24, Sb 18.07; Found: C 37.41, H 2.20, Sb 17.97.

2.2.3. Synthesis of Sb_2Se_3 nanorods

The synthesis of Sb_2Se_3 nanorods was carried out by injecting a dispersion of antimony selenobenzoate complex in 1-octadecene (ODE) (0.25 g, 0.37 mmol, 3.0 mL) into 10.0 mL of preheated oleyl amine (OLA) at 200 °C. The color of the solution changed instantly from light yellow to brownish black, indicating the formation of nanoparticles. The stirring was continued for 1 hour at 200 °C. The heating was stopped and the solution was allowed to cool to around 60 °C, at which point 30.0 mL of 1:1 mixture of methanol and acetone was added. The

product was obtained as a black precipitate which was separated by centrifugation and washed three times with acetone.

2.2.4. Deposition of Sb_2Se_3 Thin films by AACVD

Thin films of antimony selenide were deposited on borosilicate glass substrates (approx. 1 x 3 cm). The substrates were cleaned ultrasonically in nitric acid, distilled water and finally in acetone. The setup for aerosol assisted chemical vapour deposition comprises of a carbolite tube furnace and ultrasonic equipped humidifier (deurer living LB44) for generation of aerosol. For deposition of thin films, 0.2 g (0.3 mmol) of precursor was dissolved in 20.0 mL THF in 100 mL two necked round bottom flask and placed in water bath above the piezoelectric modulator of an ultrasonic humidifier. Six glass substrates were placed into the reactor tube, which was inserted into the tube furnace. A gas inlet was attached to one neck of the flask for flow of carrier gas and the other neck was attached to the reactor tube containing the substrates by reinforced tubing. The aerosol was generated by an ultrasonic humidifier and was carried towards the heating zone of the furnace with the help of carrier gas (argon) at a flow rate of 200 sccm. Thermally induced decomposition of the precursor took place on heated surface of the substrates and resulted in the deposition of Sb_2Se_3 thin films.

2.3. Characterization

2.3.1. Elemental and Thermogravimetric analysis

Microanalysis was performed using a Thermo Scientific Flash 2000 Organic Elemental Analyzer. Thermogravimetric analyses were performed using a Mettler-Toledo TGA/DSC under nitrogen gas flow rate of 10 mL/min.

2.3.2. Powder X-ray diffraction analysis

The X-ray diffraction was performed using a Bruker D8 Discover Diffractometer using CuKα radiation ($\underline{\lambda}$ = 1.54178 Å), in a 2Θ range from 10^o to 70^o. The data collected was used to determine the lattice parameters and crystal phase.

2.3.3. Transmission electron microscopy (TEM) and High Resolution TEM (HRTEM) analysis

TEM and HRTEM images were collected on a Talos F200X at 200 kV using a FEI ceta camera. The samples were prepared by drop casting few drops from dilute solution of Sb_2Se_3 nanosheets and evaporating on Formvar-coated Cu grids (150 mesh) for TEM and holey carbon grids for HRTEM analyses.

2.3.4. Scanning electron microscopy (SEM) and Energy Dispersive Xray (EDX) analysis

Scanning electron microscopy (SEM) was carried out using a Philips XL30 FEG SEM. Energy-dispersive X-ray (EDX) spectroscopy was performed using a DX4 detector. All samples were carbon coated using an Edwards coating system E306A prior to SEM analysis.

2.3.5. Raman Spectroscopy

Raman spectra were measured using a Renishaw 1000 Micro-Raman System equipped with a 514 nm laser operating at 1 mW.

2.3.6. Uv-Vis-NIR Spectroscopy

UV−Vis-NIR spectrum was recorded using a PerkinElmer Lambda 1050 instrument, using quartz cuvettes with a path length of 1 cm.

2.3.7. Electrode preparation

PEC studies were carried out using fluorine doped tin oxide (FTO) conducting glass substrates. FTO substrates were ultra- sonicated, first in acetone and then in deionized water for 10 minutes each. A slurry of Sb_2Se_3 nanorods, was prepared by dispersing the nanosheets in *iso*-propanol and sonicated for 10 minutes. Sb_2Se_3/FTO electrode was prepared by drop casting 50 µL of the Sb_2Se_3 slurry over 1 cm^2 of the FTO glass substrate, which was then annealed at 80 °C for two hours to harden the substrate layer. An increment of 10

μL of 1% nafion solution was then drop casted over the Sb_2Se_3 layer to make it withstand during the PEC measurements. Once dried Sb_2Se_3/FTO electrode was used for all subsequent PEC studies.

2.3.8. Experimental setup

A conventional three electrode cell was used for PEC studies with Sb_2Se_3/FTO electrode as the working electrode, Ag/AgCl chloride (Saturated KCl) as reference electrode and platinum wire as an auxiliary electrode. The linear scan voltammetry (LSV) results are reported against the standard hydrogen electrode (SHE) by adding 0.197 V in all the measured results.[34] All three electrodes were placed in a 5.0 mL quartz cell containing 0.5 M sodium sulfate solution (pH 6.8) as an electrolyte. To remove any dissolved oxygen the cell solution was purged with nitrogen gas for 10 minutes prior to the PEC measurements.

A solar simulator equipped with a 150 W Xenon arc lamp (Model 16S-150, Solar Light Company Inc., Glenside PA 19038, USA) was used with a 1 sun light intensity. A mini μ-Autolab potentiostat, PGSTAT101 (MetrohAutolab.B.V. Kanaalweg, 29-G, Utrecht, The Netherlands) with NOVA 2.1 software was employed in all electrochemical experiments.

2.3.9. Single crystal X-Ray structure

The single-crystal X-ray diffraction data for the complex C_{21} H_{15} O_3 Sb Se_3 was collected by using graphite monochromated Mo-Kα radiation (λ = 0.71073 A) on a Bruker APEX diffractometer. The structure was solved by direct methods and refined by full-matrix least squares on F2. All non-H atoms were refined anisotropically. Hydrogen atoms were included in calculated positions, assigned isotropic thermal parameters and allowed to ride on their parent carbon atoms. All calculations were carried out using the SHELXTL package. The refined data of the crystal is given below in Table 2.1.

Table 2.1. Structural refinement data for complex **$C_{21}H_{15}O_3SbSe_3$** obtained from X-ray single crystallography.

Empirical formula	**$C_{21}H_{15}O_3SbSe_3$**
Formula weight	673.96
Crystal system, space group	Hexagonal,R3
Unit cell dimesnions	a = 20.8414(12) A alpha = 90 deg. b = 20.8414(12) A beta = 90 deg. c = 4.2184(3) A gamma = 120 deg.
Volume	1586.84(17) A^3
Z, Calculated density	3, 2.116 Mg/m^3
Absorption coefficient	16.412 mm^-1
Crystal size	16.412 mm^-1
Theta range for data collection	4.24 to 68.30 deg.
Data / restraints / parameters	740 / 19 / 85
Goodness-of-fit on F^2	1.066
Final R indices [I>2sigma(I)]	R1 = 0.0454, wR2 = 0.1116
R indices (all data)	R1 = 0.0454, wR2 = 0.1116
Largest diff. peak and hole	1.827 and -1.210 e.A^-3
Reflections collected / unique	1532 / 740 [R(int) = 0.0294]
Limiting indices	-24<=h<=19, -25<=k<=23, -3<=l<=5

Note: CCDC # 1052440 contains the supplementary crystallographic data for this crystal.

2.4. Results and discussion

The synthesis of the antimony complex was carried out by modifying a method reported previously.[35] This method excluded the use of sodium metal which is highly pyrophoric. We used $NaBH_4$ instead of metallic sodium and formed NaHSe in first step of reaction. The second step involved the reaction of NaHSe with benzoyl chloride to form the selenobenzoate. The reaction of selenobenzoate with the $SbCl_3$ in ethanol gave the *tris*(selenobenzoato)antimony(III) complex. Elemental and thermogravimetric analysis (TGA) were used to characterise the recrystallized product, whereas suitable crystals of antimony complex were also characterised by X-ray crystallography.

2.4.1. Single X-Ray crystal structure of *tris*(selenobenzoato)antimony(III)

The single crystal structure of the antimony complex belongs to the hexagonal R3 crystal system. The Sb atom is coordinated with three Se atoms of the selenobenzoato group and the overall geometry is based on a slightly distorted trigonal (Figure 2.1). The Sb(1)-Se(1 bond distance is 2.6019(12) Å while the C(7)-Se(1) distance is 1.931(13) Å. The Se(1)#1-Sb(1)-Se(1)#2 bond angle is 92.45(4)° with the C(7)-Se(1)-Sb(1) bond angle at 88.6(3)°. The structure is comparable to the thiobenzoate analogue of antimony as reported previously.[36]

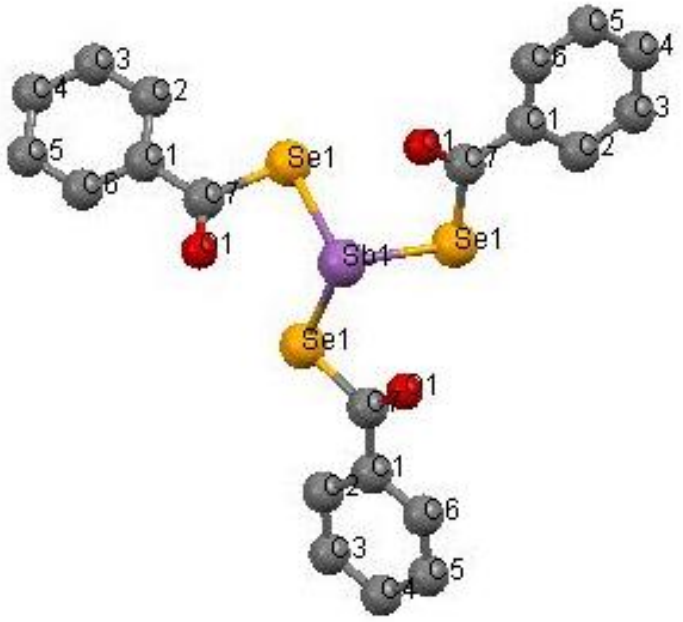

Figure 2.1. Single X-ray structure of *tris*(selenobenzoato)antimony(III) (C_{21} H_{15} O_3 Sb Se_3) with selected bond lengths (Å) and angles (°). Sb(1)-Se(1), 2.6019(12) Å , Se(1)#1-Sb(1)-Se(1)#2 92.45(4)°.

2.4.2. Thermogravimetric analysis

The TGA analysis indicates that the complex decomposed in three steps. The first step involves the major mass loss of ~36 % between the temperature range of 160 to 240 °C for antimony selenobenzoate, which is due to the loss of phenyl groups. The second step show a 14% weight loss which may be attributed to the loss of carbonyl groups, leaving behind the $SbSe_3$ fragment. The third step (13% weight loss) involved the conversion of $SbSe_3$ to Sb_2Se_3 via loss of some Se atoms.[25] The complete decomposition of the complex occurred at 390 °C giving the final residue of ~36.5% corresponding to the formation of Sb_2Se_3 respectively (Figure 2.2).

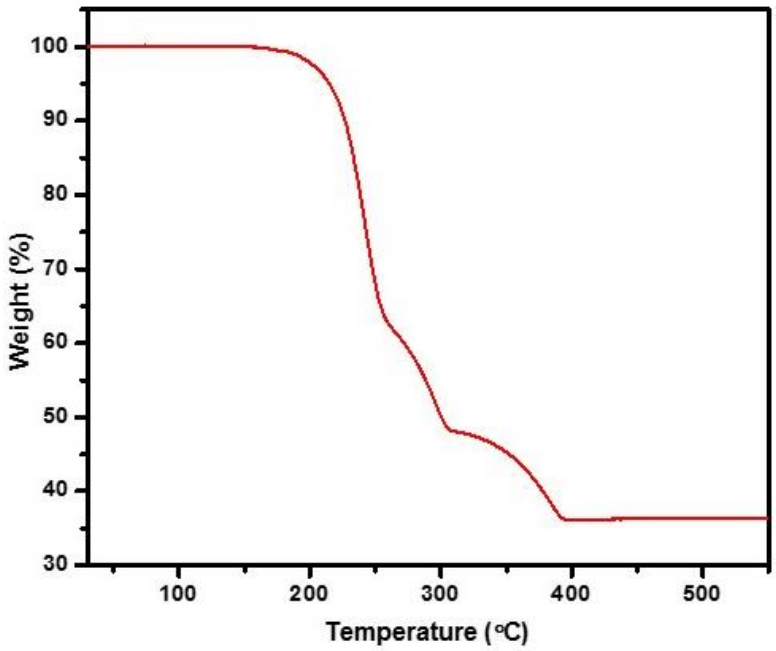

Figure 2.2. Thermogravimetric analysis of *tris*(selenobenzoato)antimony(III) complex.

2.4.3. Sb_2Se_3 nanorods

The antimony selenide nanorods were prepared from *tris*(selenobenzoato)-antimony(III) in oleylamine at 200 °C. OLA not only acts as a capping agent and solvent but also aids in the decomposition of the precursor. The decomposition of the selenobenzoate complex may follow a similar mechanism as suggested by Chin *et al*. for the decomposition of thiocarboxylate complexes in primary amines.[37, 38] Vittal *et al*. also reported the synthesis of silver selenide nanoparticles and observed that the precursor decomposes easily at room temperature in the presence of a primary alkyl amine.[39] The primary amine behaves as a nucleation initiator and accelerates the decomposition of precursor. It separates the nucleation and growth steps, which is highly desired for obtaining monodispersed nanomaterials.[40]

2.4.4. Structural characterization of Sb_2Se_3 nanorods

Figure 2.3 represents X-ray diffraction pattern of Sb_2Se_3 nanorods synthesized in OLA at 200 °C. The peaks match well with the orthorhombic antimony selenide phase (ICDD # 01-089-0821). There were no peaks indicating the presence of any impurities. The sharpness of the peaks is an indication of the high crystallinity of the nanorods. The intensity profile of the p-XRD pattern also matches well with the standard pattern, with highest intensity peak in (221) plane at 2Θ value of 31.3°.

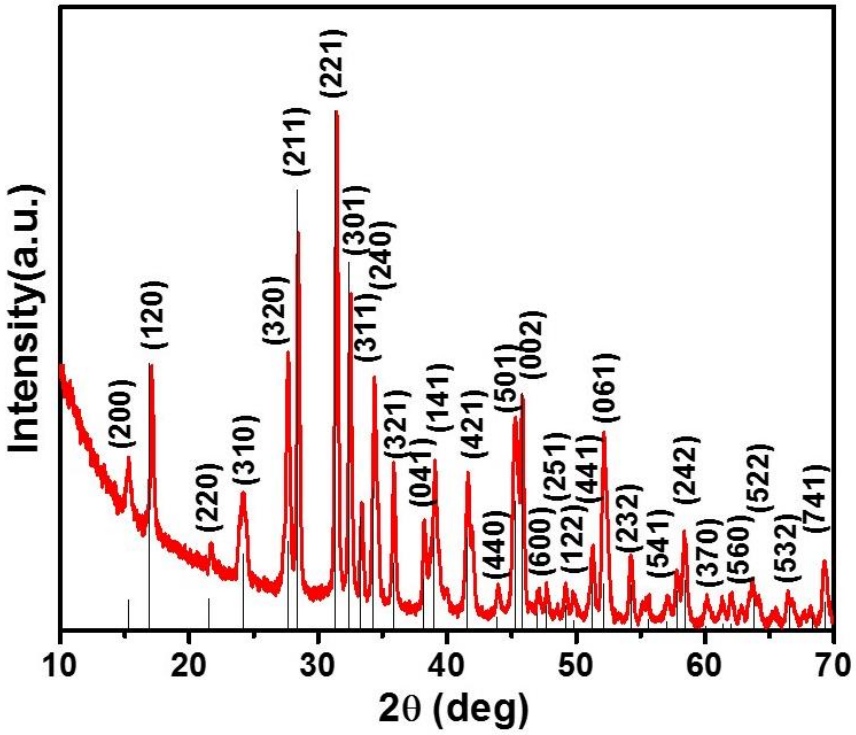

Figure 2.3 powder-XRD pattern of Sb_2Se_3 nanorods synthesized in oleylamine at 200 °C.

The TEM images show well defined Sb_2Se_3 nanostructures in the form of rods (Figure 2.4(a,b)) whose length is in the micron range. The preferential growth into rod-like morphology is largely determined by the anisotropic nature of the building blocks. The lattice fringes in the HRTEM image (Figure 2.4(c)) shows an interplanar spacing of 0.323 nm which corresponds to the (320) plane of

orthorhombic Sb_2Se_3. Well defined discrete spots were observed by SAED (Figure 2.4(d)), which shows the single crystalline nature of the nanorods and it is in agreement with the sharp peaks observed in XRD spectrum. The EDX analysis (Figure 2.5) shows the presence of only antimony and selenium (the peaks for copper are attributed to the copper grid used for analysis), with Se in slight excess.

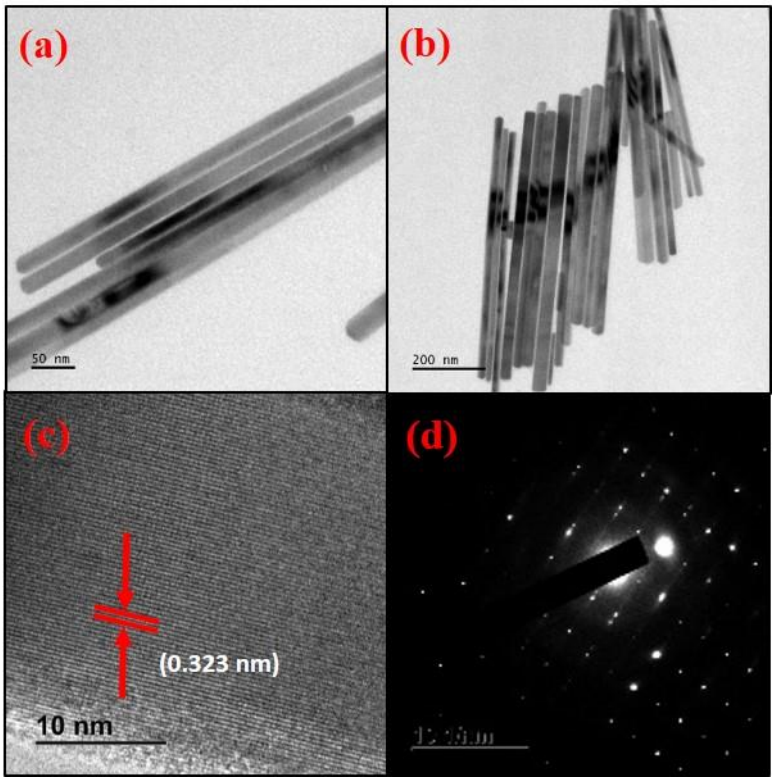

Figure 2.4 TEM images of oleylamine capped Sb_2Se_3 nanorods, (c) lattice fringes of nanorod and (d) SAED pattern.

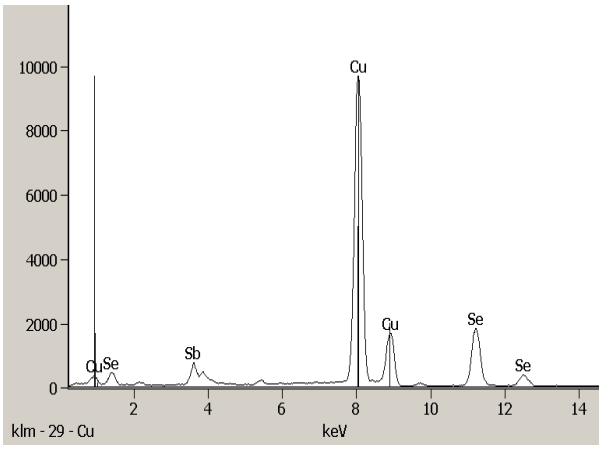

Figure 2.5 EDX analysis of Sb_2Se_3 nanorods, synthesized in oleylamine.

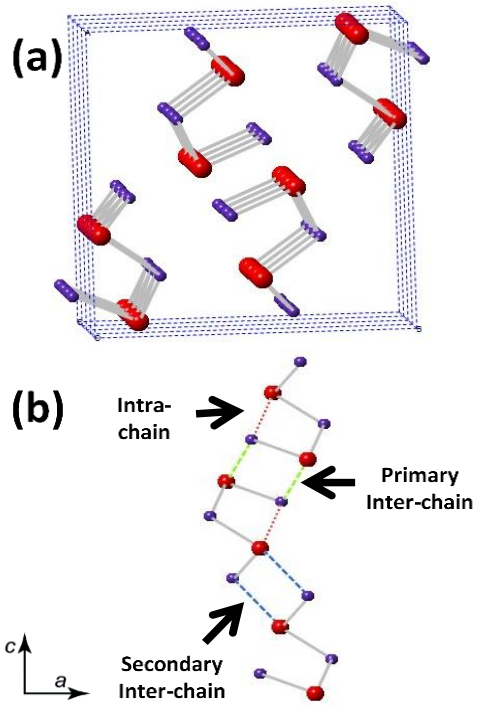

Figure 2.6 (a) Crystal structure of antimony selenide showing "infinite chains" extending through the crystal (b) section of the infinite chain highlighting the different types of atomic contacts along *c*-axis, which connect the strongly bonded 1D chains.

The structure of Sb_2Se_3 is composed of infinite long chains, extending parallel to the *c* axis with low symmetric environment of both Sb and Se atoms in the unit cell. The bonding within the chains is stronger and the chains are

interconnected by comparatively weak atomic contacts between the chain fragments, which lead to the generation of a three dimensional orthorhombic structure (Figure 2.6). The nanorods and nanowires can be synthesized by cleavage of chain fragments from the bulk phase, due to the presence of bonding anisotropy. The continuous chain like fragments which are connected to each other by weak forces, can easily break at higher temperature to give separate chain-like fragments. The injection temperature of 200 °C was high enough to break the weak inter-chain linkages and resulted in the formation of the nanorod morphology.

2.4.5. Sb_2Se_3 thin films by AACVD

Sb_2Se_3 thin films were deposited on the glass substrates using a THF solution of *tris*(selenobenzoato)antimony(III) complex. The precursor was soluble in solvents commonly used for AACVD, such as chloroform, toluene and THF. The thin films deposited using chloroform were poor in quality whereas toluene required increased deposition time. Therefore THF was chosen as the optimum solvent. As the TGA showed that the complex decomposes completely around 390 °C, the decomposition temperature was varied between 400 and 500 °C, using argon as a carrier gas with a flow rate of 200 sccm. The deposited films at all temperatures were greyish black and maximum deposition took place on the substrates which were placed in the middle to end of the quartz tube. The deposited thin films were uniform and moderately adherent. The p-XRD pattern of the thin films deposited at 400, 450 and 500 °C, is shown in Figure 2.7. The peaks match well with the antimonselite (ICDD# 01-089-0821) phase. The pattern showed significant changes in the intensity of peaks depending on the deposition temperature. This change in intensity is more obvious along the (230) plane at $2\Theta = 27.5$ which shows the decrease in peak intensity with an increase in deposition temperature. It appears as an intense peak at 400 °C and as a minor peak at 500 °C. A similar observation can be made for the (200) plane at $2\Theta = 45.95$. These observations in p-XRD patterns indicate the significant impact

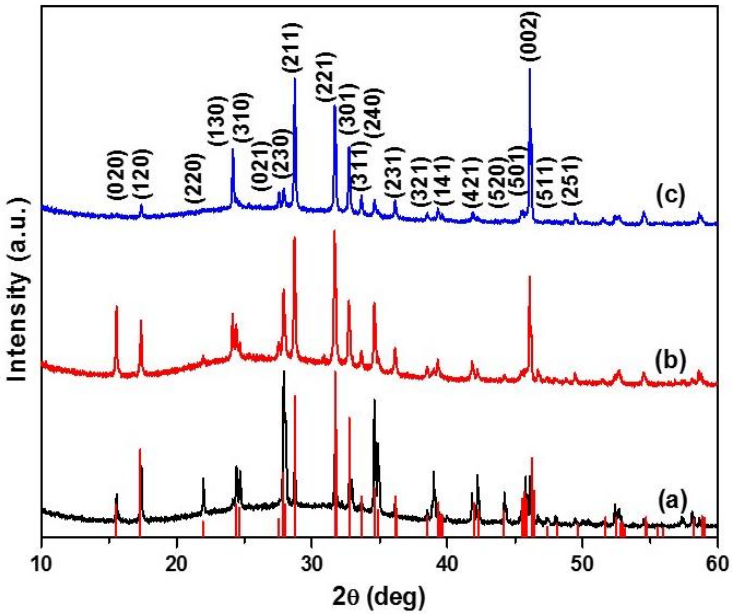

Figure 2.7. p-XRD of Sb_2Se_3 thin films deposited on glass substrates at (a) 400, (b) 450 and (c) 500 °C.

of temperature on the shape and alignment of the particles along particular planes, which in turn can have a substantial effect on the thin film morphology.

The SEM images of the thin films deposited at 400 °C at different magnifications are shown in Figure 2.8(a-d). The images showed the deposition of rod-like structures with some randomly scattered leaf-like structures with varying sizes. Elemental mapping showed the antimony and selenium were distributed uniformly throughout the film (Figure 2.9(a-c)). The thin films were slightly selenium rich as a mean Se/Sb ratio of 1.67 was observed by EDX, which is close to the stoichiometric value of 1.50 (Figure 2.10(a)).

The deposition at 450 °C resulted in the formation of exclusively rod-like structures (Figure 5(e-h)). The size of the rods ranged from 20-30 µm. A magnified SEM image (Figure 2.8(h)) reveals that the thick rods were composed of several thin ribbon-like structures. A uniform distribution of elements in the film was confirmed by elemental mapping (Figure 2.9(d-f)). The growth of the films at 450 °C showed a significant change in the stoichiometric ratio of Se/Sb (1.58) as compared to those deposited at 400 °C (1.67) (Figure 2.10(b)). The films were selenium deficient at 400 °C but selenium rich at 450 °C.

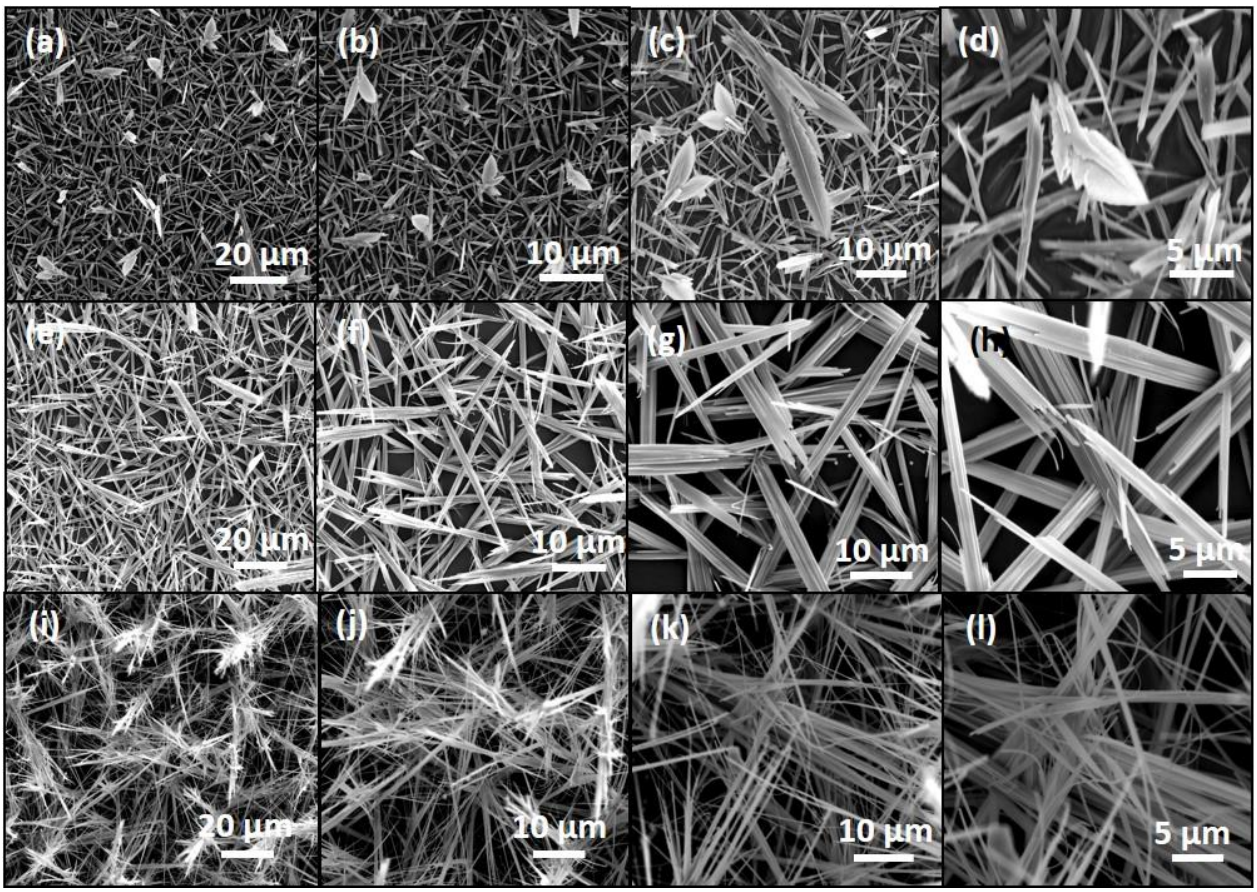

Figure 2.8. SEM images of Sb_2Se_3 thin films deposited at (a-d) 400 °C, showing leaf like morphology, at (e-h) 450 °C, showing rods like morphology and at (i-l) 500 °C, showing wire like morphology.

The morphology of thin films at 500 °C revealed the deposition of nanoribbons (Figure 2.8(i-l)). This change in shape and size of crystallites was also indicated by the change in p-XRD peaks intensity. The thickness and the lengths of these ribbons ranged from 200- 220 nm (thickness) and 40-50 µm (length). Both thermodynamic and kinetic parameters play a role in the observed morphology, as at higher temperature along with thermodynamic stability, the rate of decomposition of the precursor also increases. As shown in Figure 2.6, the nanoribbons are linked with weak interactions which start to diminish with increase in temperature. The change in morphology of the deposited thin films can be explained on the basis of the interaction between chain fragments. At a

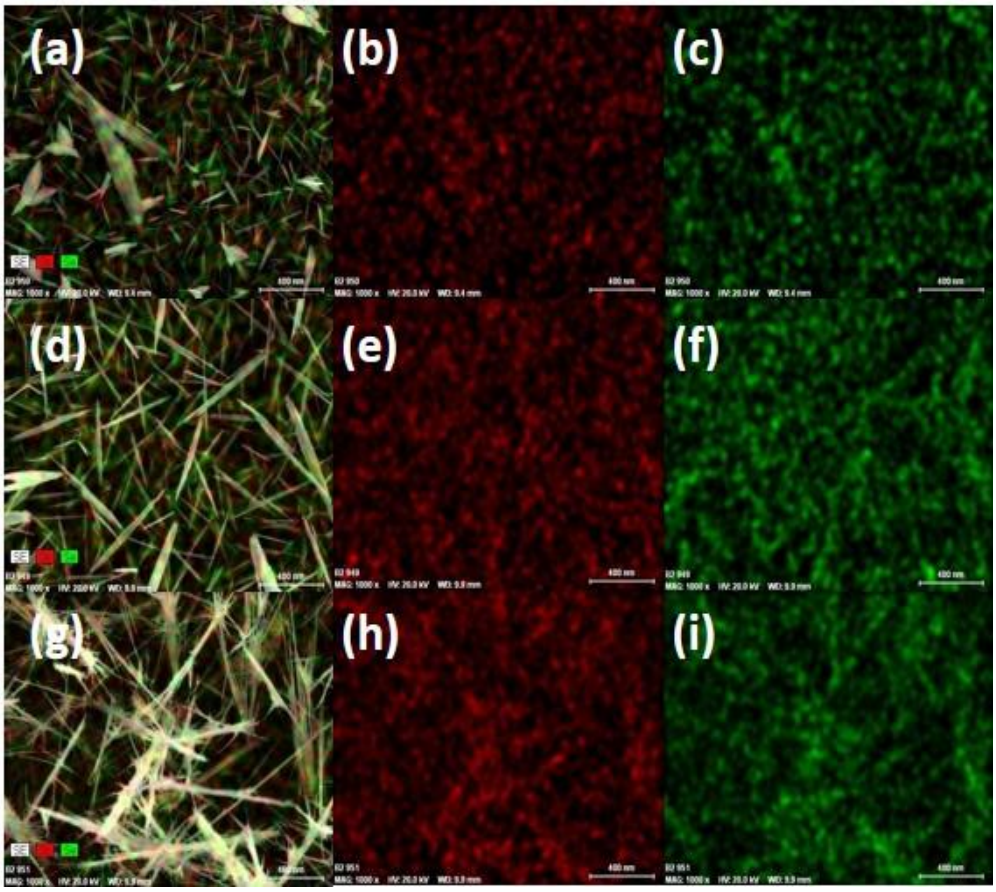

Figure 2.9. Elemental mapping of Sb_2Se_3 thin films deposited at (a-c) 400 °C, (d-f) 450 °C and (g-i) 500 °C.

deposition temperature of 400 °C the particles had large sizes, an increase in temperature to 450 °C resulted in the separation of fragments from each other. The deposition temperature of 500 °C was high enough to break the weak inter-chain linkages resulting in the formation of ribbon like morphology.

A further change in elemental stoichiometry was observed by EDX (Figure 2.10(c)) as the mean Se/Sb ratio was increased to 1.42, which shows further decrease of selenium in the deposited thin films. The elemental distribution in the thin films however was still uniform as shown in (Figure 2.9(g-i)).

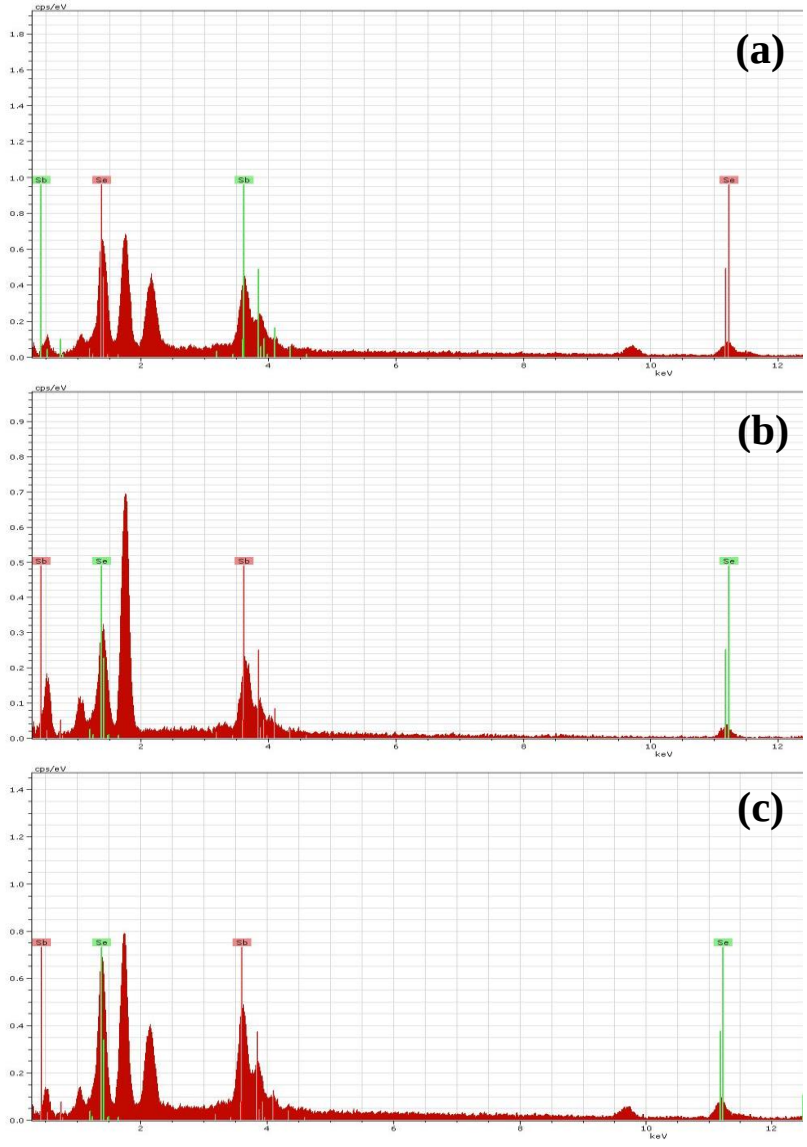

Figure 2.10. EDX spectra of Sb_2Se_3 thin films deposited at (a) 400 °C, (b) 450 °C and (c) 500 °C.

2.4.6. Optical characterization of Sb_2Se_3 nanorods and thin films

The optical properties of the Sb_2Se_3 nanorod and thin films were determined by UV-Vis-NIR spectroscopy. The thin films were immersed in acetone and scratched with a spatula. The acetone dispersions of nanorods and thin films were well sonicated for an hour before analysis. The absorption

spectrum of well dispersed Sb_2Se_3 nanorods (Figure 2.11(A)) displayed a constant rising peak with continuous absorption. The band gap of the Sb_2Se_3 nanorods as determined by the Tauc plot is estimated to be 2.1 eV, (Figure 2.12(a)). Similarly, the sonicated solution of scratched thin films was used to obtain their absorption spectra (Figure 2.11(B)). The absorption for all thin films was observed in the Vis-NIR range. A sudden sharp fall in absorption at wavelength of 860 cm^{-1} was due to the transition from NIR to Vis-region. The estimated band gap calculation for thin films indicates a successive blue shift with increase in temperature, *i.e.* 1.2, 1.35 and 1.42 eV for films deposited at 400, 450 and 500 °C respectively (Figure 2.12(b-d)). The blue shift in the band gap of both nanomaterials and thin films is in accordance with the small size in relation to the bulk.

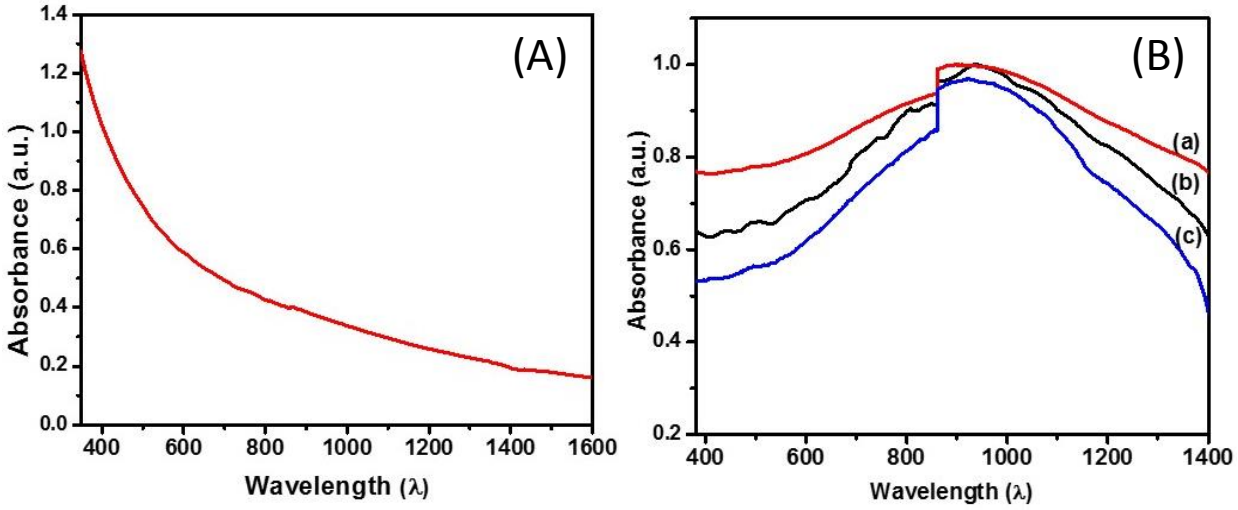

Figure 2.11. Uv-Vis-NIR spectrum of (A) Sb_2Se_3 nanorods, synthesized in oleylamine, (B) Uv-Vis-NIR spectra of Sb_2Se_3 thin films deposited at (a) 400 °C, (b) 450 °C and (c) 500 °C.

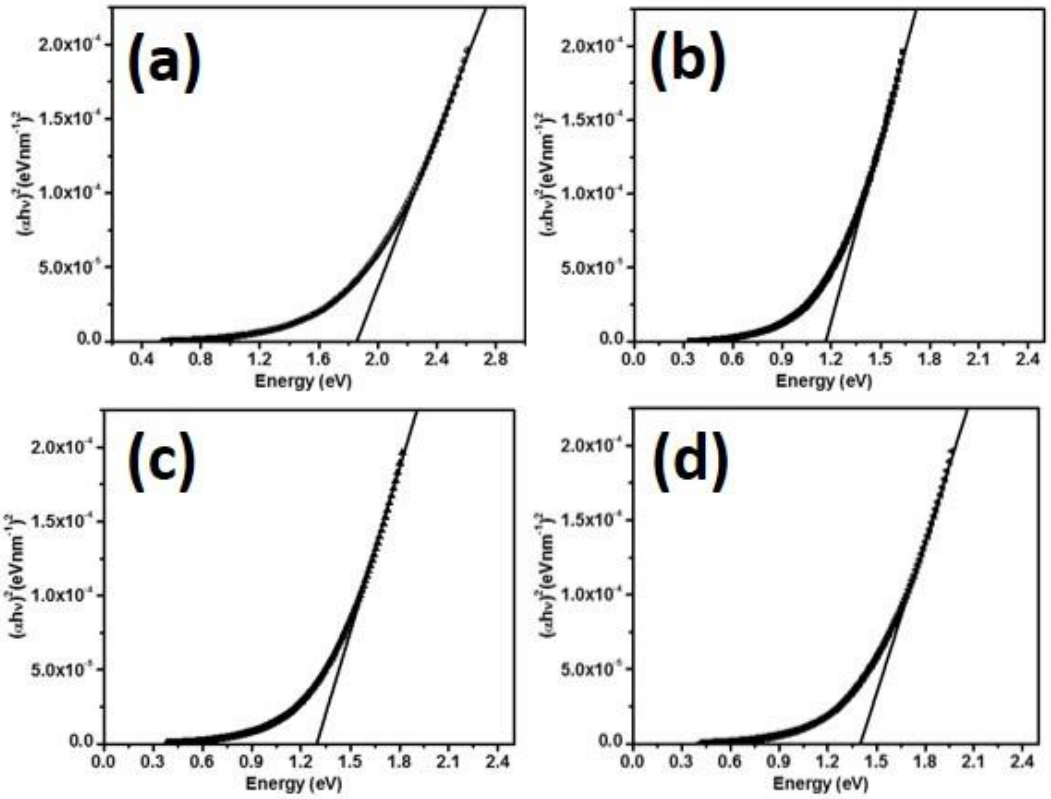

Figure 2.12. (a) Estimated band gap for Sb_2Se_3 nanorods as determined by the Tauc plot and for thin films deposited at (b) 400 °C, (c) 450 °C and (d) 500 °C.

The thin films were also characterized by Raman spectroscopy using a 514 nm laser excitation at 25 % power, and the peaks correspond well to those reported previously.[41] The vibrational modes (118 cm^{-1}, 188 cm^{-1}, 208 cm^{-1} and 252 cm^{-1}) were present in all the thin films which show that the basic lattice structure was preserved during deposition at different temperatures (Figure 2.13). However, a prominent difference was observed in the relative intensities of the bands with change in the deposition temperature. At lower temperature (400 °C), all the vibrational modes are broad and the mode with comparatively higher intensity is present at 188 cm^{-1}, whereas at higher deposition temperatures (450, 500 °C) the bands become sharper and the vibrational modes at 188 cm^{-1} and 252 cm^{-1} showed almost equal intensity. The broadening of the band is related to the presence of stress or structural defects in scattering volume and shows low

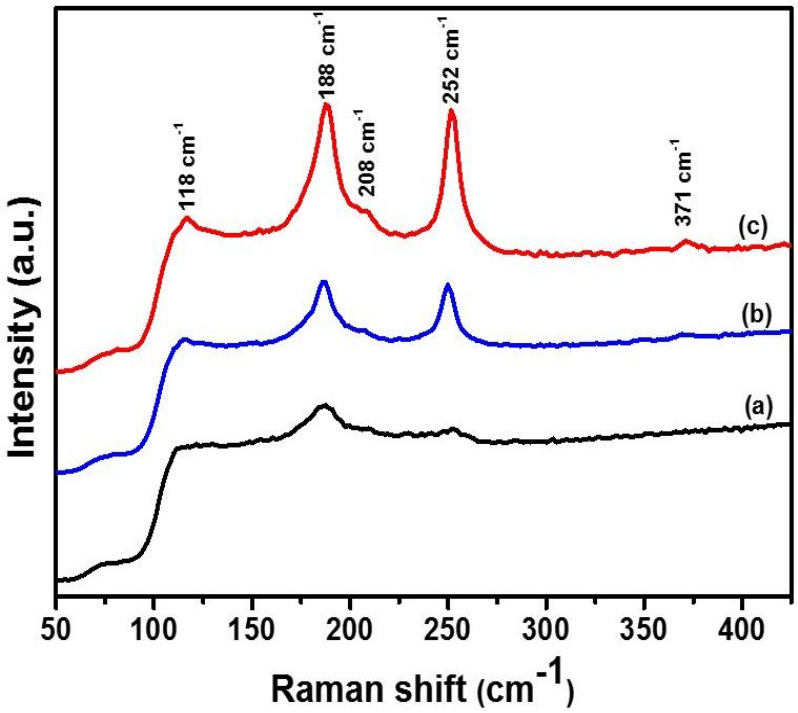

Figure 2.13. Raman spectra for Sb_2Se_3 thin films deposited at (a) 400 °C, (b) 450 °C and (c) 500 °C.

structural quality of the lattice.[42] The crystallinity of the material increased with increase in the deposition temperature so the intensity of the Raman bands. Similarly, a low intensity vibration mode at 371 cm^{-1} was only observed at a high temperature of 500 °C which, along with the intensity of other bands, can be explained on the basis of preferential orientation of crystallographic planes in the nanoribbons.

2.4.7. Photo-electrochemical water reduction catalysis

Sb_2Se_3 nanorods were observed to exhibit cathodic photocurrents indicating their p-type nature. Figure 9(a) shows the chronoamperometric performance of the Sb_2Se_3/FTO photocathode, obtained at open circuit potential (OCP) as a function of time, under simulated sunlight illumination. Once the current response was stable, the light was cut off at regular intervals. It is obvious that when light was illuminated at the surfaces of the Sb_2Se_3/FTO electrode, significant cathodic currents were generated for H_2 generation. When the light

was cut off, the photocurrent density instantaneously became negligible. This inferred that the current generated was only due to the illuminated light and not to any intrinsic properties of the Sb_2Se_3 nanostructures.[43] For Sb_2Se_3/FTO, the photo-cathodic current generated was in the range - 44.8 to - 52.1 $\mu A.cm^{-2}$.

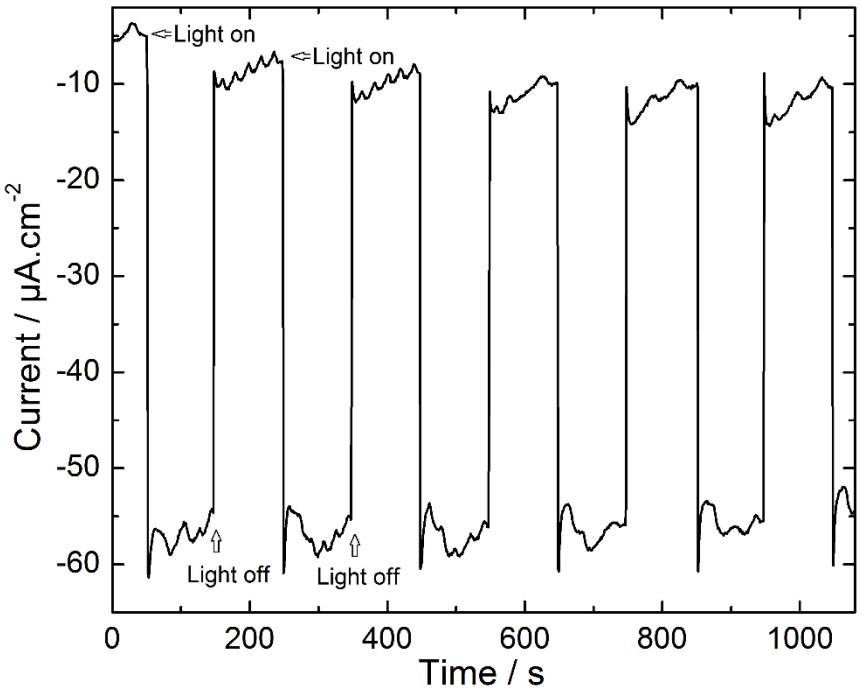

Figure 2.14. Chronoamperometric measurements with Sb_2Se_3/FTO electrode at OCP using chopping 1 sun simulated illumination.

The LSV curves obtained with the Sb_2Se_3/FTO electrode is displayed in Figure 2.15. The enhancement in the cathodic current density was observed for the electrode over the entire potential range tested. With the Sb_2Se_3/FTO electrode, in dark the current density changed from -7.2 $\mu A.cm^{-2}$ at 0 V to -231.9 $\mu A.cm^{-2}$ at 0.6 V while with the same Sb_2Se_3/FTO electrode under simulated solar light the current density changed from -35.8 $\mu A.cm^{-2}$ at 0 V to -894.46 $\mu A.cm^{-2}$ at 0.6 V.

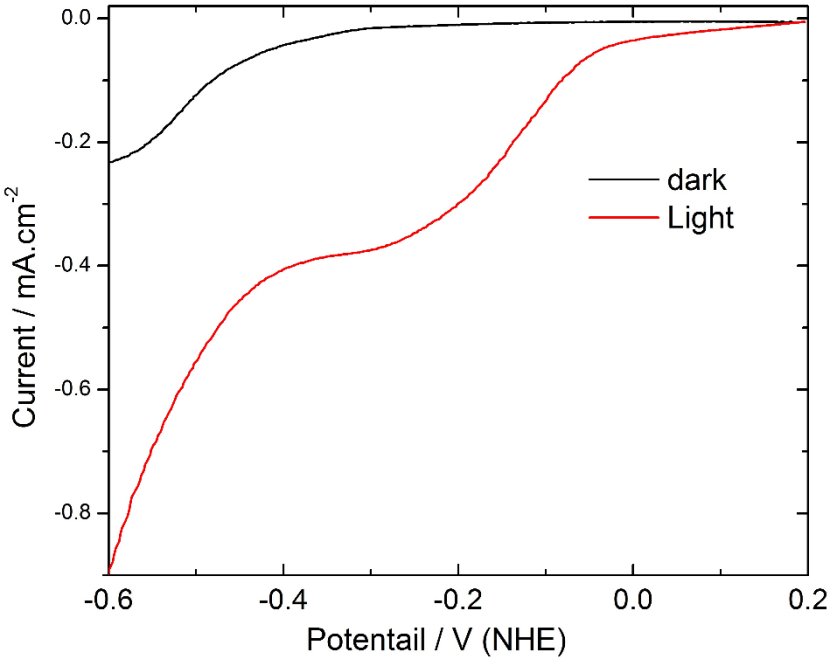

Figure 2.15. LSV curves (vs. SHE) with Sb_2Se_3/FTO electrode in dark and under continuous 1 sun simulated illumination.

The stability of the Sb_2Se_3/FTO photocathode was also assessed under dark and sunlight illumination as displayed in Figure 2.16. The electrodes showed very stable response over 600 s of testing time. The dark current was very stable while a noisy photocurrent was observed due to H_2 evolution and accumulation of H_2 bubbles at surface of the electrode.[44] A small decrease in photocurrent response was observed over time, which could be recovered once solution was stirred to remove H_2 bubbles from the electrode surface. Thus, the Sb_2Se_3/FTO photocathode acted as efficient water reduction catalyst in neutral sodium sulfate solution and could be a promising candidate for cathodic water splitting applications.

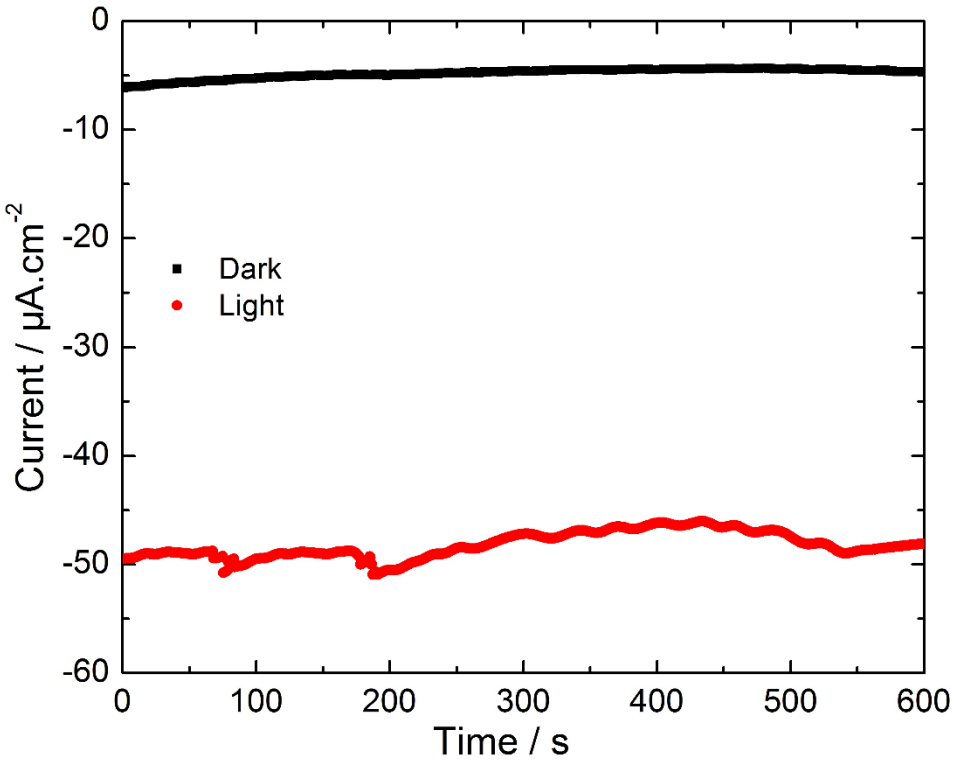

Figure 2.16. Chronoamperometric stability measurements with Sb_2Se_3/FTO electrode at OCP in dark and under continuous 1 sun simulated illumination.

2.5. Conclusions

A facile one-pot synthesis of crystalline and stable antimony selenobenzoate complex at room temperature was reported in this study. The complex was suitable to be used as cost effective precursor for the preparation of Sb_2Se_3 nanorods and thin films by AACVD. The nanorods in OLA were synthesized well below the decomposition temperature of the complex as determined by TGA, suggesting that OLA is not only a capping agent but also catalyzes the decomposition of the precursors. However, in order to obtain nanorods with better crystallinity, a reaction temperature of 200 °C was used for the synthesis of nanorods. For Sb_2Se_3 thin films, deposition temperature was found to have significant effect on the shape and preferred orientation of the particles, whereas a successive decrease in selenium was observed in thin films with increase in temperature. Hence, it is concluded that the alignment of the crystallites and stoichiometry in deposited thin films can be manipulated by

judicious control on deposition temperature. Sb_2Se_3 nanorods showed significant photo-electrochemical catalytic properties for water splitting indicating the high potential of the material as a cheap source for the production of hydrogen from water. The synthetic route can be used for facile preparation of other metal seleno-benzoate complexes for metal selenide nanoparticles and thin films.

2.6. References

1. N. J. Jeon, J. H. Noh, Y. C. Kim, W. S. Yang, S. Ryu and S. I. Seok, *Nature Materials*, 2014, **13**, 897-903.
2. S. Chen, A. Walsh, X. G. Gong and S. H. Wei, *Advanced Materials*, 2013, **25**, 1522-1539.
3. D. A. R. Barkhouse, O. Gunawan, T. Gokmen, T. K. Todorov and D. B. Mitzi, *Progress in Photovoltaics: Research and Applications*, 2012, **20**, 6-11.
4. D. Arivuoli, F. Gnanam and P. Ramasamy, *Journal of Materials Science Letters*, 1988, **7**, 711-713.
5. B. Chen, C. Uher, L. Iordanidis and M. G. Kanatzidis, *Chemistry of Materials*, 1997, **9**, 1655-1658.
6. R. Suarez, P. Nair and P. V. Kamat, *Langmuir*, 1998, **14**, 3236-3241.
7. M. R. Filip, C. E. Patrick and F. Giustino, *Physical Review B*, 2013, **87**, 205125.
8. C. E. Patrick and F. Giustino, *Advanced Functional Materials*, 2011, **21**, 4663-4667.
9. Y. Zhou, L. Wang, S. Chen, S. Qin, X. Liu, J. Chen, D.-J. Xue, M. Luo, Y. Cao and Y. Cheng, *Nature Photonics*, 2015, **9**, 409-415.
10. B. Sankapal and C. Lokhande, *Solar Energy Materials and Solar Cells*, 2001, **69**, 43-52.
11. I. Gonzalez-Valls and M. Lira-Cantu, *Energy & Environmental Science*, 2010, **3**, 789-795.
12. X. Pu, J. Liu, J. Liang, Y. Xia, W. Feng, Y. Wang and X. Yu, *RSC Advances*, 2014, **4**, 23149-23154.
13. F. Xu and L. Sun, *Energy & Environmental Science*, 2011, **4**, 818-841.
14. M. Que, W. Guo, X. Zhang, X. Li, Q. Hua, L. Dong and C. Pan, *Journal of Materials Chemistry A*, 2014, **2**, 13661-13666.
15. J. Pérez-Juste, I. Pastoriza-Santos, L. M. Liz-Marzán and P. Mulvaney, *Coordination Chemistry Reviews*, 2005, **249**, 1870-1901.
16. B. D. Busbee, S. O. Obare and C. J. Murphy, *Advanced Materials*, 2003, **15**, 414-416.
17. K. Caswell, C. M. Bender and C. J. Murphy, *Nano Letters*, 2003, **3**, 667-669.

18. S. E. Hunyadi and C. J. Murphy, *Journal of Materials Chemistry*, 2006, **16**, 3929-3935.
19. J. Hu, T. W. Odom and C. M. Lieber, *Accounts of Chemical Research*, 1999, **32**, 435-445.
20. C. Tan and H. Zhang, *Chemical Society Reviews*, 2015, **44**, 2713-2731.
21. M. Pumera, Z. Sofer and A. Ambrosi, *Journal of Materials Chemistry A*, 2014, **2**, 8981-8987.
22. P. Sajanlal and T. Pradeep, *Journal of Chemical Sciences*, 2008, **120**, 79-85.
23. X. Sun, S. Dong and E. Wang, *Langmuir*, 2005, **21**, 4710-4712.
24. Y.-F. Lin, H.-W. Chang, S.-Y. Lu and C. Liu, *The Journal of Physical Chemistry C*, 2007, **111**, 18538-18544.
25. H.-W. Chang, B. Sarkar and C. Liu, *Crystal Growth and Design*, 2007, **7**, 2691-2695.
26. R. K. Sharma, G. Kedarnath, V. K. Jain, A. Wadawale, M. Nalliath, C. Pillai and B. Vishwanadh, *Dalton Transactions*, 2010, **39**, 8779-8787.
27. C. Q. Nguyen, A. Adeogun, M. Afzaal, M. A. Malik and P. O'Brien, *Chemical Communications*, 2006, 2182-2184.
28. S. L. Benjamin, C. de Groot, A. L. Hector, R. Huang, E. Koukharenko, W. Levason and G. Reid, *Journal of Materials Chemistry C*, 2015, **3**, 423-430.
29. N. Maiti, S. H. Im, Y. H. Lee, C.-H. Kim and S. I. Seok, *CrystEngComm*, 2011, **13**, 3767-3772.
30. J. Azevedo, S. D. Tilley, M. Schreier, M. Stefik, C. Sousa, J. P. Araújo, A. Mendes, M. Grätzel and M. T. Mayer, *Nano Energy*, 2016, **24**, 10-16.
31. M. G. Walter, E. L. Warren, J. R. McKone, S. W. Boettcher, Q. Mi, E. A. Santori and N. S. Lewis, *Chemical Reviews*, 2010, **110**, 6446-6473.
32. K. Zeng, D.-J. Xue and J. Tang, *Semiconductor Science and Technology*, 2016, **31**, 063001.
33. R. J. Mehta, C. Karthik, W. Jiang, B. Singh, Y. Shi, R. W. Siegel, T. Borca-Tasciuc and G. Ramanath, *Nano Letters*, 2010, **10**, 4417-4422.
34. A. J. Bard, L. R. Faulkner, J. Leddy and C. G. Zoski, *Electrochemical Methods: Fundamentals and Applications*, Wiley New York, 1980.

35. S. Kato, H. Kageyama, K. Takagi, K. Mizoguchi and T. Murai, *Journal für Praktische Chemie*, 1990, **332**, 898-910.
36. R. Mattes and D. Rühl, *Inorganica Chimica Acta*, 1984, **84**, 125-127.
37. W. P. Lim, C. T. Wong, S. L. Ang, H. Y. Low and W. S. Chin, *Chemistry of Materials*, 2006, **18**, 6170-6177.
38. W. P. Lim, Z. Zhang, H. Y. Low and W. S. Chin, *Angewandte Chemie International Edition*, 2004, **43**, 5685-5689.
39. M. T. Ng, C. Boothroyd and J. J. Vittal, *Chemical Communications*, 2005, 3820-3822.
40. Y. C. Cao and J. Wang, *Journal of the American Chemical Society*, 2004, **126**, 14336-14337.
41. W. Farfán, E. Mosquera and C. Marín, *Advanced Science Letters*, 2011, **4**, 85-88.
42. J. Álvarez-García, J. Marcos-Ruzafa, A. Pérez-Rodríguez, A. Romano-Rodríguez, J. Morante and R. Scheer, *Thin Solid Films*, 2000, **361**, 208-212.
43. W. Smith, H. Fakhouri, J. Pulpytel, S. Mori, R. Grilli, M. A. Baker and F. Arefi-Khonsari, *The Journal of Physical Chemistry C*, 2012, **116**, 15855-15866.
44. K. Zeng and D. Zhang, *Progress in Energy and Combustion Science*, 2010, **36**, 307-326.

Chapter # 3

Facile Synthesis of Bi_2Se_3 Nanosheets and Thin Films by AACVD: Potential Catalyst for Water Reduction

3.1. Introduction

Layered materials when thinned down to their atomic limits, are referred to as 2-dimensional (2D) materials which exhibit unique properties as compared to their bulk counterparts. Bulk layered 3D crystals are composed of stacked layers which have Van der Waals interactions between the adjacent layers and strong covalent bonding within the layers. The weak Van der Waals forces between the layers allow easy cleavage. Such materials encompass a wide range of electronic structures, from metals to insulators. The thinning of the bulk layered material may result in enhanced mechanical,[1] conductive[2] and optoelectronic properties[3] which differ from the parent material.

Graphene is the most extensively studied layered material showing extraordinarily improved mechanical properties,[1] carrier transport[4] and electronic properties.[5, 6] However the drawback of graphene is the lack of a bandgap which limits its use in electronic devices. This has encouraged researchers to explore other 2D materials which also show interesting and exceptional properties.[7] Further research on 2D semiconducting layered materials led to an interesting finding that the band gap of layered semiconductors can be changed drastically, when their thickness is reduced to the monolayer level.[3] Thus, 2D semiconducting materials with atomically thin dimensions, emerged as a new interesting class of materials having tunable electronic structures.

V_2VI_3 binary metal chalcogenide materials (V = Sb, Bi or As; VI = S, Se or Te) are an important class of semiconducting materials with anisotropic structures. Bi_2Se_3 has a layered structure that exists in the rhombohedral crystal structure and has a direct band gap of ≈ 0.35 eV.[8, 9] Although Bi_2Se_3 is the most dominant and stable phase, the Bi/Se ratio may exhibit a range of compositions.[10, 11] The narrow energy gap and layered structure makes it a suitable candidate for applications such as IR spectroscopy, optoelectronics, electrochemical hydrogen storage, photo electrochemical cells and thermoelectric materials.[12-16]

Although single source precursors provide better control over size and morphology, still there are only few reports on use of single source precursors for the synthesis of bismuth selenide nanoparticles and/or deposition of thin films. Some of the common selenium based complexes used for the deposition of metal selenide nanoparticles or thin films are dialkyldiseleno phosphates,[17, 18] 2-pyridyl selenolates,[19] and selenophosphinate complexes.[20] A dialkyldiselenocarbamate metal complex has also been reported as an effective precursor for the deposition of Bi_2Se_3 semiconducting thin films by the chemical vapour deposition (CVD) technique.[21] However, phosphorus based complexes may lead either to phosphorus contamination or formation of an entirely different phosphate product. Similarly, the synthesis of diselenocarbamate precursors requires the use of highly toxic carbon diselenide (CSe_2), which is commercially unavailable and very difficult to synthesize. Mono-chalcogeno carboxylate complexes are suitable starting materials for various metal chalcogenide nanomaterials.[22-26] However, most of the work focused on the use of thio-carboxylate complexes, with little interest in the seleno or telluro analogues.

Recently, the need for developing efficient and reliable strategies for artificial photosynthesis has attracted immense attention. The use of cost effective nanomaterials for water splitting by avoiding precious metals *i.e.* gold, platinum and ruthenium, is highly desirable for industrial applications. The tuning of surface chemistry of materials to provide better charge carrier life time and electrical capabilities is very significant for H_2 production from water.[27, 28]

The seleno-carboxylate complexes of group-V have not been reported. In this chapter, the efficient synthesis of a new seleno-benzoate complex of bismuth, *i.e. tris*(selenobenzoato)antimony(III) and its use as single source precursor for the synthesis of bismuth selenide nanosheets by the hot injection method and the deposition of thin films by AACVD. Bi_2Se_3 nanosheets were also used as low cost nanomaterials for the photoelectrochemical (PEC) production of H_2 from water under sunlight illumination.

3.2. Experimental

3.2.1. Materials

The reagents and solvents *i.e.* $BiCl_3$, $NaBH_4$, benzoyl chloride, elemental selenium, ethanol, THF, I-octadecene and oleylamine were purchased from Sigma Aldrich and used as such.

3.2.2. Synthesis of *tris*(selenobenzoato)bismuth(III) complex

NaHSe was prepared by adding ethanolic solution of $NaBH_4$ (0.5 g, 12.0 mmol in 15.0 mL ethanol) into ethanolic solution of metallic Se powder (0.5 g, 6.0 mmol, in 15.0 mL) under inert conditions using a Schlenk line at room temperature. The reddish solution becomes colourless within 5 min. of stirring indicating the formation of NaHSe. Benzoyl chloride (0.89 g, 6.0 mmol) was then added dropwise into the freshly prepared NaHSe solution. The colour of the solution changed from colourless to yellow, indicating the formation of the seleno benzoate ligand. The stirring was continued for a further 15 min, after which $BiCl_3$ (0.48 g, 2.0 mmol of in 15.0 mL ethanol) was added dropwise while stirring. A dark yellow precipitate was formed which was filtered. The dried complex was then recrystallized from the THF solution to give yellowish powder. Elemental analysis Calc: (%) for Elemental analysis Calc: (%) for $C_{21}H_{15}O_3BiSe_3$: C 33.17, H 1.99, Bi 27.45; Found: C 33.39, H 1.97, Bi 27.18.

3.2.3. Synthesis of Bi_2Se_3 nanosheets

The synthesis of Bi_2Se_3 nanosheets was carried out by injecting a dispersion of *tris*(selenobenzoato)bismuth(III) complex in 1-octadecene (ODE) (0.25 g, 0.37 mmol, 3.0 mL) into 10.0 mL of preheated oleylamine (OLA) at 200 °C under vigorous stirring. The colour of the solution changed instantly from light yellow to brownish black, and a temperature drop of ≈ 15 °C was observed. The temperature was quickly readjusted to 200 °C and maintained there for one hour, after which the heating source was removed and the reaction mixture was allowed to cool to around 60 °C. The nanoparticles were precipitated by adding

30.0 mL (1:1) mixture of methanol and acetone. The product was obtained as a black precipitate which was separated by centrifugation and washed three times with acetone.

3.2.4. Deposition of Bi_2Se_3 Thin films by AACVD

Borosilicate glass slides (approx. 1 x 3 cm) were used as substrates for the deposition of bismuth selenide thin films. The surface of glass substrates was cleaned by sonicating in nitric acid, washed with distilled water and finally with acetone. The AACVD setup consist of a carbolite tube furnace and a humidifier (deurer living LB44), equipped with ultrasonic system for generation of aerosol. For deposition of thin films, freshly prepared solution of *tris*(selenobenzoato)bismuth(III) (0.3 mmol) in chloroform (20.0 mL) was prepared in two necked round bottom flask placed in water bath above the piezoelectric modulator of an ultrasonic humidifier. Six substrates were placed inside the reactor tube which was inserted into the tube furnace. One neck of the flask was attached to the gas inlet for flow of carrier gas and the other neck is attached to reactor tube by reinforce tubing. The ultrasonic humidifier generated the aerosol which was transferred to heating zone of the furnace by carrier gas (argon) at a flow rate of 200 sccm. Thermally induced reactions took place inside the heating chamber and on heated substrates which resulted in deposition of Bi_2Se_3 thin films.

3.3. Characterization

3.3.1. Elemental and Thermogravimetric analysis

Microanalysis was performed using a Thermo Scientific Flash 2000 Organic Elemental Analyzer. Thermogravimetric analyses were performed using a Mettler-Toledo TGA/DSC under nitrogen gas flow rate of 10 mL/min.

3.3.2. Powder X-ray diffraction analysis

The X-ray diffraction was performed using a Bruker D8 Discover Diffractometer using CuKα radiation (λ = 1.54178 Á), in a 2Θ range from 10^o to 70^o. The data collected was used to determine the lattice parameters and crystal phase.

3.3.3. Transmission electron microscopy (TEM) and High Resolution TEM (HRTEM) analysis

TEM and HRTEM images were collected on a Talos F200X at 200 kV using a FEI ceta camera. The samples were prepared by drop casting few drops from dilute solution of Bi_2Se_3 nanosheets and evaporating on Formvar-coated Cu grids (150 mesh) for TEM and holey carbon grids for HRTEM analyses.

3.3.4. Scanning electron microscopy (SEM) and Energy Dispersive Xray (EDX) analysis

Scanning electron microscopy (SEM) was carried out using a Philips XL30 FEG SEM. Energy-dispersive X-ray (EDX) spectroscopy was performed using a DX4 detector. All samples were carbon coated using an Edwards coating system E306A prior to SEM analysis.

3.3.5. Raman Spectroscopy

Raman spectra were measured using a Renishaw 1000 Micro-Raman System equipped with a 514 nm laser operating at 1 mW.

3.3.6. Uv-Vis-NIR Spectroscopy

UV−Vis-NIR spectrum was recorded using a PerkinElmer Lambda 1050 instrument, using quartz cuvettes with a path length of 1 cm.

3.3.7. Electrode preparation

PEC studies were carried out using fluorine doped tin oxide (FTO) conducting glass substrates. FTO substrates were ultra- sonicated, first in acetone and then in deionized water for 10 minutes each. A slurry of Bi_2Se_3 nanosheets was prepared by dispersing the nanosheets in *iso*-propanol and sonicated for 10 minutes. Bi_2Se_3/FTO electrode was prepared by drop casting 50 µL of the Bi_2Se_3 slurry over 1 cm^2 of the FTO glass substrate, which was then annealed at 80 °C for two hours to harden the substrate layer. An increment of 10

μL of 1% nafion solution was then drop casted over the Bi_2Se_3 layer to make it withstand during the PEC measurements. Once dried Bi_2Se_3/FTO electrode was used for all subsequent PEC studies.

3.3.8. Experimental setup

A conventional three electrode cell was used for PEC studies with Bi_2Se_3/FTO electrode as the working electrode, Ag/AgCl chloride (Saturated KCl) as reference electrode and platinum wire as an auxiliary electrode. The linear scan voltammetry (LSV) results are reported against the standard hydrogen electrode (SHE) by adding 0.197 V in all the measured results.[29] All three electrodes were placed in a 5.0 mL quartz cell containing 0.5 M sodium sulfate solution (pH 6.8) as an electrolyte. To remove any dissolved oxygen the cell solution was purged with nitrogen gas for 10 minutes prior to the PEC measurements.

A solar simulator equipped with a 150 W Xenon arc lamp (Model 16S-150, Solar Light Company Inc., Glenside PA 19038, USA) was used with a 1 sun light intensity. A mini μ-Autolab potentiostat, PGSTAT101 (MetrohAutolab.B.V. Kanaalweg, 29-G, Utrecht, The Netherlands) with NOVA 2.1 software was employed in all electrochemical experiments.

3.4. Results and discussion

Amongst the monochalcogeno-carboxylic acids, various compounds of thiocarboxylic acid have been reported but only a few reports of the congeners containing heavier chalcogen atoms (*i.e.* Se or Te), probably due to their instability and the handling difficulties associated with them. Selenobenzoic acid is highly sensitive and cannot be isolated, as it is easily oxidized to its dimer *i.e*. dibenzoyl diselenide. However, it can be stabilized by the formation of salt or in solution, under inert conditions. In the present study the synthesis of the bismuth-selenobenzoate complex was carried out by modifying a method reported previously.[30] In our method, the use of a sodium metal (highly pyrophoric) is avoided, instead $NaBH_4$ was used via a modified route. The $NaBH_4$ was treated with elemental selenium to form NaHSe in the first step

of the reaction. The second step involved the reaction of NaHSe with benzoyl chloride to form the selenobenzoate. The reaction of selenobenzoate with the $BiCl_3$ in ethanol gave the *tris*(selenobenzoato)bismuth(III) complex. Elemental and thermogravimetric analysis (TGA) were used to characterise the product. Repeated attempts to recrystallize this product to determine the X-ray crystal structure were unsuccessful as the product starts to decompose.

3.4.1. Thermogravimetric analysis

The thermal behaviour of the complex was analysed by TGA (Figure 3.1). The decomposition of the complex occurs in three steps. A major mass loss of ~37 % was observed between the temperature range of 160 to 240 °C, which is probably due to the loss of phenyl groups. The second step shows a 12% weight loss which may be attributed to the loss of carbonyl groups, leaving behind the $BiSe_3$ unit. In the third step, two such fragments undergo conversion from $BiSe_3$ to Bi_2Se_3 via loss of some Se atoms (9 % weight loss).[18] The complete decomposition of the complex occurred at 390 °C giving the final residue of ~ 42 % which corresponds to the formation of Bi_2Se_3 respectively (theoretically ca. 43%).

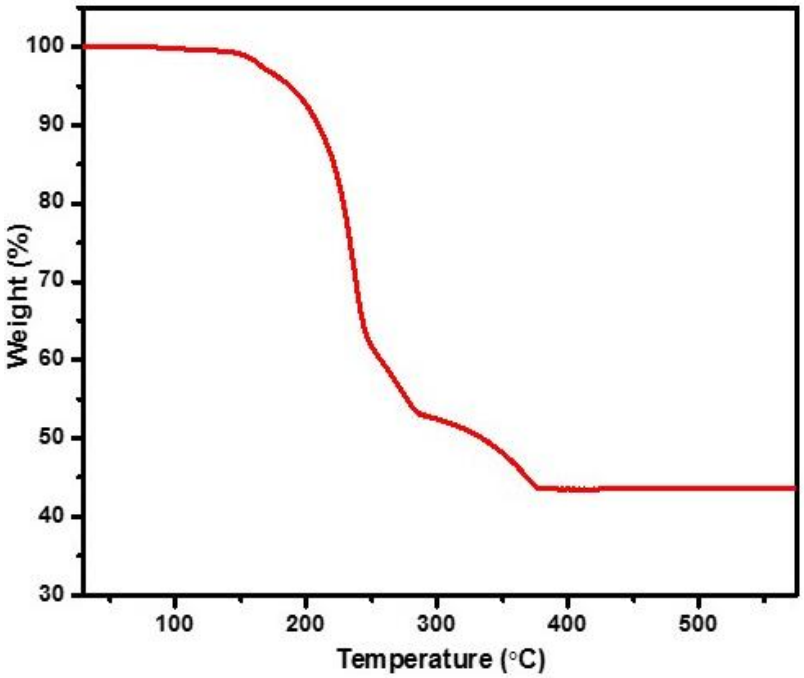

Figure 3.1. Thermogravimetric analysis of *tris*(selenobenzoato)bismuth(III) complex, showing three step decomposition.

3.4.2. Bi_2Se_3 nanosheets

The bismuth selenide nanosheets were prepared from *tris*(selenobenzoato)bismuth(III) in OLA at 200 °C by the hot injection method. The colour of the solution changed instantaneously upon injecting the complex in oleylamine, which shows that the OLA not only acts as capping agent and solvent but also initiates the decomposition of the precursors. The decomposition of the selenobenzoate complex may follow a similar mechanism as suggested by Chin *et al*. for the decomposition of thiocarboxylate complexes in primary amines.[31, 32] Vittal *et al*. also reported the synthesis of silver selenide nanoparticles and observed that the precursor decomposes easily at room temperature in the presence of a primary alkyl amine.[22] The primary amine behaves as a nucleation initiator and accelerates the decomposition of precursor. It separates the nucleation and growth steps, which is desirable for obtaining monodispersed nanomaterials.[33]

3.4.3. Structural characterization of Bi_2Se_3 nanosheets

The p-XRD pattern of bismuth selenide nanosheets is shown in Figure 3.2. The pattern observed in the p-XRD pattern of the nanosheets, shows good resemblance with the intensity profile of the standard pattern, with the highest intensity peak along the (015) plane. The intense and slightly broad peaks indicate that the synthesized nanosheets are comprised of thin crystallites. The peaks match perfectly with the rhombohedral phase (syn-paraguanajuatite, ICDD # 01-089-2008) of Bi_2Se_3. Peaks belonging to impurities such as elemental bismuth or selenium were absent.

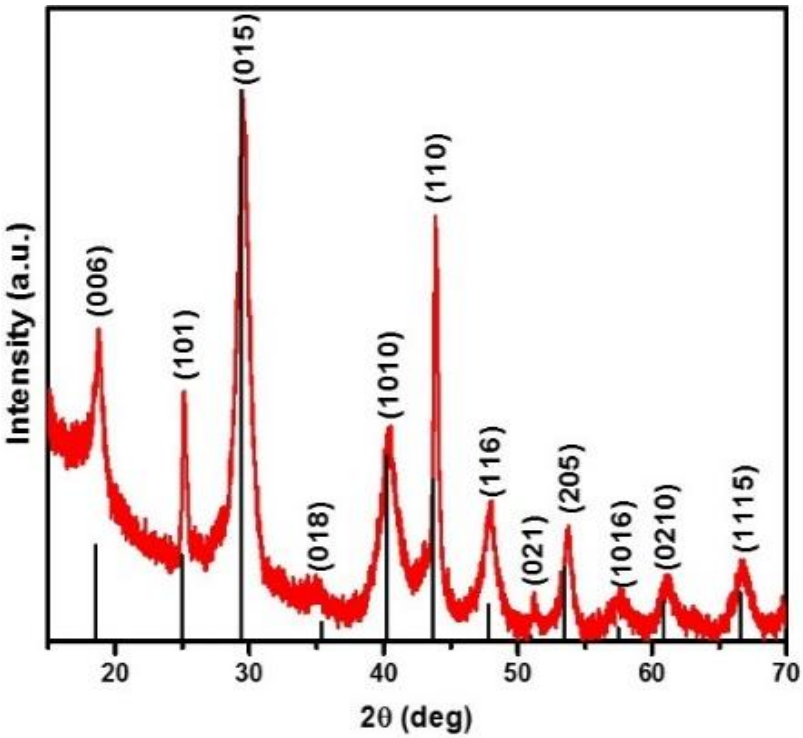

Figure 3.2. p-XRD pattern of Bi_2Se_3 nanosheets (ICDD # 01-089-2008) synthesized in OLA at 200 °C.

The thin nature of the nanosheets was further confirmed by the TEM analysis (Figure 3.3) which clearly show the overlapping thin sheets of Bi_2Se_3. The crystalline nature of these sheets can be observed by clear lattice fringes in the TEM images. These layers can be observed easily at the edges of the nanosheets (indicated by arrows in Figure 3.3(b)), and can be differentiated on the basis of the change in

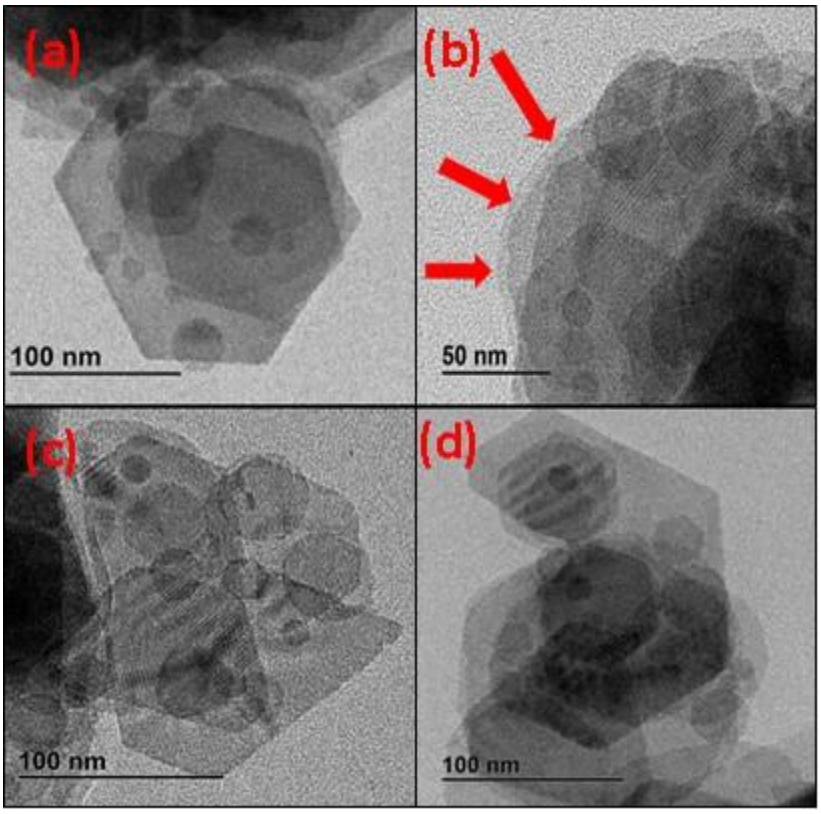

Figure 3.3. TEM images showing hexagonal shaped nanosheets, lattice fringes and stacked layers of Bi_2Se_3 nanosheets.

complexion of the layers as some of them appear quite transparent to the electron beam. The preferential growth into nanosheets is largely determined by the anisotropic nature of the building blocks. The basic unit cell of layered Bi_2Se_3 is composed of five atomic layers which are arranged in the order of $Se^{(I)}$–Bi–$Se^{(II)}$–Bi–$Se^{(I)}$ sheets.[34] The superscripts (I) and (II) are used to differentiate between the two Se atoms which are arranged in a different surrounding (Figure 3.4). The unit cell is described as quintuple layer (QL) and covalent character predominates within the QL, whereas two adjacent QLs are linked to each other with weak Van der Waals forces, giving rise to a highly anisotropic structure. The fragile interactions between the layers allow generation of mono to few QLs under judicious reaction conditions. TEM images also show the

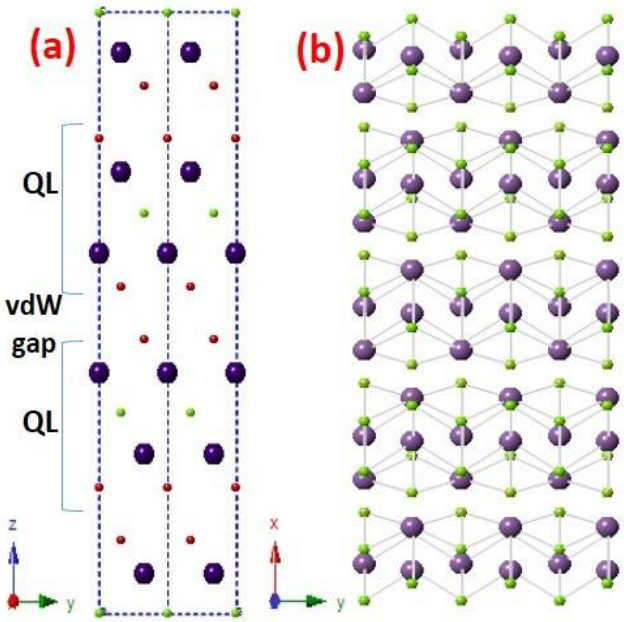

Figure 3.4. (a) Bi_2Se_3 crystal structure showing quintuple layer (QL) with Se1-Bi-Se2-Bi-Se1 arrangement and (b) layered structure of Bi_2Se_3.

stacking of thin hexagonal nanosheets and due to extremely decreased thickness, the sheets have the tendency to buckle and fold to acquire different type of shapes and sizes. The broad peaks in the p-XRD pattern also indicate the presence of very thin nanosheets of Bi_2Se_3.

3.4.4. Optical characterization of Bi_2Se_3 nanosheets

The optical properties of the Bi_2Se_3 nanosheets were determined by UV-Vis-NIR spectroscopy. The absorption spectrum of well dispersed Bi_2Se_3 nanosheets (Figure 3.5(a)) in acetone resulted in a continuous broad band with λ_{max} at 660 nm. The band gap of the Bi_2Se_3 nanosheets as determined by the Tauc plot is estimated to be 1.1 eV (Figure 3.5(b)). A blue shift in the band gap is in accordance with the reduced thickness of the sheets as compared to the parent bulk counterpart.

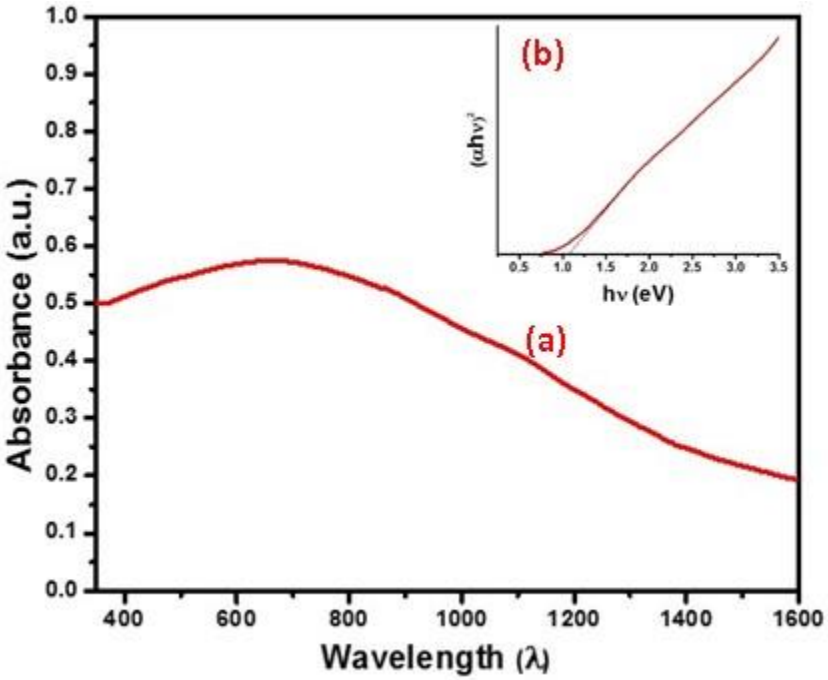

Figure 3.5. (a) Uv-Vis-NIR spectrum of Bi_2Se_3 nanosheets dispersed in acetone and (b) estimated band gap of Bi_2Se_3 by Tauc plot.

The Raman analysis was performed using a 514 nm laser excitation at 25% power. The characteristic vibration modes for Bi_2Se_3 are A^1_{1g} out of plane (72 cm^{-1}), E^2_g in-plane (130 cm^{-1}) and out-of-plane A^1_{2g} (174 cm^{-1}).[35] However, due to the broadness of the peak centred at 126 cm^{-1}, and relative high intensity, the other peaks were amalgamated and only appear as one prominent peak (Figure 3.6). The shift towards lower frequency and broadness can be due to phonon softening and increase in extent of electron-phonon coupling in a thin layered structure.[36]

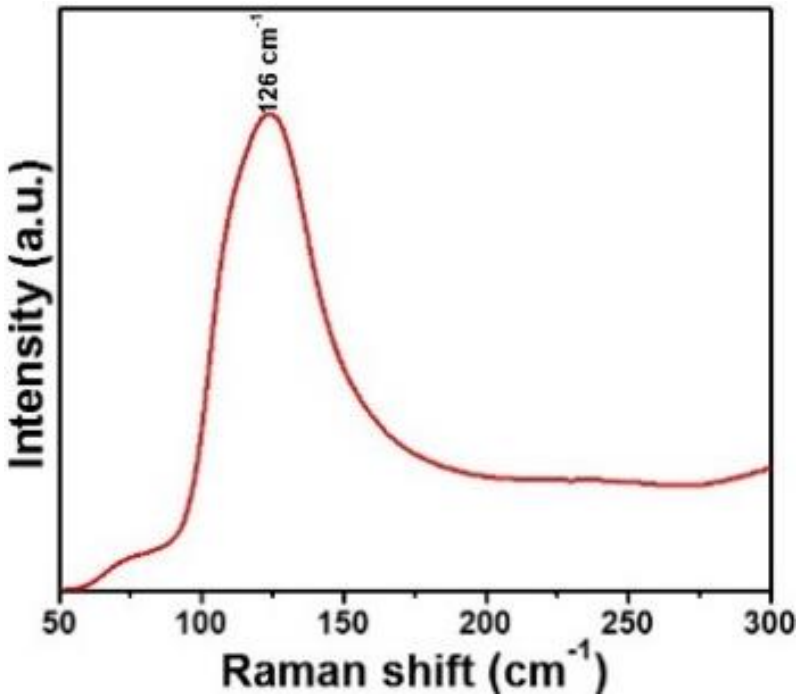

Figure 3.6. Raman spectrum of OLA capped Bi_2Se_3 nanosheets.

3.4.5. Bi_2Se_3 thin films

Thin films of Bi_2Se_3 were deposited on glass substrates from *tris*(selenobenzoato)bismuth(III) complex. The complex was soluble in solvents, commonly used for CVD, such as chloroform, THF and toluene. It was observed that the complex starts to decompose in THF after a while, during the generation of an aerosol and toluene also requires long deposition time. Therefore chloroform was chosen as a solvent for the deposition of the Bi_2Se_3 thin films. The complete decomposition of the complex was observed around 390 °C by TGA analysis, the deposition temperature was varied between 400 and 500 °C. There was only a very thin deposition on the slides placed at the start of the hot zone but thicker deposition on the slides placed at the centre to end of the glass tube. All films were black, uniform, compact and adherent. All deposition experiments were carried out until complete evaporation of the solution and took almost 30 minutes.

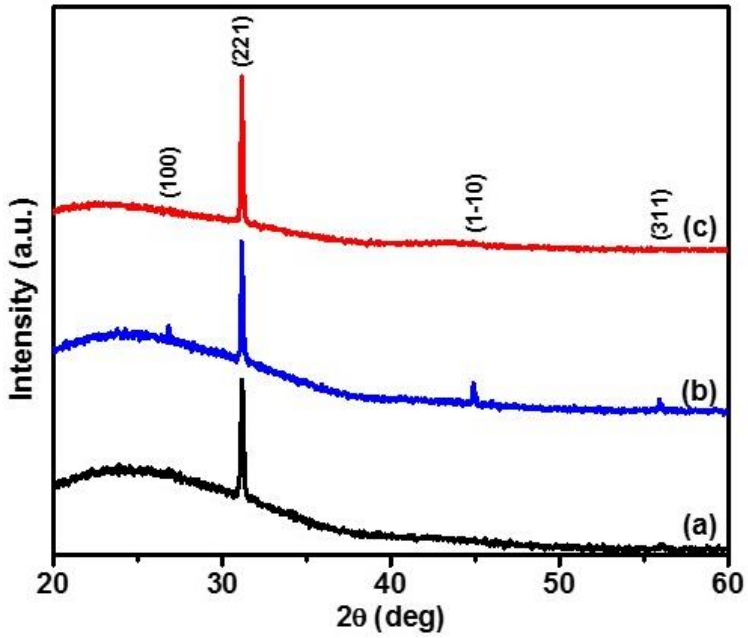

Figure 3.7. p-XRD spectra of Bi_2Se_3 thin films deposited on glass substrates at (a) 400 °C, (b) 450 °C and (c) 500 °C by AACVD.

The p-XRD pattern of the thin films deposited at 400, 450 and 500 °C, is shown in Figure 3.7. At deposition temperature of 400 °C, only an intense peak at $2\Theta \approx 31.1$ was observed, which matches with the Bi_2Se_3 phase (ICDD # 01-085-0519). The films are highly crystalline and textured along the (221) plane as indicated by the single intense peak detected in this plane. At 450 °C, other peaks were also spotted, but they appeared only as minor peaks due to their low relative intensity as compared to high intensity peak along (221) plane. At 500 °C, the intensity of this peak further increases and no other peaks were observed, probably masked by the intense peak along (221) plane. The wide hump observed in all cases is due to the amorphous glass substrate.

The observations in p-XRD patterns shows that the deposition temperature may have some effect on the growth of the crystallite size but the morphology is not affected, as preferred orientation of the crystallites in thin films deposited at different temperature remains the same. The effect of temperature on size, morphology and stoichiometry was analysed by SEM analysis. The images of thin films deposited at 400 °C are shown in Figure 3.8(a-b).

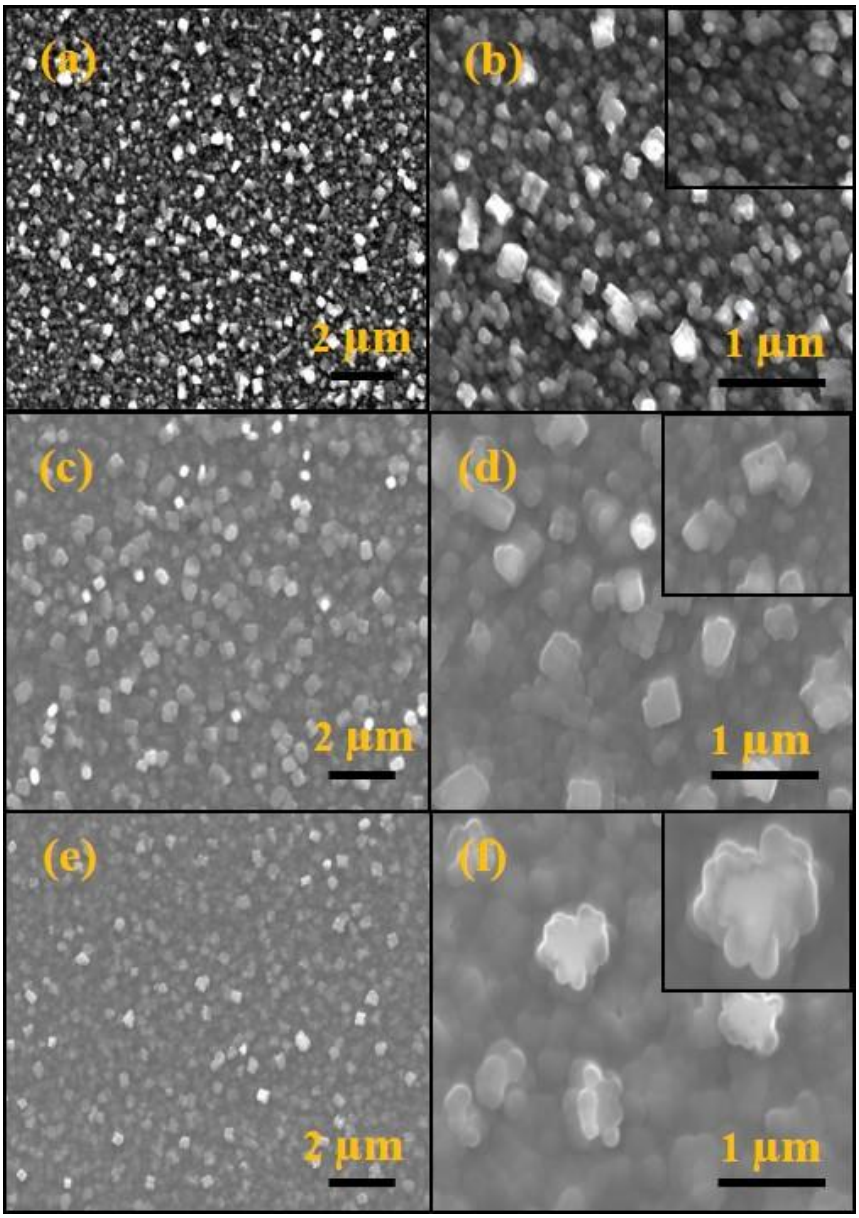

Figure 3.8. SEM images of Bi_2Se_3 thin films deposited on glass substrates at (a) 400 °C, (b) 450 °C and (c) 500 °C by AACVD.

Uniform deposition of the granular particles on the glass substrate, was shown by the SEM images, and the particles show a broad size distribution. The films were found to be selenium rich and a mean Se/Bi ratio of 1.73 was observed by EDX, which is close to the stoichiometric value of 1.50 for Bi_2Se_3 (Figure 3.9(a)).

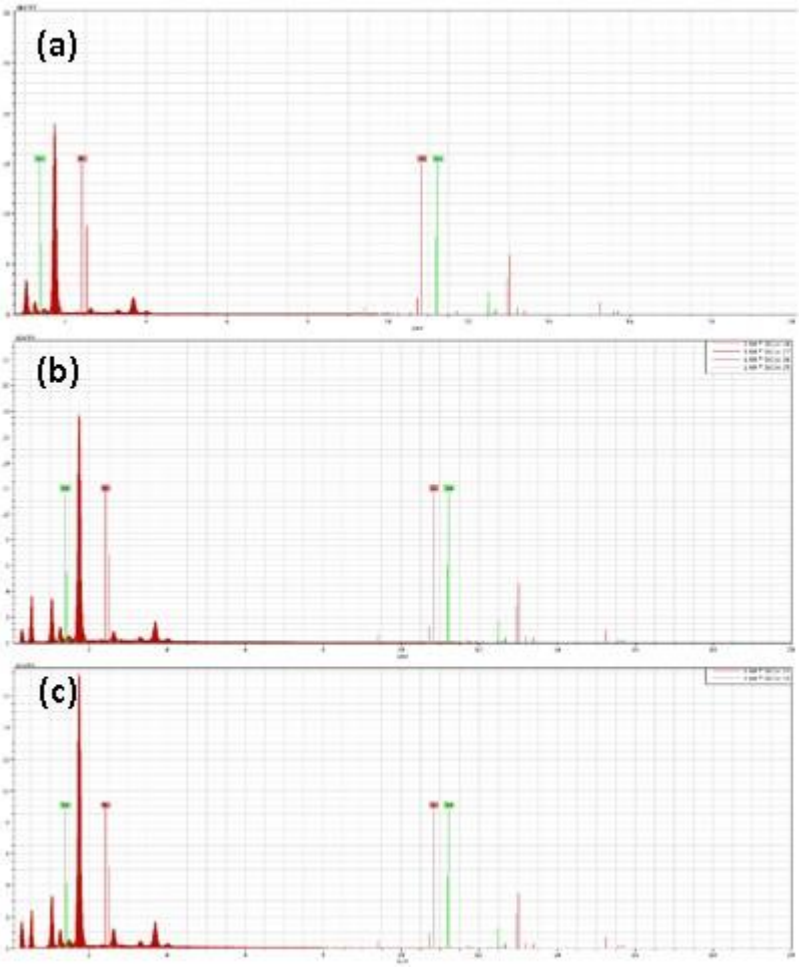

Figure 3.9. EDX analysis of Bi_2Se_3 thin films (Bi = red line and Se = green line) deposited on glass substrates at (a) 400 °C, (b) 450 °C and (c) 500 °C.

The homogeneity of the elements in the deposited films was investigated by elemental mapping, which shows uniform distribution of bismuth and selenium throughout the film (Figure 3.10(a-c)).

The growth at a higher temperature of 450 °C showed only a slight change in the size of crystallites. A small increase in the size of crystallites can be observed but generally the films showed similar morphology (Figure 3.8(c-d)). The stoichiometry of the films also changed and a mean Se/Bi ratio of 1.65 was obtained by EDX. The films are still selenium rich but to a lesser extent as compared to the films deposited at temperature of 400 °C (Figure 3.9(b)).

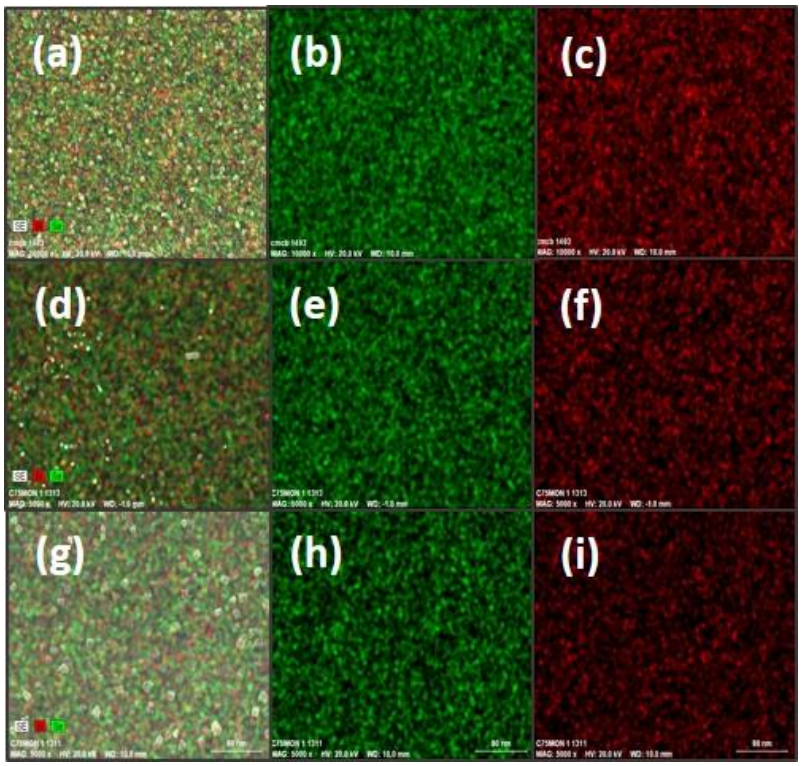

Figure 3.10. Elemental mapping of Bi_2Se_3 (Bi = red and Se = green) thin films deposited at (a-c) 400 °C, (d-f) 450 °C and (g-i) 500 °C by AACVD.

A homogenous distribution of elements in the film was shown by elemental mapping (Figure 3.10(d-f)).

Further increase in deposition temperature to 500 °C, led to the deposition of layered or sheet-like structures (Figure 3.8(e-f)) which appear to form clusters. The structure of Bi_2Se_3 consists of layers which are interconnected by weak Van der Waal's forces. The high temperature ruptures the delicate forces and results in splitting of three dimensional structure to clusters of a few layers. Under judicious reaction conditions, layers of atomic thickness can also be generated. The stoichiometry was also significantly affected, as the films deposited were deficient in selenium with a mean Se/Bi ratio of 1.37 was obtained by EDX (Figure 3.9(c)). The loss of chalcogens at higher temperature is a well-known observation, as this trend is clearly shown in the stoichiometry of all deposited films deposited at different temperatures. The elemental distribution in the thin films was still uniform as shown in (Figure 3.10(g-i)).

3.4.6. Photo-electrochemical water reduction catalysis

Bi_2Se_3 nanosheets were observed to exhibit cathodic photocurrents indicating their p-type nature. The chronoamperometric performances of the Bi_2Se_3/FTO photocathodes, obtained at open circuit potential (OCP) as a function of time, under simulated sunlight illumination is shown in Figure 3.11. Once the current response was stable, the light was cut off at regular intervals. It was evident that significant cathodic current was generated for H_2 generation only when light was illuminated at the surface of the Bi_2Se_3/FTO electrode. When the light was cut off, the photocurrent density instantaneously became negligible. This inferred that, the current generated was only due to the illuminated light and not to any intrinsic properties of the Bi_2Se_3 nanostructures.[37] The photo-cathodic current generated due to H_2 evolution for Bi_2Se_3/FTO electrode was in the range of - 48.5 to - 56.3 $\mu A.cm^{-2}$.

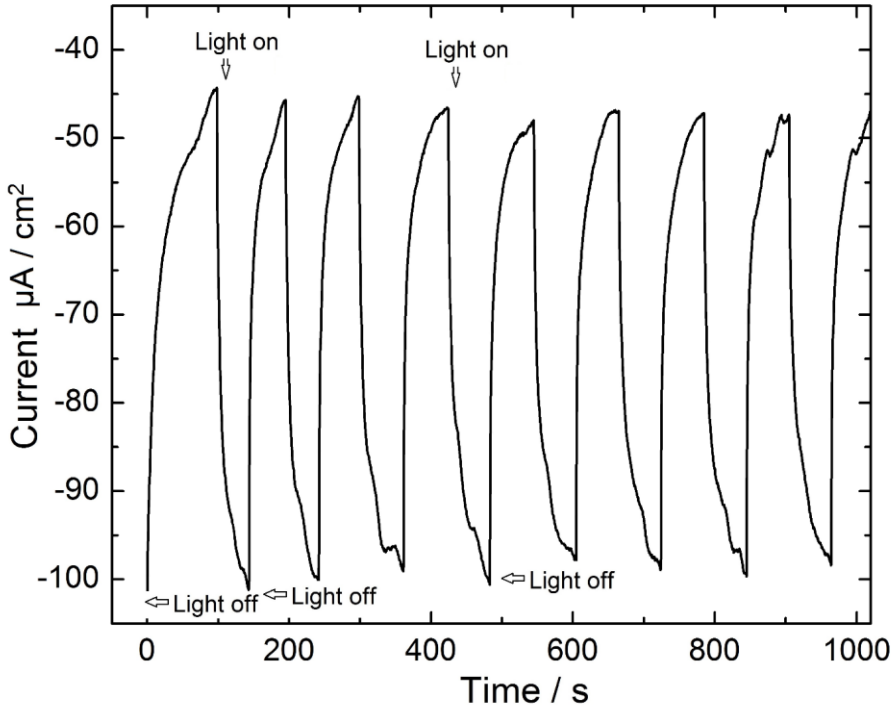

Figure 3.11. Chronoamperometric measurements with Bi_2Se_3/FTO electrode at OCP using chopping 1 sun simulated illumination.

The LSV curves obtained with the Bi_2Se_3/FTO electrode is displayed in Figure 3.12. The enhancement in the cathodic current density was observed for the Bi_2Se_3/FTO electrode over the entire potential range tested. The change in

current density in dark was, from -28.0 μA.cm^{-2} at 0V to -87.7 μA.cm^{-2} at 0.6 V while under simulated solar light the current density was -109.8 μA.cm^{-2} at 0 V, and reached to -300.5 μA.cm^{-2} at 0.6 V.

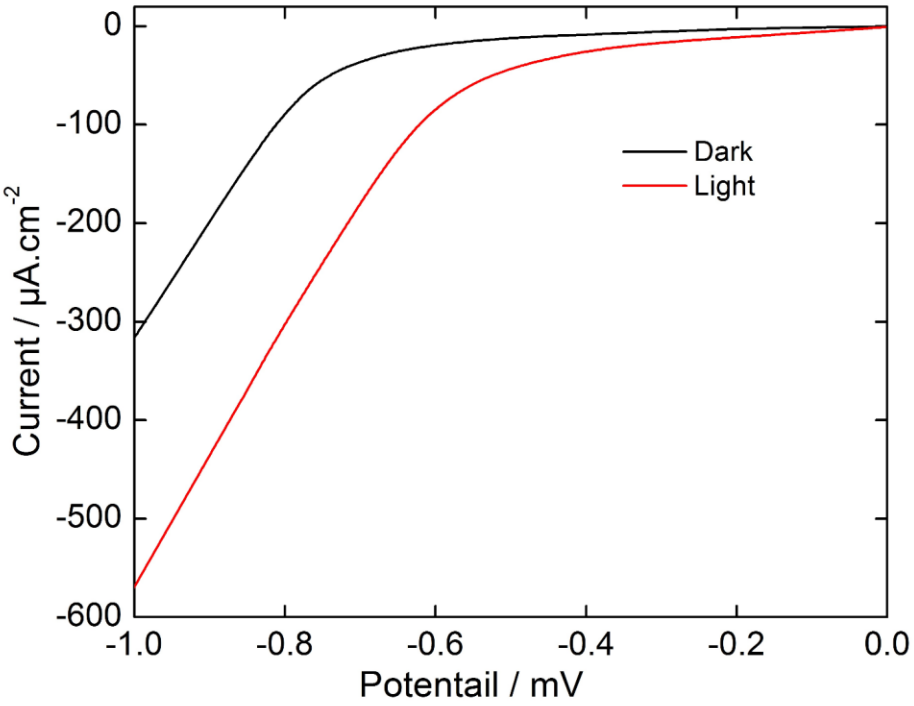

Figure 3.12. LSV curves (vs. SHE) with Bi_2Se_3/FTO electrode in dark and under continuous 1 sun simulated illumination.

The stability of Bi_2Se_3/FTO photocathode was also assessed under dark and sunlight illumination as displayed in Figure 3.13, respectively. The electrode showed very stable response over 600s of testing time. The dark current was very stable while a noisy photocurrent was observed due to H_2 evolution and accumulation of H_2 bubbles at the surfaces in the case of both the electrodes.[38] A small decrease in photocurrent response was observed over time, which could be recovered once the solution was stirred to remove the H_2 bubbles from the electrode surface. Thus the Bi_2Se_3/FTO photocathode acted as an efficient water reduction catalyst in the neutral sodium sulfate solution and could be a promising candidate for cathodic water splitting applications.

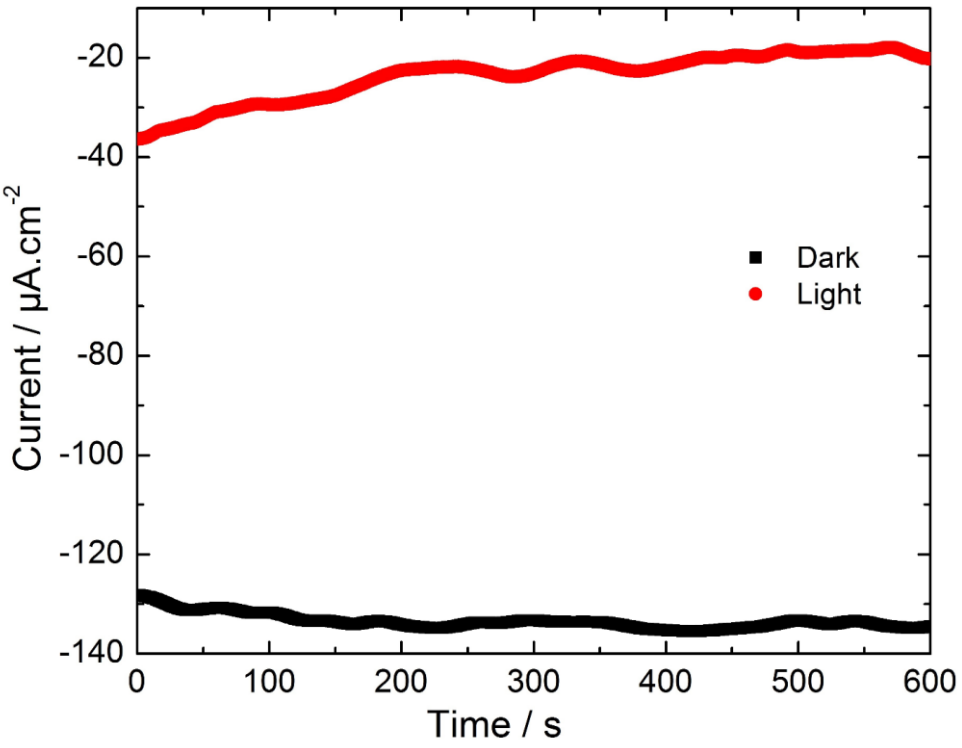

Figure 3.13. Chronoamperometric stability measurements with Bi_2Se_3/FTO at OCP in dark and under continuous 1 sun simulated illumination.

3.5. Conclusions

The facile synthesis of a mono-selenobenzoate complex, (*tris*(selenobenzoato)bismuth(III)) at ambient temperature, was reported in this study. The complex was used as a molecular precursor for the preparation of Bi_2Se_3 nanosheets and corresponding thin films. It was observed that oleylamine is not only a capping agent but also catalyzes the decomposition of the precursors well below the decomposition temperature of the complex as determined by TGA. The effect of temperature on the deposited thin films was investigated. It was observed by EDX analysis that the stoichiometry of the thin films varies significantly (from selenium rich to selenium deficient) with change in temperature. The size of the crystallites also increases with an increase in temperature however there is no significant change in morphology. Bi_2Se_3 nanosheets showed significant photo-electrochemical catalytic properties for

water splitting indicating the high potential of the material as a cheap source for the production of hydrogen from water.

3.6. References

1. C. Lee, X. Wei, J. W. Kysar and J. Hone, *Science*, 2008, **321**, 385-388.
2. K. Novoselov, A. K. Geim, S. Morozov, D. Jiang, M. Katsnelson, I. Grigorieva, S. Dubonos and A. Firsov, *Nature*, 2005, **438**, 197-200.
3. K. F. Mak, C. Lee, J. Hone, J. Shan and T. F. Heinz, *Physical Review Letters*, 2010, **105**, 136805.
4. K. I. Bolotin, K. Sikes, Z. Jiang, M. Klima, G. Fudenberg, J. Hone, P. Kim and H. Stormer, *Solid State Communications*, 2008, **146**, 351-355.
5. K. S. Novoselov, A. K. Geim, S. Morozov, D. Jiang, Y. Zhang, S. a. Dubonos, I. Grigorieva and A. Firsov, S*cience*, 2004, **306**, 666-669.
6. A. C. Neto, F. Guinea, N. Peres, K. S. Novoselov and A. K. Geim, *Reviews of Modern Physics*, 2009, **81**, 109.
7. K. Novoselov, D. Jiang, F. Schedin, T. Booth, V. Khotkevich, S. Morozov and A. Geim, *Proceedings of the National Academy of Sciences of the United States of America*, 2005, **102**, 10451-10453.
8. L. E. Bell, *Science*, 2008, **321**, 1457-1461.
9. C. Mann, D. West, I. Miotkowski, Y. P. Chen, S. Zhang and C.-K. Shih, *Nature Communications*, 2013, **4**.
10. H. Okamoto, *Journal of Phase Equilibria*, 1994, **15**, 195-201.
11. H. Lind, S. Lidin and U. Häussermann, *Physical Review B*, 2005, **72**, 184101.
12. H. Xu, G. Chen, R. Jin, D. Chen, J. Pei and Y. Wang, *CrystEngComm*, 2013, **15**, 5626-5632.
13. Z. Sun, S. Liufu, X. Chen and L. Chen, *Chemical Communications*, 2010, **46**, 3101-3103.
14. C. Yang, H. Zhao, Y. Hou and D. Ma, *Journal of the American Chemical Society*, 2012, **134**, 15814-15821.
15. B. Zhang, X. Ye, W. Hou, Y. Zhao and Y. Xie, *The Journal of Physical Chemistry B*, 2006, **110**, 8978-8985.
16. S. Mishra, S. Satpathy and O. Jepsen, *Journal of Physics: Condensed Matter*, 1997, **9**, 461.

17. Y.-F. Lin, H.-W. Chang, S.-Y. Lu and C. Liu, *The Journal of Physical Chemistry C*, 2007, **111**, 18538-18544.
18. H.-W. Chang, B. Sarkar and C. Liu, *Crystal Growth and Design*, 2007, **7**, 2691-2695.
19. R. K. Sharma, G. Kedarnath, V. K. Jain, A. Wadawale, M. Nalliath, C. Pillai and B. Vishwanadh, *Dalton Transactions*, 2010, **39**, 8779-8787.
20. C. Q. Nguyen, A. Adeogun, M. Afzaal, M. A. Malik and P. O'Brien, *Chemical Communications*, 2006, 2182-2184.
21. O. C. Monteiro, T. Trindade, F. A. A. Paz, J. Klinowski, J. Waters and P. O'Brien, *Journal of Materials Chemistry*, 2003, **13**, 3006-3010.
22. M. T. Ng, C. Boothroyd and J. J. Vittal, *Chemical Communications*, 2005, 3820-3822.
23. L. Tian, M. T. Ng, N. Venkatram, W. Ji and J. J. Vittal, *Crystal Growth & Design*, 2010, **10**, 1237-1242.
24. T. C. Deivaraj, J.-H. Park, M. Afzaal, P. O'Brien and J. J. Vittal, *Chemistry of Materials*, 2003, **15**, 2383-2391.
25. S. K. Batabyal, L. Tian, N. Venkatram, W. Ji and J. J. Vittal, *The Journal of Physical Chemistry C*, 2009, **113**, 15037-15042.
26. J. J. Vittal and M. T. Ng, *Accounts of Chemical Research*, 2006, **39**, 869-877.
27. J. Azevedo, S. D. Tilley, M. Schreier, M. Stefik, C. Sousa, J. P. Araújo, A. Mendes, M. Grätzel and M. T. Mayer, *Nano Energy*, 2016, **24**, 10-16.
28. M. G. Walter, E. L. Warren, J. R. McKone, S. W. Boettcher, Q. Mi, E. A. Santori and N. S. Lewis, *Chemical Reviews*, 2010, **110**, 6446-6473.
29. A. J. Bard, L. R. Faulkner, J. Leddy and C. G. Zoski, *Electrochemical Methods: Fundamentals and Applications*, Wiley New York, 1980.
30. S. Kato, H. Kageyama, K. Takagi, K. Mizoguchi and T. Murai, *Journal für Praktische Chemie*, 1990, **332**, 898-910.
31. W. P. Lim, C. T. Wong, S. L. Ang, H. Y. Low and W. S. Chin, *Chemistry of Materials*, 2006, **18**, 6170-6177.
32. W. P. Lim, Z. Zhang, H. Y. Low and W. S. Chin, *Angewandte Chemie International Edition*, 2004, **43**, 5685-5689.

33. Y. C. Cao and J. Wang, *Journal of the American Chemical Society*, 2004, **126**, 14336-14337.
34. J. Wiese and L. Muldawer, *Journal of Physics and Chemistry of Solids*, 1960, **15**, 13-16.
35. Y. Kim, X. Chen, Z. Wang, J. Shi, I. Miotkowski, Y. Chen, P. Sharma, A. Lima Sharma, M. Hekmaty and Z. Jiang, *Applied Physics Letters*, 2012, **100**, 071907.
36. J. Zhang, Z. Peng, A. Soni, Y. Zhao, Y. Xiong, B. Peng, J. Wang, M. S. Dresselhaus and Q. Xiong, *Nano Letters*, 2011, **11**, 2407-2414.
37. W. Smith, H. Fakhouri, J. Pulpytel, S. Mori, R. Grilli, M. A. Baker and F. Arefi-Khonsari, *The Journal of Physical Chemistry C*, 2012, **116**, 15855-15866.
38. K. Zeng and D. Zhang, *Progress in Energy and Combustion Science*, 2010, **36**, 307-326.

Chapter # 4

Synthesis of SnSe nanosheets and deposition of thin films by AACVD from organotin- selenobenzoate complex

4.1. Introduction

Layered metal chalcogenides have been extensively studied recently. Colloidal nanosheets are an important class of layered 2D materials with applications in catalysis, solar cells and batteries.[1-3] Dimension dependent studies of colloidal nanosheets can provide a new insight to unanticipated applications. Graphene is a good example of a material with 2D geometry which is responsible for diverse and unique applications.[4, 5] The discovery of the remarkable properties of graphene has encouraged researchers to explore layered 2D materials beyond graphene, with exceptional properties. An important observation is that the band gap of layered semiconductors can be drastically changed by reducing the thickness to the monolayer.[6] Hence, layered semiconductors when thinned down to the atomic level, comprised a new interesting class of materials with tunable electronic properties.

Recently, IV-VI semiconductors have attracted attention due to their interesting structure and electronic properties. In particular, SnSe is a p-type semiconductor which has both direct and indirect narrow band gap (1.30 eV direct and 0.90 eV indirect) and falls within optimum range for solar cells (*i.e.* E_g = 1.0-1.5 eV).[7-9] Furthermore it has an advantage of chemical stability, earth abundance and comparatively low toxicity. SnSe adopts a layered structure with atoms arranged in GeS-type crystal structure which favours 2D structural growth.[10] Similar to other layered semiconducting members of the group IV-VI (SnS, GeS and GeSe etc), SnSe has covalent bonding within the layers and the layers are linked to one another by weak Van der Waals forces (where the separation between adjacent layers is ≈*ca.* 1 angstrom).[11, 12] The layered structure of orthorhombic SnSe is favourable by preferred growth along the [100] direction (Figure 4.1).

Various routes have been used for the synthesis of SnSe nanoparticles and thin films. Wang *et al.* investigated effect of range of alkaline solutions on the morphology and orientation of SnSe nanocrystals using $SnCl_2$ and elemental

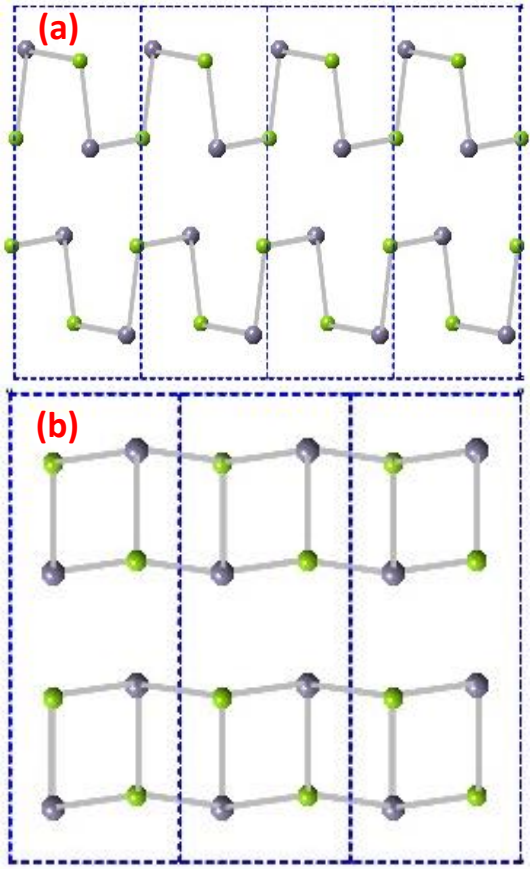

Figure 4.1.(a) Layered structure of SnSe held by weak intermolecular forces viewed along [001] and (b) [100] direction.

selenium.[13] Colloidal SnSe was formed by injecting selenourea into the solution of $Sn_6O_4(OH)_4$ in oleyl amine-oleic acid mixture at 140 °C.[14]

SnSe with tunable thickness and uniform lateral dimensions was reported by Vaughn *et al.* by reacting $SnCl_2$ with trioctylphosphine selenide (TOPSe) in oleyl amine at 240 °C.[15] Nanowires of SnSe with size larger than 10 μm and a mean diameter of 20 nm was synthesized by the reaction of $Sn[N(SiMe_3)_2]_2$ and TOPSe in oleyl amine.[16] Irregular shaped SnSe nanocrystals were prepared by Baumgardner and co-workers by the thermolysis approach using $Sn[N(SiMe_3)_2]_2$ and TOPSe as precursors in oleylamine.[9] Another solution based approach for phase controlled synthesis of SnSe and $SnSe_2$ was reported whereby di-tert-butyl diselenide was treated with $SnCl_2$ in a mixture of dodecylamine and dodecanethiol.[8]

SnSe microparticles were synthesized by Singh *et al.* by reacting elemental selenium and tin at 1150 K in an evacuated bomb.[17] Microparticles were used to deposit thin films on glass substrates by flash evaporation. Parkin and co-workers prepared SnSe and $SnSe_2$ thin films, using $SnCl_4$ and Et_2Se_2 as precursors by atmospheric pressure chemical vapor deposition at temperature range of 300 to 650 °C.[18] SnSe thin films were also deposited by the thermal evaporation method, in which SnSe nanoparticles were first synthesized and then thermally evaporated for deposition of SnSe on glass substrates at different temperatures (150-450 °C).[19]

The use of tin complexes as single source precursors (SSP) for the synthesis of SnSe in the form of nanoparticles and thin films is limited. Six membered cyclic molecular precursors with general formula $(R_2SnX)_3$ (where R = Ph, Bn and X = S, Se) were used to deposit tin chalcogenide thin films.[20, 21] A similar kind of molecular precursors in the linear form *i.e.* $(R_2Sn)_2X$ (where R = Ph, Bn and X = S, Se, Te) were also used for deposition of polycrystalline thin films.[22] 2-pyridyl selenolate complexes $[R_2Sn(2\text{-}SeC_5H_4N)_2]$ where (R = Me, Et or ^tBu) were used as SSPs however only the tert-butyl derivative was effective for the deposition of SnSe thin films.[23] O'Brien and co-workers reported a novel complex bis(diphenylphosphinediselenoato)tin(II) $[Sn(Ph_2PSe_2)_2]$ as a SSP for SnSe thin films via the aerosol assisted chemical vapour deposition (AACVD) method.[24]

In this chapter, a new phosphorus free molecular precursor *bis*(selenobenzoato)dibutyltin(IV) $[Bu_2Sn(PhCOSe)_2]$, as a suitable candidate for the synthesis of thin colloidal nanosheets and morphological controlled thin films via the AACVD method.

4.2. Experimental

4.2.1. Materials

The reagents and solvents *i.e.* Bu_2SnCl_2, $NaBH_4$, benzoyl chloride, elemental selenium, oleylamine, trioctylphosphine and ethanol were purchased from Sigma Aldrich and were used as received.

4.2.2. Synthesis of *bis*(selenobenzoato)dibutyltin(IV) complex

A solution of NaHSe was freshly prepared by adding 15.0 mL ethanolic solution of $NaBH_4$ (0.5 g, 12 mmol) into an ethanolic solution of metallic Se powder (0.5 g, 6.0 mmol) under inert conditions using schlenk line at room temperature. The solution was stirred vigorously and the reddish solution becomes colourless within 5 min, which indicates formation of NaHSe. Benzoyl chloride (0.89 g, 6.0 mmol) was then added slowly into the freshly prepared NaHSe solution and the colour of solution immediately changes from colourless to yellow, indicating the formation of the selenobenzoate ligand. The solution was stirred for 10 min, after which Bu_2SnCl_2 (0.95 g, 3 mmol) in 15.0 mL ethanol was added dropwise. After 30 min of continuous stirring, 50.0 mL distilled water was added which results in the formation of a yellowish oily product. Chloroform was used to separate the product by solvent extraction, followed by evaporation to afford the product as yellow oil. Elemental analysis cal. (%) for $C_{22}H_{28}O_2SnSe_2$: C 43.96, H 4.69, Sn 19.74; Found: C 44.22, H 4.74, Sn 19.45.

4.2.3. Synthesis of SnSe nanosheets

SnSe nanosheets were synthesized by dispersing (0.25 g, 0.42 mmol) $[Bu_2Sn(PhCOSe)_2]$ complex in 2.0 mL of trioctylphosphine (TOP) and injected into preheated oleylamine (OLA) at 200 °C under nitrogen atmosphere. A slight delay in decomposition was observed and after two minutes, the solution changes color to brownish black, which indicates the decomposition of the complex and formation of the nanosheets. The temperature dropped slightly (≈ 10 °C) upon injection, but then quickly readjusted to 200 °C. The temperature was maintained for 10 min with constant stirring, after which the reaction was quenched and nanosheets were precipitated by adding

30.0 mL (1:1) mixture of acetone and methanol. The nanoparticles were separated from solution by centrifugation and washed three times with acetone to remove excess capping agent.

4.2.4. Deposition of SnSe thin films by AACVD

Thin films of tin selenide were deposited on borosilicate glass substrates (approx. 1 x 3 cm). The substrates were cleaned ultrasonically in nitric acid, distilled water and finally in acetone. The setup for aerosol assisted chemical vapour deposition comprises of a carbolite tube furnace and ultrasonic equipped humidifier (deurer living LB44) for generation of aerosol. For deposition of thin films, 0.2 g of precursor was dissolved in 20.0 mL of THF in 100 mL two necked round bottom flask and placed in water bath above the piezoelectric modulator of an ultrasonic humidifier. Six glass substrates were loaded into the reactor tube, which was placed inside the tube furnace. A gas inlet was attached to one neck of the flask for flow of the carrier gas and other neck was attached to the reactor tube containing the substrates by reinforced tubing. The aerosol was generated by ultrasonic humidifier and was carried towards the heating zone of the furnace with the help of carrier gas (argon). Thermally induced decomposition of the precursor took place on heated surface of the substrates and resulted in the deposition of SnSe thin films.

4.3. Characterization

4.3.1. Elemental and Thermogravimetric analysis

Microanalysis was performed using a Thermo Scientific Flash 2000 Organic Elemental Analyzer. Thermogravimetric analyses were performed using a Mettler-Toledo TGA/DSC under nitrogen gas flow rate of 10 mL/min.

4.3.2. Powder X-ray diffraction analysis

The X-ray diffraction was performed using a Bruker D8 Discover Diffractometer using CuKα radiation (λ = 1.54178 Å), in a 2Θ range from 10^{o} to 70^{o}. The data collected was used to determine the lattice parameters and crystal phase.

4.3.3. Transmission electron microscopy (TEM) and High Resolution TEM (HRTEM) analysis

TEM and HRTEM images were collected on a Talos F200X at 200 kV using a FEI ceta camera. The samples were prepared by drop casting few drops from dilute solution of SnSe nanosheets and evaporating on Formvar-coated Cu grids (150 mesh) for TEM and holey carbon grids for HRTEM analyses.

4.3.4. Scanning electron microscopy (SEM) and Energy Dispersive X-ray (EDX) spectroscopy

Scanning electron microscopy (SEM) was carried out using a Philips XL30 FEG SEM. Energy-dispersive X-ray (EDX) spectroscopy was performed using a DX4 detector. All samples were carbon coated using an Edwards coating system E306A prior to SEM analysis.

4.3.5. Raman Spectroscopy

Raman spectra were measured using a Renishaw 1000 Micro-Raman System equipped with a 514 nm laser operating at 1 mW.

4.3.6. Uv-Vis-NIR Spectroscopy

UV−Vis-NIR spectrum was recorded using a PerkinElmer Lambda 1050 instrument, using quartz cuvettes with a path length of 1 cm.

4.3.7. Electrochemical study

The electrochemical work station (Auto Lab, Netherland) was used for all the photoelectrochemical measurements (PEC). The three electrode system was used for the PEC measurements consisted of SnSe coated FTO as the working electrode, platinum as counter electrode and Ag/AgCl as reference electrode.

4.4. Results and discussion

The synthesis of the single source precursor was carried out in two steps by modifying a previously reported synthetic protocol,[25] using $NaBH_4$ instead of the highly pyrophoric metallic sodium. In the first step, the ligand was formed by the dropwise addition of an equimolar quantity of benzoyl chloride in freshly prepared ethanolic solution of NaHSe. The ethanolic solution of Bu_2SnCl_2 was then added slowly to the ligand solution. The purity of the complex was determined by elemental analysis and thermogravimetric analysis (TGA) was performed to observe the thermal stability.

The complex is thermally stable and no mass loss was indicated upto 230 °C, after which rapid mass loss was observed and complete decomposition occurs at 310 °C in a single step (Figure 4.2). The differential curve shows that the maximum weight loss was observed at 290 °C, and a minor weight loss may be indicated by presence of a slight shoulder peak. The final residue was ca. 17.5 % of the original mass, which is less than what is required for the formation of SnSe (theoretical mass = 32.8 %). The experimental weight loss does not correspond to any oxide of tin, elemental selenium or tin. In order to investigate the decomposition behaviour and nature of the residue, a small amount of the precursor in a ceramic combustion boat was placed in a glass tube, which was sealed and inserted in carbolite tube furnace.

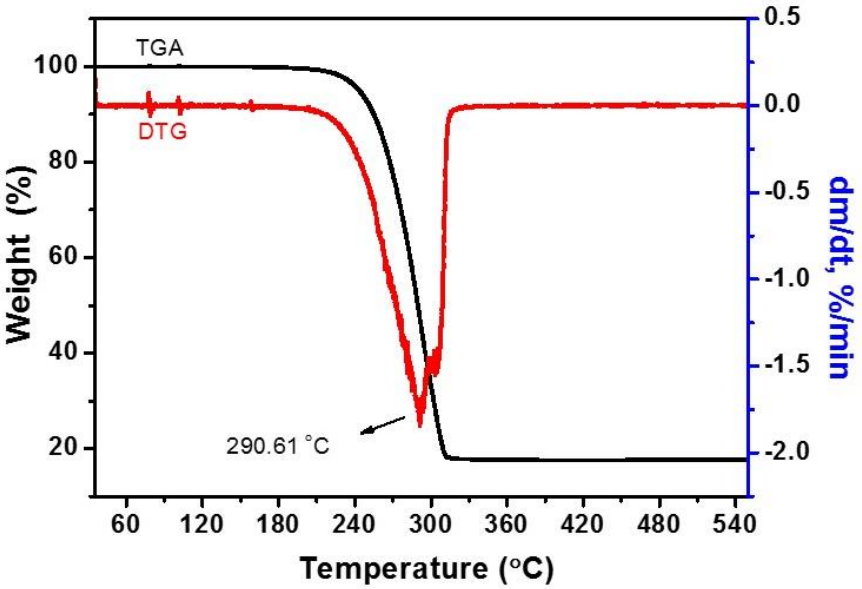

Figure 4.2. TGA and DTG analysis of the *bis*(selenobenzoato)dibutyltin(IV) complex.

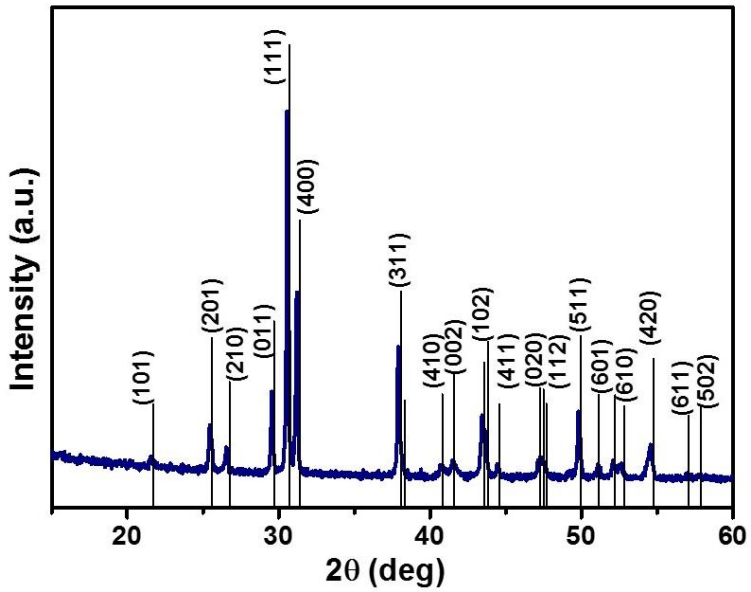

Figure 4.3. p-XRD of the residue obtained by decomposition of *bis*(selenobenzoato)dibutyltin(IV) complex.

The furnace was slowly heated to 500 °C, under constant nitrogen flow, for one hour. It was observed that above 200 °C, some of the precursor sublimates and

is deposited at the end of the glass tube. The resultant black residue was characterized by p-XRD as shown in Figure 4.3, confirming the formation of SnSe. Hence, the sublimation of the precursor during thermogravimetric analysis prevents to obtain the accurate value of the residue.

SnSe nanosheets were synthesized by the hot injection method at temperature of 200 °C in oleylamine, which acted as a capping agent and also aids in the decomposition of precursor. The decomposition of selenobenzoate complex may follow the same mechanism as suggested by Chin *et al*. for the decomposition of metal thiocarboxylate complexes in primary amines.[26, 27] Vittal *et al*. also reported the synthesis of silver selenide nanoparticles and observed that the precursor decomposes easily at room temperature in the presence of a primary alkyl amine.[28] The primary amine behaves as a nucleation initiator and accelerates the decomposition of precursor. However, in our case the decomposition proceeded with slight delay, primarily due to high thermal stability of the precursor. The relative stability lowers the rate of the nucleation step, which is particularly desirable in injection based synthesis,[29] as injection temperature need not to be very high *i.e.* ≥ 300 °C. Similarly, the nucleation and growth steps become almost independent of the injection, hence the prerequisite of rapid injection is not required to synthesize monodisperse nanocrystals in reproducible way. A relatively large quantity of stock solution can be used for injection as initial nucleation takes as long as tens of seconds.

Figure 4.4 represents X-ray diffraction pattern of OLA capped SnSe nanosheets synthesized at 200 °C. The peaks match well with the orthorhombic tin selenide phase (ICDD # 03-065-6459) with the absence of any impurity peaks. The intensity is an indication of the superior crystallinity of the nanosheets, whereas the slight broadness shows that the nanosheets are quite thin.

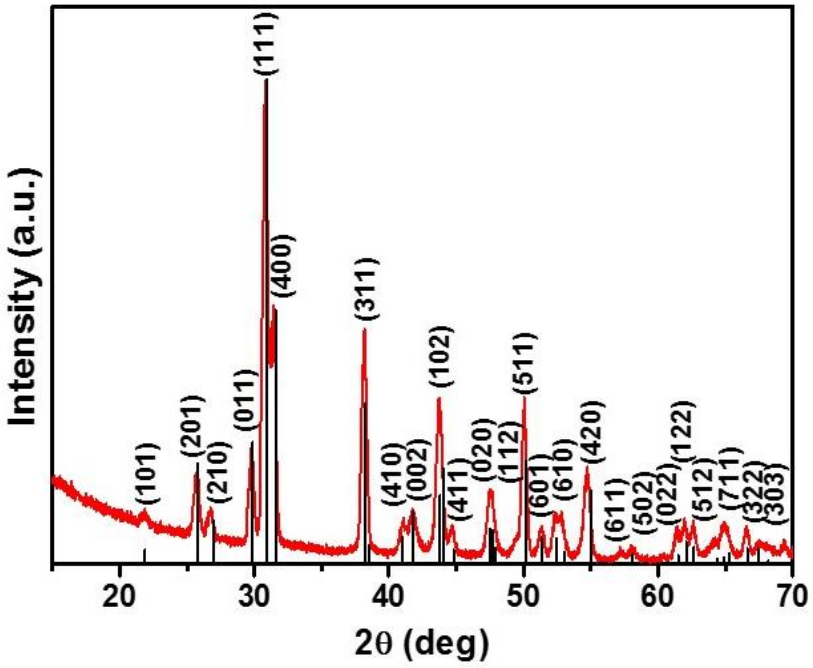

Figure 4.4. p-XRD pattern of OLA capped SnSe nanosheets, synthesized at 200 °C for 30 min.

TEM analysis further confirms the thin nature of the SnSe nanosheets (Figure 4.5). Large nanosheets in the order of microns were observed along with some comparatively small sheets stacked on to larger sheets. The thin layers can be observed easily at the edges and can be differentiated on the basis of change in complexion of the layers as some of them appear quite transparent to the electron beam. The crystalline nature of the sheets was indicated by the HR-TEM image (Figure 4.6(a)), where clear lattice fringes can be observed easily, and well defined discrete spots were obtained by selected area electron diffraction (SAED) pattern (Figure 4.6(b)). The results are in agreement with the intense peaks observed in the p-XRD pattern.

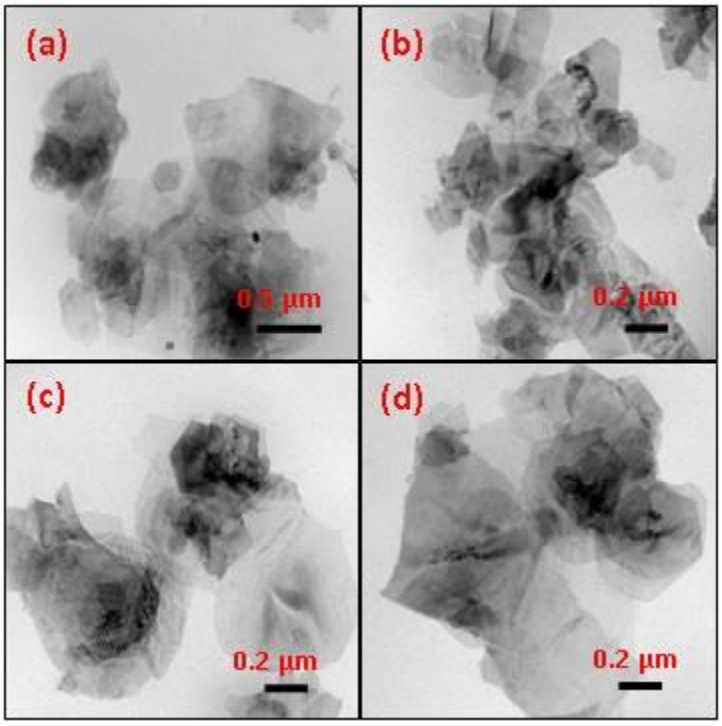

Figure 4.5. TEM images of OLA capped SnSe nanosheets synthesized at 200 °C.

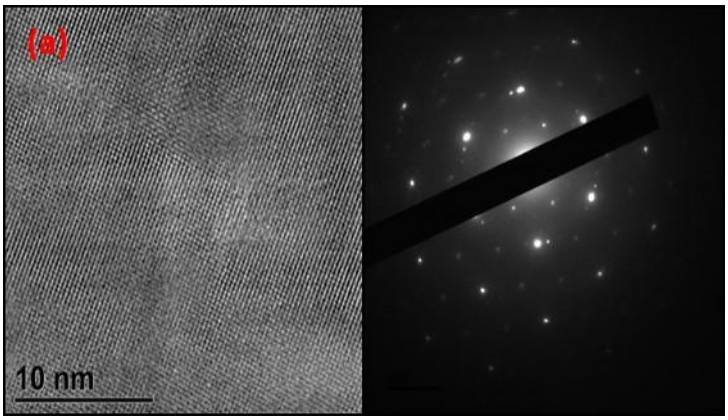

Figure 4.6. HRTEM image showing lattice fringes and (b) Selective area electron diffraction pattern of OLA capped SnSe nanosheets synthesized at 200 °C.

UV-Vis-NIR spectroscopy was performed on OLA capped SnSe nanosheets. The nanosheets were dispersed in acetone and sonicated for half an hour. A continuously descending, broad absorption spectrum was obtained as shown in Figure 4.7(a). The direct band gap as determined by the Tauc plot shows a slight blue shift, whereas the indirect energy gap was not affected.

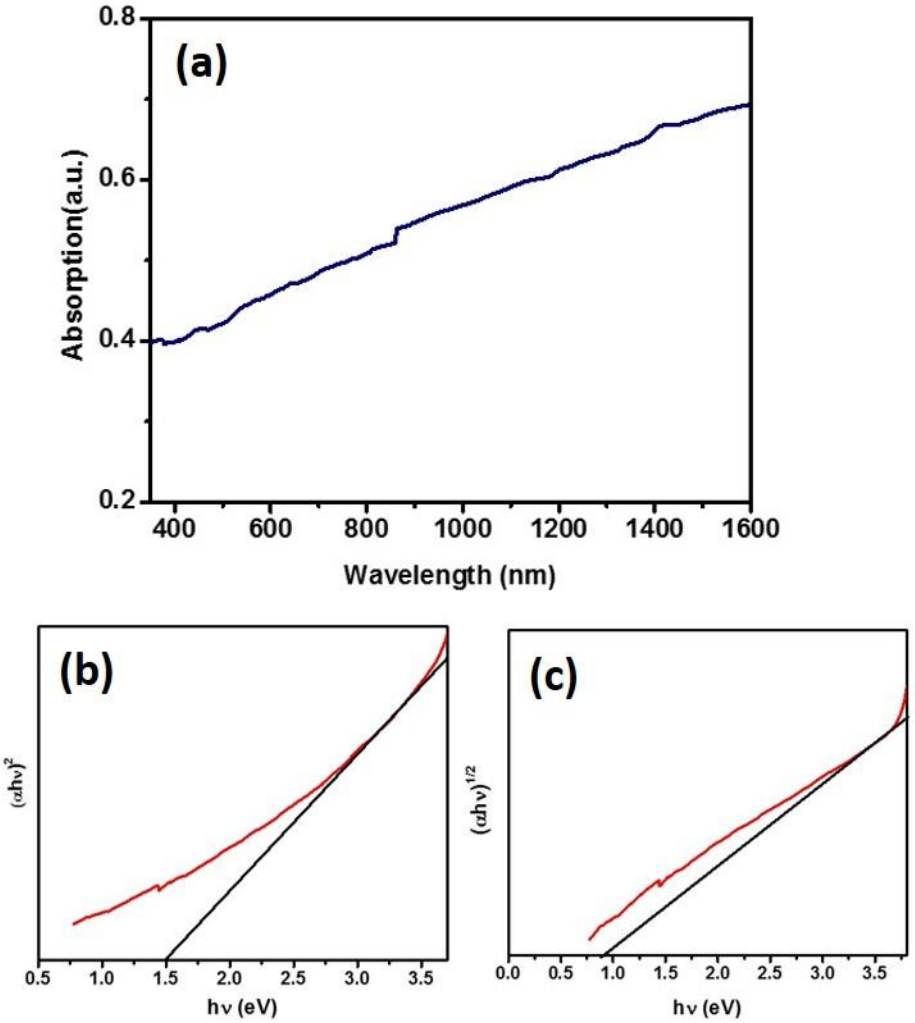

Figure 4.7. (a) UV-Vis-NIR spectrum of OLA capped nanosheets dispersed in acetone, (b) direct band gap as determined by the Tauc plot and (c) indirect band gap estimated by Tauc plot.

4.4.1. SnSe thin films by AACVD

Tin selenide thin films were deposited on the glass substrates using THF solution of *bis*(selenobenzoato)dibutyltin(IV) complex. The SSP was soluble in solvents commonly used for AACVD, such as chloroform, toluene and THF. Toluene requires long deposition time and to avoid chlorinated solvent, THF was used for the deposition. The precursor decomposes completely around 310 °C, therefore thin film deposition was attempted at 325 °C, however only slight and non-uniform deposition was observed at this temperature. To obtain uniformly deposited crystalline thin films, the temperature was then varied between 375 and 475 °C, using argon as the carrier gas at a flow rate of 200 sccm. The deposited films at all temperatures were black. It was observed that uniform deposition took place on the substrates which were placed in the middle and at the end of the tube. The deposited thin films were uniform and moderately adherent and could be scratched easily by a spatula.

The p-XRD patterns of the thin films deposited at 375, 425 and 475 °C, are shown in Figure 4.8. The peaks match well with orthorhombic SnSe (ICDD # 03-065-6459). The intensity profile matches well with the standard pattern at deposition temperature of 375 °C, however it varied significantly with change in temperature. A prominent change in intensity was observed along the (111) plane, which was the most intense peak at 375 °C. Whereas an increase in temperature results in decrease in intensity of the (111) plane and preferential growth in direction of the (040) plane was observed, which appears as the most intense plane at deposition temperature of 475 °C. The intensity variation indicates that the alignment of particles in a particular plane changes by the change in deposition temperature, and substantially affects the morphology of the deposited thin films.

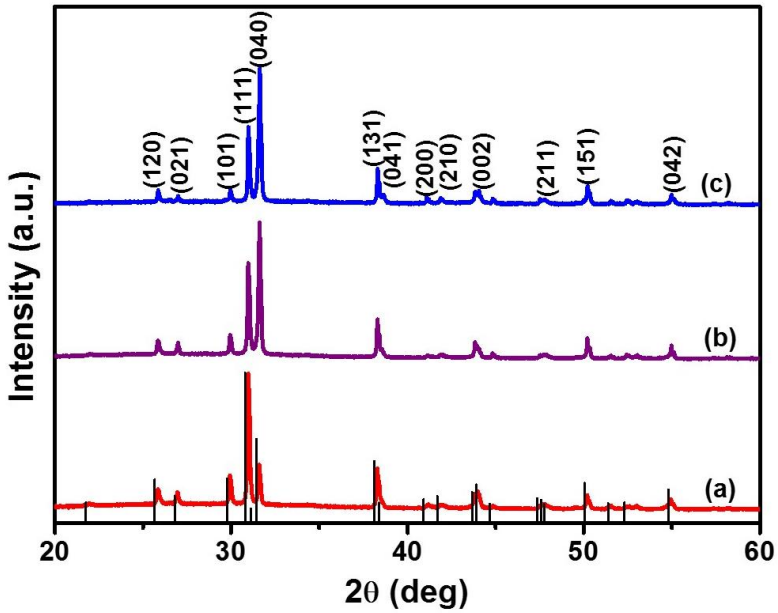

Figure 4.8. p-XRD spectra of SnSe thin films deposited at (a) 375 °C, (b) 425 °C and (c) 475 °C by AACVD on glass substrates.

SEM images for thin films deposited at 375 °C is shown in Figure 4.9. The films were covered with large and thick SnSe plates randomly oriented on the substrate. The size and thickness of the plates is roughly the same (with few exceptions). Elemental mapping was performed to observe the homogeneity of the deposited thin films and it indicates that the tin and selenium were distributed uniformly throughout the film (Figure 4.10(a-c)). The thin film was slightly selenium deficient as a mean Sn/Se ratio of 1.13 was observed by EDX, which is close to the stoichiometric value of 1 (Figure 4.11(a)).

At 425 °C, it was observed that the thickness of the plates decreases considerably and few rod-like crystallites were also present as indicated by the arrows (Figure 4.12). The length of the rods is in the range of microns and appeared randomly throughout the film. A uniform distribution of elements in the film was shown by elemental mapping (Figure 4.10(d-f)). The increase in temperature marginally affects the stoichiometric ratio of Sn/Se to 1.19 as determined by EDS (Figure 4.11(b)), which shows that the deposited thin films are slightly selenium deficient.

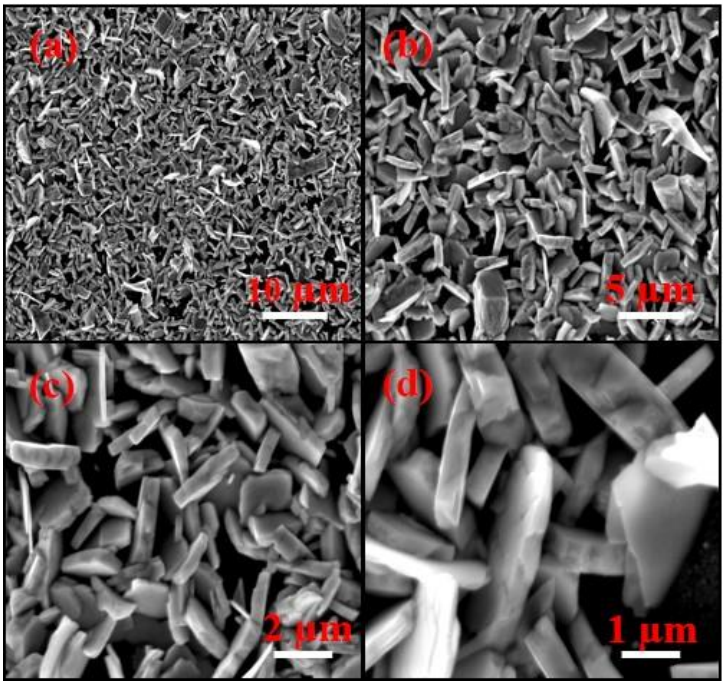

Figure 4.9. SEM images of SnSe thin film deposited at 375 °C, showing plate like morphology.

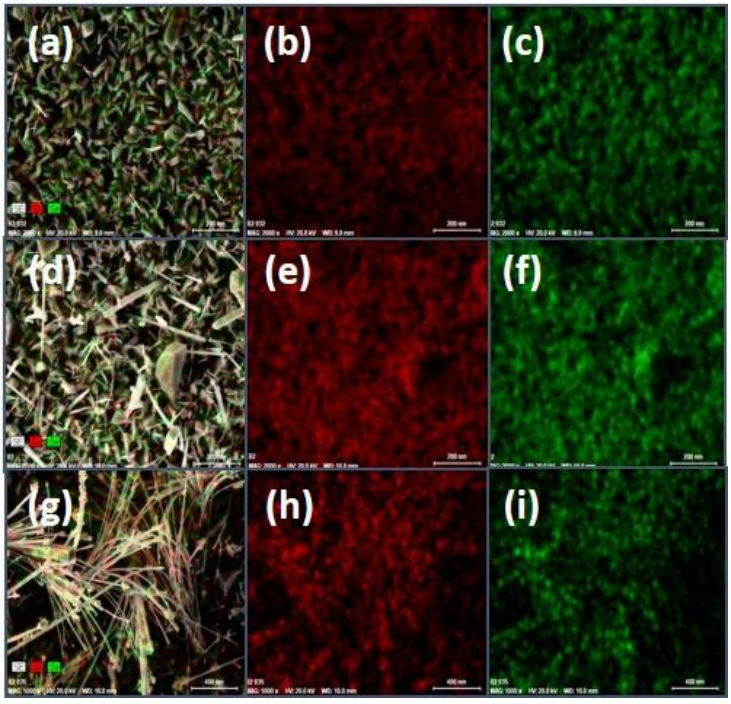

Figure 4.10. Elemental mapping of SnSe thin films deposited at (a-c) 375 °C, (d-f) 425 °C and (g-i) 475 °C.

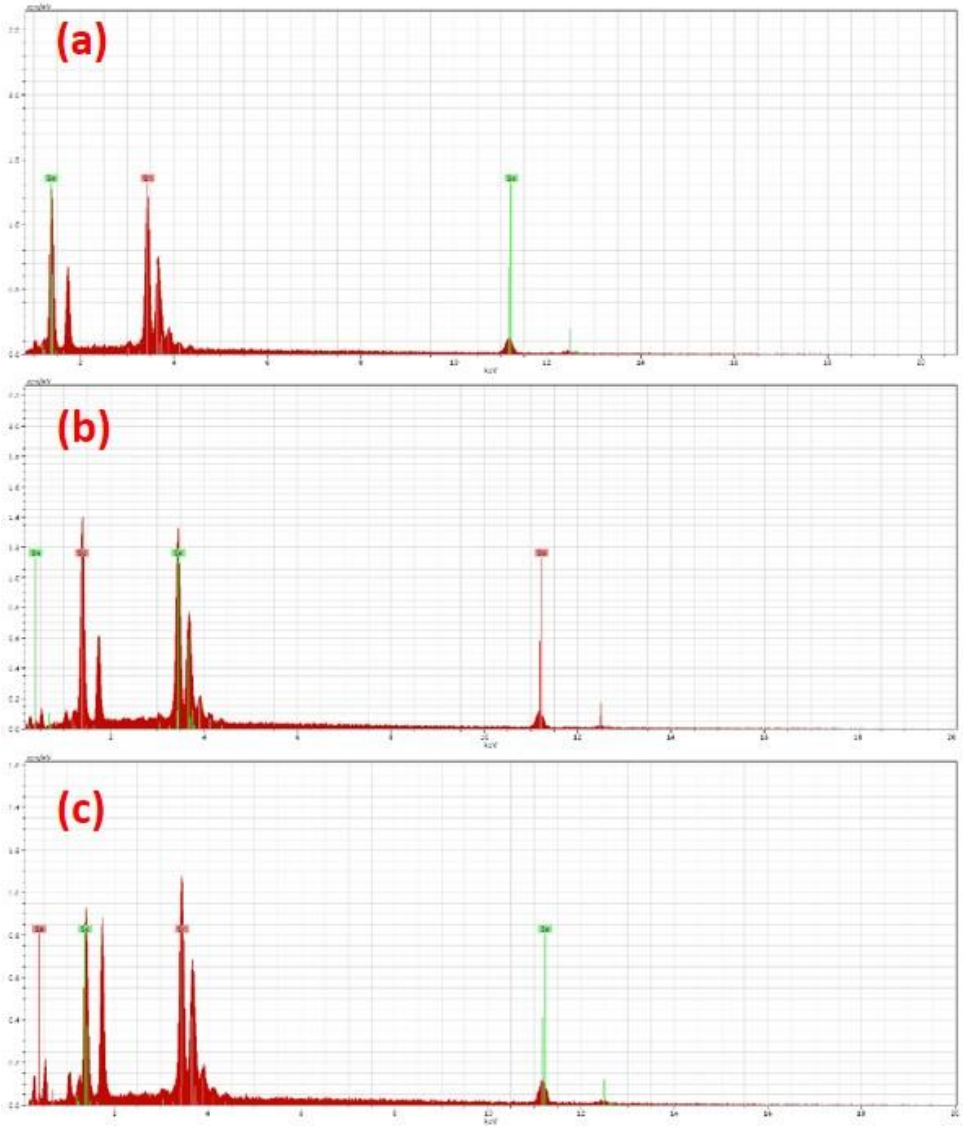

Figure 4.11. EDX spectra of SnSe thin films deposited at (a) 375 °C, (b) 425 °C and (c) 475 °C by AACVD.

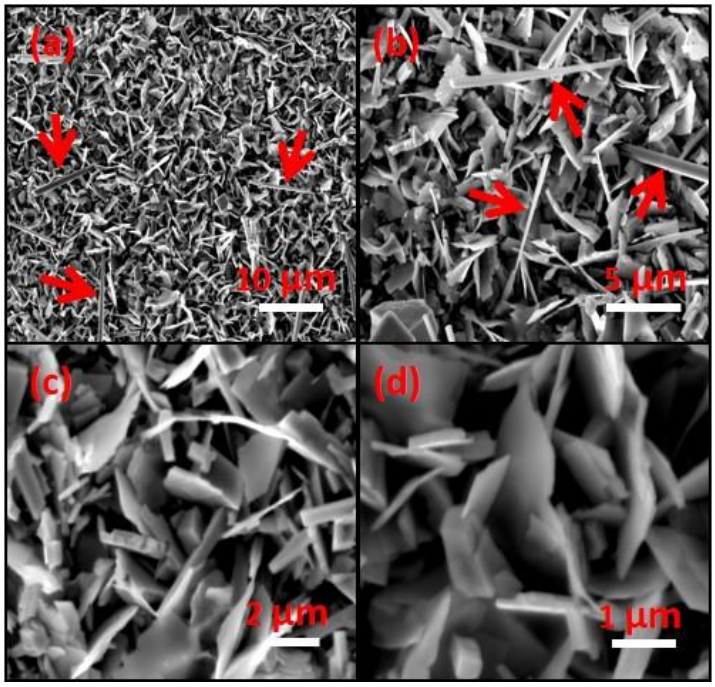

Figure 4.12. SEM images of SnSe thin film deposited at 425 °C, presence of rods is indicated by arrows along with plate like morphology.

The morphology of thin films deposited at 475 °C was completely different, showing cuboid rod-like crystallites (Figure 4.13). The change in the morphology was also indicated by the p-XRD pattern, where a specified orientation was observed by modification in the intensity profile of the peaks. The cuboid rods were of similar diameter (≈ 0.4-05 µm) and the length was greater than 10 µm. A magnified SEM image shows the end of a solid cuboid rod. Both thermodynamic and kinetic parameters play a role in controlling the morphology, as at higher temperature along with thermodynamic stability, the rate of decomposition of the precursor also increases. The layers are attached with Van der Waals forces which can be diminished at high temperature. At 375 °C, the plates were thick and increase in temperature (*i.e.* 425 °C) results in thinning of the plates, probably due to separation of attached layers as Van der Waals forces weakened and a further increase results in the breakdown of these forces of attraction, leading towards formation of cubic rods. A further change in elemental stoichiometry was observed by EDS (Figure 4.11(c)) as the mean Sn/Se ratio was

increased to 1.24, which shows further deficiency of selenium in the deposited thin films. The elemental distribution in the thin films however was still uniform as shown in Figure 4.10(g-i).

A combined SEM image of all thin films deposited at different temperatures, with different magnification is shown in Figure 4.14, which clearly shows change in morphology of crystallites from plates to cuboid-like crystallites.

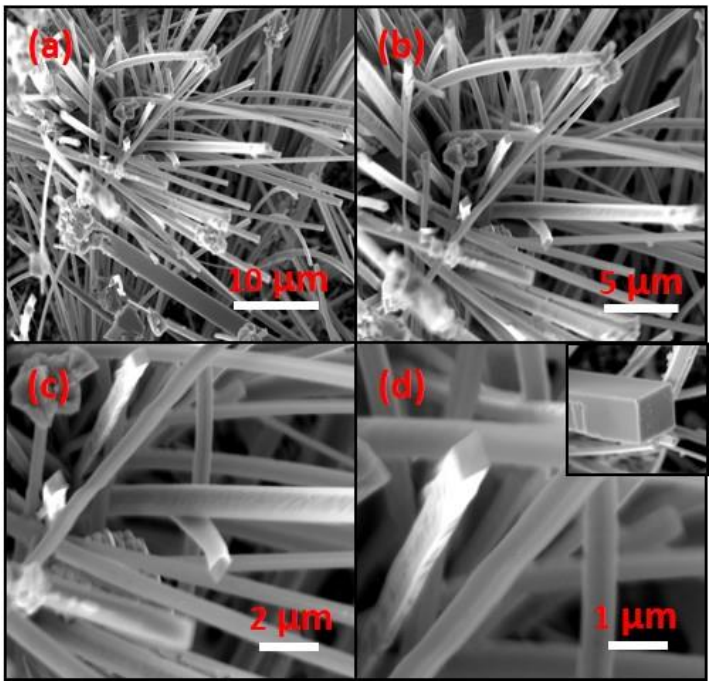

Figure 4.13. SEM images of SnSe thin film deposited at 475 °C, showing cuboid rods.

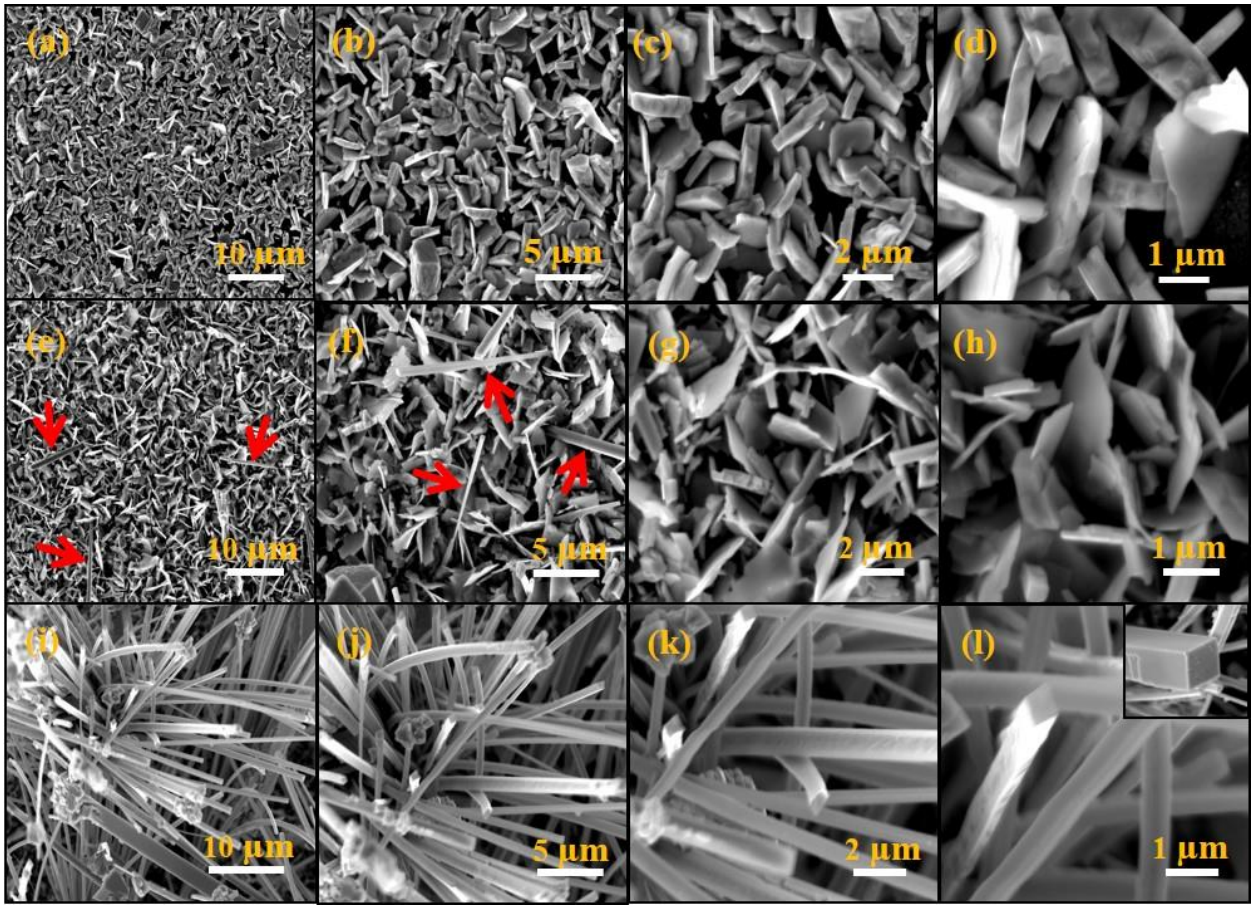

Figure 4.14. Combined SEM images of SnSe thin films deposited at (a-d) 375 °C, (e-h) 425 °C and (i-l) 475 °C by AACVD.

The thin films were also characterized by Raman spectroscopy, the peaks correspond well to the earlier reported literature (Figure 4.15).[30] The Raman shift for thin films deposited at 375 °C was not prominent, only vibrational modes present at 70 cm^{-1} and 108 cm^{-1} were identified and rest were difficult to assign because of the broadness of the peaks. However, distinct peaks were observed for thin films deposited at 425 °C, with high intensity mode present at 108 cm^{-1}. The bands becomes sharper and intense as the deposition temperature was further increased to 475 °C. The broadening of the band is related to the presence of stress or structural defects in scattering volume and shows low structural quality of the lattice.[31, 32] As the crystallinity of the material enhances with increase in temperature, the highest intensity ratio was observed for the thin film deposited at high temperature which shows higher structural quality of the film.

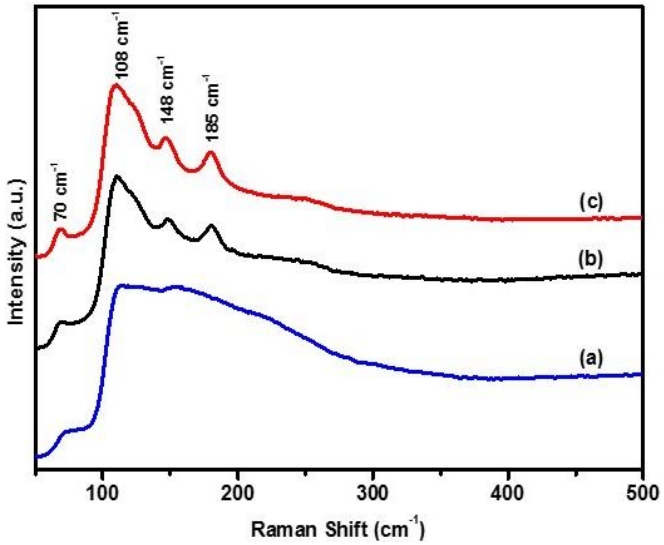

Figure 4.15. Raman spectra for SnSe thin films deposited at (a) 375 °C, (b) 425 °C and (c) 475 °C by AACVD.

4.5. Photoelectrochemical investigation of the SnSe nanosheets

SnSe thin films were prepared on the surface of the FTO glass for photoelectrochemical (PEC) investigation of the synthesized material. The SnSe coated FTO glass was used as a working electrode in a three electrode system. It was exposed to 1 Sun solar simulator at regular intervals to explore the behavior of the SnSe coated films under dark and light in 0.5 M Na_2SO_4 medium at pH 7.0. Uncoated FTO glass has a negligible photo response current, however, after coating with SnSe slurry, the photocurrent was significantly improved. The photocurrent density was found to be 11 $\mu A/cm^2$, even at an open circuit potential (OCP). The photocurrent density was measured using chronoamperometry by switching the light in ON/OFF approach after regular intervals. In this way, the photoactive material is exposed to dark and light after regular intervals. The SnSe coated FTO demonstrated a unique photoactive behavior in the presence of light. When the coated FTO was irradiated with light, the current started to decrease sharply towards the negative value and in dark, again it reached back to the initial value. This behavior of the SnSe coated FTO displayed that hydrogen evolution reaction (HER) is taking place at 0V (Figure 4.16 A). The PEC reaction at the surface of electrode was entirely changed when the applied potential was switched to 0.1 V. The current was significantly increased under simulated 1 sun light irradiation and gradually

leveled off and return back to original value in the dark. It is evident that the oxygen evolution reaction (OER) was initiated at 0.1 V (Figure 4.16 B) whereas with increase of applied potential to 0.2 V, the photocurrent was increased to about 30μA/cm^2 (Figure 4.16 C).

The stability of the SnSe coated FTO was measured for OER at 0.2 V. I-t curves were obtained in the presence and absence of light from solar simulator (Figure 4.16 D). It was revealed from the chronoamperometric measurement, that the SnSe nanosheets have high stability under light and in the dark. The study indicates that it could be one possible application of the synthesized SnSe nanosheets. This material could be applied for both HER and OER just by switching the applied potential.

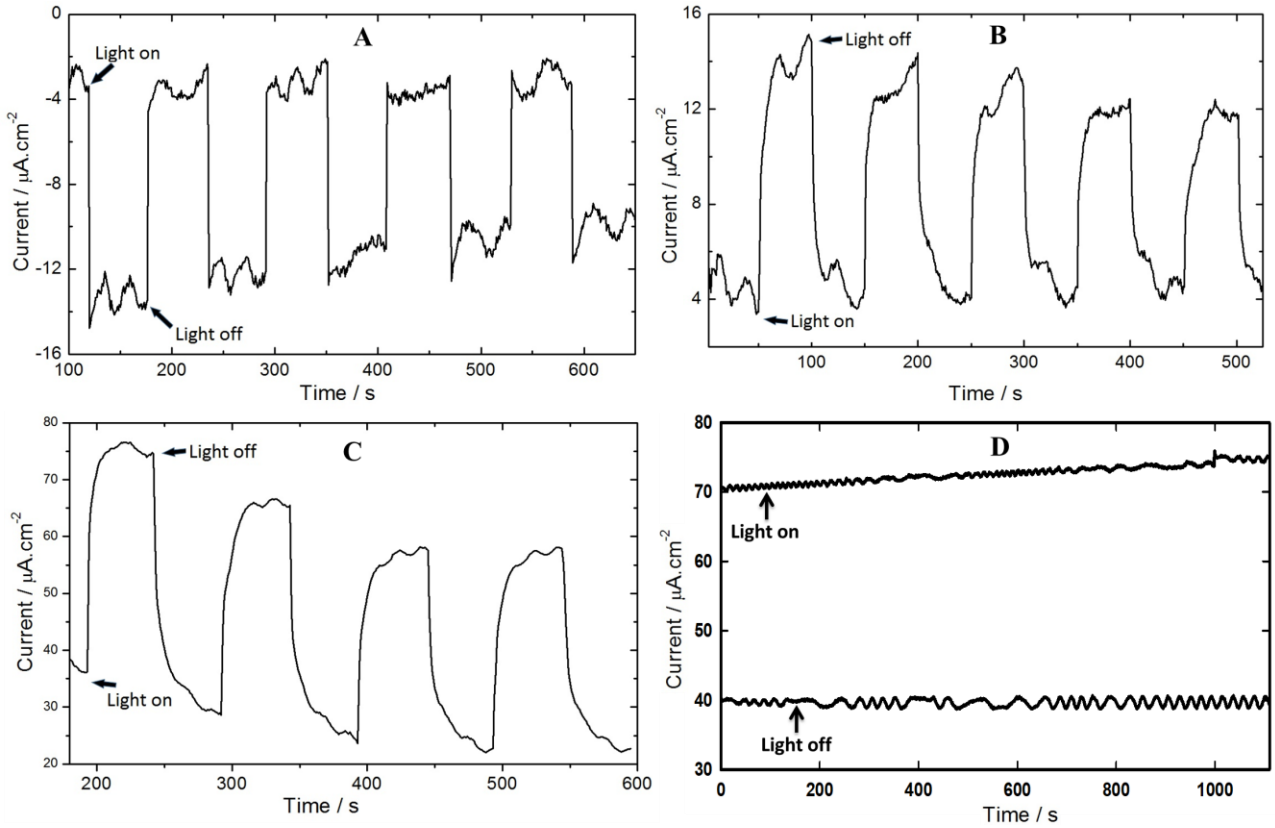

Figure 4.16. Chronoamperometry measurements of SnSe coated FTO showing the photocurrent densities at (A) 0.0, (B) 0.1, (C) 0.2 V. (D) I-t stability curves under light and dark.

4.6. Conclusion

A new tin complex has successfully been used as a precursor for the synthesis of SnSe nanosheets and thin films by AACVD. The nanosheets in OLA were synthesized well below the decomposition temperature of the complex as determined by TGA, which shows that OLA is not only a capping agent but also an initiator for decomposition of the precursor. Thin films were deposited at three different temperatures by AACVD and the deposition temperature was found to have significant effect on the shape and preferred orientation of the particles. The effect of temperature was investigated by p-XRD, SEM and Raman spectroscopy. It was observed that the alignment of the crystallites and stoichiometry in deposited thin films can be manipulated by judicious control on deposition temperature. Photo-electrochemical studies show the potential of the material for water splitting.

4.7. References

1. W. J. Youngblood, S.-H. A. Lee, K. Maeda and T. E. Mallouk, *Accounts of Chemical Research*, 2009, **42**, 1966-1973.
2. A. Takagaki, M. Sugisawa, D. Lu, J. N. Kondo, M. Hara, K. Domen and S. Hayashi, *Journal of the American Chemical Society*, 2003, **125**, 5479-5485.
3. O. C. Compton and F. E. Osterloh, *The Journal of Physical Chemistry C*, 2008, **113**, 479-485.
4. C. N. R. Rao, A. K. Sood, K. S. Subrahmanyam and A. Govindaraj, *Angewandte Chemie International Edition*, 2009, **48**, 7752-7777.
5. R. Mas-Balleste, C. Gomez-Navarro, J. Gomez-Herrero and F. Zamora, *Nanoscale*, 2011, **3**, 20-30.
6. K. F. Mak, C. Lee, J. Hone, J. Shan and T. F. Heinz, *Physical Review Letters*, 2010, **105**, 136805.
7. I. Lefebvre, M. Szymanski, J. Olivier-Fourcade and J. Jumas, *Physical Review B*, 1998, **58**, 1896.
8. M. A. Franzman, C. W. Schlenker, M. E. Thompson and R. L. Brutchey, *Journal of the American Chemical Society*, 2010, **132**, 4060-4061.
9. W. J. Baumgardner, J. J. Choi, Y.-F. Lim and T. Hanrath, *Journal of the American Chemical Society*, 2010, **132**, 9519-9521.
10. L. Makinistian and E. Albanesi, P*hysica Status Solidi (b)*, 2009, **246**, 183-191.
11. P. D. Antunez, J. J. Buckley and R. L. Brutchey, *Nanoscale*, 2011, **3**, 2399-2411.
12. B. Pejova and I. Grozdanov, *Thin Solid Films*, 2007, **515**, 5203-5211.
13. C. Wang, Y. Li, G. Zhang, J. Zhuang and G. Shen, *Inorganic Chemistry*, 2000, **39**, 4237-4239.
14. J. Ning, K. Men, G. Xiao, L. Wang, Q. Dai, B. Zou, B. Liu and G. Zou, *Nanoscale*, 2010, **2**, 1699-1703.
15. D. D. Vaughn, S.-I. In and R. E. Schaak, *ACS Nano*, 2011, **5**, 8852-8860.
16. S. Liu, X. Guo, M. Li, W. H. Zhang, X. Liu and C. Li, *Angewandte Chemie International Edition*, 2011, **50**, 12050-12053.
17. J. Singh and R. Bedi, *Thin Solid Films*, 1991, **199**, 9-12.

18. N. D. Boscher, C. J. Carmalt, R. G. Palgrave and I. P. Parkin, *Thin Solid Films*, 2008, **516**, 4750-4757.
19. R. Indirajith, T. Srinivasan, K. Ramamurthi and R. Gopalakrishnan, *Current Applied Physics*, 2010, **10**, 1402-1406.
20. S. R. Bahr, P. Boudjouk and G. J. McCarthy, *Chemistry of Materials*, 1992, **4**, 383-388.
21. P. Boudjouk, D. J. Seidler, D. Grier and G. J. McCarthy, *Chemistry of Materials*, 1996, **8**, 1189-1196.
22. P. Boudjouk, D. J. Seidler, S. R. Bahr and G. J. McCarthy, *Chemistry of Materials*, 1994, **6**, 2108-2112.
23. R. K. Sharma, G. Kedarnath, A. Wadawale, C. Betty, B. Vishwanadh and V. K. Jain, *Dalton Transactions*, 2012, **41**, 12129-12138.
24. P. Kevin, S. N. Malik, M. A. Malik and P. O'Brien, *Chemical Communications*, 2014, **50**, 14328-14330.
25. S. Kato, H. Kageyama, K. Takagi, K. Mizoguchi and T. Murai, *Journal für Praktische Chemie*, 1990, **332**, 898-910.
26. W. P. Lim, C. T. Wong, S. L. Ang, H. Y. Low and W. S. Chin, *Chemistry of Materials*, 2006, **18**, 6170-6177.
27. W. P. Lim, Z. Zhang, H. Y. Low and W. S. Chin, *Angewandte Chemie International Edition*, 2004, **43**, 5685-5689.
28. M. T. Ng, C. Boothroyd and J. J. Vittal, *Chemical Communications*, 2005, 3820-3822.
29. Z. A. Peng and X. Peng, *Journal Of American Chemical Society*, 2001, **123**, 183-184.
30. H. Chandrasekhar, R. Humphreys, U. Zwick and M. Cardona, *Physical Review B*, 1977, **15**, 2177.
31. J. Álvarez-García, J. Marcos-Ruzafa, A. Pérez-Rodríguez, A. Romano-Rodríguez, J. Morante and R. Scheer, *Thin Solid Films*, 2000, **361**, 208-212.
32. T. Fukunaga, S. Sugai, T. Kinosada and K. Murase, *Solid State Communications*, 1981, **38**, 1049-1052.

Chapter # 5

Synthesis, characterization and band gap tuning of the $Sb_2(S_{1-x}Se_x)_3$ solid solution using single source precursors

5.1. Introduction

Antimonselite (Sb_2Se_3) is considered a relatively non-toxic and earth abundant material having a direct, narrow band gap (approximately 1.2 eV) with an excellent light absorption coefficient (>10^5 cm^{-1} at short wavelength).[1, 2] It is also cost effective and can be easily scaled up as a light absorber in thin film solar cells.[3, 4] In addition, Sb_2Se_3 based solid state cells[5] and photoelectrochemical cells[6] exhibit high performance which attracts attention to its photo response activity. However, Sb_2Se_3 may cover a broader range of solar spectrum for energy harnessing, (optimal range: E_g = 1.3-1.5 eV) and the device efficiency can be enhanced significantly by energy band optimization.[7-9] Some popular methods for tuning the band gap includes size tuning, formation of core/shell structures or compositional engineering such as doping, stoichiometric variation or by alloying.[10-12] Nevertheless, core/shell systems require multistep synthesis and the growth of shell with suitable thickness, which also increases the overall size of the nanocrystals.[13, 14] An effective method of engineering the band gap is the mixing of binary semiconductors to generate alloyed ternary (MA_xB_{1-x}) materials.[15] The physical and chemical properties of such alloys can be controlled by their composition, besides their size, and they often inherit interesting properties, which cannot be achieved by simple size tuning of their parent binary analogues.[15, 16]

In the case of antimony selenide, a ternary alloy solid solution can be formed by either replacing antimony with an atom of comparable size and charge such as bismuth, or substitution of selenium by another chalcogenide such as sulfur or tellurium. Bi_2Se_3 is rhombhohedral and Sb_2Se_3 is orthorhombic, hence a complete solid solution with entire compositional range is difficult. The chalcogenide atom can be easily replaced by another chalcogenide *i.e.* sulfur, as Sb_2Se_3 (antimonselite) and Sb_2S_3 (stibnite) are isostructural and belongs to group V-VI class of semiconductors, having a chain-like structure and crystallizes in orthorhombic system (*pbnm* space group).[17, 18] The development of a thio-seleno

based ternary alloy system is highly feasible and they may show composition dependent bandgap energies.

The synthesis of the $Sb_2Se_{3-x}S_x$ ternary alloy system is not well explored thus far, with only a few examples in the literature. A rapid thermal evaporation technique was used for the deposition of $Sb_2(Se_{3-x}S_x)$ thin films (where x = 0, 1, 2 or 3) but they were either amorphous or sulfur incorporation was difficult.[19, 20] Polycrystalline thin films of $Sb_2(Se_{1-x}S_x)_3$ ($0 \leq x \leq 1$) were reported by Bo Yang *et al.* using hydrazine based metal and chalcogenide solutions respectively.[21] Chemical bath deposition was employed for the ternary alloy thin films, however uniform distribution was not evident and the control on composition was difficult.[22, 23] The colloidal synthesis of $Sb_2(Se_{3-x}S_x)$ alloy nanotubes was reported by Deng *et al.*, by injecting an antimony-complex solution into a preheated solution of S, Se or S/Se mixture in paraffin.[24] Microwave synthesis was also used to synthesize sulfurized Sb_2Se_3 nanorods, where trioctylphosphine-selenide and thioglycolic acid were used as the sulfur/selenium source.[25, 26] The only example of the use of the single source precursor method is reported by Schulz *et al.* using trialkylantimony chalcogenide precursors.[27] Overall, an environmently friendly route (hydrazine, metal-alkyl and phosphine free), with the use of suitable single source precursors, for composition controlled synthesis of $Sb_2(S_{1-x}Se_x)_3$ solid solution in the entire range is missing in the literature.

The synthesis of a $Sb_2(S_{1-x}Se_x)_3$ solid solution in the entire range of composition, using chalcogeno (thio and seleno) benzoate complexes of antimony by the hot injection method, using oleylamine as decomposition initiator and capping agent is described. The single source precursors provide efficient incorporation of sulfur and better control over composition was achieved by a facile synthetic approach. The band gap determination indicates compositional dependence and increases with increase in sulfur concentration.

5.2. Experimental

5.2.1. Materials

The reagents and solvents *i.e.* oleylamine (OLA), $SbCl_3$, $NaBH_4$, KOH, elemental selenium, benzoyl chloride, thiobenzoic acid and ethanol were procured from Sigma Aldrich and used as received.

5.2.2. Synthesis of *tris*(selenobenzoato)antimony(III) complex (1)

NaHSe was prepared by adding ethanolic solution of $NaBH_4$ (12.0 mmol in 15.0 mL ethanol) into ethanolic solution of metallic Se powder (0.5 g, 6 mmol) under inert conditions using Schlenk line at room temperature. The reddish solution becomes colourless within 5 min. Benzoyl chloride (6.0 mmol) was then added into freshly prepared NaHSe solution and the colour of the solution immediately changes from colourless to yellow, indicating the formation of the seleno benzoate ligand. The stirring was continued for further 15 min, after which 2.0 mmol of $SbCl_3$ in 15.0 mL ethanol was added dropwise. The precipitates formed were filtered and recrystallized by THF to afford the product. Elemental analysis cal. (%) for $C_{21}H_{15}O_3SbSe_3$: C 37.42, H 2.24, Sb 18.07; Found: C 37.41, H 2.20, Sb 17.97.

5.2.3. Synthesis of *tris*(thiobenzoato)antimony(III) complex (2)

Sodium salt of thiobenzoic acid was prepared by adding an ethanolic solution (25.0 mL) of KOH (15.0 mmol) in ethanolic solution (25.0 mL) of thiobenzoic acid (15.0 mmol) while stirring. The stirring was continued for 15 min. at room temperature, afterwhich ethanolic (20.0 mL) solution of $SbCl_3$ was added dropwise under inert conditions. The precipitate formed was collected, washed with excess of ethanol and recrystallized by THF to afford the product.

5.2.4. Synthesis of ternary $Sb_2(S_{1-x}Se_x)_3$ solid solution

The solid solution was synthesized by dispersing a mixture of complex **(1)** and **(2)** in appropriate molar compositions in OLA (2.0 mL) and injected into preheated OLA (8.0 mL) at 200 °C under continuous stirring. The temperature was maintained for 30 min. after which the reaction mixture was removed from heating source for cooling. A

mixture of acetone and methanol (1:1) was used for precipitation, the synthesized material was washed and separated by centrifugation.

5.3. Characterization

5.3.1. Elemental and Thermogravimetric analysis

Microanalysis was performed using a Thermo Scientific Flash 2000 Organic Elemental Analyzer. Thermogravimetric analyses were performed using a Mettler-Toledo TGA/DSC under nitrogen gas flow rate of 10 mL/min.

5.3.2. Powder X-ray diffraction

The X-ray diffraction was performed using a Bruker D8 Discover Diffractometer using CuKα radiation (λ = 1.54178 Á), in a 2Θ range from 10^{o} to 70^{o}. The data collected was used to determine the lattice parameters and crystal phase.

5.3.3. Transmission electron microscopy (TEM) and High Resolution TEM (HRTEM) analysis

TEM and HRTEM images were collected on a Talos F200X at 200 kV using a FEI ceta camera. The samples were prepared by drop casting few drops from dilute solution of sample and evaporating on Formvar-coated Cu grids (150 mesh) for TEM and holey carbon grids for HRTEM analyses.

5.3.4. Scanning electron microscopy (SEM) and Energy Dispersive X-ray (EDX) Spectroscopy

Scanning electron microscopy (SEM) was carried out using a Philips XL30 FEG SEM. Energy-dispersive X-ray (EDX) spectroscopy was performed using a DX4 detector. All samples were carbon coated using an Edwards coating system E306A prior to SEM analysis.

5.3.5. Raman Spectroscopy

Raman spectra were measured using a Renishaw 1000 Micro-Raman System equipped with a 514 nm laser operating at 1 mW.

5.3.6. Uv-Vis-NIR Spectroscopy

UV−Vis-NIR spectrum was recorded using a PerkinElmer Lambda 1050 instrument, using quartz cuvettes with a path length of 1 cm.

5.4. Results and discussion

Solid solutions are a type of alloys in which one or more constituents of a compound are partially replaced by another component while keeping the same structure. These alloys are homogenous and the lattice structure is maintained at different compositions, with slight contraction or expansion of the crystal lattice, depending upon the substituting component. The degree of solubility can be determined by applying Hume-Rothery rules,[28] which indicate that formation of solid solution is facilitated by (a) comparable electronegativity of solute and solvent (b) the difference in radii of solute and solvent must be less than 15 % (c) similar valency, and (d) same crystal structures of solute and solvent for complete solubility. Based on these rules, the chalcogenide atoms (S and Se) can easily replace one another, due to their similar behaviour.

The decomposition product of both precursors was observed by the thermogravimetric analysis (Figure 5.1). The TGA of complex **(1)** indicates a three step decomposition. A major mass loss of ~36 % in between the temperature range of 160 to 240 °C was observed in first step, which is probably due to the loss of phenyl groups. The second step shows a ~14% weight loss which may be attributed to the loss of carbonyl groups, leaving behind the $SbSe_3$ fragment which undergoes rearrangement to Sb_2Se_3 via loss of some Se atoms (~13% weight loss).[29] The complete decomposition of the complex occurred at 390 °C giving the final residue of ~36.5% corresponding to the formation of Sb_2Se_3 respectively (theoretically *ca.* 35.6%). Complex **(2)** decomposes in a single step and complete decomposition occurs around 330 °C with a residue of 32.6%, which corresponds to the formation of Sb_2S_3 (theoretically *ca.* 31.8%).

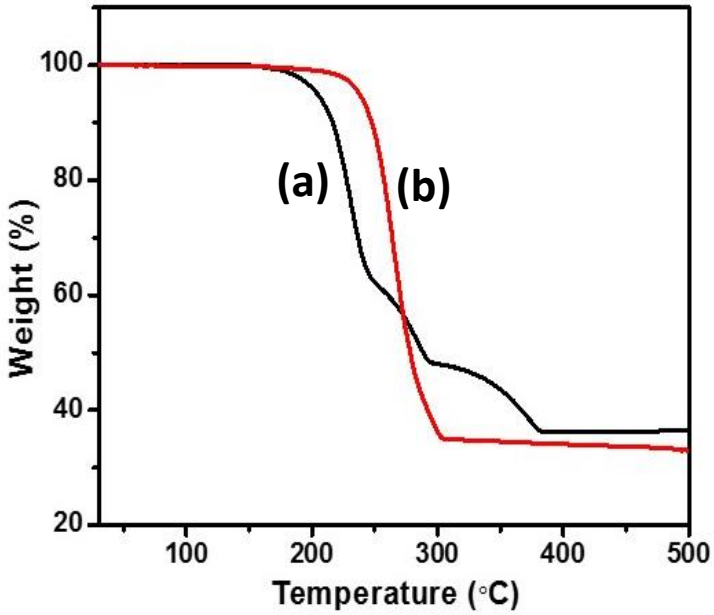

Figure 5.1. Thermogravimetric analysis of (a) complex 1 and (b) complex 2.

Chalcogenocarboxylate complexes of antimony were used for the synthesis of Sb_2Se_3, Sb_2S_3 and $Sb_2(S_{1-x}Se_x)_3$ solid solution, with controlled stoichiometry, in OLA by hot injection method at 200 °C under nitrogen. Although the decomposition temperature of both complexes, as determined by the TGA is above 300 °C, the primary amine, being a strong nucleophile, acts as catalyst and decomposes the complexes at even below 100 °C. Previously, thio- and selenobenzoate complexes were observed to decompose at room temperatures in the presence of coordinating ligands such as primary amines.[30-32] However, a temperature below 150 °C yields a product with poor crystallinity and the broadness in the diffraction pattern causes difficulty in accurate determination of the peak shift in the alloy system. Hence, 200 °C was used as the optimized temperature. The p-XRD patterns are shown in Figure 5.2. The diffraction pattern of Sb_2S_3 shows a good resemblance with the orthorhombic stibnite phase (ICDD# 01-075-1310), whereas the p-XRD of Sb_2Se_3 indicates the formation of the orthorhombic antimonselite phase (ICDD # 01-089-0821).

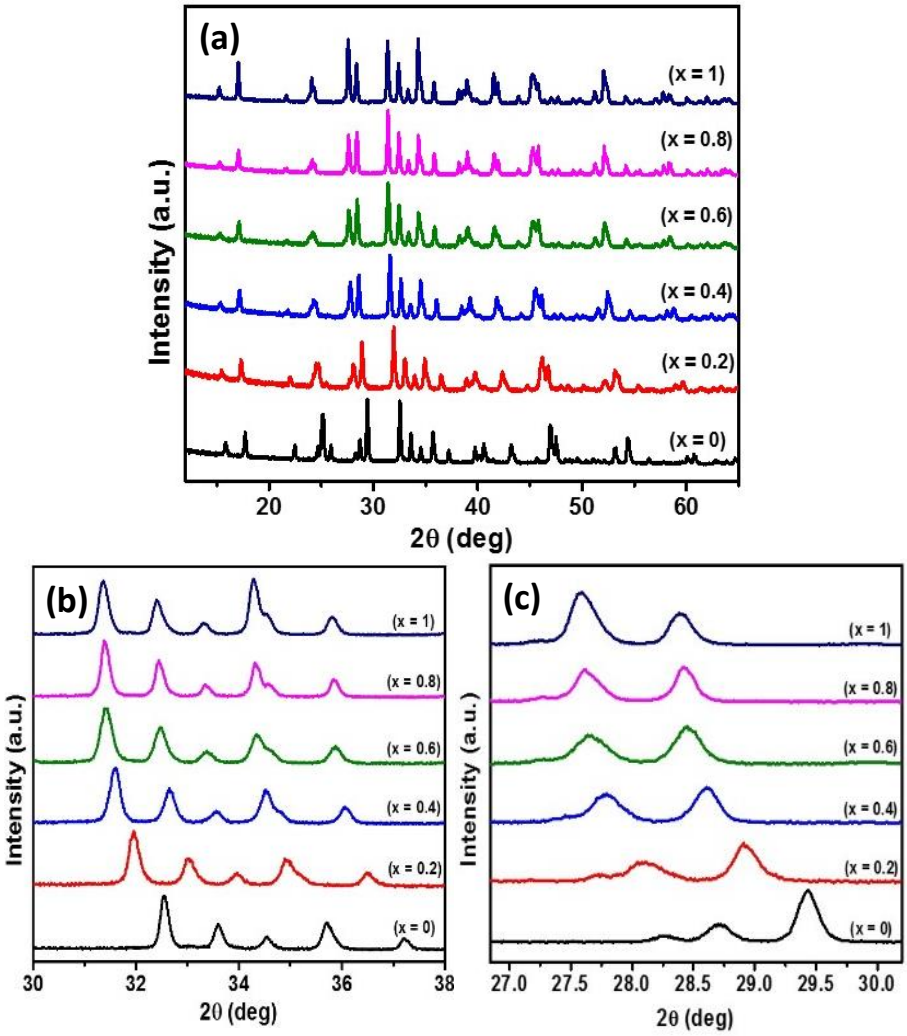

Figure 5.2. (a) p-XRD pattern of Sb_2S_3 (x = 0), $Sb_2(S_{1-x}Se_x)_3$ and Sb_2Se_3 (x = 1), (b) extended part of p-XRD to show the shift in the peaks. (c) Change in intensity of the peaks with substitution of sulfur by selenium.

The diffraction peaks for the solid solution, ordered with increasing selenium concentration from x = 0 to x = 1, were located in between the diffraction peaks of Sb_2S_3 and Sb_2Se_3. A gradual shift in the diffraction peaks was observed with change in composition. Furthermore, there is no indication of multiple sets of peaks, which shows the formation of a single phased solid solution. A shift in p-XRD was observed in accordance with the Vegard's law *i.e.* the lattice constant of alloy system varies linearly with gradual change in

composition. The shift was towards the lower theta value with increase in selenium content, which indicates an expansion of the lattice parameters with substitution of smaller sulfur atoms (1.84Å) by the larger selenium atoms (1.98Å). The unit cells of both stibnite and antimonselite is shown in Figure 5.3 along with their bond distances, which indicates a similar crystal structure of both minerals and slightly bigger size of antimonselite unit cell.

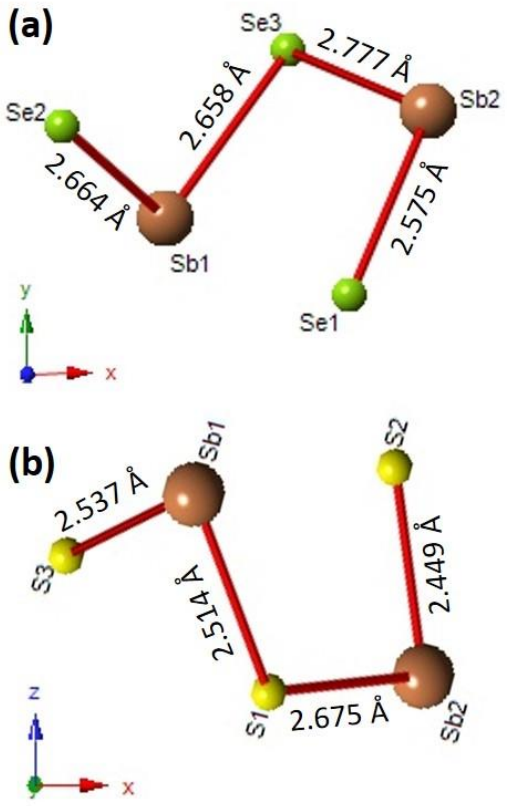

Figure 5.3. Unit cell of (a) antimonselite (ICDD # 01-089-0821) and (b) stibnite (ICDD# 01-075-1310) along with their bond distances.

The gradual change in the intensity of the peaks present at 2θ = 29.4° and 28.7° was also observed, along with the shift, upon selenium incorporation (Figure 5.2(c)). The intensity profile for both peaks were reversed, as the intensity of the

peak at 2θ = 29.4° was lowered, whereas the intensity for peak at 2θ = 28.7° enhances progressively, in moving from Sb_2S_3 to Sb_2Se_3.

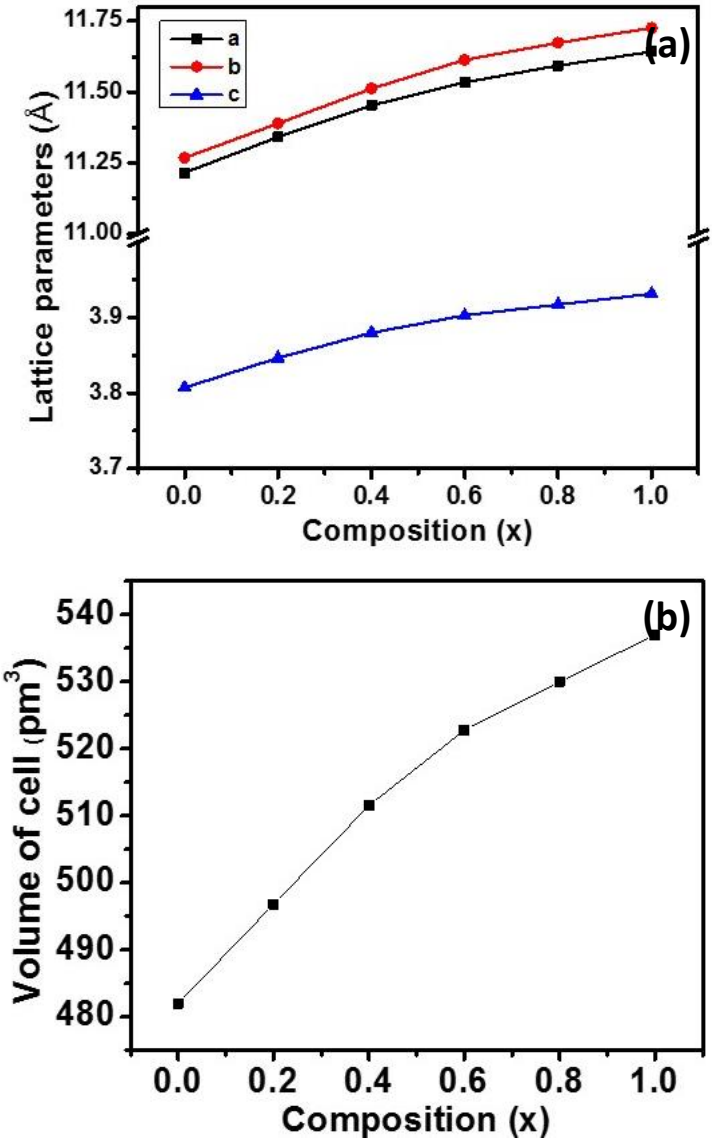

Figure 5.4. (a) Lattice constants a, b, and c derived from p-XRD diffraction peaks, and (b) shows change in volume of the cell plotted as functions of Se concentration 'x' in the $Sb_2(S_{1-x}Se_x)_3$ alloy system.

The experimentally determined lattice parameters confirm the expansion of the cell and the values of lattice constants a, b and c show a near-linear relationship between composition and lattice spacing (Figure 5.4). The composition dependant variation was

observed in all lattice constants, which indicate that there was no preferential substitution of selenium in any particular direction. The volume of the cell changes monotonously from 484 to 538 $Å^3$ on replacement of sulfur by selenium.

The chemical composition of the synthesized nanomaterials were analysed by EDX spectroscopy. The quantitative elemental analysis indicates the sequential increase in selenium concentration with decrease in sulfur content by changing the Se/(Se+S) composition between x = 0 to 1 (Figure 5.5). The analysis was carried out at three arbitrary points and averaged out to obtain the final results, listed in Table 5.1. A linear trend between selenium and sulfur was obtained, whereas the percentage of antimony almost remains the same except at 40 and 60 percent, where a slight deficiency of antimony was observed.

Table 5.1. Summary of the required composition of the elements and composition observed by EDX analysis.

Composition [Se]/[Se]+[S]	**Target composition**	**Required Stoichiometry**	**EDX Sb:S:Se**	**Alloy stoichiometry**
0 (Sb_2S_3)	Sb_2S_3	40:60	40.6:59.4	$Sb_{2.03}S_{2.97}$
0.2	$Sb_2S_{2.4}Se_{0.6}$	40:48:12	40.8:46.6:12.4	$Sb_{2.04}S_{2.30}Se_{0.66}$
0.4	$Sb_2S_{1.8}Se_{1.2}$	40:36:24	38.4: 38.2:23.4	$Sb_{1.92}S_{1.90}Se_{1.18}$
0.6	$Sb_2S_{1.2}Se_{1.8}$	40:24:36	37.4:25.2:37.4	$Sb_{1.87}S_{1.26}Se_{1.87}$
0.8	$Sb_2S_{0.6}Se_{2.4}$	40:12:48	40.4:12.3:47.2	$Sb_{2.02}S_{0.62}Se_{2.36}$
1 (Sb_2Se_3)	Sb_2Se_3	40:60	40.4:59.6	$Sb_{2.02}Se_{2.98}$

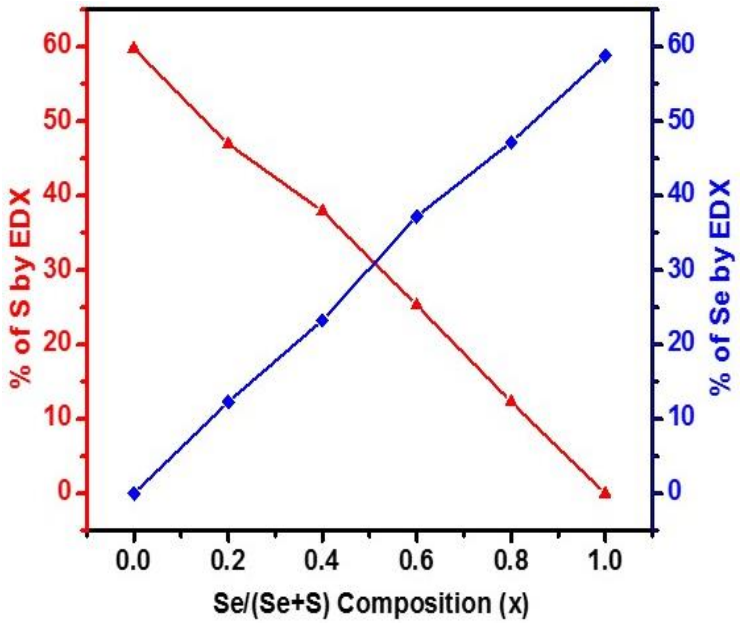

Figure 5.5. Plot showing change in concentration of selenium and sulfur content against Se/(Se+S) composition.

The homogeneity of the elements in the synthesized nanocrystals was observed by EDX elemental mapping, and the analysis validates an even distribution of antimony, sulfur and selenium (Figure 5.6) throughout the nanocrystals, which further confirms the absence of separate phases.

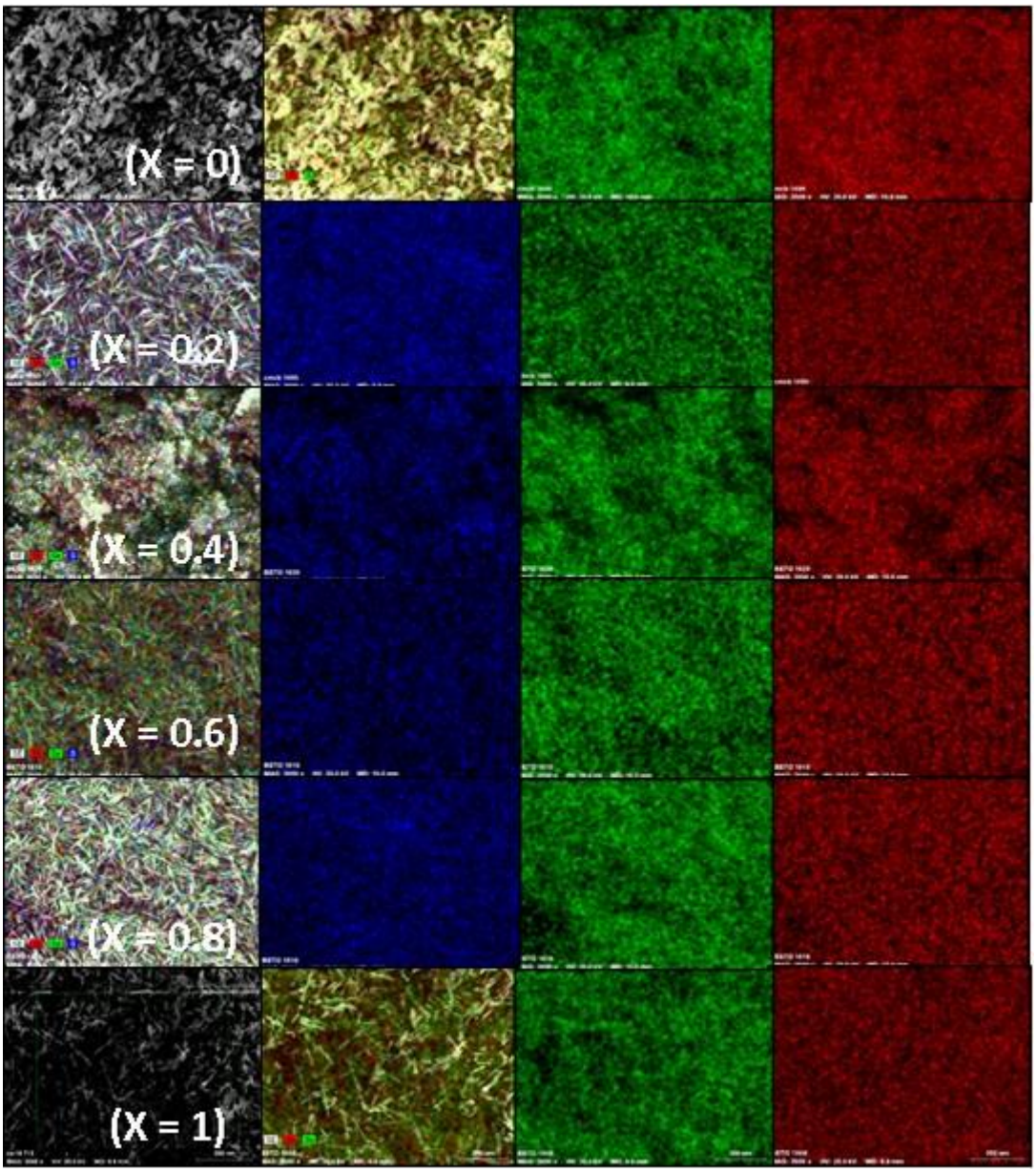

Figure 5.6. Elemental mapping of samples with different selenium concentration, showing uniform distribution of antimony, sulfur and selenium.

The morphology of $Sb_2(S_{1-x}Se_x)_3$ system was observed by SEM analysis (Figure 5.7), marked with different selenium concentration from x = 0 to 1. Sb_2S_3 shows nanopeg-like structure (Figure 5.7(a)), the alloy nanorods indicate fractal splitting and attachment of nanorods by oriented attachment (Figure 5.7(b-e)). The morphology of

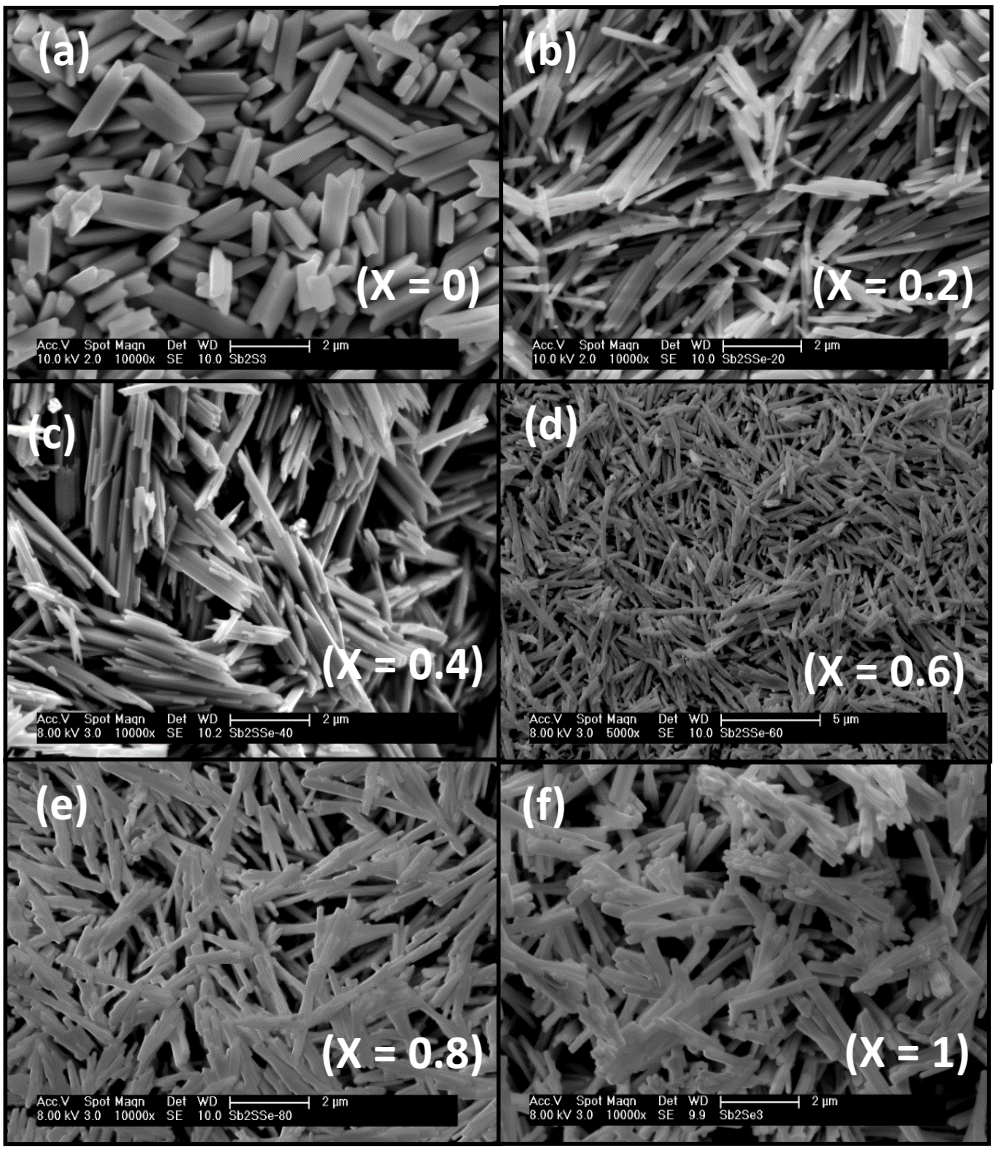

Figure 5.7. Sem images of (a) Sb_2S_3, (b-e) $Sb_2(S_{1-x}Se_x)_3$ and (f) Sb_2Se_3 nanorods synthesized by hot injection method.

the Sb_2Se_3 consists of a bunch of nanorods that grow from one center developing into a broom like architecture (Figure 5.7(f)).

Apart from crystal splitting, as further confirmed by TEM analysis (Figure 5.8), all the samples generally showed a rod-like morphology. Sb_2S_3 and Sb_2Se_3 are both isostructural and the growth of 1-dimensional nanorods can be explained on the basis of orientation and anisotropic nature of their building blocks. The crystal structure of Sb_2S_3 is composed of $(Sb_4S_6)_n$ chain fragments with two types of Sb and three types of S

atoms arranged parallel to the c-axis. Within the fragments, the atoms are connected with strong covalent bonds, making infinite long chains. However, one of the sulfur atom is weakly connected to the antimony metal of the second chain, placed in parallel direction, by Vander Waals forces of attraction, and the weak interconnection between infinite chains lead to the generation of a three dimensional orthorhombic structure. The rupture of the vander Waals bond is responsible for crystal cleavage, thus separating the infinite long chains leading to the formation of 1-dimensional nano-structures.

The splitting ability of the minerals depend on their crystal structure. Antimony chalcogenides show strong splitting ability, attributed to the crystalline chain-like structure, as reported previously.[33-36] The splitting is related to the rapid crystal formation, whereas the growth of nanoparticles generally consists of initial growth of nuclei at supersaturation point and later subsequent growth of the nuclei. At elevated temperature, the rate of generation of nuclei enhances considerably, the primary particles may undergo crystallization. The initially formed particles may grow via oriented attachment mechanism, however, due to the quick growth rate, the primary particles may not be able to align themselves properly therefore causing misorientations and the crystal grows by perfect/imperfect oriented attachment mechanism.[37]

Alivisatos *et al.*[38] reported that the splitting is also favourable in the presence of capping agents with strong surface stabilizing ability. As new surface area is generated with the splitting of crystals and the balance of surface energies by stabilizing agents can dictate a particular crystal size. The crystal splitting is then favourable due to the stabilization offered by strong adhesion of capping agent with the newly formed energetic surfaces. OLA is a strong coordinating agent and also facilitates the decomposition of the precursors, hence based on above discussion, splitting can be explained in context of quick growth rate, imperfect oriented attachment and surface stabilization of nanoparticles by OLA.

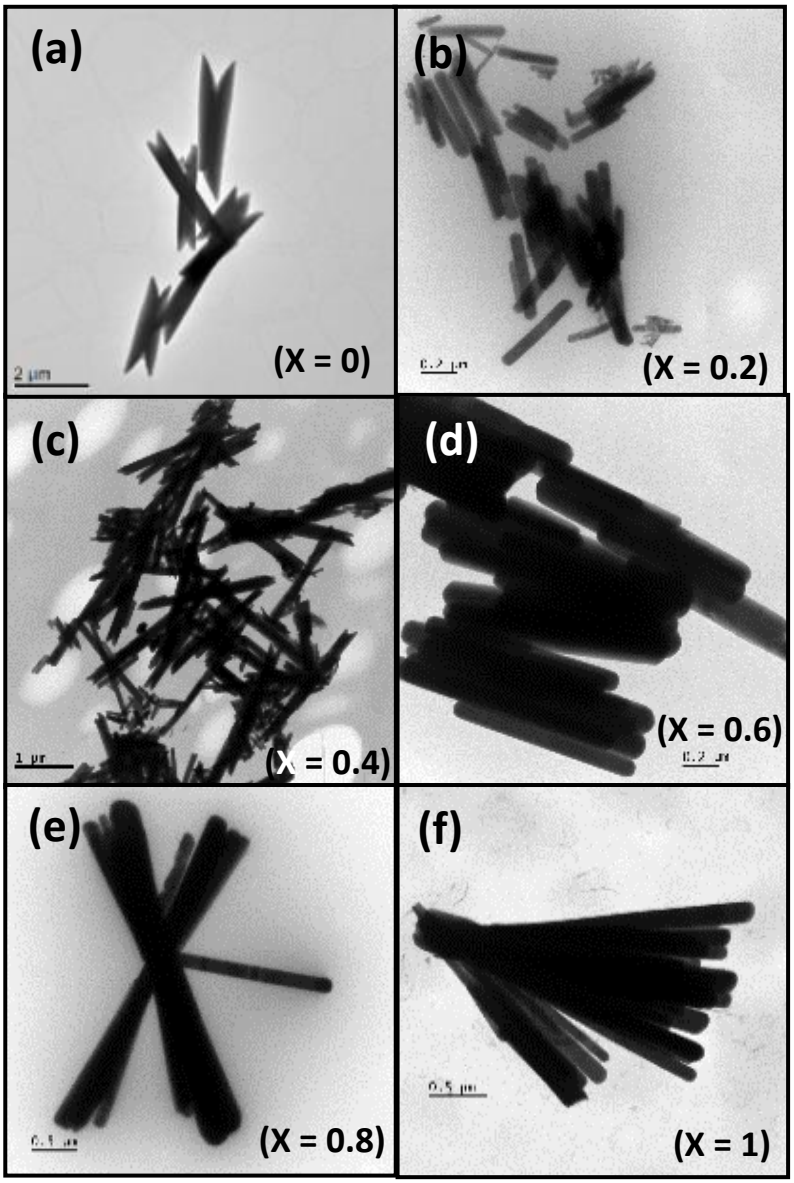

Figure 5.8. TEM images of (a) Sb_2S_3, (b-e) $Sb_2(S_{1-x}Se_x)_3$ and (f) Sb_2Se_3 nanorods indicating crystal splitting and rod-like morphology.

Raman spectroscopy was performed on synthesized nanomaterials using a 514 nm laser excitation at 25 % power, and the peaks for both Sb_2S3 and Sb_2Se_3 matches well with earlier reports. The vibrational modes (118 cm^{-1}, 188 cm^{-1} and 252 cm^{-1}) were present in all the samples which shows that the basic lattice structure was similar in synthesized nanomaterials (Figure 5.9). However, a substantial change was indicated in the relative intensities of the bands in moving from Sb_2S_3 to Sb_2Se_3. The most intense peak for Sb_2S_3 was observed at ≈ 252 cm^{-1} whereas with increase in selenium mole

fraction the intensity for this peak decreases and intensity of the peak at ≈ 188 cm^{-1} starts increasing, which eventually becomes the peak with highest intensity for Sb_2Se_3. Similarly, the peak at ≈ 147 cm^{-1} observed for Sb_2S_3 vanishes with addition of selenium, instead a new shoulder peak appears at ≈ 208 cm^{-1}. The bands were broad which may indicate presence of stress or structural defects in scattering volume.

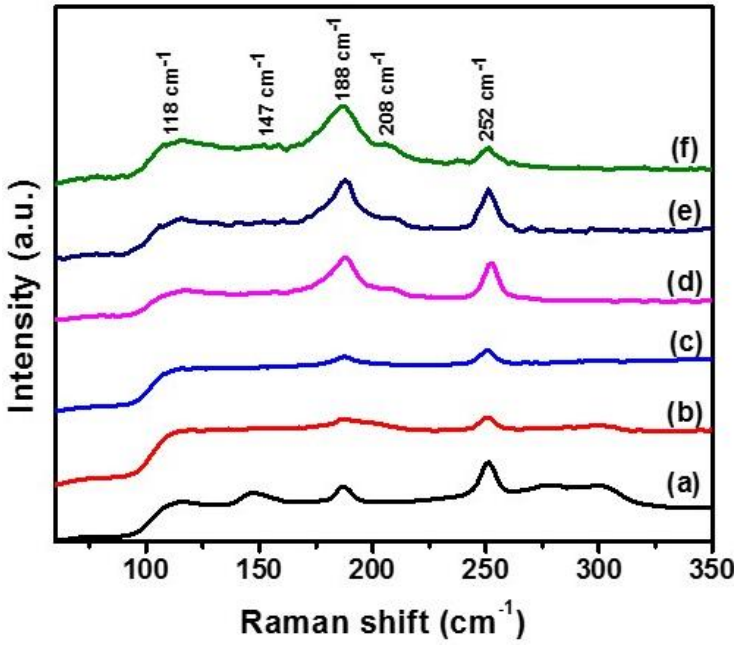

Figure 5.9. Raman spectra for (a) Sb_2S_3, (b-e) $Sb_2(S_{1-x}Se_x)_3$ and (f) Sb_2Se_3 nanorods.

The optical characterization of the binary and ternary alloy nanomaterials were carried out by UV-Vis-NIR spectroscopy (Figure 5.10). A uniform dispersion of the nanomaterials in acetone was obtained by sonication for half an hour. It was observed that the absorption spectrum shows a blue shift in moving from Sb_2Se_3 to Sb_2S_3, depending on the stoichiometry of the material.

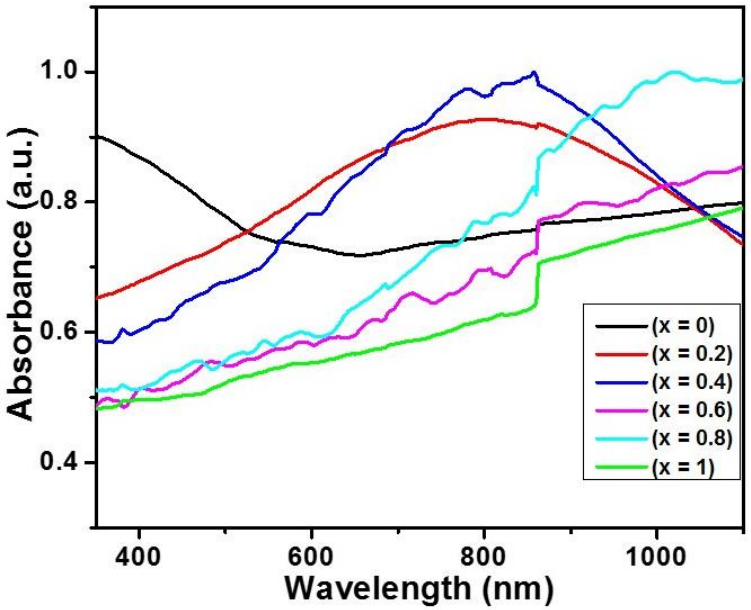

Figure 5.10. UV-Vis-NIR spectroscopic analysis of the binary and ternary nanomaterials with different stoichiometry of $Sb_2(S_{1-x}Se_x)_3$ (where $0 \leq x \leq 1$), indicating shift in absorption peaks.

As expected, the calculated band gap of the nanomaterials indicate a change with respect to change in the value of X (Figure 5.11). The band gap of antimony sulfide is higher than that of the antimony selenide, as the selenium was added the band gap was decreased. The band gap for ternary alloy nanomaterials lies in between band gap of both binary compounds. The dependence of the energy band gap and composition of the nanomaterials can be elucidated by plotting a graph between them. With a gradual change in lattice constant, a steady change in the band gap can be seen clearly. An almost linear trend was observed, with a slight deviation attributed to either morphology or stoichiometric variations.

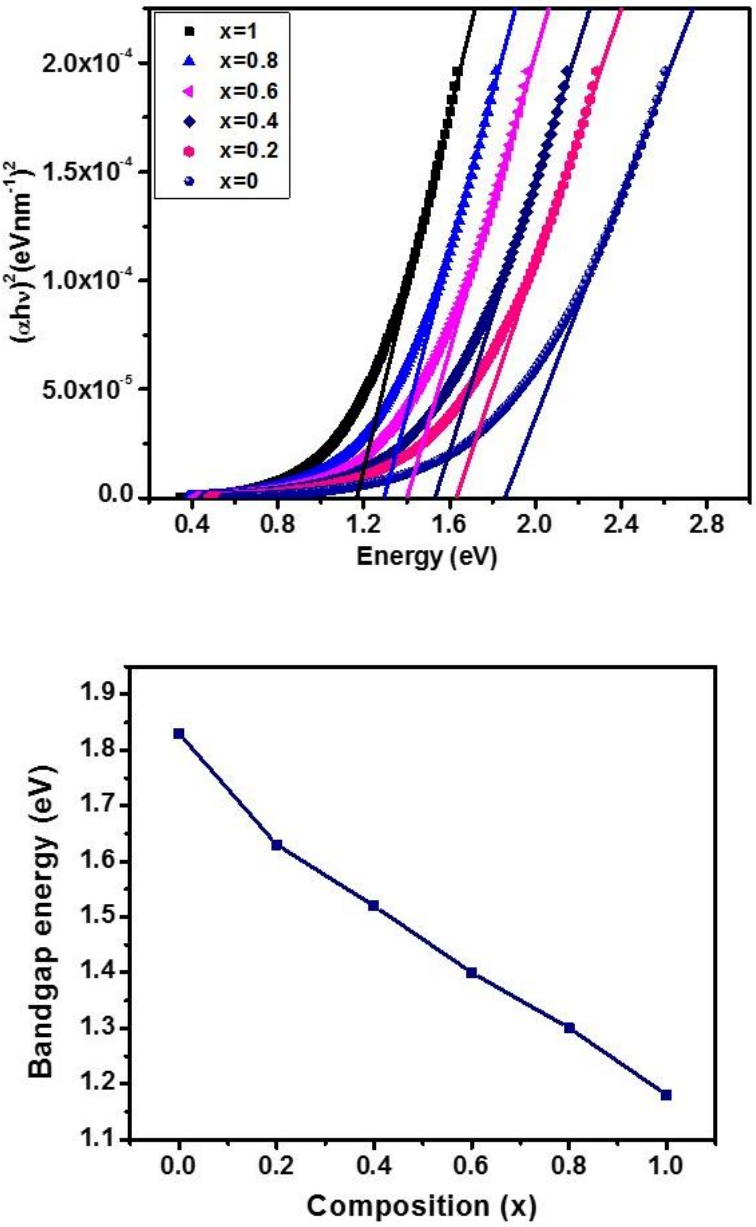

Figure 5.11. The plots between *(αhν)²* and photon energy to determine the band gap of the alloy system and plot between the band gap and selenium concentration of the $Sb_2(S_{1-x}Se_x)_3$ (where $0 \leq x \leq 1$) alloy nanomaterials.

5.5. Conclusion

Chalcogeno carboxylic acid complexes of antimony have been prepared by a facile method and used successfully for the preparation of $Sb_2(S_{1-x}Se_x)_3$ (where $0 \leq x \leq 1$) solid solution with varying stoichiometries between end members. The complexes decompose easily in the presence of oleylamine, at temperature as below as 100 °C, but yields product with low crystallinity. The shift in lattice parameters was calculated, which confirms the incorporation of Se in the crystal lattice. The morphology was also observed to vary along with change in composition and almost all samples show crystal splitting. The raman spectra indicate that the basis lattice structure was retained in all the samples, however the intensity profile was changed in moving from Sb_2S_3 to Sb_2Se_3. The optical studies showed a shift in the band gap and found to be vary as function of Se concentration. The use of molecular precursors not only provide precise control over stoichiometry but also reduces the problem of the composition variation from batch to batch by using dual source route.

5.6. References

1. M. R. Filip, C. E. Patrick and F. Giustino, *Physical Review B*, 2013, **87**, 205125.
2. Y. Zhou, M. Leng, Z. Xia, J. Zhong, H. Song, X. Liu, B. Yang, J. Zhang, J. Chen and K. Zhou, *Advanced Energy Materials*, 2014, **4**.
3. X. Liu, J. Chen, M. Luo, M. Leng, Z. Xia, Y. Zhou, S. Qin, D.-J. Xue, L. Lv and H. Huang, *ACS Applied Materials & Interfaces*, 2014, **6**, 10687-10695.
4. M. Leng, M. Luo, C. Chen, S. Qin, J. Chen, J. Zhong and J. Tang, *Applied Physics Letters*, 2014, **105**, 083905.
5. Y. Zhou, L. Wang, S. Chen, S. Qin, X. Liu, J. Chen, D.-J. Xue, M. Luo, Y. Cao and Y. Cheng, *Nature Photonics*, 2015, **9**, 409-415.
6. B. Sankapal and C. Lokhande, *Solar Energy Materials and Solar Cells*, 2001, **69**, 43-52.
7. I. Lefebvre, M. Szymanski, J. Olivier-Fourcade and J. Jumas, *Physical Review B*, 1998, **58**, 1896.
8. M. A. Franzman, C. W. Schlenker, M. E. Thompson and R. L. Brutchey, *Journal of the American Chemical Society*, 2010, **132**, 4060-4061.
9. W. J. Baumgardner, J. J. Choi, Y.-F. Lim and T. Hanrath, *Journal of the American Chemical Society*, 2010, **132**, 9519-9521.
10. R. Jin, Z. Liu, L. Yang, J. Liu, Y. Xu and G. Li, *Journal of Alloys and Compounds*, 2013, **579**, 209-217.
11. Y. Li, Y. Zhou, J. Luo, W. Chen, B. Yang, X. Wen, S. Lu, C. Chen, K. Zeng and H. Song, *RSC Advances*, 2016, **6**, 87288-87293.
12. S. Dey, S. Chen, S. Thota, M. R. Shakil, S. L. Suib and J. Zhao, *The Journal of Physical Chemistry C*, 2016, **120**, 20547-20554.
13. L. A. Swafford, L. A. Weigand, M. J. Bowers II, J. R. McBride, J. L. Rapaport, T. L. Watt, S. K. Dixit, L. C. Feldman and S. J. Rosenthal, *Journal of the American Chemical Society*, 2006, **128**, 12299-12306.
14. J. P. Zimmer, S.-W. Kim, S. Ohnishi, E. Tanaka, J. V. Frangioni and M. G. Bawendi, *Journal of the American Chemical Society*, 2006, **128**, 2526-2527.
15. R. E. Bailey and S. Nie, *Journal of the American Chemical Society*, 2003, **125**, 7100-7106.

16. M. D. Regulacio and M.-Y. Han, *Accounts of Chemical Research*, 2010, **43**, 621-630.
17. N. Tideswell, F. Kruse and J. McCullough, *Acta Crystallographica*, 1957, **10**, 99-102.
18. G. Voutsas, A. Papazoglou, P. Rentzeperis and D. Siapkas, *Zeitschrift für Kristallographie-Crystalline Materials*, 1985, **171**, 261-268.
19. E. El-Sayad, *Journal of Non-Crystalline Solids*, 2008, **354**, 3806-3811.
20. B. Yang, S. Qin, D. j. Xue, C. Chen, Y. s. He, D. Niu, H. Huang and J. Tang, *Progress in Photovoltaics: Research and Applications*, 2017, **25**, 113-122.
21. B. Yang, D.-J. Xue, M. Leng, J. Zhong, L. Wang, H. Song, Y. Zhou and J. Tang, *Scientific Reports*, 2015, **5**.
22. A. Hernández-Granados, J. Escorcia-García, D. Peréz-Martínez, J. García-Cerrillo, C. Menchaca-Campos and H. Hu, *Materials Science in Semiconductor Processing*, 2016, **56**, 222-227.
23. Y. C. Choi, Y. H. Lee, S. H. Im, J. H. Noh, T. N. Mandal, W. S. Yang and S. I. Seok, *Advanced Energy Materials*, 2014, **4**.
24. Z. Deng, M. Mansuripur and A. J. Muscat, *Nano Letters*, 2009, **9**, 2015-2020.
25. C. Karthik, R. J. Mehta, W. Jiang, E. Castillo, T. Borca-Tasciuc and G. Ramanath, *Applied Physics Letters*, 2011, **99**, 103101.
26. R. J. Mehta, C. Karthik, W. Jiang, B. Singh, Y. Shi, R. W. Siegel, T. Borca-Tasciuc and G. Ramanath, *Nano Letters*, 2010, **10**, 4417-4422.
27. S. Heimann, W. Assenmacher, O. Prymak and S. Schulz, *European Journal of Inorganic Chemistry*, 2015, **2015**, 2407-2415.
28. U. Mizutani, *Hume-Rothery Rules for Structurally Complex Alloy Phases*, CRC Press, 2016.
29. H.-W. Chang, B. Sarkar and C. Liu, *Crystal Growth and Design*, 2007, **7**, 2691-2695.
30. M. T. Ng, C. Boothroyd and J. J. Vittal, *Chemical Communications*, 2005, 3820-3822.
31. W. P. Lim, C. T. Wong, S. L. Ang, H. Y. Low and W. S. Chin, *Chemistry of Materials*, 2006, **18**, 6170-6177.

32. W. P. Lim, Z. Zhang, H. Y. Low and W. S. Chin, *Angewandte Chemie International Edition*, 2004, **43**, 5685-5689.
33. H. Wang, J.-M. Zhu, J.-J. Zhu, L.-M. Yuan and H.-Y. Chen, *Langmuir*, 2003, **19**, 10993-10996.
34. G.-Y. Chen, B. Dneg, G.-B. Cai, T.-K. Zhang, W.-F. Dong, W.-X. Zhang and A.-W. Xu, *The Journal of Physical Chemistry C*, 2008, **112**, 672-679.
35. P. Roy, S. K. Srivastava, B. B. Nayak and A. K. Saxena, *Crystal Growth and Design*, 2008, **8**, 2019-2023.
36. C. Pilapong, T. Thongtem and S. Thongtem, *Journal of Alloys and Compounds*, 2010, **507**, L38-L42.
37. Q. Lu, H. Zeng, Z. Wang, X. Cao and L. Zhang, *Nanotechnology*, 2006, **17**, 2098.
38. J. Tang and A. P. Alivisatos, *Nano letters*, 2006, **6**, 2701-2706.

Chapter # 6

Synthesis of $SnS_{1-x}Se_x$ solid solution from single source precursors by colloidal and solvent-less route

6.1. Introduction

Dimensionality is one of the key parameters in determining the properties of nanomaterials. A material can exhibit completely different reactivity and/or properties based on the directional arrangements of the crystal structure *i.e.* 1D, 2D or 3D structures.[1-3] Nanostructured layered materials are 2-dimensional materials with interesting mechanical, catalytic and electronic properties.[4-7] Besides graphene, a number of metal chalcogenide layered materials have gained immense attention due to the flexibility of variety in the nature of metals and their oxidation states.[7-10] Depending upon the kind of metal and its oxidation state, a layered material can exist in different polymorphic geometries, such as octahedral, trigonal prismatic, rhombohedral and orthorhombic (also considered as the distorted rock salt structure) crystal lattices.[11, 12]

Tin chalcogenides belong to the IV-VI class of the semiconductors and exists in either the MX (+2 oxidation) or MX_2 (+4 oxidation) form. However, tin(II) chalcogenides have attracted considerable interest due to their suitable band gaps and intense absorption in the electromagnetic spectrum, which makes them suitable candidates for photovoltaic and optoelectronic applications.[13, 14] Moreover, they have low toxicity, are relatively earth abundant and cost effective materials. Hence, tin chalcogenides are highly desirable as thin films, nanocrystals and alloys with controllable morphology, size and composition for tunable electronic properties.[15, 16]

SnS and SnSe are both isostructural and exist in the orthorhombic structure, each unit cell consists of eight atoms.[17] SnSe has both direct and indirect band gaps of around 0.9 eV and 1.3 eV respectively.[18] SnSe has been used in solar cells, memory switching and as anode material.[19-21] Similarly, SnS is also a promising solar material with an absorption coefficient of the order 10^4-10^5 and its band gap commensurate to that of silicon.[22] Due to the identical crystal structure of both the materials, a solid solution over the entire range is also known.

$SnS_{1-x}Se_x$ alloy thin films were deposited by the electrodeposition method, where sodium thiosulfate ($Na_2S_2O_3$) was used as the sulfur source and selenium dioxide (SeO_2) for the selenium source along with stannous chloride ($SnCl_2$).[16, 23, 24] The effect of the different parameters, such as, potential, deposition time and composition on the electronic properties of the solid solution were studied. Another common method to prepare solid solutions is solid state synthesis, whereby the elements are mixed in stoichiometric quantities and heated at high temperature for prolonged time.[15, 25-27] The resulting alloy solid solution was used as electrodes for lithium/sodium based batteries, where significant enhancement was observed in the thermoelectric performance. The band gap was also tuned by changing the S:Se ratio. However, the solid state method has inherent problems as the process is laborious, inefficient in terms of energy and also not suitable when one of the component is volatile than others, which eventually leads to the formation of a non- stoichiometric product.

The gas phase laser photolysis method was also used for the composition tuned synthesis of $SnS_{1-x}Se_x$ alloy.[28] Although, a facile control on phase and composition was achieved, the method requires the use of highly toxic H_2S and dimethyl selenium. Single source precursors often provide better control over phase and stoichiometry. Unfortunately, the use of single source precursors for the synthesis of $SnS_{1-x}Se_x$ solid solution is not well explored, the only precursors used till now are benzyl substituted tin chalcogenides.[29, 30] Traces of elemental tin were also observed in the final product obtained by the decomposition of these precursors.

The use of suitable chalcogeno single source precursors for efficient and composition controlled synthesis of $SnS_{1-x}Se_x$ is required. Therefore organotin complexes of chelcogeno-carboxylic acid were synthesized and used to prepare $SnS_{1-x}Se_x$ alloy solid solutions by two different routes. The use of a similar type of single source precursors with different chalcogeno-congeners is highly feasible, as both may follow similar decomposition behaviour and/or intermediate steps during the reaction.

Herein, the synthesis of a $SnS_{1-x}Se_x$ solid solution in the entire range of composition, from chalcogeno- (thio/seleno) benzoate complexes of organotin by a colloidal hot injection method, using oleylamine (OLA) as capping agent, is described. For comparison, the solid solution was also synthesized by the solvent-less melt method, to observe the effect of capping agent on the synthesized alloyed materials.

6.2. Experimental

6.2.1. Materials

The reagents and solvents *i.e.* oleylamine (OLA), dibutyltindichloride, $NaBH_4$, KOH, elemental selenium, benzoyl chloride, thiobenzoic acid and ethanol were procured from Sigma Aldrich and were used as received.

6.2.2. Synthesis of *bis*(selenobenzoato)dibutyltin(IV) complex (1)

The synthesis of the complex has already been discussed in Chapter 4. Briefly, the ethanolic solution of $NaBH_4$ (12.0 mmol in 15.0 mL ethanol) was added into an ethanolic solution of metallic Se powder (0.5 g, 6.0 mmol) under inert conditions. The resultant reddish solution became colourless within 5 min of stirring. Benzoyl chloride (6.0 mmol) was then added into the freshly prepared NaHSe solution, which resulted in the formation of the seleno-benzoate ligand. The stirring was continued for further 15 min, after which Bu_2SnCl_2 (0.95 g, 3.0 mmol) in 15.0 mL ethanol was added dropwise. The oily product was separated and purified by $CHCl_3$ to afford the product. Elemental analysis cal. (%) for $C_{22}H_{28}O_2SnSe_2$: C 43.96, H 4.69, Sn 19.74; Found: C 44.22, H 4.74, Sn 19.45.

6.2.3. Synthesis of *bis*(thiobenzoato)dibutyltin(IV) complex (2)

Sodium salt of thiobenzoic acid was prepared by adding an ethanolic solution (25.0 mL) of KOH (0.85g, 15.0 mmol) in an ethanolic solution (25.0 mL) of thiobenzoic acid (2.1 g, 15.0 mmol) while stirring. The stirring was continued for 15 min. at room temperature, after which an ethanolic (20.0 mL) solution of Bu_2SnCl_2 (2.3 g, 7.5 mmol) was added dropwise under inert conditions. The reaction mixture was stirred for further

half an hour, to ensure completion of the reaction. Distilled water (50.0 mL) was added to the reaction mixture, and the solution became turbid with the formation of an oily product. The product was separated by the solvent extraction method using chloroform, magnesium sulfate was added in chloroform to remove water molecules. The chloroform solution was evaporated and an off-white precipitate appeared as product. Melting point 96-97 °C Elemental analysis cal. (%) for $C_{22}H_{28}O_2SnS_2$: C 52.04, H 5.56, Sn 23.4, S 12.62; Found: C 44.22, H 4.74, Sn 19.45.

6.2.4. Colloidal synthesis of ternary $SnS_{1-x}Se_x$ solid solution

The solid solution was synthesized by dispersing a mixture of complex **(1)** and **(2)** in appropriate molar compositions (Table 6.1) in OLA (2.0 mL) and injected into pre-heated OLA (8.0 mL) at 230 °C with continuous stirring, under nitrogen environment. The temperature was maintained for 30 min., after which the reaction mixture was removed from heating source for cooling. A mixture of acetone and methanol (1:1) was used for precipitation, and the synthesized material was washed and separated by centrifugation.

6.2.5. Solvent-less synthesis of ternary $SnS_{1-x}Se_x$ solid solution

In solvent-less method, the solid solution was prepared by thermal decomposition of the complexes **(1)** and **(2)**, mixed in required stoichiometric quantities (Table 6.1). For this purpose, both complexes were mixed together homogenously, and placed in a ceramic combustion boat. The boat, in a glass tube, was placed inside the carbolite tube furnace. The end of the tube was sealed and a vacuum was applied to remove air from the tube followed by filling of nitrogen gas. As complex **(1)** and **(2)** both have low melting points, the temperature was maintained at 100 °C for 10 min., to obtain a homogenized molten mixture of both complexes. Thereafter, the temperature was raised slowly to 330 °C and maintained for one hour under an inert atmosphere. After an hour, the heating was turned off and the combustion boat was allowed to cool naturally to room temperature. The tube was removed from the furnace and residue powder was collected for analysis.

6.3. Characterization

6.3.1. Elemental and Thermogravimetric analysis

Microanalysis was performed using a Thermo Scientific Flash 2000 Organic Elemental Analyzer. Thermogravimetric analyses were performed using a Mettler-Toledo TGA/DSC under nitrogen gas flow rate of 10 mL/min.

6.3.2. Powder X-ray diffraction

X-ray diffraction was performed using a Bruker D8 Discover Diffractometer using CuKα radiation (λ = 1.54178 Å), in a 2Θ range from 10^{o} to 70^{o}. The data collected was used to determine the lattice parameters and crystal phase.

6.3.3. Scanning electron microscopy (SEM) and Energy Dispersive X-ray (EDX) spectroscopy

Scanning electron microscopy (SEM) was carried out using a Philips XL30 FEG SEM. Energy-dispersive X-ray (EDX) spectroscopy was performed using a DX4 detector. All samples were carbon coated using an Edwards coating system E306A prior to SEM analysis.

6.4. Results and discussion

Amongst the metal complexes of chalcogeno carboxylic acids, considerable work has been done on the thio- analogues[31-33] but until the present very little work has been done on the complexes of heavier chalcogen congeners. The primary reason is the difficulty in the synthesis, the resulting acids are highly unstable.[34] In this study, a new and efficient route for the synthesis of metal selenobenzoate complexes and used it as suitable precursor for the synthesis of the respective metal selenide and alloy solid solution.

A solid solution can be generated by substitution of one or more components without destroying the crystal structure. However, slight distortions in the crystal lattice can be observed in the form of defects, which may arise due to the vacancies or stacking faults, subject to the reaction conditions.[35] The lattice parameters are affected by the type of the substituent used, leading to the

shrinkage or expansion of the cell. Generally for an alloy system, Vegard's law is expected to be obeyed.[35] The law emphasizes the fact that the sizes of the atoms, independent of the other parameters, have a marked effect on the crystal structure. A linear relationship between lattice constants-composition can be found in the alloys or solid solutions. The extent of solubility of a substituent component can be determined by Hume-Rothery rules,[36] which states that the formation of the solid solution is facilitated by (a) analogous electronegativity of solute and solvent (b) the difference in radii of solute and solvent must be less than 15 % (c) similar valency, and (d) identical crystal structures of solute and solvent for complete solubility. The chalcogenide atoms (sulfur and selenium), fulfil these requirements and favours the formation of alloys of the type $MS_{1-x}Se_x$. Hence, the thio/seleno-carboxylate complexes of the organotin were used to generate $SnS_{1-x}Se_x$ solid solution in the entire range.

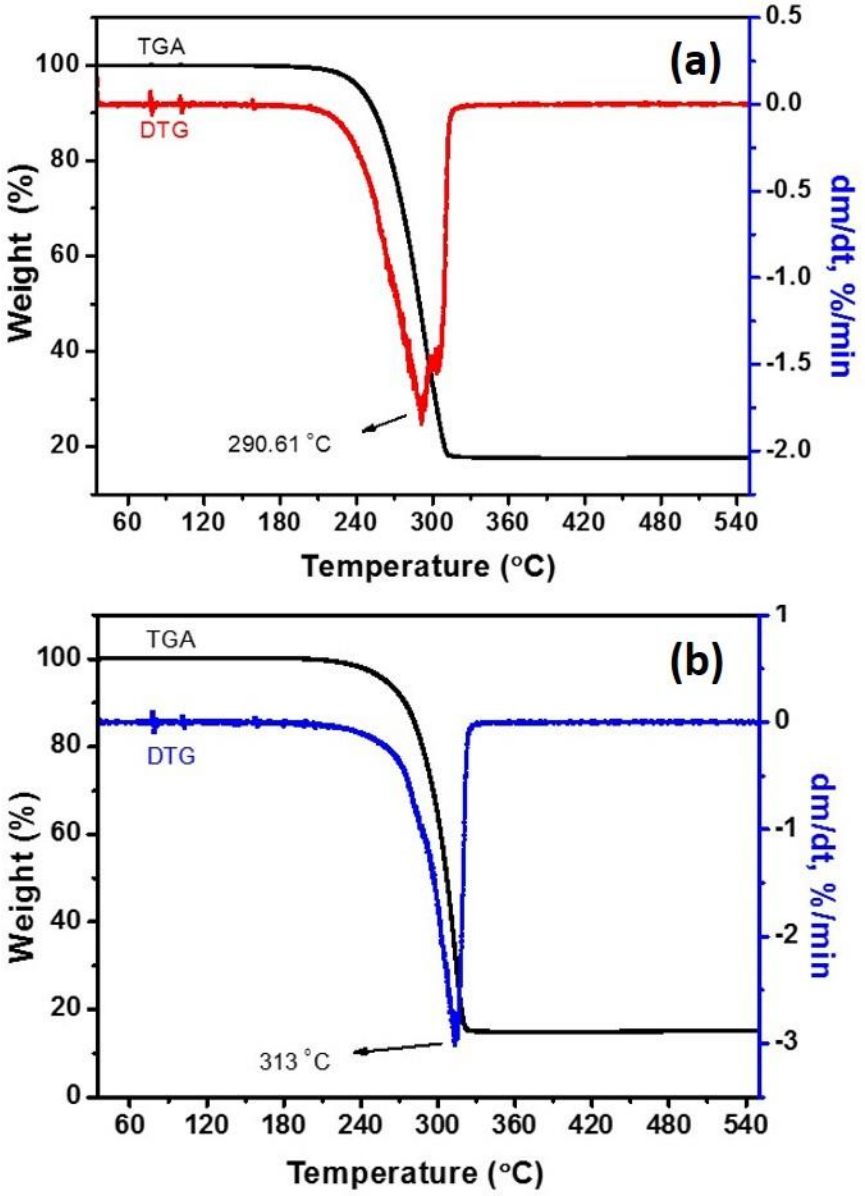

Figure 6.1. Overlapped thermogravimetric and differential thermogravimetric curves for (a) complex **(1)** and (b) complex **(2)**.

The thermal stability of both complexes was analysed by thermogravimetric analysis. The TGA curve for complex **(1)** shows decomposition in a single step (Figure 6.1(a)), and complete decomposition occurs around 310 °C.

However, the differential thermogravimetric analysis indicates that the maximum mass loss occurred at 290 °C, and a slight loss was indicated by a shoulder peak at 310 °C. Similarly, Figure 6.1(b) shows an overlapped TG/DTG curve for complex **(2)**, and a single step decomposition was observed by both TG and DTG analysis. The maximum weight loss was observed at 313 °C. The residual mass for both of the complexes was around 15 %, which is less than the expected masses required for SnSe (32.8 %) and SnS (29.7 &). The residual mass does not correspond to any other selenide or sulfide phase, elemental tin, sulfur, selenium or some oxide based product. It was observed that both organotin complexes were volatile and undergo sublimation during the thermogravimetric analysis. There are some previous reports on the sublimating nature of the organotin complexes.[9, 37] The mass loss during sublimation can prevent the accurate determination of the final residue, hence nature of residue cannot be determined simply on the basis of percentage mass left at the end.

The nature of the residue was observed by heating both complexes separately from room temperature to 500 °C in a tube furnace, under continuous nitrogen flow for one hour. After an hour, the heating was turned off and the furnace was allowed to cool to room temperature. The black residue obtained after cooling was collected and analysed by p-XRD. The analysis of residual powder obtained from decomposition of complex **(1)** shows formation of pure SnSe (Figure 6.2), whereas the decomposition product of complex **(2)** yields pure SnS (Figure 6.3).

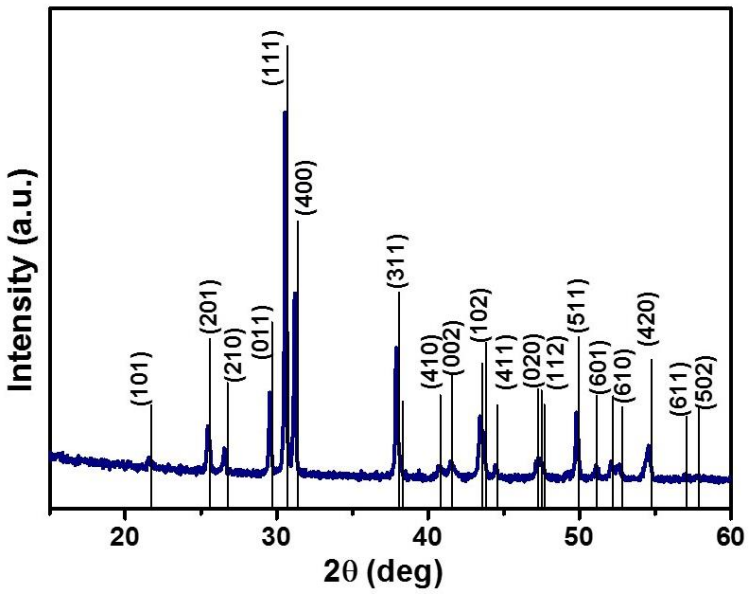

Figure 6.2. p-XRD of residue obtained by decomposition of complex **(1)** under nitrogen atmosphere showing formation of SnSe (ICDD # 00-014-0159).

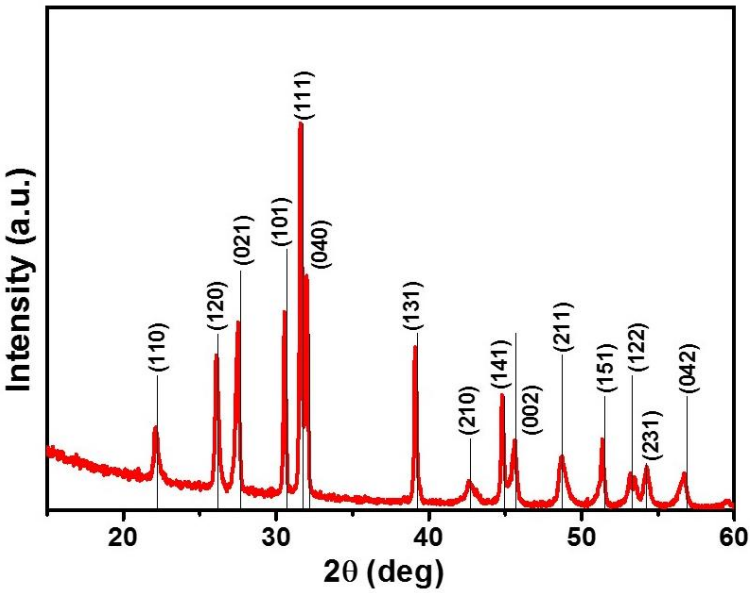

Figure 6.3. p-XRD of residue obtained by decomposition of complex **(2)** under nitrogen atmosphere showing formation of SnS (ICDD # 01-075-2115).

6.4.1. Colloidal synthesis of $SnS_{1-x}Se_x$ solid solution

Oleylamine (OLA) is a strong coordinating agent and often catalyses the breakdown of complexes at temperatures quite lower than their decomposition temperature as indicated by their TGA. During temperature optimization, it was observed that the complexes show no sign of decomposition below 190 °C, whereas at 200 °C, both complexes decompose partially and a little product was obtained. However, the complete decomposition of the complexes and product with good crystallinity and yield was obtained at 230 °C. This indicates high stability of both complexes as some other thio/seleno-benzoate complexes are reported to decompose immediately in the presence of a primary amine, even at room temperature.[32, 33, 38] Nevertheless, the degradation of both complexes below decomposition temperature, indicated by TGA shows the role of the OLA as catalyst and decomposition initiator. Hence, all reactions as part of the colloidal synthesis were performed at optimized temperature of 230 °C.

For colloidal synthesis of the solid solution, the chalcogenocarboxylate complexes of organotin, mixed in appropriate mole fractions, were dispersed in OLA and injected quickly into pre-heated OLA at 230 °C under nitrogen. The temperature decreased by almost 10 °C, but was maintained quickly. The reactions were continued for 30 min. after which washing and separation of the product was carried out for further analysis.

The p-XRD pattern of all the samples prepared by the colloidal synthesis is shown in Figure 6.4. The peaks were sharp for all the samples which confirms the crystalline nature of the product and it is also helpful to observe the shift in the peaks. The mole fraction (x = 0) represents the p-XRD pattern of SnS (ICDD # 01-075-2115) and (x = 1) shows diffraction pattern of SnSe (ICDD # 00-014-0159) and both matches well with the standard pattern. It was interesting to note that, in the starting material the Sn atom is in +4 oxidation state but both of the complexes yielded tin monochalcogenide as the main product. It is probably due

to the reductive nature of the OLA that Sn^{+4} was reduced to the Sn^{+2} state during the reaction.[39]

The diffraction peaks for $SnS_{1-x}Se_x$ solid solution lies intermediate of the diffraction peaks of SnS and SnSe. The peaks show a gradual shift with the change in the ratio of mole fraction. There was no indication of phase separation or multiple sets of peaks, only a single phased diffraction pattern was observed, which confirms the formation of the solid solution. The shift in the peaks is in agreement with Vegard's law *i.e.* change in *d*-spacing with change in the composition. The peaks shifted towards the lower theta value with increase in selenium content, due to an expansion of the lattice parameters with substitution of smaller sulfur atoms (1.84Å) by the larger selenium atoms (1.98Å).

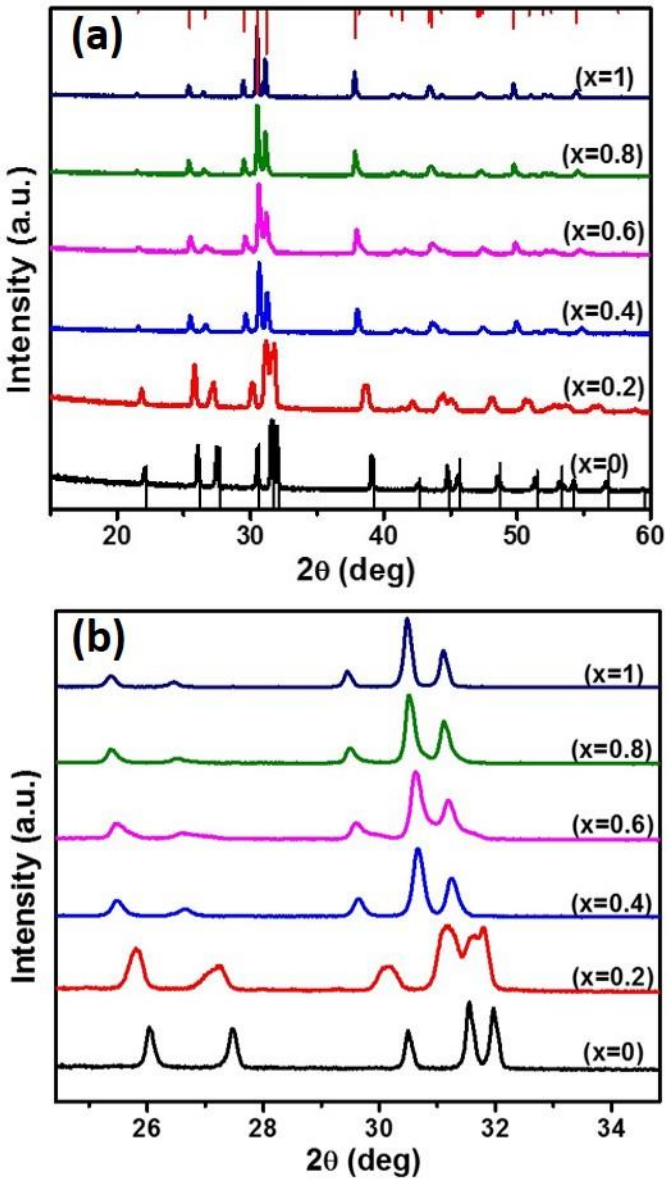

Figure 6.4. (a) p-XRD pattern of SnS (x = 0), $SnS_{1-x}Se_x$ and SnSe (x = 0) synthesized in OLA at 200 °C (b) extended part of the p-XRD to show the shift in the peaks.

The unit cells of both orthorhombic SnS and SnSe are shown in Figure 6.5 along with their bond distances and Van der Waal's interactions. The crystal structure of both materials is similar and the slightly bigger size of the selenium atom is responsible for expansion (≈2.5 %) of the SnSe unit cell.

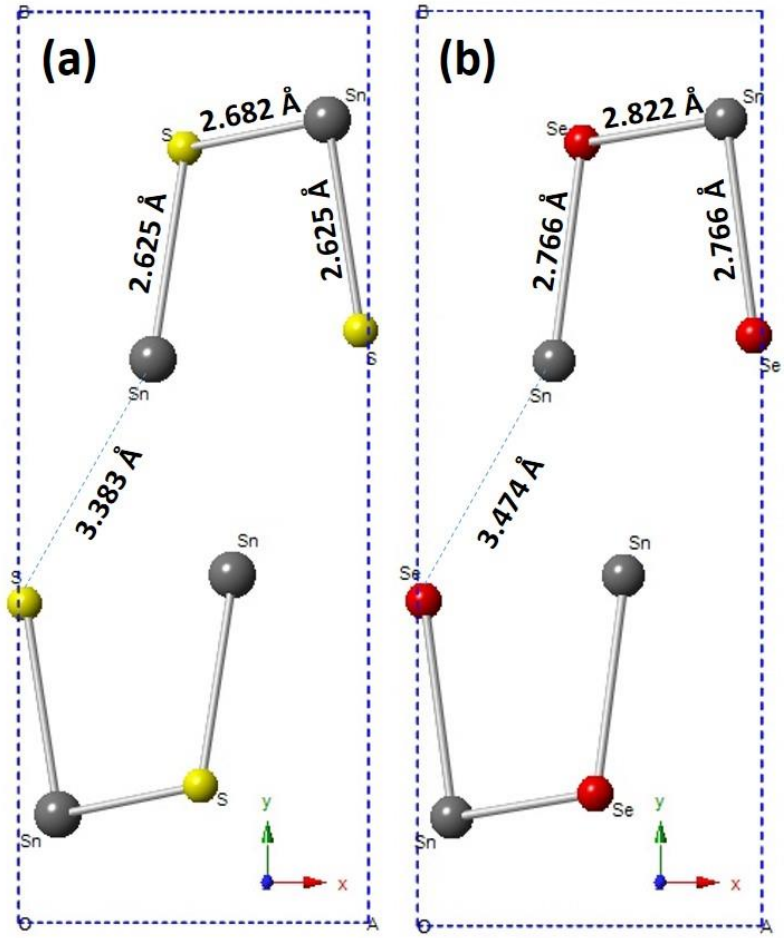

Figure 6.5. Unit cell of (a) SnS (ICDD # 01-089-0821) and (b) SnSe (ICDD# 01-075-1310) along with their bonds and Vander Waal's distances.

The change in bond lengths accounts for the gradual shift in p-XRD peaks. A change in the intensity of the peaks present at 2Θ = 27.47° and 26.03° was also observed, upon selenium incorporation (Figure 6.4). The intensity of both peaks decreases with increase in selenium mole fraction. Similarly, the intensity of peaks at 2Θ = 30.49°, 31.54° and 31.96° also changes, along with the shift to lower angle, in moving from SnS to SnSe. The intensity of the middle peak increases while the other two decreases in intensity.

The lattice parameters were calculated using p-XRD data which further confirms the expansion of the cell and the values of the lattice constants a, b and

c show a near-linear relationship between composition and the lattice spacing (Figure 6.6). The composition dependant variation was observed in all lattice constants, which indicate that there was no preferential substitution of selenium in any particular direction. The volume of the cell changes from 192.8 to 211.9 $Å^3$ on replacement of sulfur by selenium (Figure 6.7). However, the change in the volume was not very smooth and a sudden increase in size was observed in the start at the mole fraction value of x = 0.2 and x = 0.4 and little increase at later concentrations.

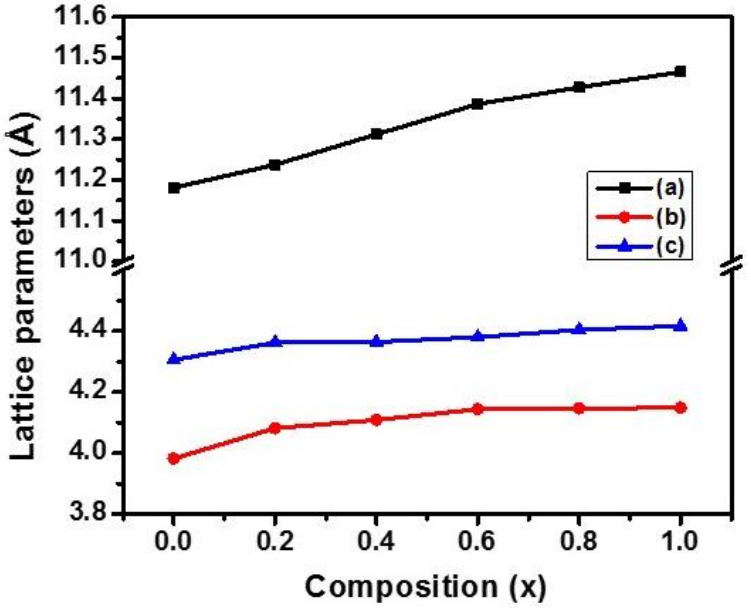

Figure 6.6. Lattice constants a, b, and c derived from p-XRD diffraction peaks, as a function of Se concentration 'x' in the OLA capped $SnS_{1-x}Se_x$ alloy system.

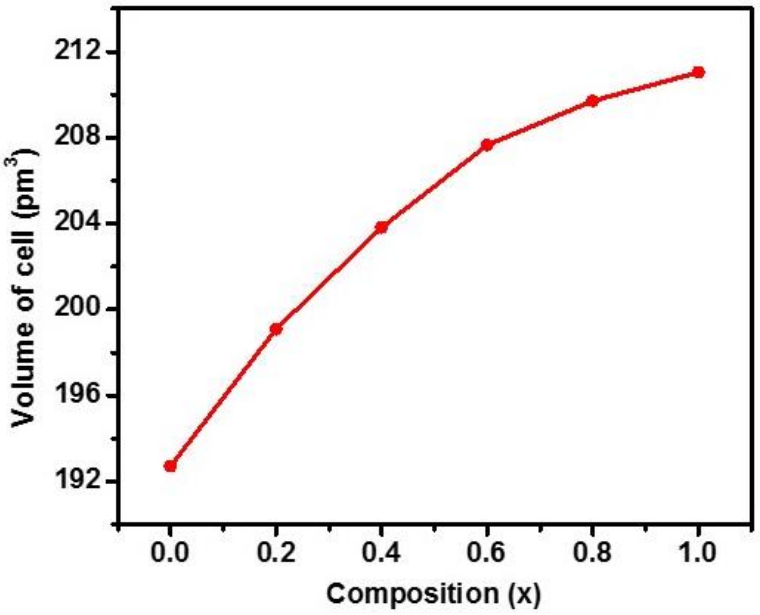

Figure 6.7. The change in the volume of the cell, as a function of Se concentration 'x' in the OLA capped $SnS_{1-x}Se_x$ alloy system.

The percentage of the elements present in the synthesized solid solution was determined by EDX spectroscopy (Figure 6.8). The qualitative analysis indicates presence of only desired elements *i.e.* Sn, S and/or Se, whereas the quantitative analysis shows a successive increase in selenium concentration with successive decrease in sulfur content by changing the Se/(Se+S) composition between x = 0 to 1 (Figure 6.9). The analysis was carried out at three arbitrary points and averaged out to obtain the final results, as listed in Table 6.1. A linear trend between selenium and sulfur was obtained, whereas the percentage of tin almost always remains the same. The stoichiometry of the alloy was found to be very close to the expected value.

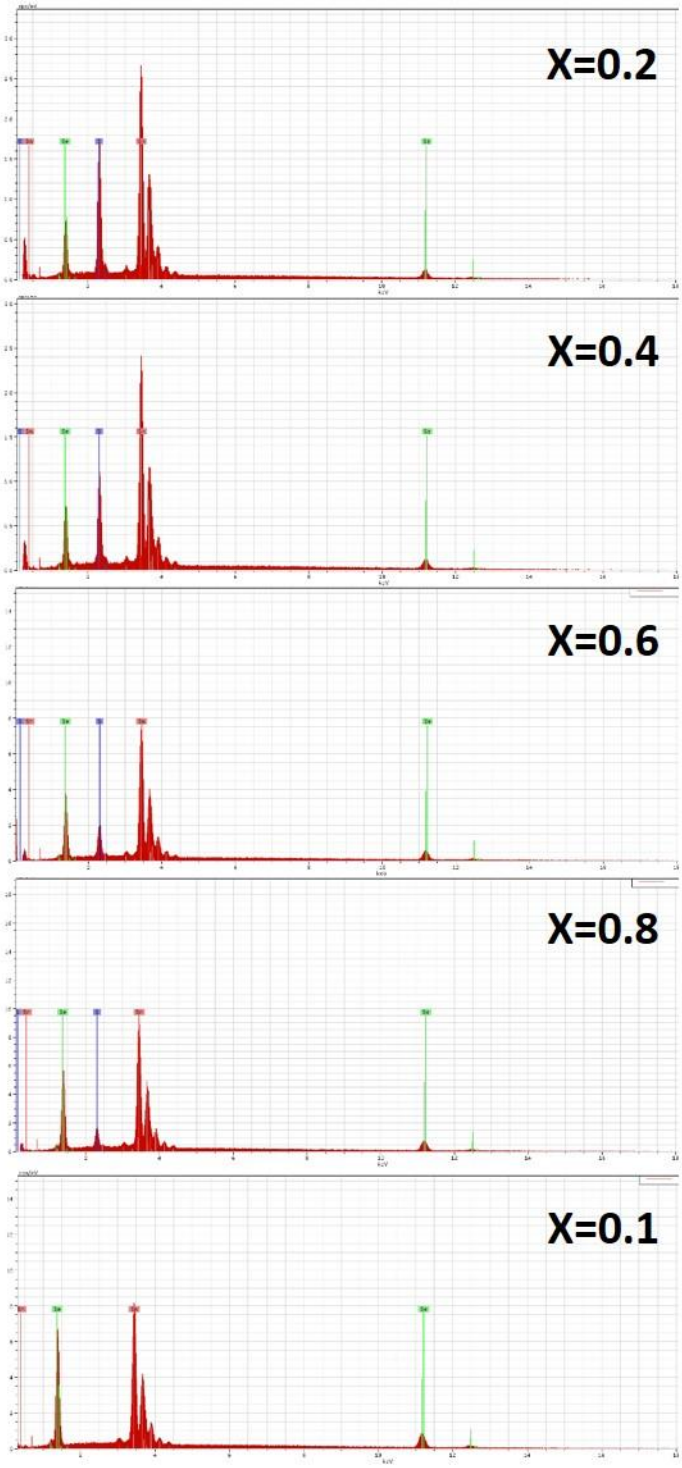

Figure 6.8. EDX analysis to measure the content of Sn, S and Se in the synthesized alloy solid solution.

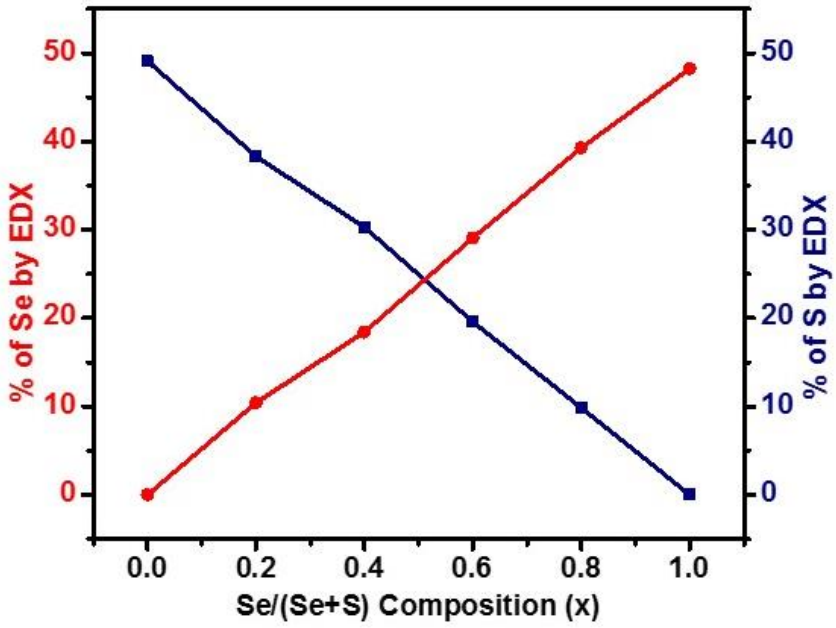

Figure 6.9. Plot showing change in the concentration of selenium and sulfur content against Se/(Se+S) composition.

Table 6.1. Summary of the required composition of the elements in solid solution and composition observed by the EDX analysis.

Composition [Se]/[Se]+[S]	**Target composition**	**Required Stoichiometry**	**EDX Sn:S:Se**	**Alloy stoichiometry**
0 (SnS)	SnS	50:50	50.9:49.1	$Sn_{1.02}S_{0.98}$
0.2	$SnS_{0.80}Se_{0.20}$	50:40:10	51.3:38.3:10.4	$Sn_{1.03}S_{0.76}Se_{0.21}$
0.4	$SnS_{0.60}Se_{0.40}$	50:30:20	51.1:30.4:18.5	$Sn_{1.02}S_{0.61}Se_{0.37}$
0.6	$SnS_{0.40}Se_{0.60}$	50:20:30	51.4:19.6:29	$Sn_{1.03}S_{0.39}Se_{0.58}$
0.8	$SnS_{0.20}Se_{0.80}$	50:10:40	50.8:9.9:39.3	$Sn_{1.02}S_{0.19}Se_{0.79}$
1 (SnSe)	SnSe	50:50	51.7:48.3	$Sn_{1.03}Se_{0.97}$

The even distribution of all the elements in the alloyed samples was analysed by the EDX elemental mapping, and a uniform distribution of Sn, S and Se was observed throughout the samples (Figure 6.10). The homogeneity of the

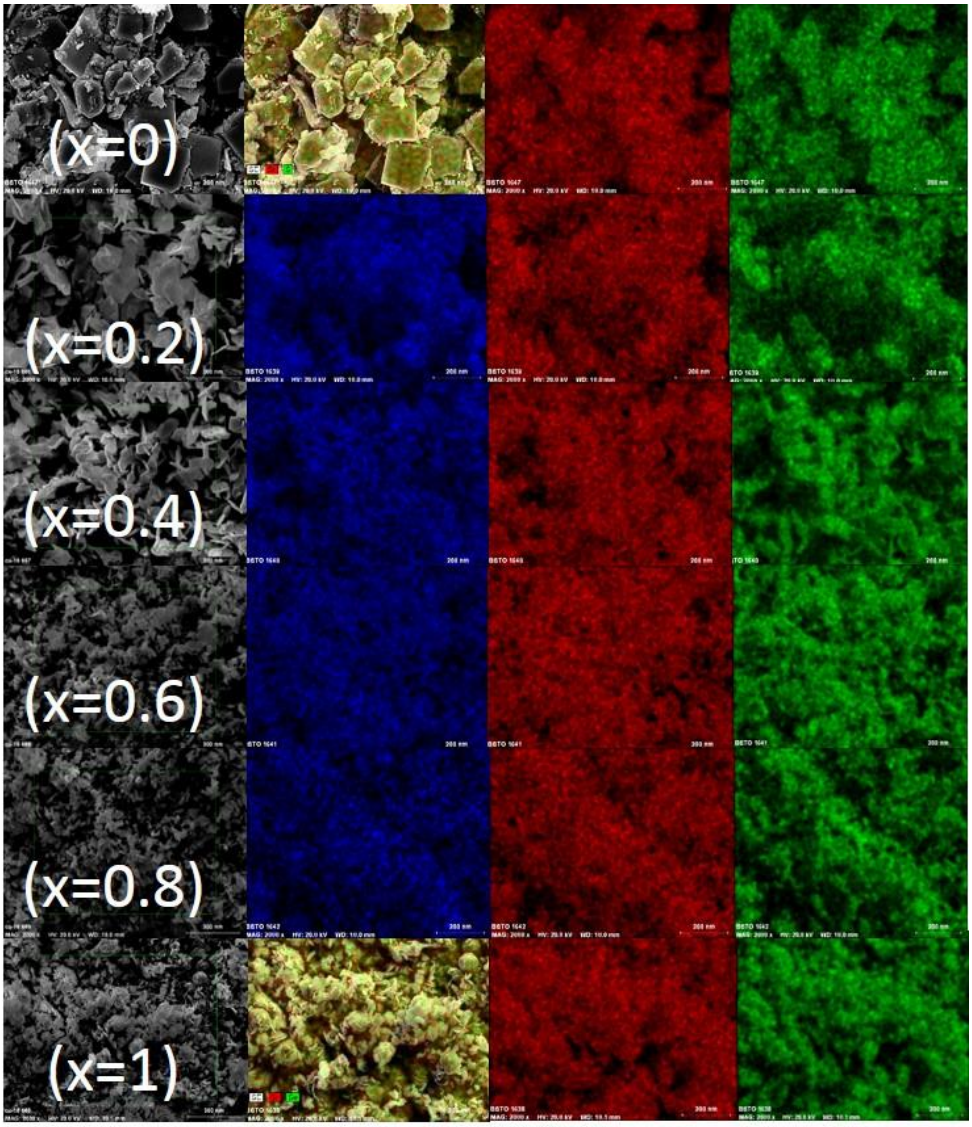

Figure 6.10. Elemental mapping of the samples with different selenium concentration, showing uniform distribution of tin, sulfur and selenium.

samples further confirms the formation of single phase and existence of both S and Se into same crystal structure.

The morphology of the synthesized binary and alloyed $SnS_{1-x}Se_x$ system was observed by SEM analysis and images are shown in Figure 6.11. The images are marked with different compositions of selenium from x = 0 to x = 1, and all presented images are taken at the same magnification for comparison.

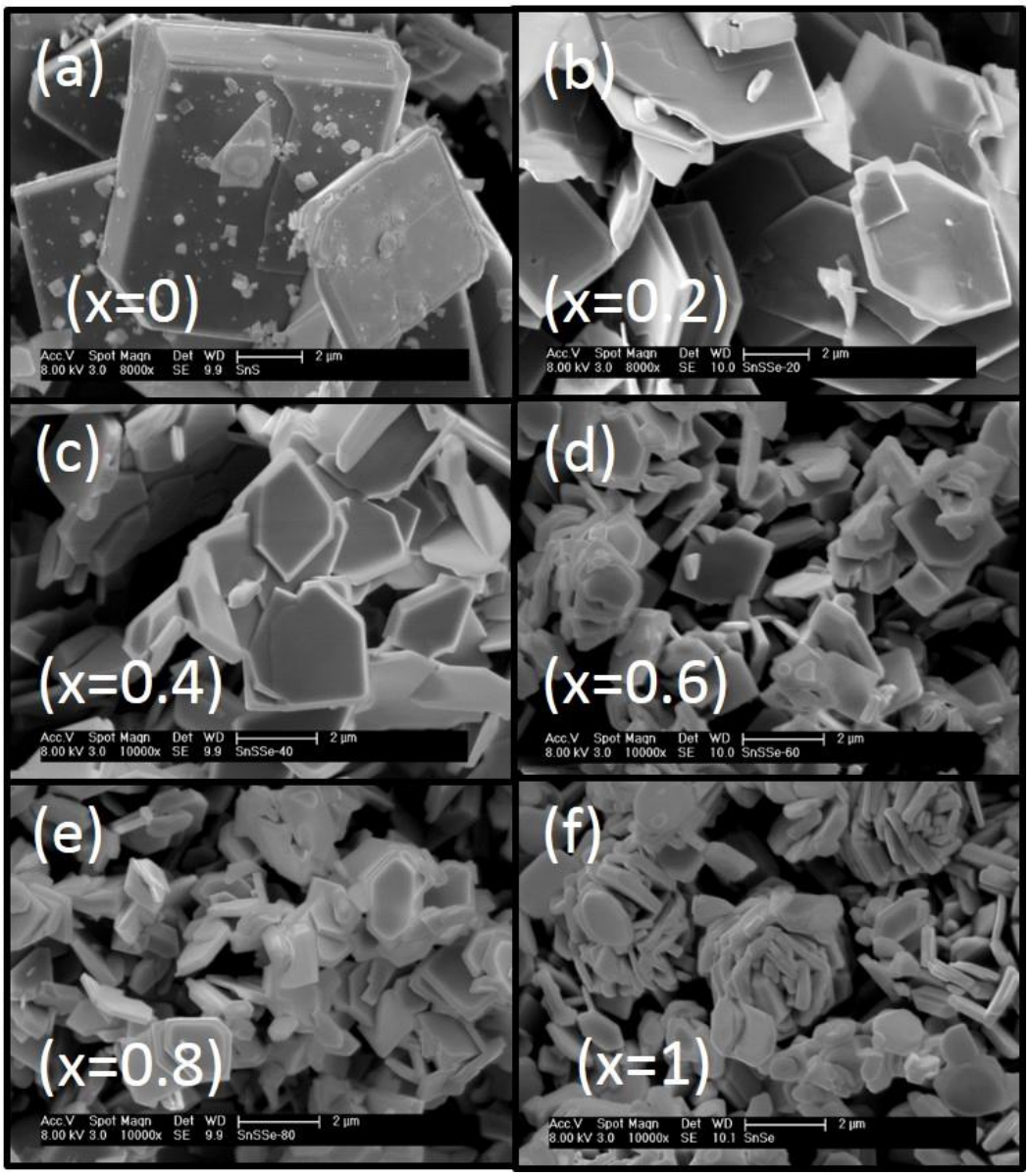

Figure 6.11. SEM images of (a) SnS, (b-e) $SnS_{1-x}Se_x$ and (f) SnSe sheets synthesized by the hot injection method.

SnS shows cubic sheet like structures, which is in the order of microns (Figure 6.11(a)). With the introduction of selenium, the sheets started transforming from cubic to a hexagonal shape (Figure 6.11(b,c)). Further increases in the selenium content resulted in the decreased size of the sheets,

and eventually short sheets or plate like structures, although still in micron range, appeared for SnSe.

In general, all the samples showed sheet like structures. Both SnS and SnSe are isostructural and growth of sheets can be explained on the basis of orientation and the kind of interactions present in their building blocks. The preferential growth crystallization for SnS is an orthorhombic structure with *Pnma* space group. Virtually, the SnS structure can be viewed as a slightly distorted rock salt structure, due to the withdrawal of electron density from Sn to more electronegative S atom.[40] Furthermore, the presence of a lone pair of electrons on the Sn atom has significant impact in distortion of the rock salt structure to the distorted orthorhombic layered structure. In the layered structure, the Sn atom is strongly connected to S atoms within the layer, with short and strong Sn-S bonds (≈ 0.266 nm), whereas the layers are interconnected to each other by comparatively long and weak Van der Waal's interactions (≈ 0.388 nm).[41] As a result, the layers of SnS can be easily separated and cleaved perpendicular to the *c*-axis. SnSe has a similar structure and bonding structure, hence all the samples showed sheet-like structure.

6.4.2. Solvent-less synthesis of $SnS_{1-x}Se_x$ solid solution

The $SnS_{1-x}Se_x$ solid solution was also synthesized by the solvent-less melt method. The melt method was used to observe the influence of the capping agent on the formation of the product. In the melt method, the compounds are heated under inert environment and the reactive melt formed undergoes decomposition, with removal of organic moieties, leading to the formation of the pure product. Thermogravimetric analysis indicates that, both complexes decompose completely in the temperature range of 305-315 °C, therefore a slightly higher temperature of 330 °C was used to ensure the complete decomposition of the complexes and high crystallinity of the product. The decomposition of the precursors yielded tin monochalcogeides respectively. The p-XRD analysis of SnS, $SnS_{1-x}Se_x$ and SnSe synthesized by the solvent-less method is shown in Figure 6.12.

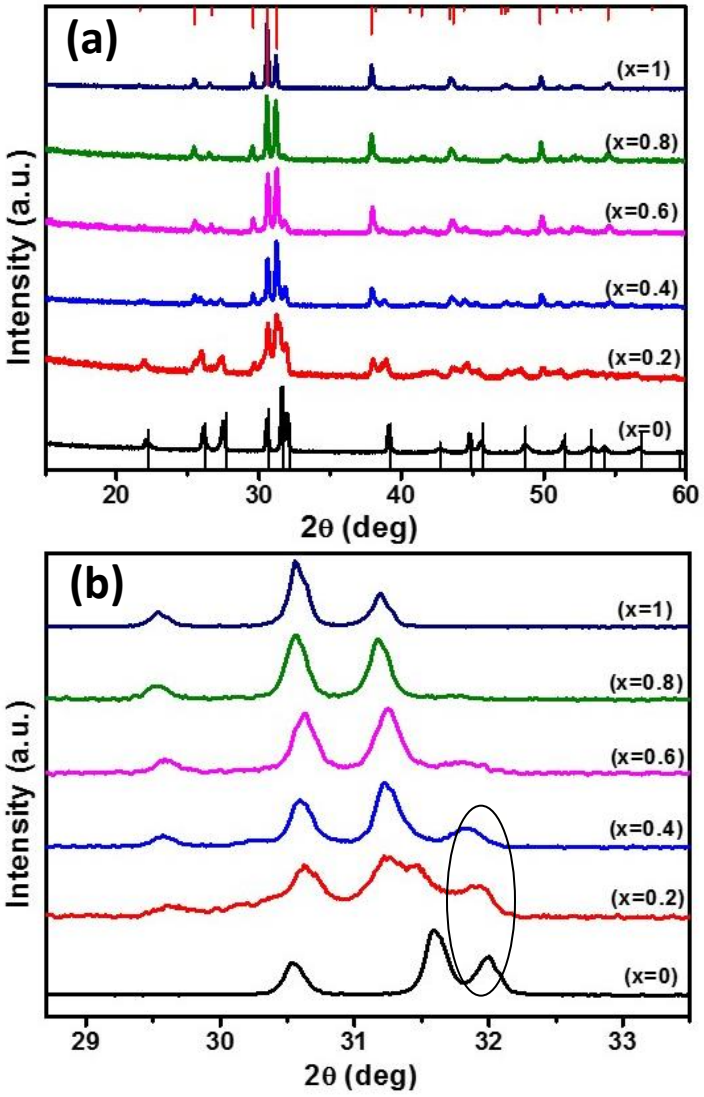

Figure 6.12. (a) p-XRD pattern of SnS, $SnS_{1-x}Se_x$ and SnSe synthesized by solvent-less route at 330 °C (b) extended part of p-XRD to show the shift in the peaks.

The peaks were sharp and the diffraction patterns for the binary tin monochalcogenides *i.e.* for the mole fraction x = 0 (SnS) and x = 1 (SnSe), matches well with the standard pattern and confirms the formation of the pure product. A shift in peak position was observed when the mixture of complexes was used to prepare solid solution, however, when the diffraction peaks were zoomed in, multiple peaks were also

observed as shoulders for the mole fraction value of x = 0.2 and x = 0.4. The splitting of the peaks present at 2θ = 30.5 to 32.5 shows that there is presence of SnS, which exist along with the solid solution and results in the phase segregation of the synthesized material. The separation was prominent at lower concentration of selenium (*i.e.* x = 0.2) and fades away at higher incorporation of selenium. The intensity profile was also different from the diffraction pattern observed for the samples synthesized by the colloidal method.

It was observed during TGA analysis that the complexes are volatile and undergo sublimation, making accurate residual mass determination difficult. Similarly, the volatile nature may be responsible for improper mixing, as some of the complex might have sublimed and decomposed on the walls of the ceramic combustion boat, and appear as an impurity in the final product. However, the selenium was also merged into the crystal lattice, which can be confirmed by the shift in the diffraction peaks due to the change in the *d*-spacing.

The expansion in the cell as a result of the change in lattice parameters was calculated from the data of the intense peaks present in the diffraction pattern (Figure 6.13). The change in the lattice parameters with respect to the composition was non-linear, it was observed that the maximum deviation occurred at the Se/(Se+S) composition of x = 0.2 and x = 0.4. The irregularity in the lattice parameters also compliments the p-XRD pattern, and the phase segregation can be seen clearly at these compositions. The change in volume of cell from SnS to SnSe was plotted against composition and as expected the alteration in the volume was also uneven (Figure 6.14).

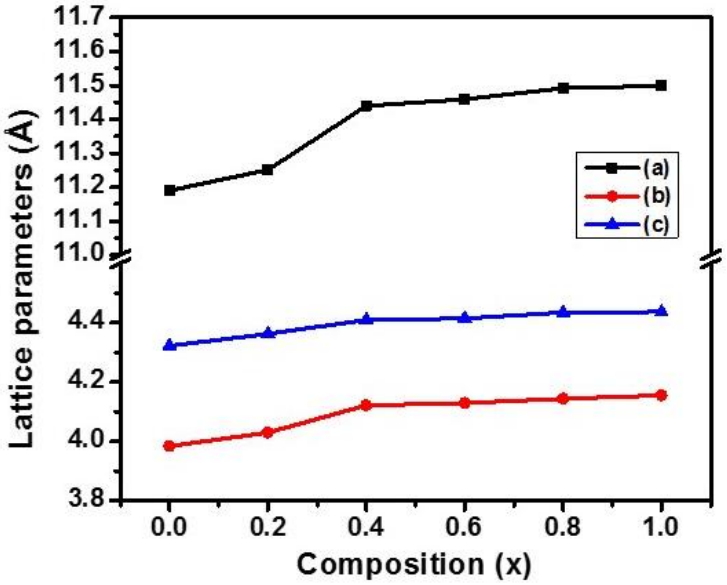

Figure 6.13. Lattice constants a, b, and c derived from the intense p-XRD diffraction peaks, as a function of Se concentration 'x' in the $SnS_{1-x}Se_x$ alloy system synthesized by the melt method.

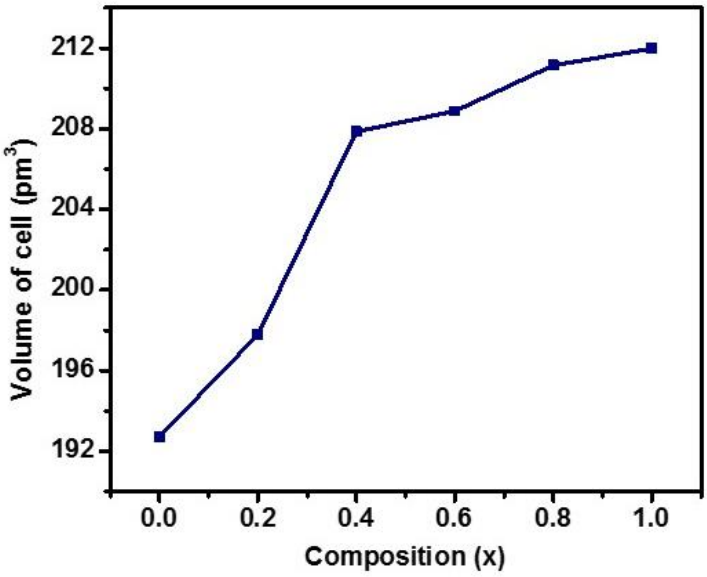

Figure 6.14. The change in the volume of the cell, as a function of Se concentration 'x' in the $SnS_{1-x}Se_x$ alloy system synthesized by the melt method.

The EDX analysis was conducted to have an insight of the composition of the solid solution synthesized by the solvent-less melt method (Figure 6.15). The analysis

reveals that the binary as well as ternary alloys were chalcogenide deficient materials. Although, the amount of both sulfur and selenium was less than the required value, it can be seen that the deviation in the case of selenium is even more as compared to sulfur. Furthermore, the composition of the binary compounds *i.e.* SnS and SnSe also shows higher deficiency of selenium in SnSe as compared to sulfur in SnS (Figure 6.16). It shows that the sulfur is more competitive in the reaction conditions used for the melt method. The deficiency of the chalcogenides is probably due to the high temperature used, and high partial pressure associated with the chalcogens. It is a common observation that thin films of metal chalcogenides deposited at high temperature are often chalcogen deficient.[42] Hence, the stoichiometry of the synthesized alloys by melt method is significantly altered (Table 6.2) as compared to the alloys prepared by colloidal method.

Table 6.2. Summary of the required composition of the elements and composition observed by EDX analysis for samples synthesized by melt method.

Composition [Se]/[Se]+[S]	**Target composition**	**Required Stoichiometry**	**EDX Sn:S:Se**	**Alloy stoichiometry**
0 (SnS)	SnS	50:50	53.5:46.5	$Sn_{1.07}S_{0.93}$
0.2	$SnS_{0.80}Se_{0.20}$	50:40:10	52.9:38.5:8.6	$Sn_{1.06}S_{0.77}Se_{0.17}$
0.4	$SnS_{0.60}Se_{0.40}$	50:30:20	52.7:29.1:18.2	$Sn_{1.05}S_{0.58}Se_{0.37}$
0.6	$SnS_{0.40}Se_{0.60}$	50:20:30	55.5:18.8:25.7	$Sn_{1.11}S_{0.37}Se_{0.52}$
0.8	$SnS_{0.20}Se_{0.80}$	50:10:40	54.3:9:36.7	$Sn_{1.08}S_{0.18}Se_{0.74}$
1 (SnSe)	SnSe	50:50	55.5.:44.5	$Sn_{1.11}Se_{0.89}$

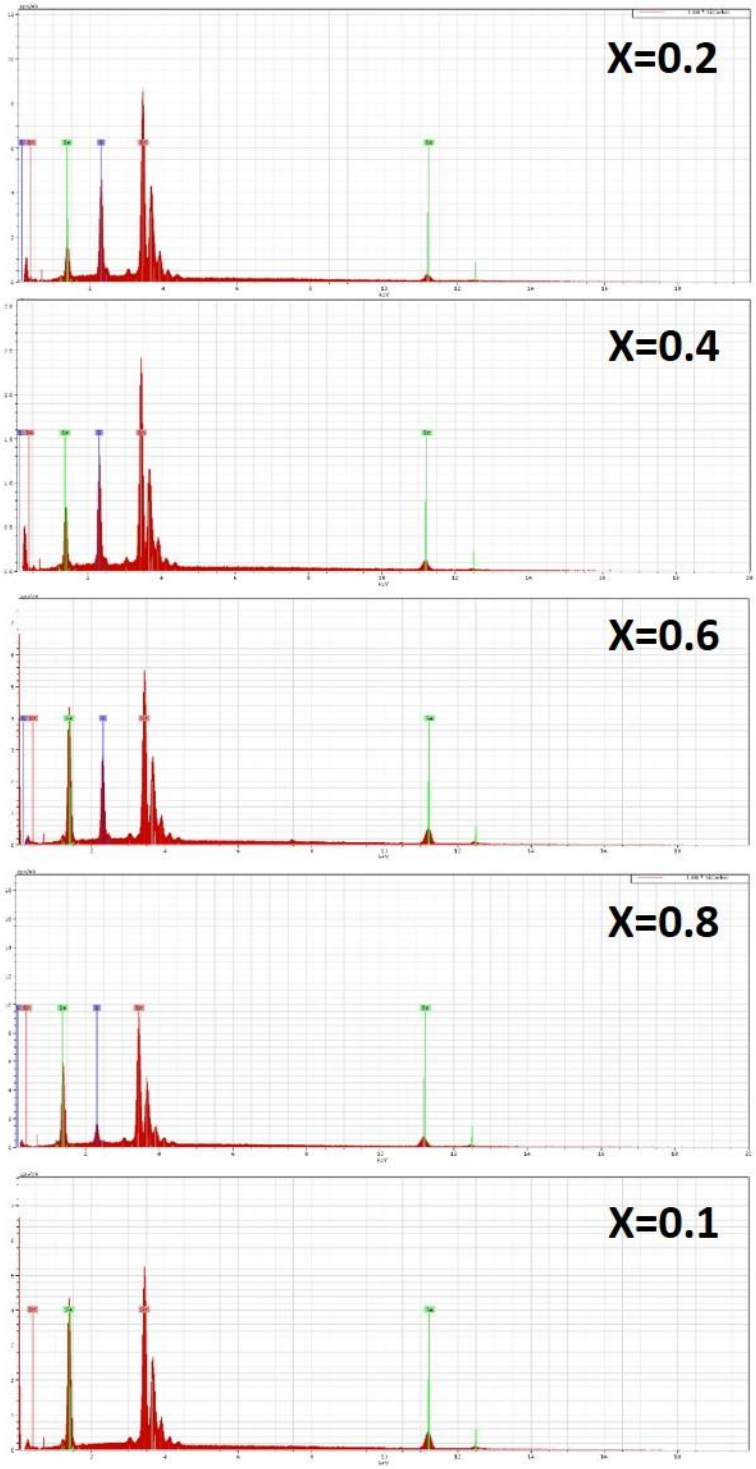

Figure 6.15. EDX analysis to measure the content of Sn, S and Se in the synthesized alloy solid solution.

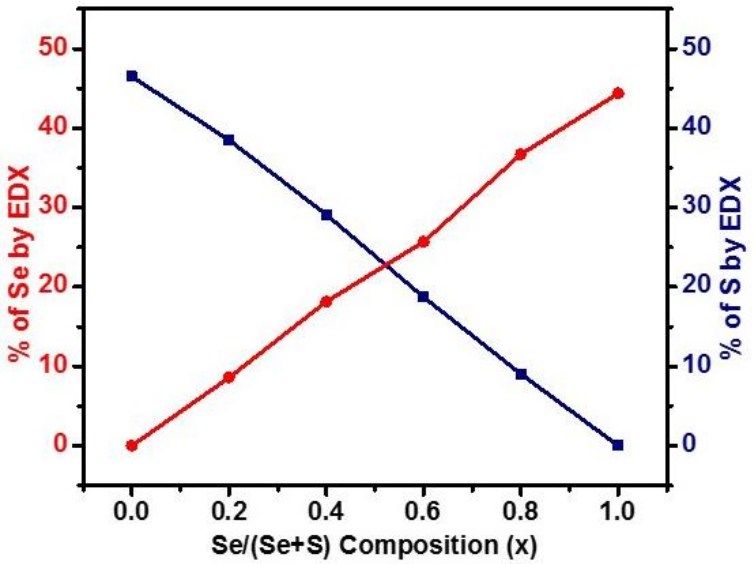

Figure 6.16. Plot showing change in the concentration of selenium and sulfur content against Se/(Se+S) composition.

The morphology as determined by SEM, indicates the formation of sheet-like structures for all samples, which shows that the morphology was not influenced by the difference in the method of preparation (Figure 6.17). The Van der Waal's interactions between the sheets are too fragile to sustain under harsh conditions such as presence of strong nucleophilic ligand and/or high temperature. The control over size also becomes challenging in such situations. It can be seen that the size of the SnS sheets (Figure 6.16(a)) is in the micron range and unlike OLA capped SnS, which shows predominantly cube like sheets, a mixture of irregular and hexagonal shaped plates were observed.

After the inclusion of selenium in the lattice, the morphology of the sheets showed a hexagonal-like structure but with some eroded edges. At higher selenium concentration *i.e.* when x = 0.6 and 0.8, the shape became more defined and the size of the crystallites was also decreased. The trend of decreasing size in moving from SnS to SnSe, was similar to the pattern observed for the samples synthesized by the colloidal synthesis.

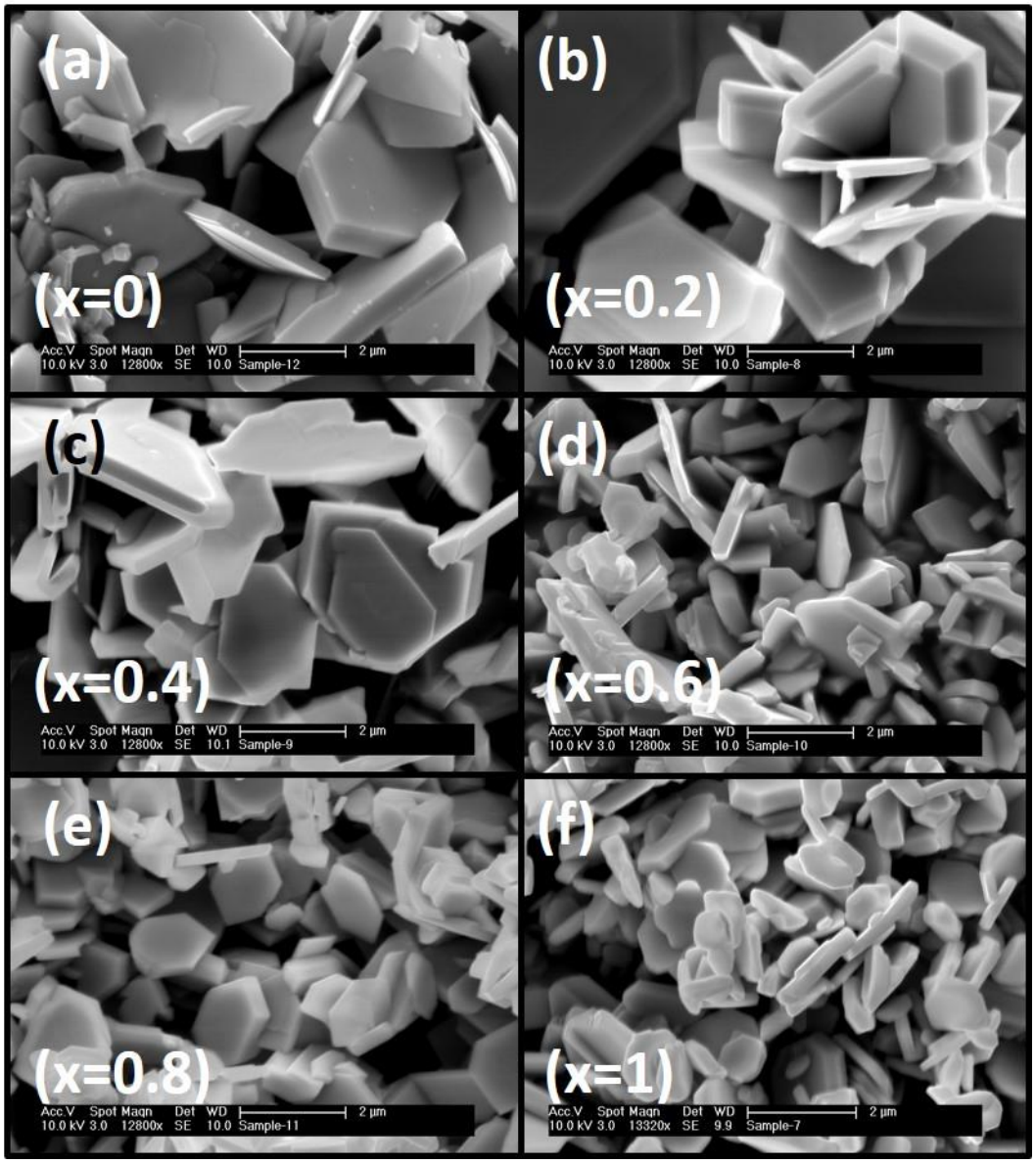

Figure 6.17. SEM images of (a) SnS, (b-e) $SnS_{1-x}Se_x$ and (f) SnSe sheets synthesized by the melt method.

The homogenized distribution of all the elements in the $SnS_{1-x}Se_x$ system was observed by elemental mapping (Figure 6.18). The images show uniform distribution of the elements throughout the material.

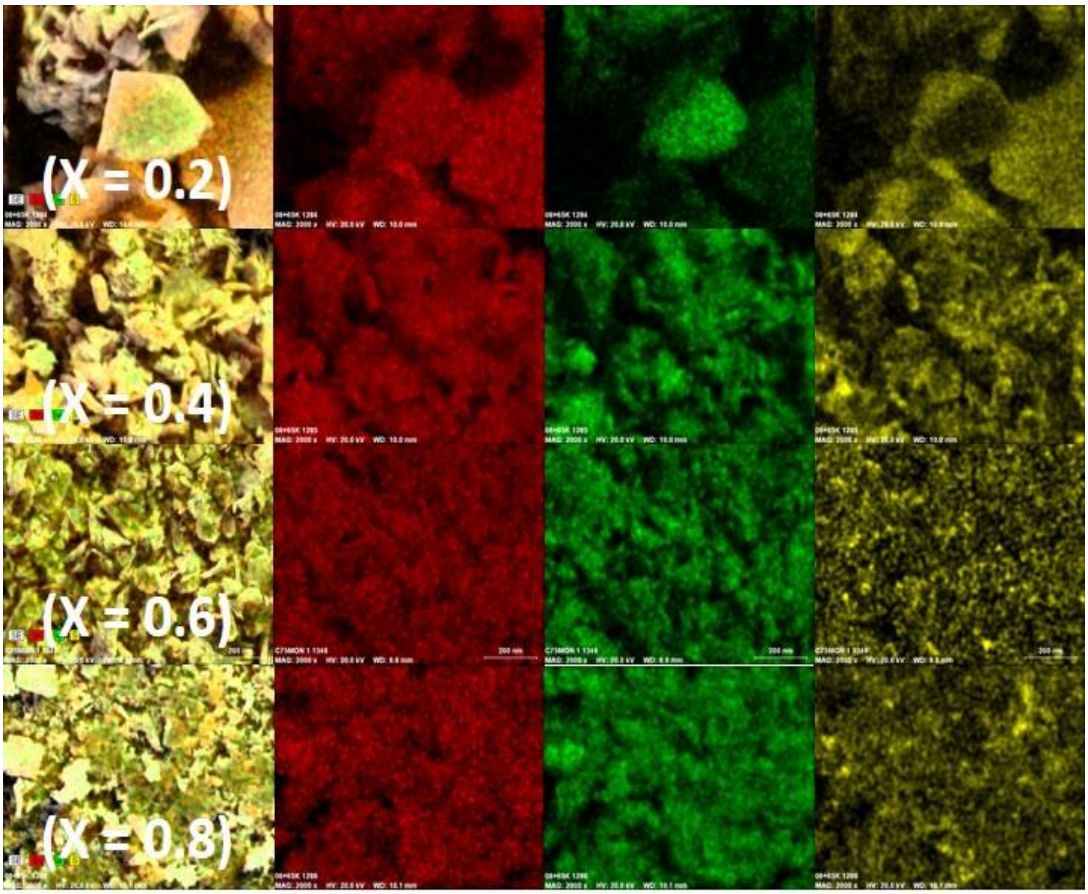

Figure 6.18. Elemental mapping of the samples with different selenium concentration, showing uniform distribution of tin, sulfur and selenium.

The optical behaviour of the solid solution series was investigated by the UV-Vis-NIR spectroscopy and is shown in Figure 6.19. The stoichiometry of the solid solution obtained by colloidal method was comparatively better, hence, only those samples were used for the optical studies. The band gap decreases slightly (from 1.48 to 1.1 eV) with addition of selenium, and it can be seen that there is a little difference in band gaps of $SnS_{1-x}Se_x$ system. Similar observations have been reported earlier and it can be assumed that it is due to the similar nature of their band structures.

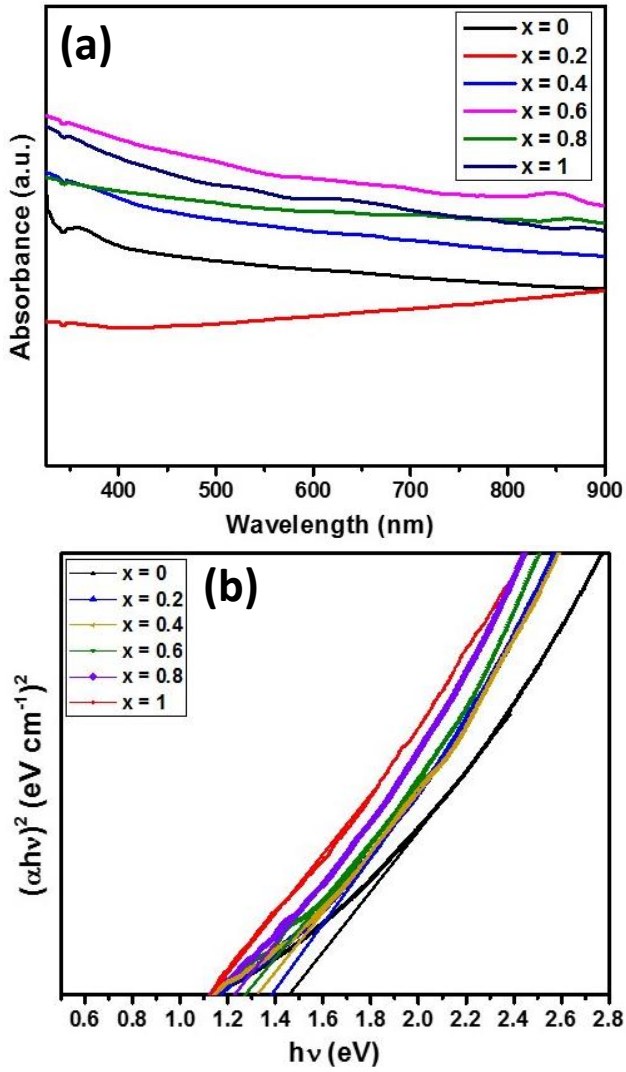

Figure 6.19. (a) The UV-Vis-NIR spectra and (b) band gaps of the solid solution prepared by colloidal method.

6.5. Conclusion

Thio/seleno-benzoate complexes of organotin were synthesized and used as single source precursors for the synthesis of SnS, SnSe and $SnS_{1-x}Se_x$ solid solution over entire range, by two different synthetic routes. Although the complexes were volatile, which results in ambiguity in TGA but p-XRD indicates clean decomposition to SnS and /or SnSe. In the colloidal route, OLA was used as the capping agent which helps in the decomposition of the complexes at

temperatures lower than their decomposition temperature. Whereas, the melt method requires a high decomposition temperature of 350 °C. The volatility of complexes causes some problems such as, sublimation of the complexes and the resultant decomposition products were also observed to be chalcogen deficient.

The single source precursors provide efficient incorporation of selenium and a better control over composition was achieved by colloidal hot injection method, as determined by EDX analysis and gradual change in lattice parameters. In comparison, the change in lattice parameters was not smooth for the product obtained by the melt method and EDX analysis also shows a wider deviation from the required percentage. The morphology was independent of the method used, and a similar trend in size and shape was observed for both approaches. The route can be used for scalability of the solid solution and can be extended to other systems as well.

6.6. References

1. C. Lin, W. Cheng, Z. Guo, G. Chai and H. Zhang, *Physical Chemistry Chemical Physics*, 2017, **19**, 23247-23253.
2. K. Peng, H. Wu, Y. Yan, L. Guo, G. Wang, X. Lu and X. Zhou, *Journal of Materials Chemistry A*, 2017.
3. Y. Zhang, S. Hao, L.-D. Zhao, C. Wolverton and Z. Zeng, *Journal of Materials Chemistry A*, 2016, **4**, 12073-12079.
4. C. Lee, X. Wei, J. W. Kysar and J. Hone, *Science*, 2008, **321**, 385-388.
5. K. I. Bolotin, K. Sikes, Z. Jiang, M. Klima, G. Fudenberg, J. Hone, P. Kim and H. Stormer, *Solid State Communications*, 2008, **146**, 351-355.
6. K. F. Mak, C. Lee, J. Hone, J. Shan and T. F. Heinz, *Physical Review Letters*, 2010, **105**, 136805.
7. C.-J. Liu, S.-Y. Tai, S.-W. Chou, Y.-C. Yu, K.-D. Chang, S. Wang, F. S.-S. Chien, J.-Y. Lin and T.-W. Lin, *Journal of Materials Chemistry*, 2012, **22**, 21057-21064.
8. H. Ramakrishna Matte, A. Gomathi, A. K. Manna, D. J. Late, R. Datta, S. K. Pati and C. Rao, *Angewandte Chemie International Edition*, 2010, **49**, 4059-4062.
9. M. D. Khan, J. Akhtar, M. A. Malik, M. Akhtar and N. Revaprasadu, *New Journal of Chemistry*, 2015, **39**, 9569-9574.
10. A. Gupta, T. Sakthivel and S. Seal, *Progress in Materials Science*, 2015, **73**, 44-126.
11. J. Wilson and A. Yoffe, *Advances in Physics*, 1969, **18**, 193-335.
12. F. Hulliger, *Levy (D. Reidel Publishing Company, Dordrecht, 1976)*, 1976, 279.
13. F. K. Butt, M. Mirza, C. Cao, F. Idrees, M. Tahir, M. Safdar, Z. Ali, M. Tanveer and I. Aslam, *CrystEngComm*, 2014, **16**, 3470-3473.
14. J. Vidal, S. Lany, M. d'Avezac, A. Zunger, A. Zakutayev, J. Francis and J. Tate, *Applied Physics Letters*, 2012, **100**, 032104.
15. Y.-M. Han, J. Zhao, M. Zhou, X.-X. Jiang, H.-Q. Leng and L.-F. Li, *Journal of Materials Chemistry A*, 2015, **3**, 4555-4559.
16. T. Mahalingam, V. Dhanasekaran, G. Ravi, R. Chandramohan, A. Kathalingam and J.-K. Rhee, *ECS Transactions*, 2011, **35**, 1-10.
17. H. G. Von Schnering and H. Wiedemeier, *Zeitschrift für Kristallographie-Crystalline Materials*, 1981, **156**, 143-150.

18. I. Lefebvre, M. Szymanski, J. Olivier-Fourcade and J. Jumas, *Physical Review B*, 1998, **58**, 1896.
19. M. A. Franzman, C. W. Schlenker, M. E. Thompson and R. L. Brutchey, *Journal of the American Chemical Society*, 2010, **132**, 4060-4061.
20. K. A. Campbell and C. M. Anderson, *Microelectronics Journal*, 2007, **38**, 52-59.
21. J. Ning, G. Xiao, T. Jiang, L. Wang, Q. Dai, B. Zou, B. Liu, Y. Wei, G. Chen and G. Zou, *CrystEngComm*, 2011, **13**, 4161-4166.
22. P. Sinsermsuksakul, L. Sun, S. W. Lee, H. H. Park, S. B. Kim, C. Yang and R. G. Gordon, *Advanced Energy Materials*, 2014, **4**.
23. V. Dhanasekaran, K. Sundaram, J. Jung and T. Mahalingam, *Journal of Materials Science: Materials in Electronics*, 2015, **26**, 1641-1648.
24. B. Subramanian, C. Sanjeeviraja and M. Jayachandran, *Materials Research Bulletin*, 2003, **38**, 899-908.
25. X. Wang, D. Chen, Z. Yang, X. Zhang, C. Wang, J. Chen, X. Zhang and M. Xue, *Advanced Materials*, 2016, **28**, 8645-8650.
26. L. Lu, L. Zhang, H. Zeng, B. Xu, L. Wang and Y. Li, *Journal of Alloys and Compounds*, 2017, **695**, 1294-1300.
27. H. Ju, M. Kim, D. Park and J. Kim, *Chemistry of Materials*, 2017, **29**, 3228-3236.
28. H. S. Im, Y. Myung, Y. J. Cho, C. H. Kim, H. S. Kim, S. H. Back, C. S. Jung, D. M. Jang, Y. R. Lim and J. Park, *RSC Advances*, 2013, **3**, 10349-10354.
29. P. Boudjouk, M. P. Remington, D. J. Seidler, B. R. Jarabek, D. G. Grier, B. E. Very, R. L. Jarabek and G. J. McCarthy, *Materials Research Bulletin*, 1999, **34**, 2327-2332.
30. P. Boudjouk, D. J. Seidler, D. Grier and G. J. McCarthy, *Chemistry of Materials*, 1996, **8**, 1189-1196.
31. R. Mattes and D. Rühl, *Inorganica Chimica Acta*, 1984, **84**, 125-127.
32. W. P. Lim, C. T. Wong, S. L. Ang, H. Y. Low and W. S. Chin, *Chemistry of Materials*, 2006, **18**, 6170-6177.
33. W. P. Lim, Z. Zhang, H. Y. Low and W. S. Chin, *Angewandte Chemie International Edition*, 2004, **43**, 5685-5689.
34. O. Niyomura and S. Kato, *Chalcogenocarboxylic Acid Derivatives*, 2005, 1-12.

35. J. Bréger, M. Jiang, N. Dupré, Y. S. Meng, Y. Shao-Horn, G. Ceder and C. P. Grey, *Journal of Solid State Chemistry*, 2005, **178**, 2575-2585.
36. U. Mizutani, *Hume-Rothery Rules for Structurally Complex Alloy Phases*, CRC Press, 2016.
37. D. Menezes, G. De Lima, F. Carvalho, M. Coelho, A. Porto, R. Augusti and J. Ardisson, *Applied Organometallic Chemistry*, 2010, **24**, 650-655.
38. M. T. Ng, C. Boothroyd and J. J. Vittal, *Chemical Communications*, 2005, 3820-3822.
39. Z. Huo, C.-k. Tsung, W. Huang, X. Zhang and P. Yang, *Nano Letters*, 2008, **8**, 2041-2044.
40. W. Tremel and R. Hoffmann, *Inorganic Chemistry*, 1987, **26**, 118-127.
41. N. Koteeswara Reddy, M. Devika and E. Gopal, *Critical Reviews in Solid State and Materials Sciences*, 2015, **40**, 359-398.
42. Z. Zainal, S. Nagalingam, A. Kassim, M. Z. Hussein and W. M. M. Yunus, *Solar Energy Materials and Solar Cells*, 2004, **81**, 261-268.

Chapter # 7

Summary, Conclusion and Future work

7.1. Summary and Conclusion

Anisoptropic nanomaterials are important class of semiconductor materials, due to their directional behaviour. The efficiency of the materials can be enhanced many folds, which is difficult to be achieved simply by the size control. The use of single source is advantageous, as they are equally suitable for both powdered nanomaterials and thin films. Moreover, a precise control over stoichiometry, phase and morphology can be achieved easily as compare to use of dual or multi source precursors. Similarly, the deposition of thin films from multi source route is cumbersome; more chances of pre-reaction and reproducibility is difficult due to stoichiometric variations. Hence, the use of single source precursor is highly desirable.

Among metal chalcogenides, the single source precursors for metal sulphide nanoparticles/thin films are well explored, however, little research has been done on use of selenium or tellurium based molecular precursors. The apparent reason of limited literature on the use of molecular precursors with heavier chalcogen atoms (Se, Te), is tedious synthetic routes and low stability. Similarly, phosphorus based complexes have been well explored, which might result in either phosphorus contamination or entirely different phosphate/phosphide product. Hence, a simple, atom efficient and comparatively non-toxic route is required to address the problems and to explore the deposition of metal selenide thin films and nanoparticles.

In our study, we have developed a new facile route, for the synthesis of selenobenzoate complexes in high yields, that too in short duration of time. The reagents used in synthesis were also comparatively non-toxic, and the complexes were formed *in situ*, without isolating the selenobenzoate ligand. The metals used for complexation (Sb, Bi, Sn), intrinsically favours the formation of anisotropic metal selenides and crystal structure of Sb_2Se_3 was also determined. The complexes were used for the synthesis of respective nanorods (Sb_2Se_3) and/or nanosheets (Bi_2Se_3, SnSe) by colloidal synthesis. The powdered product was also used for the electrochemical water splitting and promising results were

obtained. The efficiency of Sb_2Se_3 nanorods, for water splitting was found to be comparatively better than Bi_2Se_3 nanosheets. The electrochemical studies of SnSe nanosheets, indicates a bifunctional behaviour and can be used potentially for both oxygen evolution reaction and hydrogen evolution reaction.

Furthermore, the suitability of the complexes, for deposition of metal selenide thin films, was also established by the AA-CVD method. Sb_2Se_3 thin films showed rod like morphology, which changes to ribbon like morphology at higher temperature. Bi_2Se_3 films showed sheet like morphology, which doesn't seemed to be much affected by the change in temperature. The morphology of SnSe thin films was drastically changed from platelets to cubic rods with increase in temperature.

The complexes were also used in combination with thio- analogues to prepare metal sulfoselenide solid solution over the entire range. The $Sb_2(S_xSe_{1-x})_3$ solid solution was synthesized by colloidal route and optical properties were tuned with respect to change in composition. $SnS_{1-x}Se_x$ solid solution was prepared by solution and solvent less methods, and better results were obtained by solution synthesis of alloy nanomaterials.

The results indicate high versatility and potential for phosphorus free synthesis of morphology controlled metal selenide nanoparticles and thin films.

7.2. Future work

The work will be further extended to prepare metal selenide nanoparticle/thin films of other transition metals, such as, cobalt, nickel, iron and manganese. The complexes will also be used to prepare their solid solutions for optimization of their optical and electrical properties. The same synthetic route will also be used for the synthesis of tellurobenzoate complexes for the deposition of metal telluride thin films and nanoparticles.